To the Graduate Council:

I am submitting herewith a dissertation written by Mladen Totev Matev entitled "Self–Consistent Description of Rotational Properties of Highly Deformed States in Atomic Nuclei Far From Stability". I have examined the final paper copy of this dissertation for form and content and recommend that it be accepted in partial fulfillment of the requirements for the degree of Doctor of Philosophy, with a major in Physics.

Witold Nazarewicz, Major Professor

We have read this dissertation
and recommend its acceptance:

Carrol Bingham

Joseph March

Robert N Compton

Accepted for the Council:

Vice Provost and Dean of
Graduate Studies

Self-Consistent Description of Rotational Properties of Highly Deformed States in Atomic Nuclei Far From Stability

A Dissertation
Presented for the
Doctor of Philosophy
Degree
The University of Tennessee, Knoxville

Mladen Totev Matev
August 2003

Thesis
2003b
.M38

Copyright © 2003 by Mladen Totev Matev
All rights reserved.

This dissertation is dedicated to my parents and sister.

На моите родители,
к.ф-м.н. Тотю Трошев и Надежда Трошева
и на моята сестра Йорданка Матева
за обичта и безрезервната подкрепа във всичко
посвещавам този труд.

"What *are* we ?" he asked. "Why, we are the miracle of force
and matter making itself over into imagination and will.
Incredible. The Life Force experimenting with forms.
You for one. Me for another. The Universe has shouted itself alive.
We are one of the shouts. Creation turns in its abyss.
We have bothered it, dreaming ourselves to shapes.
The void is filled with slumbers; ten billion on a billion
bombardments of light and material that know not themselves.
Among so much that is flight and ignorance, we are the
blind force that grope like Lazarus from a billion-light-year tomb.
We say, O Lazarus Life Force, truly come ye forth. So the Universe,
a motion of deaths, fumbles to reach across Time to feel its own flesh
and know it to be ours. We touch both ways and find each other
miraculous because we are One ..."

— Ray Bradbury, Long After Midnight (G.B.S. – Mark V) [1]

Acknowledgements

As the writing of this work is coming to an end, I would like to express herewith my deepest gratitude to the many people, who helped me accomplish this dissertation.

I am most thankful to my academic Advisor, Professor Witold Nazarewicz for his guidance, encouragement, support, and patience, and for so many other things, which are impossible to list here. It has been a great pleasure for me to be able to work with a remarkable scientist and mentor, who helped me shape my ideas, and understand the complex material, which is the main subject of this work. His resourcefulness, keen constructiveness and wisdom were of immense importance for my achievement, and I was pleased with the fact that he entrusted me with the flexibility to pursue my studies in my own style and methods. So many times it was his direction and advice that kept me on track and made the accomplishment of this work possible. I am also very grateful to him for his financial support, and I enjoyed being his Teaching and Research Assistant during my years at the University of Tennessee. Witek, it is impossible for me to express my gratitude for everything you did to make this work come to a successful end — I will always remember you as my Advisor, Supporter and Friend, in this most rewarding intellectual accomplishment !

I would like to express my deepest gratitude to the members of my Ph.D. Committee, Professors Carrol Bingham, Joseph Macek, and Robert Compton, for their attention to the specifics of my Ph.D. work and physics qualification, as well as for their patience, support, and the careful reading of this dissertation. My special thanks goes to Professor Soren Sorensen, for his support and constructiveness with the technicalities related to my successful graduation from the Physics Ph.D. program at UT. Although on a very busy schedule, as the Head of the Department of Physics, his door was always open for me when I needed his advice or help. I want to thank the Nuclear Physics group at UT, for giving me the possibility to work in this fascinating field, to use the facilities, and to have ample opportunities to communicate about my nuclear physics problems at all levels. In the Group I also had the rare opportunity to meet our collaborators, Professors Jacek Dobaczewski (Warsaw), Mark Riley (FSU), and Drs. George Lalazissis (TU Münich / Thessaloniki), Wojciech Satuła (Warsaw), Anatoly Afanasjev, and S. Mizutori, with whom we were able to accomplish the publications covering part of the material in this work. I would like to especially thank Professor Lee Riedinger, who was the leader of the Nuclear Physics Group during my studies. His example has always been a great inspiration to me in my pursuits in Nuclear Structure, and for me he is a synonym for excellence and leadership in scientific research. I also learned a great deal about nuclear structure, spectroscopy and experiments with exotic nuclei, as well as their applications from the Nuclear Structure Seminar, led by Professors Riedinger, Bingham, and Nazarewicz during these years. I would like to also acknowledge my conversations and discussions with Dr. Alfredo Galindo–Uribarri, and Dr. Cyrus Baktash from the Oak Ridge National Laboratory. I have profitted immensely from my association with these men — it has been a long and marvelous journey, and I was only able to finish it with their generous professional support.

My former advisor, Professor Michael Guidry, deserves special recognition. He was the first person from UT I ever met, more than a decade ago in my home country, and his encouragement played a crucial role in my decision to come to UT Knoxville to pursue my Ph.D. degree. Under his supervision and informal guidance I made my first steps as a researcher in Nuclear Physics at the University and ORNL, and I was able to learn a lot from him in the fields of Nuclear Structure, Group Theory, and Computational Physics, and explore the beauty of the Fermion Dynamical Symmetry approach (FDSM). Thank you, Dr. Guidry for everything I learned under your thoughtful supervision, about physics, computation, and directions for my professional life

— I miss the time when I was your student, and you will always have a special place in my heart ! I would also like to gratefully acknowledge the support and cooperation of Dr. Yang Sun (my work on the Projected Shell Model, and numerical projection methods at high spin), as well as that of Professors Michael Strayer (UT/ORNL), Da–Hsuan Feng (Drexel University), Cheng–Li Wu (Taiwan), and Dr. Eric Ormand, with whom I had the honour to work and communicate in my early period in the Ph.D. program.

I would also like to express my gratitude to Drs. Jing-ye Zhang, David Dean, Darryl Hartley, Omar Zejdan, Bradley Smith, Robert Laird (FSU), William Mueller, Toshiyuki (Max) Misu, and many others for the fruitful discussions and information related to the theoretical and experimental aspects of my work. I want to specially recognize my supervisors as a Teaching Assistant at the Department of Physics, Prof. James Parks, and Prof. Alvin Sanders, whose attention, interest, and leadership opened my eyes to the beauty of physics research and teaching at UT. Herewith, I would also like to thank all the faculty of the Department, for the support, inspiration, and understanding of physics, which I was able to achieve with their consultations, teaching, and thoughtful mentorship. Thank you, Drs. Mario Stoitsov, Vesselin Dimitrov, Dimiter Balabanski, Anton Antonov, Georgi Kirchev, Pavel Kamenov, Matej Mateev, and of course most of all, Professor Borislav Slavov, my advisor at Sofia University, for your encouragement, and for openning so many doors in front of me in Nuclear Physics and related fields ! It is a special moment, which gives me an opportunity also to gratefully remember all my Physics professors, advisors and teachers, whose keen spirit has led me consistently to my goals as a physicist and computational scientist over the years, and my colleagues and students, with whom I have worked and communicated on an everyday basis. It is also my pleasure to thank the personnel of the UT Department of Physics, the Joint Institute for Computational Science (JICS), and the Joint Institute for Heavy–Ion Research / Physics Division of the Oak Ridge National Laboratory, who did everything within their possibilities to facilitate my work. This work was partially supported by the U.S. Department of Energy under Contract Nos. DE–FG02–96ER40963 (UT), DE–AC05–00OR22725 with UT–Battelle, LLC (ORNL), and the Polish Committee for Scientific Research (KBN), contract No. 2 P03B 040 14. I want to especially thank Kenneth Roche and Melinda Foster, who carefully read the final version of this manuscript for all of their remarks and suggestions.

I reserve this special paragraph for the expression of my deepest gratitude to my parents, Dr. Totyu Troshev and Nadezhda Trosheva, and my sister, Yordanka Mateva, CFA/MBA, who have always stood by me. Although most of the time thousands of miles away, they are always very close to my heart. Without their keen spiritual support, I hardly would have been able to make it to the end successfully. Thank you so much, I have had to rely on you in some of my most difficult moments ! Finally, I want to thank Edward Sevik, Ivan and Christina Filev, Dr. Elena Ivanova, Kristian, and all my many friends, Kenneth Roche, Dr. Christof Stumpf, Melinda Foster, Michael MacHaffey, Dr. P. Kumar Sarkar, Dr. Ludger Wirtz, Dr. George and Galina Daskalov, Dr. Plamen and Yolina Denchev, Dr. Stefan and Dessi Kirov, George and Diana Hranov, Steven McDaniel, Ali Maysam, Martin Djongolov, Mohammed Noor Tantawy, Robert Mahurin, Patrick Brantley, and my friends from the UT Sailing, Scuba, and Fencing Clubs, and the International House, with whom I had a marvelous and memorable time during my stay here. Thank you all for the love, fellowship, and the immense inspiration and encouragement towards my accomplishment of this arduous intellectual journey !

Abstract

This dissertation presents a theoretical study of rotational configurations in nuclei away from the line of β–stability : *i)* systematics of highly–deformed nuclear systems with moderate proton excess in the A$\sim$130 mass region, with the lightest of them closely approaching the proton drip line, *ii)* neutron–rich ^{30,32,34,36,38}Ne and ^{32,34,36,38,40}Mg nuclei, farthest away from the stability valley, with more than twice as many neutrons as protons. It uses successfully the mean–field approach for describing deformed nuclear states at high angular momenta, affirming that the self–consistent mean–field theories are well justified for use with a variety of different rotating nuclear systems, for which they offer significant predictive power.

We present the first fully self–consistent global set of high–spin calculations in the A$\sim$130 superdeformed region, using two conceptually different mean field theories : the non–relativistic cranked Skyrme Hartree–Fock method with SLy4 effective interaction (CSHF), and the cranked Relativistic Mean Field approach (CRMF). The results for 183 bands in CSHF and 105 bands in CRMF are used as a platform for the verification of the validity of the additivity approach in the A$\simeq$130 superdeformed region, providing computational infrastructure for extracting sets of effective single–particle quadrupole moments and angular momentum alignments, which can be used directly in experimental analyses. The high precision of the additivity approach, and the accumulated statistics in this systematics allows us to perform a comparative study among the two self–consistent models. Its success implies that the extreme shell model concept is well justified at high angular momenta. The provided effective single–particle values and relative total Routhians for the bands in the same nucleus allows experimentalists to calculate easily the expected deformations and alignments in superdeformed bands, and serve as guidelines for spectroscopical analyses. This dissertation includes for the first time also the quantitative impact of the effective values of q_{22} as corrections to the main effective quadrupole components q_{20} for the evaluation of the transition quadrupole moments q_t, allowing us to separate out the deformation components in this region known for its relatively well pronounced γ–softness. The results indicate that the single–particle alignments are robust quantities, not varying significantly among self–consistent models. The effective alignments in CSHF are overall different from the corresponding values of the single–particle alignments, indicating the importance of the shape polarization effects in the self–consistent mean field studies. The high precision of the additivity results gives reasons to believe that there is a conceptual universality in the self–consistent models for rotating superdeformed nuclei in the wider mass range A=128–160.

Our investigation of the properties of the very neutron–rich Ne and Mg nuclei leads for the first time to a quantitative understanding of their possible rotational behavior. The results show that there are sound physical reasons preventing the weakly bound intruder neutrons from "breaking away" under the influence of Coriolis and centrifugal forces at high cranking frequencies, thus offering a possibility for observation of rotational bands. The expected effect of the variation of the neutron shell structure with neutron number, mainly influencing the position of the high-j unique–parity shell, is balanced by the fact that the Coriolis force mainly acts on the high-j orbitals, which are strongly localized within the nuclear volume. As a result, no strong isovector effects (due to neutron halo or skin) are to be expected at high spins; the proton and neutron deformations are very similar even at extremely high rotational frequencies. The results show that for these nuclei the root–mean–square radii for protons and neutrons remain constant or within a narrow interval throughout the cranking frequency range. This work also makes predictions for the extent of the neutron drip line in the even–even Ne–Mg region, presents the very first cranking calculations for rotational bands in halo/skin nuclei, and discusses the structure of their yrast bands.

Contents

1 Introduction **1**
1.1 Historical Remarks 2
1.2 Rotational Properties and Nuclear Shapes 4
1.2.1 Superdeformation at High Angular Momenta 5
1.2.2 Deformed High Spin Systems Far From Stability 7
1.2.3 Rotating Mean Field 7
1.3 Brief Outline of the Following Chapters 9

2 Mean–Field Theory of Nuclear Rotation **13**
2.1 Rotating Deformed Mean Field 13
2.1.1 Deformation Parameters 14
2.1.2 Deformed Shell Model 16
2.1.3 Quantum Numbers of Deformed Orbitals 17
2.2 Nuclear Shapes at High Angular Momenta 19
2.2.1 Cranking Method and the Particle-plus-Rotor Model 20
2.2.2 Parity and Signature Quantum Numbers 23
2.2.3 Cranked–Model Analysis of Rotational Bands 24
2.3 Self–Consistent Mean Field 25
2.3.1 Hartree–Fock Method and Equations 25
2.3.2 Skyrme HF and RMF — An Overview 27
2.3.3 The Skyrme Hartree–Fock Method 28
2.3.4 Relativistic Mean Field Theory 34
2.4 Rotational Bands in HFODD 37
2.4.1 Self–Consistent Symmetries 37
2.4.2 Routhian Diagrams : The A$\simeq$130 Region 38
2.4.3 Level Crossings, Diabolic Points and Diabaticity 40
2.5 Jahn–Teller Mechanism of Core Polarization 42
2.6 Microscopic Origin of HD Rotational States 42
2.7 Phenomenology of Rotational Bands 44
2.7.1 End of Collective Rotation : Band Termination 47
2.7.2 Deformation of High–Spin Bands 50
2.7.3 Definitions 50
2.8 Additivity in Superdeformed Bands 51
2.8.1 The Case for Additivity 51
2.8.2 Additivity Assumptions and Procedure 52

3 Superdeformation in the A≃130 Nuclear Mass Region **55**
3.1 Overview of Superdeformed A∼130 Region 56
3.1.1 Typical Features of the Superdeformed Bands 56
3.1.2 SD Bands in the A∼130 Mass Region 56
3.2 HFODD Calculations — Convergence and Accuracy 59
3.2.1 Convergence of HFODD versus the HO Basis Deformation 59
3.2.2 Accuracy and Precision of the Additivity Analysis 61
3.3 The Core and Excited Configurations in ^{131}Ce 65
3.4 Results of the Additivity Analysis 65
3.4.1 Effective Quadrupole Moments for the Nilsson Orbitals 70
3.4.2 Effective Transition Moments q_t and q_{22} Corrections 74
3.4.3 Effective Angular Momenta of the Orbitals 76
3.4.4 Comparison With ^{142}Sm — HF Consistency Across the Region 76
3.5 Example Cases of SD Bands 79

4 High–Spin States in Light Neutron–Rich Nuclei **93**
4.1 Properties of Exotic Neutron–Rich Nuclei 93
4.2 Neutron Drip–Line Nuclei in the Ne–Mg Region 95
4.2.1 Theoretical Interpretations 96
4.3 Rotational Properties of Neutron–Rich Na and Mg Nuclei : Skyrme HF Results 98
4.3.1 The N=20 and N=22 Isotones 98
4.3.2 N=24 Isotones 103
4.3.3 Drip–Line Ne and Mg Isotopes with N=26 and 28 105
4.3.4 Shapes and Angular Momentum Alignments 105

5 Conclusion **113**

Bibliography **116**

Appendix **130**

A Doppler–Shift Attenuation Measurement of Q_o^π **131**

Vita **134**

List of Tables

3.1 Band configurations in low–lying SD bands in ^{131}Ce, calculated in the CHF+SLy4 model. 68
3.2 The CHF+SLy4 assigned configurations in ^{131}Ce. 69
3.3 Effective quadrupole moments $q_{20} \equiv q_{20}^{\rm eff}$ calculated in CHF and CRMF models. 71
3.4 Effective quadrupole moments q_t calculated in the framework of the Cranked Hartree-Fock with the Skyrme SLy4 and the Cranked Relativistic Mean Field. . 75
3.5 Effective single–particle angular momenta $i^{\rm eff}$ calculated in CHF and CRMF. . . 77
3.6 Some of the CHF+SLy4 configurations in ^{130}Ce. 80
3.7 The CHF+SLy4 configurations in ^{132,134}Ce. 84
3.8 The CHF+SLy4 configurations in ^{133}Ce. 85
3.9 The CHF+SLy4 configurations in ^{130,131}Pr. 86
3.10 The CHF+SLy4 configurations in ^{132,133}Pr. 87
3.11 The CHF+SLy4 configurations in ^{132,133}Nd. 88
3.12 The CHF+SLy4 configurations in ^{134,135}Nd. 89
3.13 The CHF+SLy4 configurations in ^{133,134}Pm. 90
3.14 The CHF+SLy4 configurations in ^{135,136}Pm. 91
3.15 The CHF+SLy4 configurations in ^{135,136,137}Sm. 92

List of Figures

1.1 Single–particle energy levels of an axially–symmetric deformed 3-dimensional oscillator potential well as a function of the deformation parameter δ_{osc}. 6
1.2 Portions of the Table of Isotopes showing the location and deformation ranges of the enhanced deformation (ED) and superdeformed (SD) mass regions A≃80, A≃130, A≃150, A≃190. 8
1.3 Experimental (Ref. [2], closed symbols with error bars) versus theoretical (this work, open symbols) differential transition quadrupole moments Q_t as a function of the number of neutrons. 11

2.1 Single–particle energy levels of an axially–symmetric deformed Nilsson Hamiltonian as a function of the deformation parameter ε_2. 18
2.2 Coupling of the collective ($\vec{R}$) and single–particle angular momenta ($\vec{j}$) in the particle–plus–rotor picture. 22
2.3 Diagram of the single–particle Routhians for the lowest ^{131}Ce superdeformed band as functions of the cranking frequency. 38
2.4 Single–neutron Routhians for ^{131}Ce calculated for the ν [18,19,18,18] configurations with (left) and without (right) the 6_1 intruder orbital. 41
2.5 Total Routhian surfaces for ^{132}Ce configuration (π, r)=(+,1) in the (β, γ) plane at fixed values of the cranking frequency, for which the ν $i_{13/2}$ gets occupied. . . 43
2.6 Schematic representation of a potential energy curve for ^{132}Ce illustrating the interplay between the normal deformation (ND) and superdeformed (SD) minima. 45
2.7 Schematic representation of the definitions of the phenomenological parameters of rotational bands and their behavior at a band crossing. 46
2.8 Calculated rotational band in ^{30}Ne, an example of band termination. 49

3.1 Nilsson diagram for the superdeformed rotating configurations in the Skyrme CHF calculations, showing the deformed region of interest, and the locations of the intruder and extruder orbitals. 57
3.2 Convergence of the ^{131}Ce core configuration as a function of the deformation of the basis q. 60
3.3 Side–by–side comparisons of the deviation distributions of the additive–fitted values for the quadrupole moment Q^{π}_{20}, and the total angular momentum I from their calculated values. 63
3.4 Similar to Fig. 3.3, but for Q^{π}_{22}. 64
3.5 Neutron single–particle Routhian diagram for the ^{131}Ce core configuration aligned in frequency with the observed level sequence in the superdeformed band SD-1. 66

3.6 Assignments for the two experimentally–observed SD bands in ^{131}Ce and comparison between their spectroscopic parameters and the corresponding Skyrme HF results. 67
3.7 Nilsson and Routhian diagram of the core configuration with the calculated effective neutron quadrupole moments q_{20}. 72
3.8 Similar as in Fig. 3.7 but for protons. 73
3.9 Routhian diagrams for superdeformed bands SD-1,2 in ^{142}Sm. 78
3.10 Neutron Routhians corresponding to band SD-3 in ^{130}Ce. 81
3.11 Single–particle Routhians of the two lowest candidates for the r=1 bands SD-2,4 in ^{130}Ce. 83

4.1 Part of the nuclear landscape showing halo nuclei and some of the structures far from stability. 94
4.2 Neutron (left) and proton (right) Nilsson diagrams in the vicinity of the ^{34}Mg Fermi level as a function of Q^{π}_{20}, calculated in CHF (*cf.* Fig. 2.1). 97
4.3 Single–particle Routhians, moments of inertia, and total angular momenta for the N=20 isotones of Ne and Mg as a function of ω. 99
4.4 Similar to Fig. 4.3 but for the lowest configurations in ^{32}Ne. 101
4.5 Single-particle Routhian diagram for $[7,7,4,4]_n$ configuration in ^{34}Mg 102
4.6 Single-particle Routhian diagram for the $\nu 3^4$ band in ^{34}Mg 103
4.7 Single–particle Routhian diagram for the lowest bands in the N=24 isotones of Ne and Mg. 104
4.8 Single-particle Routhian diagrams for the lowest bands in the N=26 isotones of Ne and Mg. 106
4.9 Single–particle Routhian diagrams for the N=28 isotones. 107
4.10 The ratio $\frac{I_\nu A}{IN}$ and $\frac{I_\pi A}{IZ}$ versus rotational frequency for the calculated bands in Ne and Mg. 108
4.11 Total energy, plotted with respect to a smooth reference, as a function of angular momentum in Ne bands (left), and Mg (right) isotopes. 109
4.12 Neutron and proton static ($\mathcal{J}^{(1)}$) and dynamic ($\mathcal{J}^{(2)}$) moments of inertia in Ne and Mg isotopes. 110
4.13 Neutron and proton (β_2,γ) deformation trajectories of the lowest band(s) in neutron–rich Ne and Mg isotopes starting with zero frequency (right ends). . . 111
4.14 Root–mean–square radii as functions of rotational frequency for several rotational bands in Ne (left) and Mg (right) isotopes. 112

A.1 Schematic diagram of the Doppler Shift Attenuation (DSAM), illustrating the relation between lifetime and the range between unshifted and fully shifted centroids of the transitions. 132

Chapter 1

Introduction

"Mind is the law–giver to Nature."

— I. Kant, *Critique of Pure Reason* (1781)

The atomic nucleus is one of the most interesting quantal many–body systems. Over the decades, nuclear science has allowed us to amass an impressive amount of structure information about the interacting constituents of the nucleus and their behavior, both theoretically and experimentally. The fact that the nucleus is a very tightly packed object, incorporating most of the mass of the atom, the early indications that it consists of particles held together by forces of enormous strength, the quantum laws unseen before, acting on a very small distance scale, and many other aspects of this new type of object, promised a wealth of insight into the ways multiparticle systems are formed and behave. Interest in the physical qualities and quantities of many–body systems, combined with the novel concepts of classical and quantum physics, providing possibilities to model mathematically the behavior of such objects, along with the opportunity to measure some of their physical features directly, became the moving force for discovering entirely new physics — the set of conceptual paradigms we often associate with the modern views of physical Nature. It would be fair to say that nuclear structure perhaps is the field of physics facing the many–body problem in its full complexity, leading to the development of ***ad hoc*** mathematical methods and models, which are also useful in other fields and applications. Our understanding of nuclear phenomena, in theory and experiment, made it possible to continue the study of the structure of matter at deeper levels of complexity, analytically and synthetically, towards more complete systematics of nucleon and sub–nucleon properties. We owe it to the vast variety of nuclear isotopes, "natural" and synthetic, to the experimental physics information collected about them, and to the multiple manifestations of the intrinsic properties of these systems, that we are able to to make conclusions about their mechanisms of behavior, microscopic and macroscopic, and with a degree of certainty comparable or better than that for some of the more classical objects around us.

The existing nuclear models necessarily involve the interpretation of properties of a multitude of isotopes at once — in the present work a couple of dozens of them. It is one of the purposes of this work to illustrate that the nuclear theoretical models we have at hand, although relatively simple, give us enough predictive power to describe properties of nuclei in different mass ranges,

stable and far from stability, having a variety of shapes, and with different (dis)balance of their proton–neutron composition. The fact that we can use these theoretical tools today is due, to a great extent, to the enormous progress in computational methods, along with their technological implementations achieved during the last century. It is my duty therefore to start with a brief outline of the historical developments of these ideas before I continue with the presentation of this dissertation. The sequence of these concepts, some of which were introduced many decades ago, comes to illuminate the marvelous unity of the physical world around us, the humble study of which is the main motivation for my work.

1.1 Historical Remarks

The atomic nucleus can take a wide variety of shapes, and the occurrence of highly-deformed configurations in nuclei has been known for decades. Within several years of the radioactivity studies of Henri Becquerel, and the team Maria Skłodowska–Curie—Pierre Curie (with Gustave Bémont), the α-scattering experiments of Ernest Rutherford shifted the attention to the nucleus at atom's core. With the intention to verify the charge distribution hypothesis of J. J. Thompson, Rutherford discovered [3, 4], that the atomic nucleus is a very dense and compact object (less than 100 fm in diameter), located in the center of the atom and concentrating more than 99% of its mass. The interpretation of nuclear properties and their impact on atomic physics, spectroscopy, and chemistry went along with the development of the concepts of quantum mechanics and the understanding that the nucleus is an essentially quantum–physical object. The aspects of nuclear physics that established links between the classical and quantum theories have been inseparable since the beginning of the nuclear era. The first suggestion that the nucleus can have a variety of different shapes, in ground or excited configurations, was made by W. Pauli in 1924 [5], who hypothesized that the hyperfine structure of electron levels in atoms and nuclei may be due to their Coulomb interaction with a non–spherically symmetric nuclear charge. His prediction was proven experimentally a decade later [6]. The discovery of the neutron by J. Chadwick [7, 8], and the induced nuclear transformations and radioactivity ((α, π)-reactions, in modern parlance) by I. Curie and F. Joliot [9], along with that of the positron by C. Anderson, made possible the use of nuclear reactions for obtaining structural information. The experimental confirmation of Pauli's hypothesis became the basis for the 1935 comprehensive study of total nuclear energy by Weizsäcker [10], and for Niels Bohr's introduction of the liquid drop model (LDM), in which nuclear surface shape vibrations around an equilibrium shape were considered for the first time [11]. Soon thereafter, a practical way of studying nuclear shapes and configurations by producing excited nuclear states in nuclear reactions and observing the emitted γ-spectra was proposed by N. Bohr and his student F. Kalckar [12, 13], who also estimated the energies of the lowest–energy rotational modes, and introduced the nuclear moment of inertia (also to be explored the next year [14]). At that time nobody could predict how fruitful this event in experimental methodology would turn out to be — it marked the beginning of spectroscopic methods for nuclear structure analysis. Their implementation led to the development of γ-ray spectroscopy, which is now the main work–horse methodology for gathering nuclear structure data. It is interesting to mention that the nuclear shape, although not directly observable, already was at the center of attention of the nuclear physics community immediately before World War II, due to its importance for the understanding of the nuclear fission process. The effects of shape and stability of a charged liquid drop were studied by Feenberg [15], and then by Meitner and Frisch [16], and Bohr and Wheeler [17]. The antebellum and war periods are also characterized by a significant (even by modern criteria) accumula-

tion of nuclear structural and reaction data, particularly in relation to the analysis and study of the fission process in actinides, which was subject to most extensive scrutiny at the time, and required systematic theoretical explanation. It became clear that rotational states, being abundantly produced by nuclear reactions, could provide very valuable information about the nuclear single–particle and collective modes.

The experimental data quickly piling up, their interpretation required novel concepts and quantitative approaches. The basic assumption, from which most of the low–energy theoretical models started, was that the atomic nucleus can be viewed as a set of non-relativistic nucleons interacting with each other via a two–body interaction, or an approximation thereof. A significant breakthrough in the early attempts to find such approximation was achieved by Göppert–Mayer and Jensen, who developed the nuclear shell model [18, 19] [1]. The stunning success of the shell model and its implications, suggesting analogies with the atomic shell structure and orbital classification schemes, led to feverish activity to interpret the existing nuclear data throughout the isotope table. Although we are still very far from fully understanding the form of the interaction in the nuclear medium, the important parts of it, crucial for nuclear structure studies, could be inferred from pion exchange and other few–meson exchange contributions. One of the most significant achievements of the Göppert–Mayer and Jensen's approach was their setting the stage for the establishment of the concept of nuclear *mean field* theories — the notion that the nucleons move "almost independently" from each other in an average, or mean field generated by their interactions with all other nucleons, at least at low excitation energies. The mean field paradigm is based on the assumption that the average nuclear interaction acting on the individual nucleons is roughly the same for every one of them (separately for protons and neutrons), and that it can be approximated with a scalar potential function in the Hamilton's equations, with its explicit form to be inferred from the density distribution of nuclear matter. From general phenomenological observations it was deduced that one–pion exchange terms would have the highest contributions to the average, their significance increasing with the density of real/virtual mesons in the nuclear medium with which the nucleon can "come into contact". The fact that the bare nucleon–nucleon interaction (*i.e.*, outside the medium) has both strong attractive (at long distances) and repulsive components (at short distances) is not a serious challenge to this picture, because the Pauli–blocking in the antisymmetrized wave function guarantees the mean–free path of the nucleons to be nearly the size of the nucleus itself. This justifies the concept of the nucleons moving quasi–independently in a "soup" of exchange pions, or other mesons, interacting with them through lowest–order interaction terms. The mean–field approach plays a significant role in our modern understanding of the nuclear mechanisms, and will be central to the ideas and interpretations discussed in this dissertation.

It became clear early in the development of nuclear structure physics that the majority of the known atomic nuclei are deformed in their ground states, and are capable of showing collective behavior even at very low excitation energies. The observations suggested that even though the nucleonic motion may seem "independent" in the static models, the average nuclear mean field, for the existence of which there is ample evidence, can give rise to highly–correlated modes, giving rise to vibrational–, or rotational–like spectral sequences. This necessitated further extensions of the theoretical models for the nuclear many–body problem to include collective behavior, especially in the context of the coupling between single–particle and collective nuclear degrees of freedom and different forms of their mixing in the full Hamiltonian. They culminated in the introduction of the nuclear collective model by A. Bohr, B. Mottelson, and J. Rainwater [20, 21] [2], which, together with the deformed ("Nilsson") shell model [23], developed at the

[1] They received the Nobel Prize in Physics for it in 1963.

[2] They were awarded the Nobel Prize in Physics for it in 1975, [22].

same time, became the paradigm for the interpretation of nuclear structure for decades to come. The first step in this direction was made by Flügge [24], who discussed nuclear surface vibrations and rotations, and suggested that nuclear rotations could be seen experimentally as rotational spectra. The observation of large quadrupole moments in atomic nuclei led Rainwater to conjecture as early as 1950 [20], that a single odd nucleon could polarize the nuclear shape. Bohr and Mottelson's approach recognized the fact that the static shape and orientation of the nuclear surface and the collective deformation parameters are closely related. It confirmed triumphantly the hypothesis of W. Pauli, that stable or quasi–stable deformed nuclear shapes are prevalent in the world of nuclear physics, and are fundamental for the understanding of nuclear properties at all levels. It also became a program for many discoveries of features of nuclear behavior which occurred in the field.

The beginning of the 1960's led to the experimental observation of fission isomers by Polikanov, *et al.* [25] in the actinide region, their existence being attributed to the possible formation of deformed minima in the potential energy surface (PES) [26, 27], and the studies of the "double–humped" fission barrier and more complicated fission landscape structures. This significant breakthrough led to further possibilities for exploring the conditions for the existence of highly–deformed and exotic nuclear shapes, together with the development of macroscopic–microscopic theoretical models for their interpretation. The observation of transitions from spherical to deformed and highly–deformed nuclear shapes, the breaking of reflection symmetry, *etc.*, are attributed to "phase transitions" caused by the interplay of the cumulative effects of nuclear interaction terms to the mean field. Many regions of the nuclear chart have become known as consisting of nuclei with stable shape deformation in ground or low excited states, and some nuclei exhibited excited states with deformation decidedly different from that of their ground states ("shape coexistence"). Prolate shapes approaching and exceeding 2:1 axis ratio of their principal axes, which are of considerable interest to our work, were first considered and parameterized for the understanding of the observed fission isomers in the Plutonium–Americium region. The concept of the "double–humped", "triple–humped" energy profiles, the quantitative understanding of fission barriers, the systematic studies of the nuclear potential energy surface (PES), *etc.* paved the way to a much more consistent picture of the interplay between shell structure and bulk nuclear properties. It also created a framework for the quantitative analysis of the nuclear forces, which shed light on the mechanisms of stabilization of complex nuclear shapes, and the microscopic reasons for the establishment of nuclear deformation. The experimental approaches of this period were characterized by significant progress in lithium–drifted germanium detectors to study short–lived states, including spectroscopy in the "second potential well" [28]. The spectroscopy of fission fragments provided a wealth of information about neutron–rich nuclei, which, combined with neutron and fragment detectors, shed light onto the mechanisms of compound nuclear formation, and the time scale of nuclear processes and phenomena, and created the necessary infrastructure for the study of reactions with accelerated light and heavier ions. The use of paired Ge–Li detectors in the 1970's became the basis for the spectroscopic study of high–spin states in nuclei.

1.2 Rotational Properties and Nuclear Shapes

In the context of this work, it is important to mention some of the basic concepts of the high–spin nuclear structure, which will be unfolded further in the next Chapters. The rapid improvement of spectroscopic detectors and the exploration of high–spin states in nuclei led to the observations that rotation may have significant effect on nuclear shape ([29, 30], and references therein).

These effects were first studied in the framework of the rotating liquid drop model (RLDM) by Cohen, Plasil and Swiatecki, in which a rigidly–deformed nuclear drop was cranked around a chosen axis [31]. At low rotational frequency, the initially spherical liquid drop develops a slightly oblate ellipsoidal deformation, which increases with angular momentum until a critical frequency is reached, beyond which triaxial shapes are energetically favored. This behavior became the basis for extensive study of potential energy surfaces of fissile heavy nuclei, for which the development of triaxiality precedes the formation of the fission fragments. The value of the maximal limiting angular momentum was studied and found to have a broad maximum for mass number around A $\simeq$ 130.

For the nuclear systems of interest in this work, the global rotational behavior based on the Cohen–Plasil–Swiatecki's picture does not tell the full story, because the single–particle degrees of freedom (*i.e.* the quantum effects) are known to impact nuclear behavior significantly. However, the generic dependence of the nuclear shape on rotational frequency exhibits features similar to those of the liquid drop, showing a tendency to stretch due to the centrifugal effects. When the nucleus has a stable prolate–deformed ground–state shape, it can gradually evolve to noncollective oblate shapes at high frequencies by showing transitions via different stages of triaxiality and regimes of rotation [32].

The discovery of the so–called *backbending* phenomenon, — *i.e.*, the sudden smooth change of the nuclear moment of inertia with rotation [33, 34] — was thought at first to be related to a phase transition of nuclear matter from superfluid to non-superfluid state. However, further studies provided evidence that this interesting behavior was associated with rotational alignment of pairs of nucleons in rotating mean field — a remarkable discovery, made by Stephens, *et al.* [35, 36], which led to tremendous progress in extracting nuclear structure information about the formation of total angular momentum and the relation between single–particle structure and collectivity. The spectroscopic data provided a wealth of information about the spin of valence nucleons, the energies of single–nucleon orbitals, shell gap widths, angular momenta and composition of rotational bands, and their deformation. Through the long series of discoveries [37] it became clear that the change of deformation of nuclear shape between and within rotational bands plays a paramount role in high–spin nuclear structure. The conjectured relation between the locations of shell gaps and the possibilities for stabilization of deformed nuclear shapes, particularly at higher angular momenta, fueled the interest into the search for nuclear shape isomerism and the investigation of mechanisms for its occurrence.

1.2.1 Superdeformation at High Angular Momenta

The experimental observation of fission isomers [25] in 1962 in the A$\sim$240 actinide region led to the hypothesis of the existence of deformed minima in the potential energy surface [26, 27] and the introduction of the "double-humped" fission barrier, and more complicated deformation structures. The first experimentally–observed prolate shape corresponding to the 2:1 ratio of principal axes ("superdeformed shape") was seen in the fission isomer of ^{242}Am [25, 40]. Deformed shell model calculations were first to indicate, that the highly–deformed nuclear mean field favors the appearance of energy gaps for certain ratios of ellipsoid axes. As one can see from Fig. 1.1, illustrating the single–particle spectrum of the deformed harmonic oscillator, energy gaps can indeed be expected for ellipsoidal shapes with axis ratios around 2:1, 3:1, *etc.*

In the framework of macroscopic–microscopic methods [41], shell gaps are displaced from their expected locations, and their sizes change significantly. In the early 1980's, theoretical calculations suggested that not only can the superdeformed configurations be observable for heavy nuclei at low angular momenta, but that for lighter nuclei they can be energetically

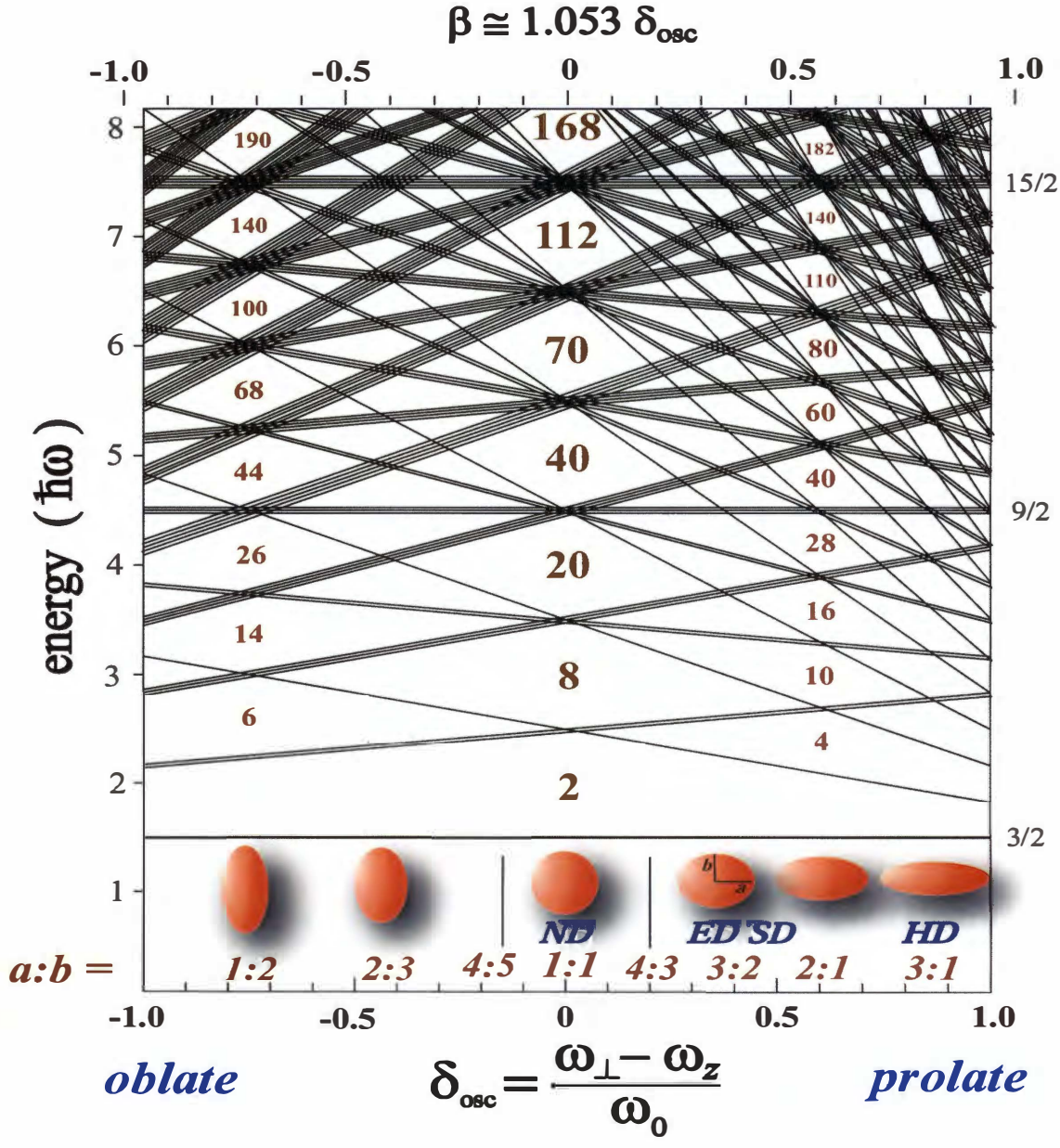

Figure 1.1: Single–particle energy levels of an axially–symmetric deformed 3-dimensional oscillator potential well as a function of the deformation parameter δ_{osc}. The degeneracy of states is indicated for each level by parallel lines. Note the occurrence of shell gaps at rational semi–axis ratios of a/b = 2:1, 3:1, *etc.* for prolate shapes. The notations are explained in Chapter 2. Adapted from [38, 39, 30].

favored at higher spins and become lowest in energy (*"yrast"*), and therefore become visible experimentally [27, 42, 43, 44]. They conjectured that superdeformed shapes could be found at high angular momenta in the rare–earth nuclei [45, 38, 46]. It became evident, for example, that the 3:2 ratio gaps could be more distinctly observed and expected to play a role for the light rare-earth nuclei and A$\sim$80 proton–rich nuclei. The 2:1 shapes are favored in fission isomers and A$\simeq$150 rare–earth systems.

The interest in systematizing rotational bands of nuclei with a perspective for studying states with higher deformation led to the development of very advanced γ–spectroscopic systems and facilities, and was fueled by the need for structure information. From the point of view of experimental methodology, it was the era of small arrays of γ–ray detectors, such as TESSA at the Daresbury Laboratory, UK. The calculations indicated that such highly–deformed shapes are likely to be seen in systems with considerable deviation of the neutron–to–proton number ratio from that for the valley of stability. The need to produce higher quantities of such "exotic" compound nuclear systems at high angular momenta made it necessary to use heavy–ion accelerators. The first experimental evidence for high–spin superdeformation was seen in the A$\simeq$150 region by B. Nyakó, *et al.* , in γ–γ correlations (quasicontinuum spectroscopy) of ^{152}Dy [47] (related to an earlier correlation study [48]). The authors deduced that the quadrupole deformation for the observed structures reached values as high as $\beta \approx 0.60$, corresponding to elongated shapes with axis ratios of 2:1:1, and soon thereafter the entire discrete superdeformed band was found [49]. This was a marvelous confirmation of calculations and a triumph for the predictive power of the existing models. It was followed by a feverish activity in the spectroscopy of rotating nuclei away from the β–stability area, which confirmed the shell–model expectations that highly–deformed shapes could be stabilized by shell effects, even far from the stability line. In 1986 a highly–deformed band in ^{132}Ce was discovered [50], and this put the A$\simeq$130 superdeformed mass region on the map for exploration. The quantitative and qualitative description of some of the systematized structure information from the observed highly–deformed bands in this region is one of the central themes in this dissertation.

1.2.2 Deformed High Spin Systems Far From Stability

Intense experimental studies of deformed structures across the chart of the nuclides has resulted to date in the discovery of several "islands" of high deformation, in the mass regions near A$\simeq$ 60, 80, 130, 150, 190, and 240, as well as in the neutron–rich Lu–Hf (N =92–96) region. They are shown in Fig. 1.2 (a) [51, 52, 53].

As one can see clearly from the Figure the observed bands with high deformation lie on the proton–rich side of the valley of β–stability, many of them several isospin units away from the nearest abundant isobar. Measurement of discrete rotational transitions from unstable compound nuclei, produced at very small cross–sections, necessitate the use of Compton–suppressed germanium detector systems in 4π-geometry, like GAMMASPHERE, EUROGAM, GASP. These developments also made it possible to carry out high–precision lifetime measurements, and directly determine deformation parameters of rotating nuclei.

1.2.3 Rotating Mean Field

A direct interpretation of the properties of highly–deformed nuclei with high excess of protons or neutrons demands the use of sophisticated theoretical models suitable for solving the nuclear many–body problem at high spin for configurations far from stability. The 1990's were a period of remarkable progress in the refinement of the existing microscopic models based on the shell–

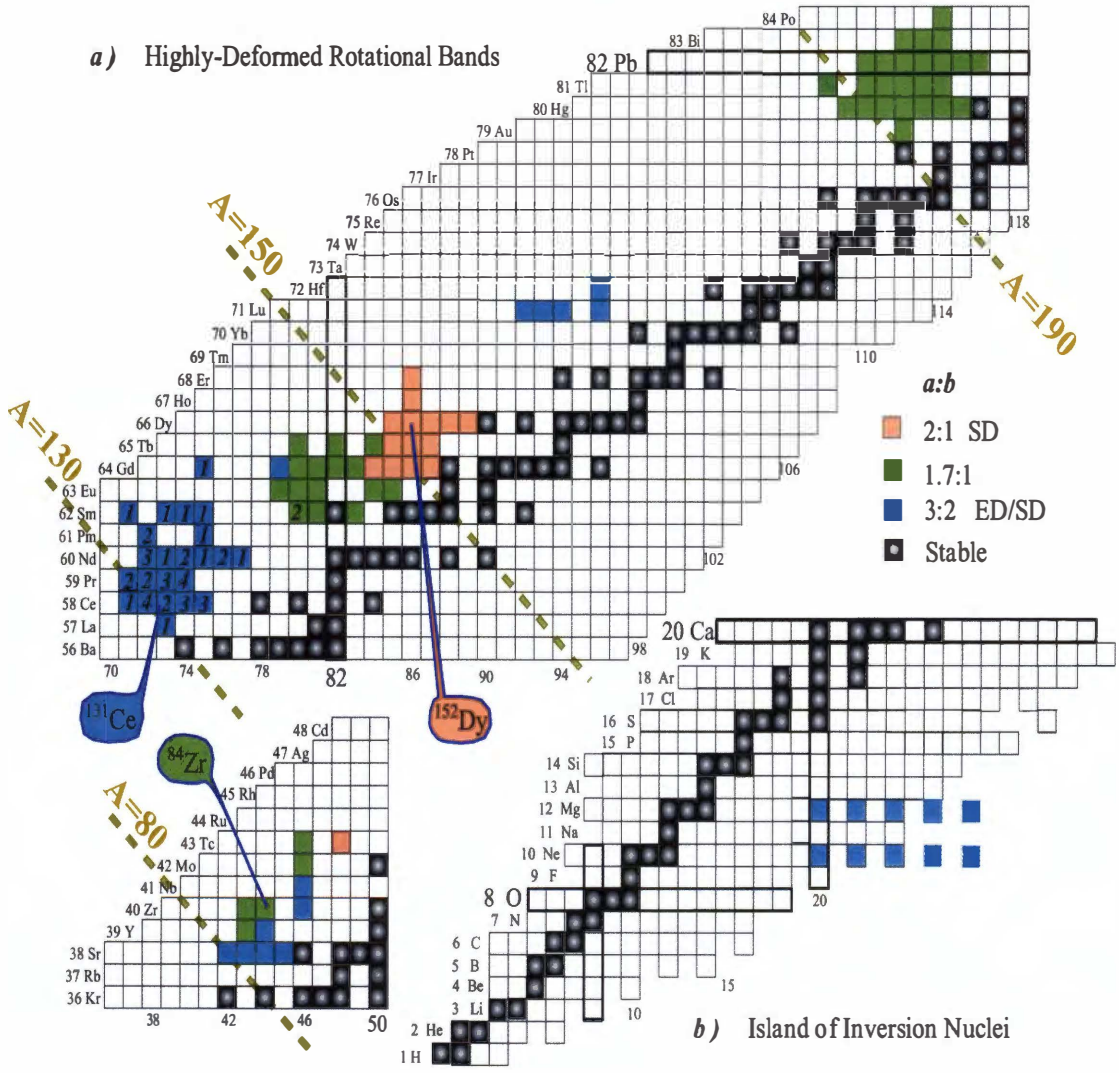

Figure 1.2: Portions of the Table of Isotopes showing the location and deformation ranges of the enhanced deformation (ED) and superdeformed (SD) mass regions A≃80, A≃130, A≃150, A≃190 (a). The numbers in the boxes give the number of highly–deformed bands observed experimentally for the nuclei in the ^{131}Ce region discussed in Chapter 3. (Adapted from Ref. [53].) Portion (b) shows the deformed "island of inversion" for Ne–Mg neutron–rich nuclei, explored in Chapter 4.

model paradigm, as well as self–consistent models based on parameterizations of the effective nucleon–nucleon interaction. These successes went hand–in–hand with re–evaluations of the validity of the mean–field paradigm and attempts to find the limits of its applicability. Arguments can be found in the literature [54] suggesting that mean–field models may be generally inadequate because the mean–field approximation may be invalid at ordinary nuclear densities, or that essential parts of the correlations are, one way or another, not included. These arguments seem to be misleading, because they perceive implicitly the mean–field calculations as Hartree or Hartree–Fock procedures, performed on the underlying nucleon interaction. However, in reality the procedure involves full Hartree plus exchange correlation *functionals*, described better by the Kohn–Sham density functional theory (DFT) [55, 56, 57]. We would like to emphasize that the mean–field theories are thus characterized by a universal energy functional of the density, which is then iteratively minimized through the variational procedure for each nucleus separately while including auxiliary single (quasi–)particle states. The emphasis is on the *universality* of this approach, because it allows shifting the difficulties of obtaining the many solutions for different nuclei to that of finding the energy functional *once*. If it can be found in a feasible and affordable way, then the calculations can be scaled to obtain the structural information for large numbers of nuclei.

The commonly used mean–field models can roughly be divided into two major classes, according to the type of energy functionals they employ — non–relativistic and relativistic (covariant) energy functionals. The non–relativistic (Skyrme) models ([58], and references therein) are based on a particular family of non–relativistic forms of zero–range density–dependent forces used for generating non–relativistic energy functionals consisting of powers and gradients of the isoscalar and isovector densities, the corresponding kinetic energy densities, and spin currents. As such they can be considered Kohn–Sham functionals [59, 60, 61].

The relativistic mean–field models are derived from Lagrangians containing couplings between nucleons and heavy mesons [62, 63, 64, 65]. The name relativistic (or, rather, covariant) implies that they describe the kinematic relativistic effects (high velocities, respectively large p/M ratios), which are associated with small corrections in the non–relativistic models.

The success of the extension of self–consistent models to high–spin configurations and nuclei approaching the particle drip lines has led to the thorough understanding of the mean–field approach and the different components of the effective interaction. In this work we utilize two of the most versatile implementations of the self–consistent approximation to the nuclear mean field, the Skyrme Hartree–Fock (HF) method, and the relativistic mean–field (RMF) approach.

1.3 Brief Outline of the Following Chapters

We begin (Chapter 2) with an introduction to the concept of nuclear mean field, as it is applied to high–spin nuclear rotation. The shell model approach to this paradigm is first explained briefly, and then used as a guide into the realm of self–consistent models.

In Chapter 3 we apply the Skyrme HF and the relativistic mean–field models to carry out a systematic study of deformations and angular momenta of superdeformed bands in the A$\simeq$130 mass region. The resulting systematics is used for a comprehensive analysis of single–particle structures of the bands, and multivariate statistics ("additivity analysis") is applied to extract the effective quadrupole moments and relative alignments for single–particle orbitals in the vicinity of the superdeformed shell gaps.

The appearance of highly–deformed configurations in nuclei is associated with microscopic (shell) effects, and shape polarization effects caused by the presence of anisotropic orbitals

(*e.g.*, high-j "intruders"). Studies of superdeformed bands show that the interaction of the collectively–rotating mean field and the single–particle nucleonic motion can lead to decoupling of pair(s) of nucleons with opposite spins, and the alignment of their angular momenta along the rotation axis. This mechanism, first introduced by Stephens, *et al.* [35, 36], suggests that the single–particle contributions to the properties of the rotating nuclear system can be obtained by analyzing the individual contributions from the decoupled nucleons. This has been a standard procedure for studying the microscopic structure of rotational bands ever since, its success even more important in view of the fact that the self–consistent many–body theories predict the alignment of nucleons also to have a notable effect on the mean field.

The deformation effect due to the unpaired nucleons is known also to have very strong dependence on the position of the chemical potential λ within the shell with high–j intruders [66, 67], and is a consequence of the fact that the short range of nuclear interactions favors states with wave functions having maximal overlap (this mechanism is often referred to as MONA [68]). The change of deformation is associated with the Jahn–Teller effect [69]; it is discussed in Chapter 2 and commented on *in extenso* in the context of the superdeformed A$\simeq$130 region (Chapter 3).

For example, the first backbending (the crossing of the ground–state band, g–band) by the first excited band (also referred to as *Stockholm*, or s–band), in the A$\simeq$130 nuclei is associated with the rotational alignment of the $i_{13/2}$ neutrons from the $\mathcal{N}$=6 shell. In the s-band, one nucleonic pair is broken. The breaking of the pair(s) also leads to significant overall reduction in the pairing correlations in the system [70], which is seen as a decrease of the pairing gap Δ with frequency [71]. One can think of this effect as of a disappearance of the *static pairing*, evidence for which can be found in the study of crossings of rotational bands ([72], and references therein). However, since the nucleus is a finite system, we have no good reasons to disregard the *dynamic pairing* correlations, often referred to as *pairing vibrations*, which may be non-negligible even at high frequencies. We can minimize this effect by choosing to evaluate rotational bands at frequencies high enough for the pairing interactions to become insignificant, and then considering *relative* changes with respect to a chosen reference core configuration. The dynamic pairing effects are expected to cancel to a large extent.

In our study, one of the microscopic mechanisms for causing shape deformation is of special importance — the nuclear Jahn–Teller (JT) effect [69] originating from coupling between the collective excitations of the system and the single-particle motion [73]. A recent comprehensive work showed [74] that the JT effect on its own can cause the occurrence of odd–even staggering in the binding energy, otherwise solely attributed to pairing. The influence of the JT effect decreases in superconducting nuclei. This is a consequence of the fact that when residual interactions are introduced (pairing being one of them), they tend to effectively reduce the magnitude of the JT coupling [75, 76]. Although pairing correlations in atomic nuclei can give rise to a large residual energy which, in general, weakens the deformation effects, the polarization effect of the odd nucleon is still present. The bottom line of this discussion is that pairing can be excluded safely from the self–consistent mean–field calculations at this stage, with a significant gain in computational performance, and without sacrificing the quality of the results, at least when considering rotational SD shapes at a high–enough frequency. Of course, the more general question about the relative role of the JT effect and pairing is very much worth exploring further, but it is outside of the scope of this work. We shall return briefly to this discussion in Chapter 2, where dynamic and static polarization is considered in the context of time–reversal invariance in the self–consistent models.

Combined with the results of a systematic measurement of deformation in the A$\simeq$130 region, our results show a remarkable agreement between the *relative* transition quadrupole moments

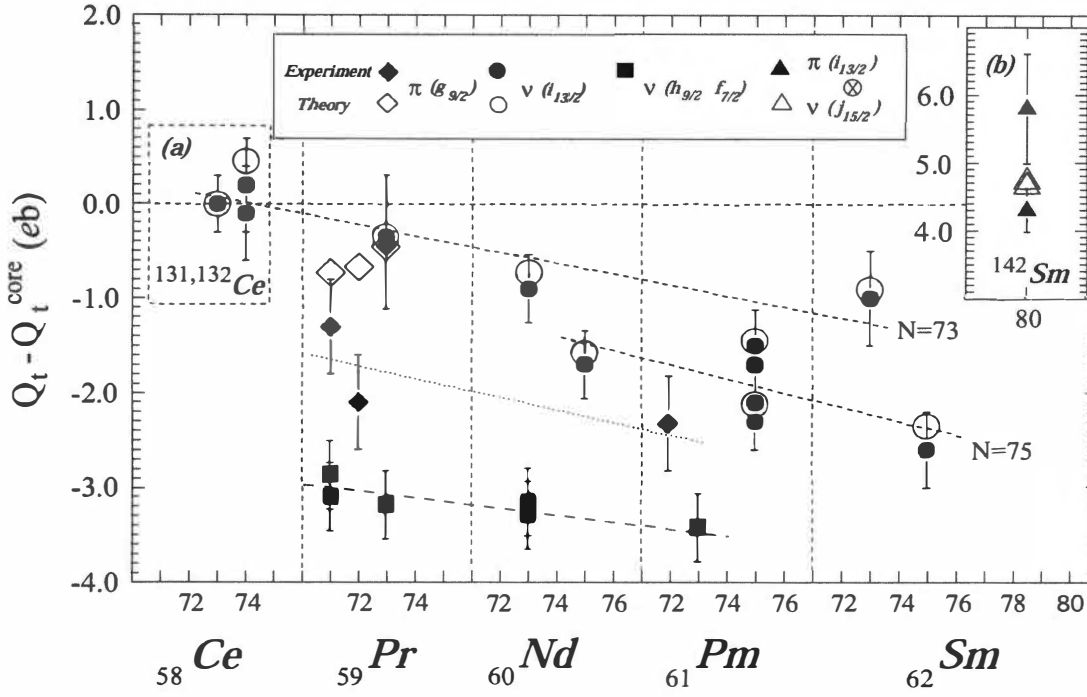

Figure 1.3: Experimental (Ref. [2], closed symbols with error bars) versus theoretical (this work, open symbols) differential transition quadrupole moments Q_t as a function of the number of neutrons. The calculations were carried out using the SD band of ^{131}Ce as a reference. From [2], see the comments in the text and in Chapter 3 for further interpretation and analysis.

for more than a dozen SD bands [2]. Our results have been checked for consistency by comparing them with the experiment for the two known SD bands of ^{142}Sm — a connecting link to the extensively–studied superdeformed A∼150 mass region, for which this kind of calculation was first carried out [77]. We can see in Fig. 1.3 that our multivariate analysis for a total of nearly 200 bands in the cranked Skyrme HF reproduces the experimental values quite nicely. The results for the single–particle contributions, summarized in a set of tables for both Skyrme HF and RMF, allow for simple, back–of–the–envelope calculations for deformations and angular momenta, given a particle–hole configuration with respect to the known core.

Our analysis proves successful in confirming the interpretation of highly–deformed nuclear shapes in the entire A∼130 SD region, from light La nuclei to ^{137}Sm. The extracted single–particle contributions to the shape–polarization effect, as well as to the angular momenta, are in good agreement with the experiment [67]. The successful application of our Skyrme calculations to the lowest SD bands confirms the assumption that single–particle motion of the nucleons around the Fermi energy is, to a considerable extent, undisturbed by the residual interactions.

We carry on along the lines of this hypothesis in Chapter 5, where the cranked Skyrme Hartree–Fock model is applied to the study of yet–unobserved rotational configurations of light neutron–rich drip–line nuclei. We concentrate our attention on ten even–even nuclei in the Ne–Mg region, with neutron numbers between the N=20 and N=28. These nuclei, being very unstable, are difficult to synthesize and study — only the isotopes closer to N=20 have been

observed, with spectroscopic evidence suggesting a latitude of shapes. The calculations in this region (sometimes referred to as the "island of inversion") suggest that the excess of neutrons leads to softening of the nuclear shape, with very interesting shape effects expected to arise with rotation. This region is of special interest in view of the recent progress in spectroscopic studies with radioactive ion beams. Our calculations are the very first studies of neutron–drip–line systems at high spin.

I close this dissertation with a general Conclusion, and a brief summary.

Chapter 2

Mean–Field Theory of Nuclear Rotation

"Everything existing in the Universe is
the fruit of chance and of necessity"

— Democritus of Abdera, 460–370 B.C.

In this Chapter, we introduce briefly the notion of mean field in atomic nuclei, viewed as many–body systems of nucleons (neutrons and protons) interacting via nuclear forces, and then concentrate on the procedures for finding the appropriate energy functionals used in the quantitative analysis. We start with a schematic introduction to effective interactions applied in the mean–field approaches, and then continue with a summary of definitions pertaining to deformed rotating nuclei. This naturally leads us to the description of self–consistent mean field methods.

Since the subject of my study is high–spin physics, I concentrate on the inclusion of rotational degrees of freedom into the mean–field Hamiltonian. I start with the phenomenological Hamiltonians and then describe the two self–consistent cranked models used in this dissertation : (i) the non–relativistic Hartree–Fock method with Skyrme effective interactions, and (ii) the relativistic mean–field theory. Their implementations are outlined along with the necessary information on the particular form of the nuclear interactions and computational procedures used.

2.1 Rotating Deformed Mean Field

There have been many attempts to describe the nuclear many–body system in terms of the interaction field acting on all nucleons [78]. The belief that such many–body interaction can be constructed in the form of a potential function(al) dependent on nucleonic coordinates, momenta, spins, and isospins usually starts with the assumption that the interaction can be expressed as

a series of terms involving two–body, three–body, *etc.*, terms :

$$V_{\text{eff}}(1,\ldots,A) = V^{(2)} + V^{(3)} + \ldots \simeq \sum_{i<j} V(i,j) + \sum_{i<j<k} V(i,j,k), \tag{2.1}$$

where $i,j,k = 1,\ldots,A$ label the interacting nucleons. The motivation for such decomposition stems from the ambition to derive the functional forms of these terms from general symmetries, using extensive knowledge of the bare nucleon–nucleon interaction. In practice, one is using effective interactions, described by relatively few parameters adjusted to experimental data.

As we shall see in the next Section, it is often possible to decompose the effective interaction in such a way as to extract the mean interaction potential $V(i)$ acting on each of the nucleons separately. While this potential is a result of the interactions of all the other nucleons averaged over the entire nuclear volume, it depends on the coordinates of individual nucleons. We refer to this potential as a *single–particle mean field*, or simply *mean field*. The fact that the mean field has a one–body character allows for significant simplifications.

The first successful implementation of the mean–field approach in nuclear physics was introduced by Göppert–Meyer and Jensen [18, 19]. The remarkable accuracy and flexibility of the shell–model picture fueled the discussions on the existence of nuclear mean field for decades. The idea of the existence of a nucleon mean field has proven to be very insightful in nuclear structure theory with its inherent benefits of computational feasibility and intuitiveness.

Without going into the details of the spherical nuclear shell model, we shall mention that the sphericity of the potential leads to sphericity of the density distribution and *vice versa*, with the quality of the approximation improving rapidly with the nuclear mass. The fact that the spherical nuclei are very conveniently scattered in different regions of the isotope table made it possible to fine–tune the full set of shell–model parameters and get a good understanding of the nuclear many–body problem for nuclei ranging all the way from oxygen to lead.

The parts of the nuclear interaction (2.1) which remain outside of the mean–field picture are usually referred to as *residual interactions* [78]. Over the decades, considerable success has been achieved in including various parts of the residual interactions into the independent–particle picture.

2.1.1 Deformation Parameters

In this section we shall define briefly the parameterization of the two most–commonly used versions of the deformed shell model approach — the Nilsson (modified harmonic oscillator) model [23, 79], and the deformed Woods–Saxon model [80, 81, 82]. For the sake of clarity we follow the description given in Ref. [78].

Nuclear Shape Parameters

The nuclear shape is usually described as the shape of a properly–defined nuclear surface in a body–fixed coordinate system of a nucleus. Thanks to the incompressibility of nuclear matter, one can assume that the volume of the nuclear shape is preserved for a relatively wide range of deviations from sphericity. If the radius of the spherical shape is denoted as R_0, we can parameterize the radius of the deformed nucleus in spherical coordinates by expanding it in multipoles :

$$R(\theta,\varphi;\{\alpha\}) = C(\{\alpha\})R_0 \left(1 + \sum_{\lambda=0}^{\infty} \sum_{\mu=-\lambda}^{\lambda} \alpha_{\lambda\mu} Y_{\lambda\mu}(\theta,\varphi)\right), \tag{2.2}$$

where $C(\{\alpha\})$ guarantees that the volume inside the surface defined by $R(\theta,\varphi;\{\alpha\})$ is conserved. The coefficients $\alpha_{\lambda\mu}$ with $\lambda = 0,1,2,3,4,\ldots$ are referred to as monopole, dipole, quadrupole, octupole, hexadecapole, *etc.*, deformation terms. By the proper choice of the origin one can eliminate the terms with α_{00} and $\alpha_{1\mu}$ and set these coefficients to zero. Under these assumptions it becomes evident that the leading non-trivial terms in the expansion are the *quadrupole* terms, *i.e.*, the ones proportional to $\alpha_{2\mu}$, $\mu = -2,-1,0,1,2$. Three of these five parameters determine the nuclear orientation and are equivalent to the set of three Euler angles. By rotating the body–fixed frame, we can choose $\alpha_{21} = \alpha_{2,-1} = 0$ and $\alpha_{22} = \alpha_{2,-2}$, thus reducing the set of five coefficients $\alpha_{2\mu}$ to only two independent ones : α_{20} and α_{22}. This allows making a very convenient transformation to a different set of shape variables, the *Hill–Wheeler coordinates* β_2 and γ :

$$\alpha_{20} = \beta_2 \cos\gamma, \tag{2.3}$$

$$\alpha_{22} = -\frac{\beta_2}{\sqrt{2}}\sin\gamma. \tag{2.4}$$

$$\sum_\mu |\alpha_{2\mu}|^2 = \alpha_{20}^2 + 2\alpha_{22}^2 = \beta_2^2. \tag{2.5}$$

The first of these parameters, β_2, is associated with the *elongation* of the quadrupole shape, and is commonly referred to as *quadrupole deformation.* The parameter γ given in degrees is often called *triaxiality*, and it measures the deviation of the nuclear surface from an axially symmetric shape. The expansion (2.2) in the Hill–Wheeler parameterization becomes [78]

$$R(\theta,\varphi) = CR_0\left[1 + \beta_2\sqrt{\frac{5}{16\pi}}\left(\cos\gamma(3\cos^2\theta - 1) - \sqrt{3}\sin\gamma\sin^2\theta\cos 2\varphi\right)\right]. \tag{2.6}$$

In this formula we have neglected the terms of order $\lambda > 2$. The symmetries of equation (2.2) allow us to limit the intervals for the deformation parameters to $\beta_2 \geq 0$ and $0° \leq \gamma \leq 60°$. The prolate (elongated) shapes correspond to $\gamma = 0°$, and the oblate (flattened) to $\gamma = 60°$. In the context of rotation, we follow the *Lund convention* [83], in which the rotation is parameterized around the shortest ($0° \leq \gamma \leq 60°$), intermediate ($-60° \leq \gamma \leq 0°$), and longest ($-120° \leq \gamma \leq -60°$) semi-axis of the deformed ellipsoid. In a quantum–mechanical treatment of rotation there cannot be collective rotation of a nuclear shape around its symmetry axis; hence rotational modes occurring in the vicinity of $\gamma = 60°$ and $\gamma = -120°$ are referred to as noncollective rotations.

For axially–deformed nuclei ($\beta_\lambda \equiv \alpha_{\lambda 0}$), the values of the quadrupole moment Q_{20} are related to the deformation parameters of the nuclear shape in the β expansion [84] :

$$Q_{20} = \frac{3}{\sqrt{5}}ZR_0^2\left(2\beta_2 + \frac{2}{7}\sqrt{\frac{5}{\pi}}\beta_2^2 + \frac{20}{77}\sqrt{\frac{5}{\pi}}\beta_4^2 + \frac{12}{7\sqrt{\pi}}\beta_2\beta_4\right) + O\left(\beta^3\right). \tag{2.7}$$

The shape parameters β_2 and β_4 are called the quadrupole and hexadecapole deformation parameters. To second order, the value of β_2 also can be obtained from Q_{20} by means of the relation

$$\beta_2 = -7\sqrt{\frac{\pi}{80}} + \sqrt{\frac{49\pi}{80} + \frac{7\pi Q_{20}}{6ZeR_0^2}}. \tag{2.8}$$

In the context of this work, we roughly classify rotational states by their deformations. We divide them into the following four families of shapes (see Fig. 1.1 and [85]) :

- *normal–deformed prolate*, $\beta_2 \simeq 0.2 \pm 0.1$, major-to-minor semi-axis ratio $\sim$ 4:3,
- *normal–deformed oblate*, $\beta_2 \simeq$ -0.15 $\pm$ 0.05, axis ratio $\sim$ 4:5,
- *enhanced–deformed prolate* (ED), $\beta_2 \simeq 0.35 \pm 0.05$, axis ratio $\sim$ 7:5,
- *superdeformed prolate* (SD), $\beta_2 \simeq 0.60 \pm 0.20$, axis ratio $\sim$ 3:2.

2.1.2 Deformed Shell Model

The inclusion of shape deformations into the average potential picture led Nilsson to the introduction of the modified harmonic oscillator model in the middle of the 1950's [23, 79]. Soon thereafter it became the main tool for describing deformed nuclei, for both small deformations (ground states of the majority of nuclei) and high deformations, including super- and hyper-deformations. It is hard to overestimate the importance of the Nilsson model and it should come as no surprise that its terminology, quantum number classifications and notations are widely used in nuclear spectroscopy. This dissertation is not an exception.

In the axial case, the Nilsson single–particle Hamiltonian is given by a deformed harmonic oscillator potential :

$$\hat{H} = \frac{\vec{p}^2}{2m} + \frac{m}{2}\left[\omega_\perp(x^2+y^2) + \omega_z z^2\right] + C\vec{l}\cdot\vec{s} + D\vec{l}^2 \tag{2.9}$$

where $\omega_\perp \equiv \omega_x = \omega_y$ is the oscillator frequency in the transverse plane, and ω_z is the one along the symmetry axis z. The terms proportional to $\vec{l}\cdot\vec{s}$ and $\vec{l}^2$ are included to provide the correct order of single–particle states.

The oscillator frequencies are directly related to the oscillator radii in the x–y and z directions, which are necessarily linked to the nuclear radius in the spherical case. If the spherical oscillator frequency is calculated from the nuclear size using the expression

$$\hbar\omega_0 = 41.A^{-1/3}\ \text{MeV}, \tag{2.10}$$

we can introduce deformation by means of the *Nilsson deformation parameter* ε_2 :

$$\omega_\perp = \omega_0(1+\tfrac{1}{3}\varepsilon_2), \tag{2.11}$$
$$\omega_z = \omega_0(1-\tfrac{2}{3}\varepsilon_2). \tag{2.12}$$

With this definition of ω_0 and ε_2, the Nilsson model Hamiltonian can be rewritten as

$$\hat{H} = \frac{\vec{p}^2}{2m} + \frac{1}{2}m\omega_0^2 r^2 - m\omega_0^2 r^2 \varepsilon_2 \frac{4}{3}\sqrt{\frac{\pi}{5}}Y_{20}(\theta,\varphi) + C\vec{l}\cdot\vec{s} + D\vec{l}^2, \tag{2.13}$$

where $r^2 = x^2+y^2+z^2$, and the constants C and D are usually expressed as

$$C = 2\hbar\omega_0\kappa, \quad \text{and} \quad D = \hbar\omega_0\kappa\mu, \tag{2.14}$$

where κ and μ are adjusted to the data. The oscillator deformation then can be quantified using the parameter

$$\zeta = \frac{\omega_\perp}{\omega_z} \qquad \left(\varepsilon_2 = \frac{3(\zeta-1)}{2\zeta+1}\right). \tag{2.15}$$

Shapes with ζ approaching positive integer numbers are also characterized with large gaps in the single–particle spectrum, as seen in Fig. 1.1. Cases with $\zeta \approx 2$ are referred to as *superdeformed*, and those with $\zeta \approx 3$ – as *hyperdeformed*.

The diagonalization of the Nilsson Hamiltonian can be done analytically in the simplest cases to obtain the single–particle eigenenergies ϵ_i as a function of the deformation parameter ε_2. The plot of ϵ_i versus ε_2 demonstrates the effect of quadrupole deformation on the splitting of single–particle orbitals, and is commonly referred to as a *Nilsson diagram* even in cases when the mean–field Hamiltonian is not in the Nilsson form. The parameter ε_2 is closely related to β_2 and can be used for comparison with other shape parameterizations [84].

The deformed Woods–Saxon model [80, 81, 82] is a significant improvement over the Nilsson model. Since the harmonic oscillator potential is infinite, it can not properly describe the weakly–bound and unbound states. Moreover, its quadratic dependence at small distances is unrealistic. For these and many other reasons [78] it is important to have a phenomenological mean–field model with a potential profile more closely resembling that of the nucleon density distribution. This approach leads to the introduction of a potential which stays flat inside the nuclear volume and smoothly drops to zero close to the nuclear surface. By introducing a more realistic potential, one of course sacrifices the simplicity and the ease of calculations. The deformed Woods–Saxon potential can be defined as

$$V_{W.-S.} := V(\vec{r}, \beta) + V_{ls} + V_C, \tag{2.16}$$

where the first term is the analytical form of the mean–field potential profile

$$V(\vec{r}, \beta) = \frac{V_0}{1 + exp(\pm |\vec{r} - \vec{r}_S| / a)}. \tag{2.17}$$

In this expression $\vec{r}_S$ is the point on the surface nearest to $\vec{r}$, and a is the diffuseness parameter. The minus (plus) sign is taken for $\vec{r}$ inside (outside) the nuclear surface. The spin–orbit term V_{ls} is usually defined as

$$V_{ls} = \frac{\lambda_{so}}{2} \left(\frac{\hbar}{mc}\right)^2 \left[\left(\vec{\nabla} V(\vec{r}, \beta)\right) \times \vec{p}\right] \cdot \vec{s}, \tag{2.18}$$

and V_C is the Coulomb energy term calculated for $(Z - 1)$ protons using uniform charge distribution integrated classically over the volume inside the nuclear surface.

2.1.3 Quantum Numbers of Deformed Orbitals

The single–particle orbitals of the axially–deformed mean field are labeled by the set of quantum numbers. For spherical shapes, one uses the spherical quantum numbers n_r, ℓ, j, and j_z. Using the standard convention, n_r is the radial quantum number, ℓ — the orbital quantum number, j — that of the total angular momentum, and $j_z = m$. The labeling convention for spherical orbitals is, following the spectroscopic conventions, given in the form $n_r \ell_j$, where the values of $\ell = 0, 1, 2, 3, 4, \ldots$ are denoted in letter form : s,p,d,f,g,h,. . ., and each of the states is $(2j+1)$–fold degenerate.

When the shape of the potential becomes axially deformed (Fig. 2.1), the spherical symmetry is violated, but the Hamiltonian remains cylindrically symmetric around the z-axis, so the separation of variables in cylindrical coordinates (z, ρ, φ) defines the three quantum numbers (n_z, n_ρ, λ). The main (*principal oscillator*) quantum number $\mathcal{N}$ from the spherical model, representing the total number of oscillator quanta, is now given by

$$\mathcal{N} = n_z + 2n_\rho + \Lambda = n_\perp + n_z, \tag{2.19}$$

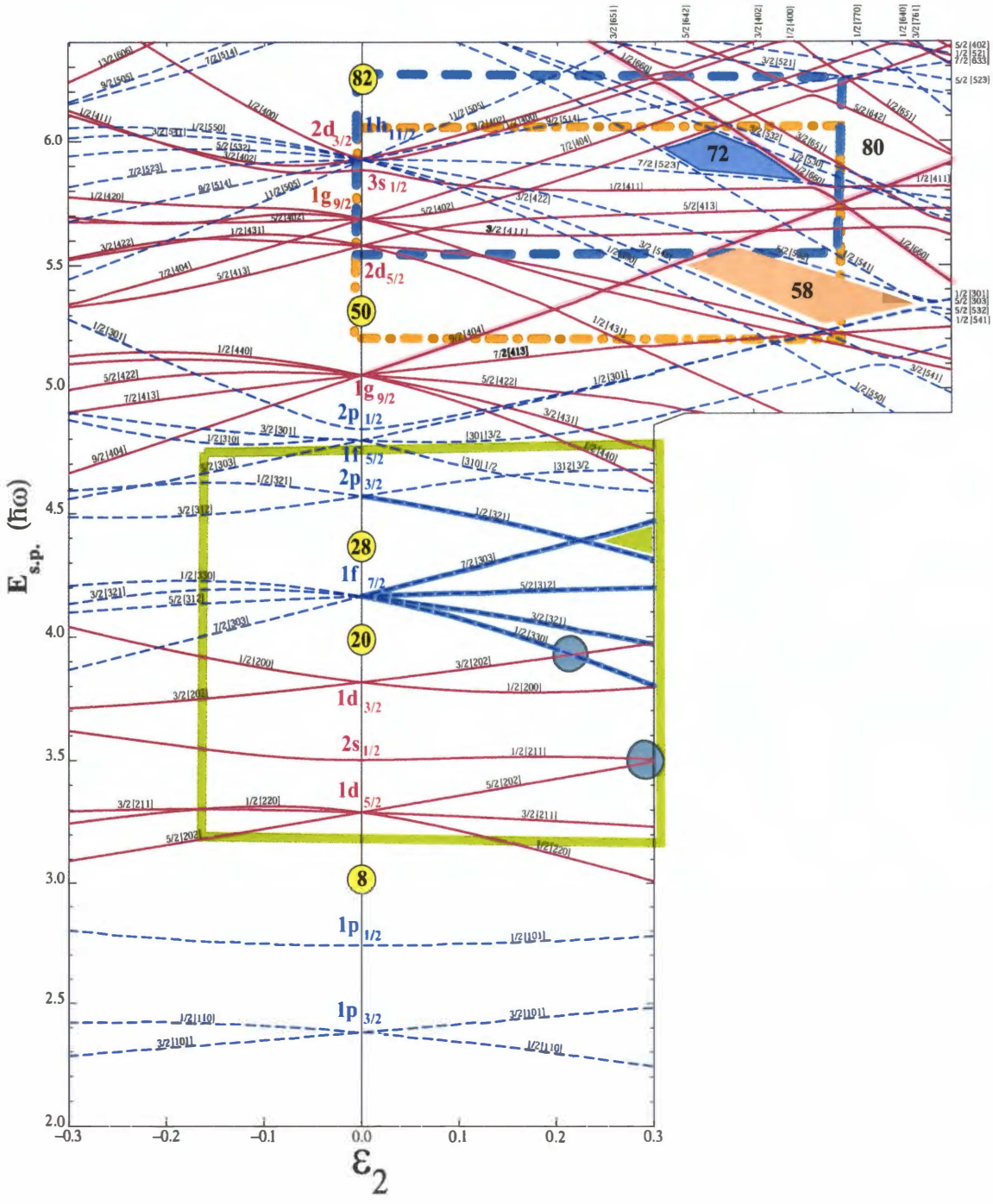

Figure 2.1: Single–particle energy levels of an axially–symmetric deformed Nilsson Hamiltonian as a function of the deformation parameter ε_2. Each state is two–fold degenerated. Marked are the regions, gaps, and orbitals of particular interest for this dissertation.

and is not a good quantum number anymore, and $n_\perp$ and n_z are the quantum numbers of the axially–symmetric Hamiltonian. One can compare at this point Fig. 2.1 with the one for the deformed harmonic oscillator (Fig. 1.1), where the energies of the states are shown as functions of the deformation parameter $\delta_{\rm OSC}$ related directly to ε_2. The slope of a level is proportional to $2n_z - n_\perp = 3n_z - \mathcal{N}$, and the orbital with the highest value of n_z within the shell carries the highest quadrupole deformation.

Due to the non-sphericity of the potential, the angular momentum quantum number j is broken, but the remaining cylindrical symmetry of axial shapes conserves $\Lambda \equiv \ell_z$, and $\Omega \equiv j_z$. Since Λ is broken by the spin–orbit interaction term, the only good quantum numbers of the Nilsson model are Ω and the parity $\pi = \pm 1$. At very large deformations, the $\vec{\ell} \cdot \vec{s}$ and $\vec{\ell}^2$ terms in the Hamiltonian become small, so that the quantum numbers, $\mathcal{N}$, n_z, Λ, appearing in Eq. (2.19) become approximate constants of motion. This set of quantum numbers, appropriate for very elongated shapes (*asymptotic quantum numbers*), usually is given in the notation $[\mathcal{N}, n_z, \Lambda]$. For a particular Nilsson state, its spectroscopic label is written as follows (Fig. 2.1) :

$$[\mathcal{N}, n_z, \Lambda]\, \Omega^\pi \qquad \text{or} \qquad \Omega^\pi\, [\mathcal{N}, n_z, \Lambda]\,. \tag{2.20}$$

Comparing with Fig. 1.1, one can notice the occurrence of shell gaps for highly–deformed prolate shapes for particle numbers 58 and 72. They will be subjects of Chapter 3.

2.2 Nuclear Shapes at High Angular Momenta

In the context of this work, it is important to mention some of the basic concepts of nuclear high–spin physics. As mentioned in the Introduction, the rapid improvement of spectroscopic detectors led to the discovery of nuclear states with high angular momentum, and of different shapes [29, 30]. These effects were first studied in the framework of the rotating liquid drop model (RLDM) by Cohen, Plasil, and Swiatecki, in which a structureless deformed drop of nuclear matter was cranked around a chosen axis [31].

At low rotational frequencies, the nuclear liquid drop develops a slightly–oblate ellipsoidal deformation (*Maclaurin shape*), which increases with angular momentum until a *critical frequency* ω_I is reached (*bifurcation point, Jacobi instability*), beyond which triaxial (*Jacobi*) shapes become energetically favored. Beyond the bifurcation point, the Maclaurin shapes are still stationary, but they no longer have energy minimal in all deformation degrees of freedom (*secularly unstable shapes*) [86]. This kind of behavior was studied extensively in the potential energy surfaces of fissile heavy nuclei, for which the triaxiality eventually channels the nuclear system into a highly–deformed prolate shape. In realistic cases, the transition (also referred to as *superbackbending*) may pass through a series of quasi–stable triaxial shapes, which have their origins in the shell effects. For uniformly–rotating *gyrostatic* frictionless nuclear systems, the secularly–unstable configurations can be viewed as representing stable motion (*ordinary stability*) [87]. In the case of the rotating structureless liquid drop, the transition is characterized by the value of the maximal limiting angular momentum I_c for the fission channel. Its value increases roughly proportional to the mass number A reaching a wide maximum of $I_c \simeq 95\hbar$ at around A $\simeq$ 130, asymptotically approaching zero around A $\simeq$ 320.

For the nuclear systems of our interest, the rotational behavior depends to a great extent on the shell structure [42], so the macroscopic liquid drop results can be taken only as qualitative guidance. The single–particle degrees of freedom and the quantum effects change the rotating drop picture, while revealing structural information on the properties of individual nucleons in the vicinity of the Fermi energy. The generic dependence of the nuclear shape on rotational

frequency exhibits features similar to that of the liquid drop, showing a tendency to stretch due to the centrifugal force. Nuclei with prolate ground state shapes generally make their transition towards noncollective oblate shapes at high frequencies via different stages of triaxiality [32] (see Refs. [29, 88, 30] for details).

Examples of quantum phenomena associated with interplay between shape degrees of freedom and rotation include shape coexistence, band termination, superdeformation, and wobbling motion. In the following, we briefly classify the variety of rotational structures one can expect to see at high spins in terms of their (β_2, γ) deformations :

- *Non-collective oblate* shapes in the vicinity of $\gamma = 60°$, resulting from a partial or full alignment of nucleonic angular momenta. Examples of such shapes are the predicted terminating bands in the neutron–rich Ne–Mg region (see Chapter 4).
- *Prolate collective rotors* in the vicinity of $\gamma = 0°$, which constitute the vast majority of collective rotating configurations. These are exemplified by the highly–deformed (HD) and superdeformed (SD) shapes studied in Chapter 3.
- *Oblate collective rotors*, as exemplified by a few cases at relatively low spin [89, 90, 91] with typical axis ratios of 3:2. At higher spins, these configurations can compete with prolate ones only if very strong shell effects are present.
- *Non-collective prolate* shapes in the vicinity of γ=–120°, resulting from the complete alignment of (quasi)particle spins. These states, having the smallest possible moment of inertia, owe their existence to significant shell effects. They do not appear low enough in energy to be considered in the calculations in this work.

2.2.1 Cranking Method and the Particle-plus-Rotor Model

In order to establish the connection between rotation as a collective property of the nuclear system and its microscopic structure, we employ the so–called *cranking model* [92, 93]. Comprehensive review of the model can be found in Refs. [94, 94, 88].

If we assume that the nuclear symmetry axis is the third axis, Oz, the collective rotation is possible only around any axis perpendicular to it — here we chose the x–axis. The transformation from the laboratory reference frame (x, y, z) to that (x', y', z') rotating with a constant rotational frequency ω takes the form :

$$\begin{aligned} x' &= x \\ y' &= y\cos\omega t + z\sin\omega t \\ z' &= -y\sin\omega t + z\cos\omega t. \end{aligned} \tag{2.21}$$

The operator that generates this rotation can be written as

$$\hat{\mathcal{R}} = e^{-i\omega t\hat{J}_x}. \tag{2.22}$$

The time–dependent Schrödinger equation in the laboratory (non-rotating) frame

$$i\hbar\frac{\partial}{\partial t}|\Psi\rangle = \hat{H}|\Psi\rangle \tag{2.23}$$

can be expressed alternatively in the rotating reference frame :

$$i\hbar\frac{\partial}{\partial t}|\Psi'\rangle = \left(\hat{H} - \hbar\omega\hat{J}_x\right)|\Psi'\rangle, \tag{2.24}$$

where

$$\hat{H}' = \mathcal{R}^{-1}\hat{H}\mathcal{R} = \hat{H} - \hbar\omega\hat{J}_x \tag{2.25}$$

is the Hamiltonian in the rotating system (*Routhian*), and

$$|\Psi'\rangle = \hat{\mathcal{R}}^{-1}|\Psi\rangle \tag{2.26}$$

is the intrinsic wave function.

By performing this "cranking" transformation, we have essentially separated the collective rotation from other modes of the system. The Routhian $\hat{H}'$ is commonly referred to as the *cranking Hamiltonian* of the system [88]. This transformation of the Hamiltonian is mathematically equivalent to its classical mechanics analogon. In the latter case, the rotation with a constant angular velocity $\vec{\omega} = (\omega, 0, 0)$ gives rise to the *Coriolis force*, and the *centrifugal force* in the rotating reference frame :

$$\vec{f}_{\text{Coriolis}} = -2m\vec{\omega} \times \dot{\vec{r}}', \tag{2.27}$$

$$\vec{f}_{\text{centrifug}} = -m\vec{\omega} \times (\vec{\omega} \times \vec{r}') = m\left(0, \omega^2 y', \omega^2 z'\right). \tag{2.28}$$

The centrifugal force can be formally obtained from a centrifugal "potential"

$$V_{\text{centrifug}} = -\frac{1}{2}m\omega^2\left(y'^2 + z'^2\right). \tag{2.29}$$

The Coriolis force can be generated by a vector potential $\vec{A} = m\vec{\omega} \times \vec{r}'$, similar in form to the Lorentz force acting on a charged moving particle. The corresponding transformed Hamiltonian can be written as

$$H_{\text{classic}} = \frac{1}{2m}\left(\vec{p}' - m\vec{\omega} \times \vec{r}'\right)^2 - \frac{1}{2}m\omega^2\left(y'^2 + z'^2\right) = \frac{1}{2m}\vec{p}'^2 - \omega\left(\vec{r}' \times \vec{p}'\right)_{x'}, \tag{2.30}$$

in which the last term is proportional to the x-component of the angular momentum

$$\vec{L}' = \vec{r}' \times \vec{p}'. \tag{2.31}$$

Therefore, the effect of cranking on the classical Hamiltonian is the appearance of a cranking (Lagrange) term in the form $-\vec{\omega} \cdot \vec{L}'$. The resulting function

$$H_{\text{classic}} = \frac{1}{2m}\vec{p}'^2 - \vec{\omega} \cdot \vec{L}' \tag{2.32}$$

is also called *cranking Hamiltonian* or *classical Routhian*.

The nuclear mean–field models appearing in this rotating picture are called *cranked mean–field models*. In particular, the cases of the phenomenological models introduced so far are referred to as *cranked Nilsson model*, *cranked Woods-Saxon model*, *etc.* In the next section we shall see how rotation can be introduced into the self–consistent mean–field theories, which are the main framework for carrying out the rotational calculations in this dissertation. However, we still need to introduce some definitions and concepts, which will give us a better conceptual understanding of the underlying physics.

In the *particle–plus–rotor model*, nuclear rotation is analyzed in terms of a rotating *"core"* subsystem with a nucleon moving around it and interacting with the core via a particle–core interaction term. When the core is deformed, there are two basic mechanisms of formation of its total spin : *single–particle rotation* and *collective rotation*. The total angular momentum $\vec{I}$

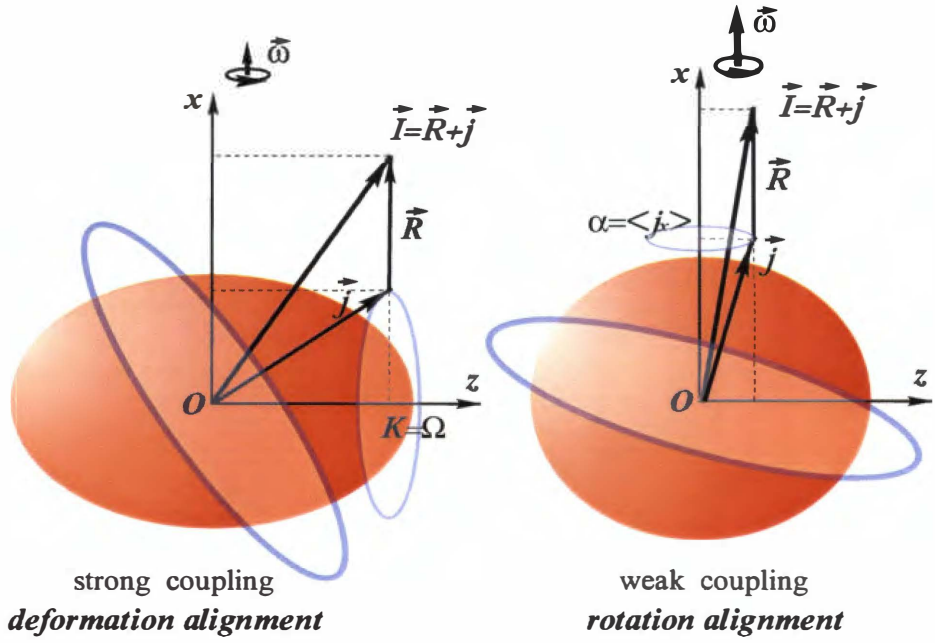

Figure 2.2: Coupling of the collective ($\vec{R}$) and single–particle angular momenta ($\vec{j}$) in the particle–plus–rotor picture.

of the system can be expressed as a sum of that of the core $\vec{R}$ and the single–particle angular momentum $\vec{j}$:

$$\vec{I} = \vec{R} + \vec{j}. \tag{2.33}$$

If we choose again the x–axis as the rotation axis, and z as the symmetry axis, the z–projections of the collective angular momentum $\vec{R}$ and $\vec{j}$, dubbed K and Ω respectively, are equal (Fig. 2.2; see also the detailed discussion in [30]). The rotational energy of the core is obtained by evaluating the expectation value of the rotational part of the Hamiltonian

$$\begin{aligned} \hat{H}_{\rm rot} &= \frac{\hat{\vec{R}}^2}{2\mathcal{J}} = \frac{(\hat{\vec{I}} - \hat{\vec{j}})^2}{2\mathcal{J}} = \frac{1}{2\mathcal{J}}\left((\hat{I}_x - \hat{j}_x)^2 + (\hat{I}_y - \hat{j}_y)^2\right) \\ &= \frac{1}{2\mathcal{J}}\left[\hat{\vec{I}}^2 - I_z^2 + \left(\hat{j}_x + \hat{j}_y\right)^2 - \left(\hat{I}_+\hat{j}_- + \hat{I}_-\hat{j}_+\right)\right] \end{aligned} \tag{2.34}$$

where $\mathcal{J}$ is the collective moment of inertia, and $I_\pm \equiv I_x \pm iI_y$, and $I_\pm \equiv I_x \pm iI_y$. The rotational energy can then be written as

$$E_{\rm rot}(I,K) = \frac{\hbar^2}{2\mathcal{J}}\left[I(I+1) - K^2\right] + \frac{\left\langle \hat{j}_x^2 + \hat{j}_y^2 \right\rangle}{2\mathcal{J}} - \frac{1}{\mathcal{J}}\left\langle \hat{I}_x\hat{j}_x + \hat{I}_y\hat{j}_y \right\rangle. \tag{2.35}$$

The last term in (2.35) is the *Coriolis coupling* energy. Like the classical Coriolis interaction (obtained from (2.27)), this term tries to align the axis of a rotating gyroscope (or a nucleon) with the rotation axis of the system. The Coriolis term plays a significant role in the analysis

of rotational spectra because it directly affects the nucleonic motion in the rotating field. When the angular momentum of the core is small, the Coriolis term can be treated perturbatively. This situation is shown in Fig. 2.2, left, and often is referred to as *deformation alignment* [30]. For even-even nuclei and low-lying bands we can have the simplest case, in which $\left\langle \hat{j}_x \right\rangle$, $\left\langle \hat{j}_y \right\rangle$ are zero and $E(I,K)$ takes the form

$$E(I,K) = \frac{\hbar^2}{2\mathcal{J}} \left[I(I+1) - K^2 \right] . \tag{2.36}$$

For odd–A nuclei, in the lowest order, the rotational energy becomes

$$E_{\text{rot}}(I,K) = \frac{\hbar^2}{2\mathcal{J}} \left[I(I+1) + j(j+1) - \frac{1}{2} + a(-1)^{I+\frac{1}{2}} \left(I + \frac{1}{2} \right) \right] , \tag{2.37}$$

where a is the *decoupling parameter* present only for $\Omega = \frac{1}{2}$ orbitals :

$$a = \langle \Omega = 1/2 | \hat{j}_x | \Omega = -1/2 \rangle = \langle \nu | \hat{j}_+ | \bar{\nu} \rangle = \langle \bar{\nu} | \hat{j}_- | \nu \rangle , \tag{2.38}$$

where $\bar{\nu}$ is the time–reversed state corresponding to the state of the odd particle ν (degenerate and with opposite sign of Ω).

In the case of deformation alignment of an orbital with "pure" j and $\Omega = \frac{1}{2}$, the decoupling parameter becomes

$$a_j = (-1)^{j+\frac{1}{2}} \left(j + \frac{1}{2} \right) . \tag{2.39}$$

For example, for the $i_{13/2}$ intruder states $|j\Omega\rangle = |13/2, 1/2\rangle$ the decoupling parameter is $a = -7$ (Chapter 3).

2.2.2 Parity and Signature Quantum Numbers

The nuclear Routhian $\hat{H}'$ is often invariant with respect to the space reflections, hence the parity quantum number π is conserved. The symmetries of the finite–symmetry group $\mathcal{D}_2$ defined by the 180° rotations around three principal axes, represented by $\hat{\mathcal{R}}_\xi = e^{-i\pi \hat{J}_\xi}$ for $\xi = x', y', z'$, are broken because of $\hat{\mathcal{R}}_y J_{x'} \hat{\mathcal{R}}_y^{-1} = -\hat{J}_{x'}$ and $\hat{\mathcal{R}}_{z'} \hat{J}_{x'} \hat{\mathcal{R}}_{z'}^{-1} = -\hat{J}_{x'}$. However, the $\mathcal{C}_2$–invariance with respect to the axis x' perpendicular to the symmetry axis implies that $\hat{H}'$ is invariant under the rotation operator (called *signature operator*)

$$\hat{\mathcal{R}}_x = e^{-i\pi \hat{J}_{x'}} . \tag{2.40}$$

When $\hat{\mathcal{R}}_x$ is applied twice to a wave function of A fermions, it produces a phase [88]

$$\hat{\mathcal{R}}_x^2 = (-1)^A . \tag{2.41}$$

The eigenvalues of $\hat{\mathcal{R}}_x$ (*signature quantum numbers*) can be written as

$$r := e^{-i\pi\alpha} \tag{2.42}$$

where α, called the *signature exponent* quantum number, takes the values α=0,1 for even–A systems and $\alpha = \pm\frac{1}{2}$ for odd–A nuclei. Since the eigenvalue r is also related to the total spin I (in units of $\hbar$) of the system via [95]

$$r = (-1)^I , \tag{2.43}$$

the possible values of r are :

- even A :
  $r = +1$, (α=0), for I=0,2,4,...
  $r = -1$, (α=1), for I=1,3,5,...
- odd A :
  $r = -i$, ($\alpha = +\frac{1}{2}$), for $I = \frac{1}{2}, \frac{5}{2}, \frac{9}{2}, \ldots$
  $r = +i$, ($\alpha = -\frac{1}{2}$), for $I = \frac{3}{2}, \frac{7}{2}, \frac{11}{2}, \ldots$.

The signature exponent α is an additive quantity, which can be used for classification of rotational bands. The above relations can be summarized using the equivalent expression

$$I = \alpha \bmod 2. \tag{2.44}$$

For product states, as is usually the case in mean-field theories, the total signature α is obtained by summing up the signatures of the individual states. Alternatively, one can use the r–value, keeping in mind that it has a multiplicative property.

2.2.3 Cranked–Model Analysis of Rotational Bands

As the rotational frequency ω in the cranking model becomes non–zero, the term $\vec{\omega} \cdot \vec{j}_i$ leads to the splitting of the pairs of degenerate time–reversed single–particle states. In the deformed shell–model picture, the slope of a given single–particle Routhian ϵ_i^ω versus ω is directly related to

$$\left\langle \hat{j}_x \right\rangle = -\frac{\partial \epsilon_i^\omega}{\partial \omega}, \tag{2.45}$$

i.e., it represents the contribution of a single–particle state so–called angular–momentum *alignment*. It can be shown [30] that for prolate nuclear shapes at low cranking frequencies ω, the alignment of states with $\Omega = +\frac{1}{2}$ is given by $\left\langle \hat{j}_x \right\rangle = +\frac{a}{2}$, where a is the decoupling parameter. The separation between Routhians with opposite signature quantum numbers r is referred to as the *signature splitting*. For states with $|\Omega| > \frac{1}{2}$ there is no decoupling in the sense defined above; however, with the increase of ω, all orbitals eventually acquire non–zero values of $\left\langle \hat{j}_x \right\rangle$ due to the Coriolis mixing, their alignments gradually increase with ω, and the signature splitting appears.

Although this conceptual picture seems intuitively clear, one has to keep in mind that these changes cannot be understood properly without considering possible variations of the nuclear shape with cranking frequency, and the effects caused by the aligned particles. For most of the rotational states, the accumulation of aligned particles in the equatorial area around the rotating core leads to gradual change of the nuclear shape to an oblate ellipsoid with a symmetry axis coincident with the rotation axis. In such a case, the expectation value of $\left\langle \hat{j}_x \right\rangle$ is now conserved $\left(\left\langle \hat{j}_x \right\rangle \equiv \Omega\right)$, therefore

$$I = \sum_{i=\text{particles}} \Omega_i - \sum_{i=\text{holes}} \Omega_i. \tag{2.46}$$

Consequently, the excitation energy can be given by

$$E_{\text{exc}} = \sum_{i=\text{particles}} e_i - \sum_{i=\text{holes}} e_i. \tag{2.47}$$

This cranking regime is referred to as *non-collective rotation*. Here the valence nucleons are considered weakly coupled to deformation, or *decoupled*, and they are *rotationally aligned* (see Fig. 2.2, right). In the previously–considered example of the lowest $i_{13/2}$ state from the $N = 6$ shell with $\Omega = \frac{1}{2}$, the value of the alignment changes from $|\langle j_x \rangle| = \frac{1}{2}|a|$ =3.5 in the deformation–aligned end of the rotational configuration (small ω) to $\langle j_x \rangle = \frac{13}{2}$ =6.5 in the rotation–aligned (high ω) end of the band.

At high spin the Nilsson labels lose their validity. Therefore, the eigenvalues (π, r) are used as quantum numbers for labeling the single–particle states. The possible values of these numbers are $\pm$ 1 for π, and $\pm i$ for r, which makes it possible to separate the space of single–particle states into four *parity–signature blocks* according to the combinations of (π, r), namely $(+, +i)$, $(+, -i)$, $(-, +i)$, and $(-, -i)$.

Even though Nilsson quantum labels are broken in the cranked–model framework, we shall still refer to them on a regular basis, keeping in mind that they are only valid at $\omega = 0$.

2.3 Self–Consistent Mean Field

In this Section we introduce the notion of *self–consistent nuclear mean field*, on which the results of this dissertation are based [78]. We start with a sketchy introduction to the Hartree–Fock method and effective forces.

The notion of an effective nucleon–nucleon interaction has its roots in Brückner's theory [78] (alternatively referred to as the *G-matrix theory*); its "effective" character implies that it refers to an infinite–order expansion of the bare interaction. The direct implementation of Brückner's procedure is technically difficult due to numerical limitations. Although in its simplest form the G–matrix theory has been successful in describing properties of closed–shell nuclei, like their binding energies and radii, it has been useful mostly as a conceptual step towards the introduction of more practical approaches. Phenomenological attempts at constructing nucleon–nucleon interactions resulted in a multitude of effective forces varying significantly in their parameterizations and areas of applicability.

Closest to the intellectual spirit of Brückner's expansion are the Gogny [96], and the Skyrme families of forces [97, 98], formulated for their use with the Hartree–Fock and Hartree–Fock–Bogolyubov method. The relation of these interactions to the G–matrix expansion can be seen by making the so–called *local density approximation* [99, 100, 101]. The Skyrme interactions in particular have been fitted to a variety of structural data, including bulk nuclear properties, like binding energies, charge distributions, *etc.*

2.3.1 Hartree–Fock Method and Equations

The Hartree–Fock method has enjoyed a tremendous success in nuclear structure physics, nowadays becoming the standard microscopic approach for interpreting properties of heavy nuclei [102, 78, 103, 104, 105]. It is derived from the many–body Schrödinger equation for a Hamiltonian, usually involving 2–body effective interaction :

$$\hat{H} = \hat{T} + \hat{V}^{(2)} = \sum_{kl} t_{kl} a_k^\dagger a_l + \frac{1}{4} \sum_{klmn} \bar{V}_{klmn} a_k^\dagger a_l^\dagger a_n a_m, \tag{2.48}$$

where $\bar{V}_{klmn} = V_{klmn} - V_{klnm}$ is the antisymmetrized 2–body matrix element [78]. The main assumption of the method is that the many–body state can be well approximated by a single

Slater determinant $|\Phi\rangle$, so that the Hartree–Fock energy is evaluated as

$$\begin{aligned} E_{\rm HF}(\hat{\rho}) = \langle\Phi|\,\hat{H}\,|\Phi\rangle &= \sum_{kl} t_{kl}\,\langle\Phi|\,a_k^\dagger a_l\,|\Phi\rangle + \frac{1}{4}\sum_{klmn}\langle\Phi|\,\bar{V}_{klmn}a_k^\dagger a_l^\dagger a_n a_m\,|\Phi\rangle \\ &= \sum_{kl} t_{kl}\rho_{lk} + \frac{1}{2}\sum_{klmn}\rho_{mk}\bar{V}_{klmn}\rho_{nl} \\ &= Tr(\hat{t}\hat{\rho}) + \frac{1}{2}Tr_1Tr_1(\hat{\rho}\hat{\bar{V}}\hat{\rho}) \end{aligned} \tag{2.49}$$

where Tr_1Tr_1 is a shorthand notation for the partial traces in the sense of the above equation, and $\rho_{kl} = \langle\Phi|\,a_l^\dagger a_k\,|\Phi\rangle$ is the one–body density matrix.

The Hartree–Fock energy in a single-particle basis ϕ_k in which ρ is diagonal (the so–called *canonical basis*) has the form

$$E_{\rm HF} = \sum_{i=1}^{A} t_{ii} + \frac{1}{2}\sum_{i,j=1}^{A}\bar{V}_{ij,ij}. \tag{2.50}$$

As a result of applying the variational principle,

$$\frac{\delta E_{\rm HF}}{\delta\hat{\rho}} = 0, \tag{2.51}$$

the matrix elements between occupied (i; hole) and unoccupied (m; particle) states vanish, *i.e.*,

$$h_{im} = t_{im} + \sum_{j=1}^{A}\bar{V}_{ij,mj} = 0, \tag{2.52}$$

and the single–particle Hamiltonian is diagonal and defines the single-particle energies :

$$h_{kk'} = t_{kk'} + \sum_{i=1}^{A}\bar{V}_{ki,k'i} = \epsilon_k\delta_{kk'}. \tag{2.53}$$

Equations (2.52) and (2.53) constitute the so–called *Hartree–Fock equations.* The total HF energy can be written as

$$E_{\rm HF}^0 = \sum_{i=1}^{A}\varepsilon_i - \frac{1}{2}\sum_{i,j=1}^{A}\bar{V}_{ij,ij}. \tag{2.54}$$

In order to carry out self–consistent calculations one needs to choose the effective interaction. In the early implementations of the HF procedure, various nuclear force parameterizations were used. However, especially since the mid–1970's, a consistent approach based on density–dependent interactions, such as the zero–range Skyrme force, was introduced and carried out with immense success in nuclear structure physics.

The purpose of the next section is to define the general form of the *Skyrme interaction*, as it is used in the *Skyrme Hartree–Fock* calculations and in the code HFODD, employed for calculating most of the results obtained in this dissertation. Introduced as early as 1956 by Skyrme [97, 106, 107], this family of interactions follows the general form for nuclear interactions (2.1), consisting of two-body and three-body terms. Based on some analogies with fluid dynamics and flow properties of continuous nuclear matter, Skyrme introduced a parameterization for

the interacting nuclear matter in the form of densities of its physical characteristics, which made the implementation of the HF computation program numerically feasible and easy to carry out, along with providing good physical insight [108]. We define the general form of the Hamiltonian density of the Skyrme HF in its modern form, as described in the paper by Vautherin and Brink in 1972 [98]. The Skyrme force has been subject to extensive studies over the past 20 years, leading to dozens of different families of Skyrme–type interactions fitted to extensive sets of nuclear data. In our case we use the recently–derived Skyrme force SLy4 [109], which has been successful in interpreting a very wide variety of nuclear phenomena, including properties of infinite nuclear matter. We proceed with the definition of the SLy4 force and the physical requirements under which it was fitted. We also discuss the procedure necessary for obtaining cranking solutions in HF. This is followed by a discussion of the basic principles of the relativistically–invariant approach to the self–consistent field problem — the *relativistic mean–field* method. This concept looks more deeply into the mechanisms of the nucleon–nucleon interaction and employs an effective Lagrangian.

We end this Chapter with an example of a highly–deformed rotational band in ^{131}Ce illustrating the definition of parity–signature blocks in `HFODD`, the appearance of level and band crossings and how to treat them, the concept of diabolic points, and other technical definitions necessary for the understanding of our results presented in the dissertation.

2.3.2 Skyrme HF and RMF — An Overview

In order to find HF solutions one can use the following strategies [110] :

A Skyrme Hartree–Fock method in *spatial coordinates*, with approximate forms for the differential operators using i) Finite difference methods [111], ii) Fourier methods [112], and iii) Spline–collocation. [113, 114, 115] The solution is then obtained by using an imaginary time–evolution operator [116]. Some of the advantages of the spatial coordinates methods are that :

- a wide variety of shapes can be treated on the same footing.
- the same cubic lattice of points in 3-dimensional spatial coordinates is suitable to accomodate wave functions with arbitrary deformations, restricted in principle only by a specific symmetrization of the lattice.
- it allows studies of situations in which the asymptotic behavior of the wave functions at large distances is essential. This is very important for weakly bound nuclei [117].
- for the Skyrme zero-range interaction, the mean fields (if we exclude the velocity dependence) are *local*, and can be easily programmed in spatial coordinates.
- it is easy to carry out on parallel/vector computer architectures.

B. This approach uses a truncated harmonic oscillator (HO) basis, and solves the HF problem by the iterative diagonalization of the mean–field Hamiltonian, by the gradient method [118], or by the conjugate–gradient method [119]. It is particularly useful for the Gogny interaction [120, 121], and is important in the context of this dissertation. Some of the advantages of the HO basis representations are that :

- the basis provides a *natural cut–off* for many operators that are otherwise unbound and would require special treatment in spatial coordinates, *e.g.*, the multipole moment and the angular momentum operators, which are used often as constraints.

- iterative diagonalization of the mean–field Hamiltonian can be used to find the self–consistent solutions.
- the memory required is relatively small, so scalar or super-scalar computer architectures can be used.

As one can easily see, both approaches presented above complement each other to a great extent. In the Skyrme code HFODD used here the two techniques are very well combined with the Cartesian HO basis, applied for the appreciable benefit of providing fast, stable, and simple solution of the cranked Hartree–Fock problem. The RMF calculations have been carried out using the basis expansion method.

2.3.3 The Skyrme Hartree–Fock Method

A commonly–used family of nuclear interactions designed for use with the Hartree-Fock method are *Skyrme interactions* [78, 107, 98]. Their parameterization follows the general form of the nuclear interaction (2.1) consisting of two-body and three-body terms :

$$V_{\text{eff}} \simeq V^{(2)} + V^{(3)} \quad = \quad \sum_{i<j} V(i,j) + \sum_{i<j<k} V(i,j,k). \tag{2.55}$$

Skyrme Force Parameterizations

In its modern form, the Skyrme forces contain the zero-range two-body term (for any i, j particle doublet labeled 1,2) of the form :

$$\begin{aligned} V(1,2) &= t_0(1 + x_0\hat{P}^\sigma)\delta(\vec{r}_1 - \vec{r}_2) \\ &+ \frac{1}{2}t_1\left[\delta(\vec{r}_1 - \vec{r}_2)\vec{k}^2 + \vec{k}'^2\delta(\vec{r}_1 - \vec{r}_2)\right] \\ &+ t_2\vec{k}' \cdot \delta(\vec{r}_1 - \vec{r}_2)\vec{k} \\ &+ iW_0(\vec{\sigma}_1 + \vec{\sigma}_2) \cdot \left(\vec{k}' \times \delta(\vec{r}_1 - \vec{r}_2)\vec{k}\right), \end{aligned} \tag{2.56}$$

with $\hat{P}^\sigma \equiv \frac{1}{2}(1+\vec{\sigma}_1 \cdot \vec{\sigma}_2)$ being the spin-exchange operator, $\vec{k} = \vec{p}/\hbar = \frac{1}{2i}\left(\vec{\nabla}_1 - \vec{\nabla}_2\right)$ the relative momentum operator acting to the *right*, and $\vec{k}'$ — the complex conjugate of $\vec{k}$ acting to the *left*. The leading term (with strength t_0) is associated with a pure δ–force with spin exchange. The last term is a two-body spin–orbit interaction. The terms with t_1, t_2 mock up the effective range [78]. In old Skyrme forces the three-body interaction was approximated (for any i, j, k triplet labeled 1,2,3) by the form :

$$V(1,2,3) = t_3\delta(\vec{r}_1 - \vec{r}_2)\delta(\vec{r}_1 - \vec{r}_3). \tag{2.57}$$

The actual values of t_0, t_1, t_2, t_3, x_0, and W_0 can be fitted to different sets of data generating families of interactions labeled SkI, SkII, *etc.*

The mathematical form of the interaction outlined in the above formulas is simple enough to be implemented in Hartree–Fock codes and has enjoyed an enormous success in nuclear structure modeling, especially since the mid-1980's. In practical implementations of the Skyrme HF approach it is necessary to assume that the nuclear interactions are dependent on nuclear matter density (to account better for the in–medium effects). Their appearance of density–dependent terms in the HF Hamiltonian can be explained in the framework of the LDA, where

the total energy becomes a functional of one–body densities and currents, *e.g.*, the nucleon density $\rho(\vec{r})$, kinetic density, current densities, *etc.* [122]. In this Section we provide the set of such energy density functionals [108] used for the parameterizations of the modern Skyrme force, like SkM*, SkP, SLy4, used extensively with the HFODD code. In particular, the Skyrme parameterization can take a simpler form when the three-body term $V^{(3)}$ is approximated by a two–body density–dependent zero–range force :

$$V_0(1,2) = \frac{1}{6} t_3 (1 + P^\sigma) \delta(\vec{r}_1 - \vec{r}_2) \rho\left((\vec{r}_1 + \vec{r}_2)/2\right). \tag{2.58}$$

The studies of Waroquier *et al.* [123] demonstrated that the terms $V(1,2,3)$ and $V_0(1,2)$ contribute the same way to binding energies of even–even nuclei. As a result, the Skyrme interaction depends on only two radius–vectors, $\vec{r}_1$ and $\vec{r}_2$, which we shall denote henceforth as $(\vec{r}, \vec{r}')$.

The total HF energy is the expectation value (2.48) in the space of the Slater determinants $|\Phi\rangle$ built from the single-particle wave functions $|\phi_i\rangle, i = 1, \ldots, A$. $E_{\rm HF}$ can be expressed in the density–dependent Skyrme approach as a *local* integral functional. The basic quantity in such an approach is the *local energy density*, $\mathcal{H}(\vec{r})$ (see Appendices A and B of Ref. [124]) :

$$E_{\rm HF} \stackrel{\rm def}{=} \int \mathcal{H}(\vec{r}) d^3\vec{r}. \tag{2.59}$$

Following the model's conjecture, that the interaction depends only on the coordinates $(\vec{r}, \vec{r}')$, it is reasonable to reduce the basic quantities from which the model is derived to the *non–local densities*, $\rho_\alpha(\vec{r}, \vec{r}')$ and $\vec{s}_\alpha(\vec{r}, \vec{r}')$ (the *particle density* and the *spin density*, respectively, for nucleons of type α). Under the assumption that the total energy depends only on *local densities*, we can define them as the values of the non–local functionals evaluated at $\vec{r} = \vec{r}'$:

- the total *particle density*,

$$\rho(\vec{r}) \stackrel{\rm def}{=} \rho(\vec{r}, \vec{r}) = \rho_n(\vec{r}) + \rho_p(\vec{r}) = \sum_{i,\sigma,\alpha} |\phi_{i,\alpha}(\vec{r}, \sigma)|^2, \tag{2.60}$$

- the *spin density*,

$$\vec{s}(\vec{r}) \stackrel{\rm def}{=} \vec{s}(\vec{r}, \vec{r}) = \vec{s}_n(\vec{r}) + \vec{s}_p(\vec{r}) = \sum_\alpha \vec{s}_\alpha(\vec{r}, \vec{r}), \tag{2.61}$$

- *kinetic energy* density,

$$\tau(\vec{r}) = \tau_n(\vec{r}) + \tau_p(\vec{r}) = \left[(\vec{\nabla} \cdot \vec{\nabla}')\rho(\vec{r}, \vec{r}')\right]_{\vec{r}=\vec{r}'} = \sum_{i,\sigma,\alpha} \left|\vec{\nabla}\phi_{i,\alpha}(\vec{r}, \sigma)\right|^2, \tag{2.62}$$

- *vector kinetic energy density*, $\vec{T}(\vec{r}) = \vec{T}_n(\vec{r}) + \vec{T}_p(\vec{r})$, where

$$\vec{T}_\alpha(\vec{r}) = \left[(\vec{\nabla} \cdot \vec{\nabla}')\vec{s}_\alpha(\vec{r}, \vec{r}')\right]_{\vec{r}=\vec{r}'}, \tag{2.63}$$

- *momentum density*, $\vec{j}(\vec{r}) = \vec{j}_n(\vec{r}) + \vec{j}_p(\vec{r})$:

$$\vec{j}_\alpha(\vec{r}) = \frac{1}{2i}\left[(\vec{\nabla} - \vec{\nabla}')\rho_\alpha(\vec{r}, \vec{r}')\right]_{\vec{r}=\vec{r}'}, \tag{2.64}$$

- the *spin–current tensor*, $J_{\mu\nu}(\vec{r})$, with proton and neutron components

$$J_{\mu\nu,\alpha}(\vec{r}) = \frac{1}{2i}\left[(\nabla_\mu - \nabla'_\mu)s_{\nu,\alpha}(\vec{r},\vec{r}')\right]_{\vec{r}=\vec{r}'}, \tag{2.65}$$

  where $s_{\nu,\alpha}(\vec{r},\vec{r}')$ is the ν-th component of $\vec{s}_\alpha(\vec{r},\vec{r}')$.

In the above expressions all summations are over the set of *occupied* single-particle states. The spin density involves the spin projection σ for the nucleon at point $\vec{r}$.

The accepted "standard" format for the energy density $\mathcal{H}(\vec{r})$ is [109] :

$$\mathcal{H} := \mathcal{K} + \mathcal{H}_0 + \mathcal{H}_3 + \mathcal{H}_{\text{eff}} + \mathcal{H}_{\text{fin}} + \mathcal{H}_{\text{s.-o.}} + \mathcal{H}_{\text{sg}} + \mathcal{H}_{\text{Coulomb}} \tag{2.66}$$

which consists of the following terms :

- *kinetic energy density*,

$$\mathcal{K} = \frac{\hbar^2}{2m}\tau \tag{2.67}$$

- *zero-range term*,

$$\mathcal{H}_0 = \frac{1}{4}t_0\left[(2+x_0)\rho^2 - (2x_0+1)(\rho_p^2+\rho_n^2)\right], \tag{2.68}$$

- *density-dependent term*,

$$\mathcal{H}_3 = \frac{1}{24}\rho^\sigma t_3\left[(2+x_3)\rho^2 - (2x_3+1)(\rho_p^2+\rho_n^2)\right], \tag{2.69}$$

- *effective-mass term*,

$$\begin{aligned}\mathcal{H}_{\text{eff}} &= \frac{1}{8}\left[t_1(2+x_1)+t_2(2+x_2)\right]\tau(\vec{r})\rho(\vec{r}) \\ &+ \frac{1}{8}\left[t_2(2x_2+1)-t_1(2x_1+1)\right](\tau_p\rho_p+\tau_n\rho_n),\end{aligned}$$

- "finite–range" term,

$$\begin{aligned}\mathcal{H}_{\text{fin}} &= \left[3t_1(2+x_1)-t_2(2+x_2)\right](\vec{\nabla}\rho)^2 \\ &- \frac{1}{32}\left[3t_1(2x_1+1)+t_2(2x_2+1)\right]\left[(\vec{\nabla}\rho_p)^2+(\vec{\nabla}\rho_n)^2\right],\end{aligned}$$

- spin-orbit interaction term,

$$\mathcal{H}_{\text{s.-o.}} = \frac{1}{2}W_0\left[\vec{J}\cdot\vec{\nabla}\rho + \vec{J}_p\cdot\vec{\nabla}\rho_p + \vec{J}_n\cdot\vec{\nabla}\rho_n\right], \tag{2.70}$$

- spin–gradient term

$$\mathcal{H}_{\text{sg}} = -\frac{1}{16}(t_1x_1+t_2x_2)\vec{J}^2 + \frac{1}{16}(t_1-t_2)(\vec{J}_p^2+\vec{J}_n^2). \tag{2.71}$$

The Coulomb energy density $\mathcal{H}_{\text{Coulomb}}$, in Eq. (2.66) can be decomposed into *direct* and *exchange* parts :

$$\mathcal{E}_{\text{dir}}^{\text{Coulomb}} = \frac{e^2}{2}\int \frac{\rho_p(\vec{r}_1)\rho_p(\vec{r}_2)}{|\vec{r}_1-\vec{r}_2|}d^3\vec{r}_1 d^3\vec{r}_2, \tag{2.72}$$

$$\mathcal{E}_{\text{exch}}^{\text{Coulomb}} = \frac{e^2}{2}\int \frac{\rho_p(\vec{r}_2,\vec{r}_1)\rho_p(\vec{r}_1,\vec{r}_2)}{|\vec{r}_1-\vec{r}_2|}d^3\vec{r}_1 d^3\vec{r}_2. \tag{2.73}$$

Usually one approximates the charge density by the proton density only, thus ignoring the corrections from proton and neutron charge form–factors [125], and other electromagnetic effects [126], which are very small. The exchange Coulomb energy (2.73) is usually treated in the Slater approximation [127, 128]

$$\mathcal{E}_{\text{exch}}^{\text{Coulomb}} = -\frac{3e^2}{4}\left(\frac{3}{\pi}\right)^{1/3}\int \rho_p^{4/3}(\vec{r})d^3\vec{r}. \tag{2.74}$$

In particular, for the case of N=Z, *i.e.*, when the proton and neutron particle densities are equal, the energy functional $\mathcal{H}(\vec{r})$ takes a simple form :

$$\begin{aligned}\mathcal{H}(\vec{r}) &= \frac{\hbar^2}{2m}\tau(\vec{r}) + \frac{3}{8}t_0\rho^2(\vec{r}) + \frac{1}{16}(3t_1+5t_2)\left[\rho(\vec{r})\tau(\vec{r}) - \vec{j}^2(\vec{r})\right] \\ &- \frac{1}{64}(9t_1-5t_2)\rho(\vec{r})\nabla^2\rho(\vec{r}) + \frac{1}{16}t_3\rho^3(\vec{r}).\end{aligned}$$

The SLy4 Interaction

The Skyrme SLy4 interaction has been improved over previous Skyrme parameterizations by being capable of reproducing properties of nuclear matter in regimes ranging all the way from subnuclear densities to those typical of neutron stars. As discussed in [109], the fitting protocol had the following features :

1. SLy4 reproduced some of the essential properties of the symmetric nuclear matter. In particular, it reproduced the saturation point of the symmetric infinite nuclear matter, $\rho_0 \simeq 0.16$ fm^{-3}. Furthermore, it yields the incompressibility parameter, $K_\infty \simeq 229.9$ MeV, and the symmetry energy $a_S \simeq 32$ MeV.

2. The interaction reproduces the nuclear matter equation of state [129] rather well.

3. The interaction reproduces the properties of finite nuclei, *e.g.*, the binding energies for a chosen set of doubly–magic nuclei.

The resulting values for the standard Skyrme force parameters are [109] :
$t_0 = -2488.91$ MeV fm^3, $t_1 = 486.82$ MeV fm^5,
$t_2 = -546.39$ MeV fm^5, $t_3 = 13777.0$ MeV fm$^{3(1+\sigma)}$,
$x_0 = 0.834$, $x_1 = -0.344$, $x_2 = -1.000$, $x_3 = 1.354$,
$\sigma = 1/6$, $W_0 = 123.0$ MeV fm^5.

Code HFODD : Definitions

The code HFODD used in this work, published in Refs. [110, 130], is expected to give results comparable with the relativistic mean–field approximation on the same footing. The advantages

of the Skyrme HF procedure in Cartesian spatial coordinates employed in this work include the possibility of accommodating wave functions with arbitrary deformations. This fact is of importance in light of the expectations that the proton and neutron deformations may differ, as suggested by previous theoretical studies [131, 132]. Its capability of dealing with situations in which the asymptotic behavior of the wave functions at large distances is essential is very important for our treatment of very neutron-rich nuclei (Chapter 4), which are expected to be weakly bound [117].

In HFODD, intrinsic configurations are denoted by means of total occupation numbers in each of the four parity–signature blocks $N_{\pi,r}$ [110], denoted by

$$[N_{+,+i}, N_{+,-i}, N_{-,+i}, N_{-,-i}]. \tag{2.75}$$

In the Hartree-Fock approach, the total energy of the many-body system of nucleons is assumed to be, in the general case, a functional of the 1-body non-local density

$$\rho_\alpha(\vec{r}\sigma, \vec{r}'\sigma') = \langle\Psi| a^\dagger_{\vec{r}'\sigma'\alpha} a_{\vec{r}\sigma\alpha} |\Psi\rangle, \tag{2.76}$$

where $|\Psi\rangle$ stands for a many-body wave function and $a^\dagger_{\vec{r}\sigma\alpha}$ and $a_{\vec{r}\sigma\alpha}$ are the creation and annihilation operators respectively for neutrons or protons located at point $\vec{r}$ with spin projection σ ($+\frac{1}{2}$ or $-\frac{1}{2}$). The non-local density can be written as

$$\rho_\alpha(\vec{r}\sigma, \vec{r}'\sigma') = \frac{1}{2}\rho_\alpha(\vec{r}, \vec{r}')\delta_{\sigma\sigma'} + \frac{1}{2}\vec{s}_\alpha(\vec{r}, \vec{r}') \cdot \vec{\sigma}_{\sigma\sigma'}, \tag{2.77}$$

where

$$\rho_\alpha(\vec{r}, \vec{r}') = \sum_\sigma \rho_\alpha(\vec{r}\sigma, \vec{r}'\sigma') \tag{2.78}$$

$$\vec{s}_\alpha(\vec{r}, \vec{r}') = \sum_\sigma \rho_\alpha(\vec{r}\sigma, \vec{r}'\sigma') \langle\sigma'|\sigma|\sigma\rangle. \tag{2.79}$$

The isoscalar ($t = 0$) and isovector ($t = 1$) components can be obtained easily from neutron and proton densities. For instance,

$$\rho_{t=0,1}(\vec{r}) = \rho_n(\vec{r}) \pm \rho_p(\vec{r}). \tag{2.80}$$

With these definitions at hand, the total HF energy can be expressed as

$$E = \mathcal{E}^{\text{kinetic}} + \mathcal{E}^{\text{Skyrme}} + \mathcal{E}^{\text{Coulomb}}. \tag{2.81}$$

The first term is the *total kinetic energy* of the protons and neutrons combined,

$$\mathcal{E}^{\text{kinetic}} = \frac{\hbar^2}{2m}\left(1 - \frac{1}{A}\right)\int \tau_{t=0}(\vec{r})d^3\vec{r}, \tag{2.82}$$

in which the factor in brackets approximately takes into account the center–of–mass correction.

The second term is the *Skyrme energy*

$$\mathcal{E}^{\text{Skyrme}} = \sum_{t=0,1}\int \left[\mathcal{H}_t^{\text{even}}(\vec{r}) + \mathcal{H}_t^{\text{odd}}(\vec{r})\right]d^3\vec{r}, \tag{2.83}$$

where

$$\mathcal{H}_t^{\text{even}}(\vec{r}) = C_t^\rho \rho_t^2 + C_t^{\Delta\rho} \rho_t \Delta\rho_t + C_t^\tau \rho_t \tau_t + C_t^J \left(\sum_{\mu\nu} J_{\mu\nu,t}^2 \right) + C_t^{\nabla J} \rho_t \nabla \cdot \vec{J}_t \tag{2.84}$$

$$\mathcal{H}_t^{\text{odd}}(\vec{r}) = C_t^s \sigma_t^2 + C_t^{\Delta s} \mathbf{s}_t \Delta \mathbf{s}_t + C_t^T \vec{s}_t \cdot \vec{T}_t + C_t^j \vec{j}_t^2 + C_t^{\nabla j} \mathbf{s}_t \cdot (\vec{\nabla} \times \vec{j}_t) \tag{2.85}$$

with the vector part of the tensor density $\vec{J}_t$ defined as

$$J_{\lambda,t} := \sum_{\mu\nu} \epsilon_{\lambda\mu\nu} J_{\mu\nu,t}. \tag{2.86}$$

The *coupling constants* introduced in the expressions above (with $t = 0, 1$) can be subdivided into 10 *time–even* (C_t^ρ, $C_t^{\Delta\rho}$, C_t^τ, C_t^J, $C_t^{\nabla J}$), and 10 *time–odd* (C_t^s, $C_t^{\Delta s}$, C_t^T, C_t^j, $C_t^{\nabla j}$). They can be evaluated via their relationships with the standard parameterizations of the Skyrme interaction, as described in [133, 134].

The Coulomb energy $\mathcal{E}^{\text{Coulomb}}$ in the Skyrme energy expression can be decomposed into direct and exchange parts, as defined before (2.72–2.73). In the calculations, the direct Coulomb potential can be obtained from the proton density :

$$U^{\text{Coulomb}}(\vec{r}) = e^2 \int \frac{\rho_p(\vec{r}')}{|\vec{r} - \vec{r}'|} d^3\vec{r}'. \tag{2.87}$$

Constraints

The total HF energy is obtained by minimization under a specified set of constraining relations, which serve the purpose of making the HF solution satisfy a set of *a priori* given conditions. The minimal set of such constraints can involve, but is not limited to, restrictions on deformation, total angular momentum, *etc.* In order to impose the constraining conditions the method of Lagrange multipliers is used, in which the energy is redefined to include additional terms. In the particular form used in the code HFODD, the modified energy is

$$E' = E + \mathcal{E}^{\text{mult}} + \mathcal{E}^{\text{crank}} \tag{2.88}$$

where

$$\mathcal{E}^{\text{mult}} = \sum_{\lambda\mu} C_{\lambda\mu} \left(\left\langle \hat{Q}_{\lambda\mu} \right\rangle - \bar{Q}_{\lambda\mu} \right)^2 \tag{2.89}$$

is a quadratic form for the mass multipole–moment constraint. The coefficients $C_{\lambda\mu}$, when different from zero, play the role of stiffness constants for the constraints.

The cranking constraint $\mathcal{E}^{\text{crank}}$ would attach the converging solution to the (non–zero) cranking frequency ω_I seeking out such with a specified value for the angular momentum $\bar{I}_x$. In the code HFODD, the rotation axis has been chosen for convenience to be the Oy axis instead of Ox. The cranking constraining term can have a combined linear and quadratic form

$$\mathcal{E}^{\text{crank}} = -\omega_I \left\langle \hat{I}_y \right\rangle + C_I \left(\left\langle \hat{I}_y \right\rangle - \bar{I}_y \right)^2. \tag{2.90}$$

The physical angular frequency ω_y is obtained by

$$\omega_y = \frac{\partial \mathcal{E}}{\partial \left\langle \hat{I}_y \right\rangle} = \omega_I - 2C_I \left(\left\langle \hat{I}_y \right\rangle - \bar{I}_y \right). \tag{2.91}$$

Remarkably, the constraining term with only a linear part (*i.e.* for $C_I = 0$) turns out to give more stable convergence properties, in that case $\omega_y = \omega_I$.

2.3.4 Relativistic Mean Field Theory

In this subsection we describe the *relativistic mean field* approach used in the present work. The RMF calculations were carried out for superdeformed states in the A$\simeq$ 130 mass region.

Brief Overview

The *relativistic mean–field approach* (see [135, 136]) is a version of the self–consistent mean field method based, as in the nonrelativistic case, on the representation of the nuclear ground state $|\Psi\rangle$ as a product of independent single-particle states, which are eigenvectors of a single–particle Hamiltonian. With very few parameters (coupling constants and masses), adjusted to a small set of data for spherical nuclei, RMF has provided very good results for static properties of nuclei, *e.g.,* binding energies and radii, density distributions, deformation parameters, and moments of inertia over wide areas of the nuclear chart [137].

In most of the relativistic mean–field calculations the Fock (or *exchange*) term is neglected, although in general it does not have to be small. For example, the relativistic Hartree–Fock calculations for spherical nuclei [138, 139] have indicated that the inclusion of the Fock terms may require significant readjustments of the meson–nucleon coupling constants. Nevertheless, the fact that the parameters of the effective theory are fitted to experimental data implies that even the Hartree approximation to the mean field alone takes some part of the Fock term into account. Furthermore, from general considerations based on boson–expansion approaches, it is evident that the Fock terms can be of the same order of magnitude as the random–phase approximation (RPA) corrections.

For zero–range interaction, the exchange term has a form which (to a statistical factor) is identical to that of the direct term. However, this justification could not be used alone, because the pion exchange contribution is not predominantly short range. The pion field is included phenomenologically in the Hartree approximation in the form of the two–pion exchange (the σ-field).

Basic Concepts and Definitions

The relativistic mean–field approach [63, 140, 64, 62] has been a powerful tool in nuclear structure physics. Its advantages seem to be due, to an extent, to its good description of isotope shifts, related to an improved treatment of shell effects and deformations.

The comparison of RMF with the Skyrme theory has revealed some interesting insights. The spin–orbit potential in RMF has an implicit density dependence due to its origins in the Dirac–Lorentz structure of the interaction [141, 142]. The RMF theory has been extended successfully to deformed nuclei [131, 132, 143], where it has been able to reproduce the data fairly well, partcularly in an extensive study of the Sr region [144].

The relativistic mean–field approach is based on the description of nucleons as Dirac spinors interacting via exchange of mesons of different types. The model is formulated through a *Lagrangian density* (for this Section only, we use $\hbar = c = 1$, and bold letters denote isovectors) :

$$\begin{aligned}
\mathcal{L} &= \bar{\psi}(\not{\partial} - M)\psi + \frac{1}{2}\partial_\mu\sigma\partial^\mu\sigma - U(\sigma) \\
&- \frac{1}{4}\Omega_{\mu\nu}\Omega^{\mu\nu} + \frac{1}{2}m_\omega^2\omega_\mu\omega^\mu - \frac{1}{4}\mathbf{R}_{\mu\nu}\cdot\mathbf{R}^{\mu\nu} + \frac{1}{2}m_\rho^2\rho_\mu\cdot\rho^\mu \\
&- \frac{1}{4}F_{\mu\nu}F^{\mu\nu} - g_\sigma\bar{\psi}\sigma\psi - g_\omega\bar{\psi}\not{\omega}\psi - g_\rho\bar{\psi}\not{\rho}\cdot\tau\psi - e\bar{\psi}\frac{1-\tau_3}{2}\cdot\not{A}\psi,
\end{aligned} \tag{2.92}$$

where we used the notations $\not{\partial} := i\gamma^\mu\partial_\mu$, $\mathbf{R}_{\mu\nu}\cdot\mathbf{R}^{\mu\nu} := R^a_{\mu\nu}R^{a\mu\nu}$, $\not{\xi} := \gamma^\mu\xi_\mu$ for the vector fields $\xi = \{\omega, \rho, A\}$, the scalar product in the isospin space $\rho_\mu\cdot\rho^\mu := \rho^a_\mu\rho^{\mu a}$, τ — the isospin vector, and a — an isospin running index. The Lagrangian includes the baryon (nucleonic) fields with mass M, as well as the meson fields :

- neutral isoscalar scalar *σ–meson* with mass m_σ,
- neutral isoscalar vector *ω–meson* with mass m_ω,
- charged isovector vector *ρ–meson* with mass m_ρ,

as well as an *electrostatic field* for the protons. The ρ meson, being isovector, provides the necessary isospin asymmetry. The interaction term $U(\sigma)$ includes non-linear self-interaction couplings

$$U(\sigma) = \frac{1}{2}m_\sigma^2\sigma^2 + \frac{1}{3}g_2\sigma^3 + \frac{1}{4}g_3\sigma^4, \tag{2.93}$$

which are necessary for the adequate description of the surface properties [136] (for other non-linear forms involving σ and ρ see [145]). The other parameters in the Lagrangian density are the nucleon mass M, the σ-, ω-, and ρ-meson masses defined above, and their coupling constants g_σ, g_ω, g_ρ, along with the photon coupling constant $\alpha = e^2/(4\pi) = 1/137$. The field tensors used in $\mathcal{L}$ are defined as follows :

$$\Omega^{\mu\nu} = \partial^\mu\omega^\nu - \partial^\nu\omega^\mu \tag{2.94}$$

$$R^{\mu\nu} = \partial^\mu\rho^\nu - \partial^\nu\rho^\mu - g_\rho(\rho\times\rho)^{\mu\nu} \tag{2.95}$$

$$F^{\mu\nu} = \partial^\mu\mathbf{A}^\nu - \partial^\nu\mathbf{A}^\mu. \tag{2.96}$$

The equations of motion are derived following the standard procedure by applying the variational principle. When cranking is involved, the time–reversal symmetry is broken, and one has to consider the time–even and time–odd mean fields separately. The resulting Dirac equation for the fermion fields has the form

$$\left[-i\vec{\alpha}\cdot\vec{\nabla} + V(\vec{r}) + \beta(M + S(\vec{r}))\right]\psi_i(\vec{r}) = \epsilon_i\psi_i(\vec{r}), \tag{2.97}$$

where $V(\vec{r})$ stands for the *vector* potential

$$V(\vec{r}) = g_\omega\omega^0(\vec{r}) + g_\rho\tau^3\rho^0(\vec{r}) + e\frac{1+\tau^3}{2}\mathbf{A}^0(\vec{r}), \tag{2.98}$$

and $S(\vec{r})$ is the *scalar* potential

$$S(\vec{r}) = g_\sigma\sigma(\vec{r}), \tag{2.99}$$

which also contributes to the effective nucleon mass $M^*(\vec{r}) = M + S(\vec{r})$.

In the mean–field approximation, the meson and photon fields are described by static fields, obtained from the Klein–Gordon equations :

$$
\begin{aligned}
(-\vec{\nabla}^2 + m_\sigma^2)\sigma^2 &= -g_\sigma \rho_s(\vec{r}) - g_2\sigma^2(\vec{r}) - g_3\sigma^3(\vec{r}) \\
(-\vec{\nabla}^2 + m_\omega^2)\omega_0^2 &= -g_\omega \rho_v(\vec{r}) \\
(-\vec{\nabla}^2 + m_\rho^2)\rho_0^2 &= -g_\rho \rho_3(\vec{r}) \\
-\vec{\nabla}^2 A_0(\vec{r}) &= e\rho_p(\vec{r}),
\end{aligned}
$$

with the following definitions for the source terms :

$$
\begin{aligned}
\rho_s(\vec{r}) &= \sum_{i=1}^{A} \bar{\psi}_i(\vec{r})\psi_i(\vec{r}) \\
\rho_v(\vec{r}) &= \sum_{i=1}^{A} \psi_i^\dagger(\vec{r})\psi_i(\vec{r}) \\
\rho_3(\vec{r}) &= \sum_{p=1}^{Z} \psi_p^\dagger(\vec{r})\psi_p(\vec{r}) - \sum_{n=1}^{N} \psi_n^\dagger(\vec{r})\psi_n(\vec{r}) = \sum_{i=1}^{A} \psi_i^\dagger(\vec{r})\tau^3\psi_i(\vec{r}) \\
\rho_p(\vec{r}) &= \sum_{p=1}^{Z} \psi_p^\dagger(\vec{r})\psi_p(\vec{r}) = \sum_{i=1}^{A} \psi_i^\dagger(\vec{r})\frac{1-\tau^3}{2}\psi_i(\vec{r}).
\end{aligned}
$$

The coupled Dirac and Klein–Gordon equations have to be solved iteratively. The total energy is calculated in a way similar to the Skyrme HF, but with the following Hamiltonian density :

$$
\begin{aligned}
\mathcal{H}(\vec{r}) &= \sum_i \psi_i^\dagger(-i\vec{\nabla}\cdot\vec{\alpha} + \beta M^*(\vec{r}) + V(\vec{r}))\psi_i \\
&+ \frac{1}{2}(\vec{\nabla}\sigma)^2 + U(\sigma) \\
&- \frac{1}{2}\left((\vec{\nabla}\omega^0)^2 + m_\omega^2(\omega^0)^2 + (\vec{\nabla}\rho^0)^2 + m_\rho^2(\rho^0)^2 + (\vec{\nabla}A^0 n)^2\right).
\end{aligned} \tag{2.100}
$$

The approach outlined above is referred to as *"no–sea" approximation* because it ignores the contributions from negative-energy states, *i.e.*, it assumes that the vacuum is not polarized.

RMF Parameterization

The RMF parameterization NL1 used in this work is as follows [146] :

$M = 938.0$ MeV,

$m_\sigma = 492.25$ MeV, $m_\omega = 795.359$ MeV, $m_\rho = 763.0$ MeV,

$g_\sigma = 10.138$, $g_\omega = 13.285$, $g_\rho = 4.975$,

$g_3 = -12.172$ fm^{-1}, $g_4 = -36.265$, and $M^*/M = 0.57$.

2.4 Rotational Bands in HFODD

This Section provides some details about the cranked Skyrme code HFODD, and the way the rotational bands are computed.

2.4.1 Self–Consistent Symmetries

The self–consistent approaches to the nuclear many–body problem start with a *priori* assumptions about the nucleon–nucleon interaction and the self–consistent solutions are obtained in an iterative way. The mean field preserves symmetries of the nucleonic density [78]. It is therefore important that we start the iteration process with solutions spanned on a set of basis functions with as many broken symmetries as possible (or computationally feasible), and proceed with the self–consistent iteration process while guaranteeing that the solution(s) have the desired symmetries of the physical problem.

In the Skyrme code HFODD this is achieved by using a 3–dimensional harmonic oscillator basis in Cartesian coordinates [110, 130, 133, 134]. Since cranking takes place around the y–axis, the x–z plane is the symmetry plane for the HF states. This minimal symmetry limitation provides an ample enough basis range in which to carry out the HF procedure, while striking a good compromise for the sake of computational feasibility. The result is that the operators of parity $\hat{\mathcal{P}}$ and signature $\hat{\mathcal{R}}_y \equiv e^{-i\pi \hat{J}_y}$ can now be used to construct the so–called *y–simplex operator* in the form

$$\hat{\mathcal{S}}_y := \hat{\mathcal{P}}\hat{\mathcal{R}}_y \equiv \hat{\mathcal{P}} e^{-i\pi \hat{J}_y}. \tag{2.101}$$

Consequentially, the HF wave function $|\Psi\rangle$ obtained as a solution of the HF equations is also an eigenstate of the y–simplex operator

$$\hat{\mathcal{S}}_y |\Psi\rangle = \mathcal{S} |\Psi\rangle , \tag{2.102}$$

and its eigenvalue is the product of the parities and signatures of the occupied nucleon states.

The choice of the y–simplex (we simply call it simplex) as the conserved symmetry for HFODD has some technical advantages. For example, the average values of the multipole moments in simplex–preserving states are real

$$Q_{\lambda\mu} = \left\langle \hat{Q}_{\lambda\mu} \right\rangle \equiv \langle \Psi | \hat{Q}_{\lambda\mu} | \Psi \rangle = Q^*_{\lambda\mu} \tag{2.103}$$

because the phase factor in the condition

$$\hat{Q}_{\lambda\mu} = (-1)^\mu \hat{Q}_{\lambda,-\mu} \tag{2.104}$$

is cancelled by that from the y–simplex symmetry operation

$$\hat{\mathcal{S}}_y^\dagger \hat{Q}_{\lambda\mu} \hat{\mathcal{S}}_y = (-1)^\mu \hat{Q}_{\lambda,-\mu}, \tag{2.105}$$

thus allowing us to work only with the components of the multipole moments with $\mu \geq 0$. In addition, all of the components of $Q_{\lambda\mu}$ can be simultaneously and independently non–zero, which gives the code a significant flexibility in dealing with a wider variety of nuclear shapes.

The single–particle wave functions can be labeled with the simplex quantum number for the corresponding simplex block

$$\hat{\mathcal{S}}_y \psi_{k,\alpha}(\vec{r},\sigma) = s_k \psi_{k,\alpha}(\vec{r},\sigma), \tag{2.106}$$

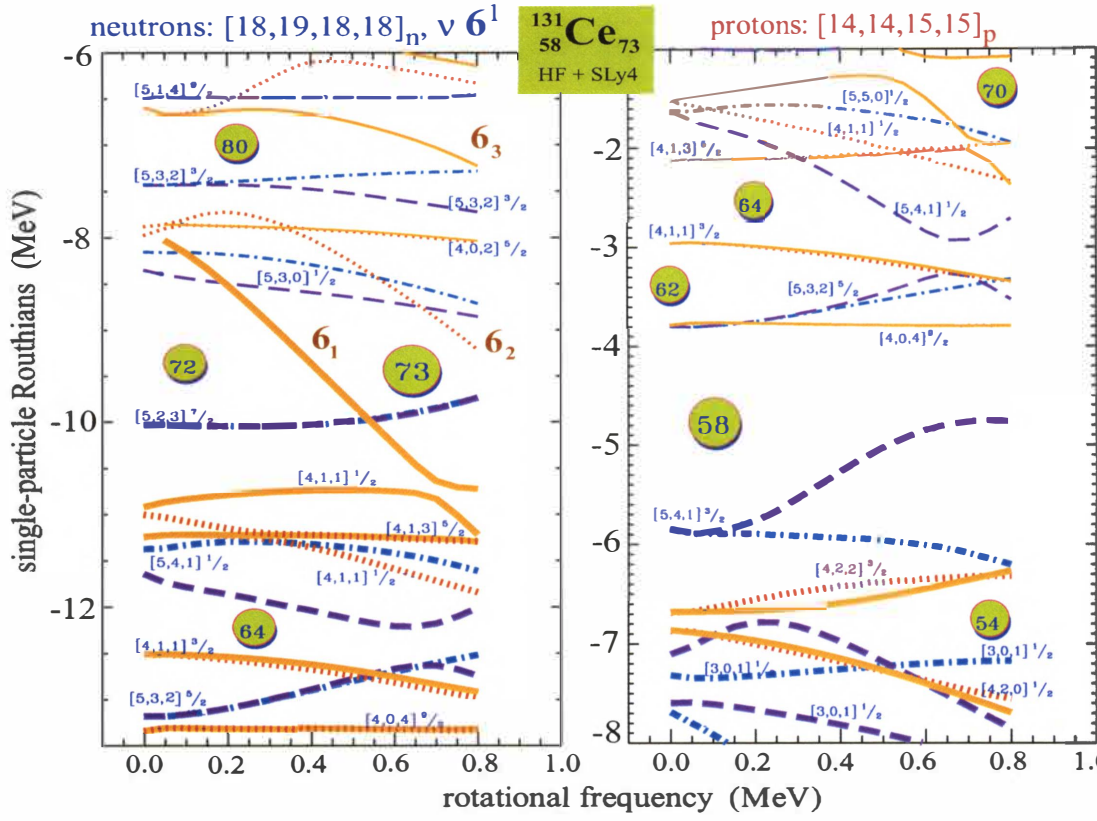

Figure 2.3: Diagram of the single–particle Routhians for the lowest ^{131}Ce superdeformed band as functions of the cranking frequency. See the text for explanation of the configuration labels.

where k is an index enumerating the single–particle wave function $\psi_{k,\alpha}(\vec{r},\sigma)$. The corresponding signature quantum numbers r_k can be obtained from the relation $s_k = \pi_k r_k$.

In the case of simultaneous conservation of both parity and signature, the multipole moments $Q_{\lambda\mu}$ are zero for odd values of λ due to the transformation property

$$\hat{\mathcal{P}}^\dagger \hat{Q}_{\lambda\mu} \hat{\mathcal{P}} = (-1)^\lambda \hat{Q}_{\lambda,-\mu}. \tag{2.107}$$

2.4.2 Routhian Diagrams : The A≃130 Region

We are now ready to give an example of a rotational band calculated using the Skyrme Hartree–Fock method. A prime candidate is the observed SD band in ^{131}Ce (Z=58, N=73) [147, 148]. This band is significant from the point of view of the interpretation of the results presented in the next Chapter.

Figure 2.3 shows the single–particle Routhian diagram for the HFODD–calculated configuration $[18,19,18,18]_n$ $[14,14,15,15]_p$, where the numbers in the square brackets are the total occupation numbers in the four parity–signature blocks [$(\pi, r) = (+1,+i)$, $(+1,-i)$, $(-1,+i)$, $(-1,-i)$], and their sum is equal to the total particle number (N and Z for neutrons and protons, respectively). The line–style of the plotted single–particle states is used to denote various *parity–signature*

combinations : we use dotted, solid, dot–dashed, and dashed lines to indicate states from the simplex blocks in the order chosen above. Thick or thin lines represent occupied or unoccupied states, respectively. For convenience, the states are also labeled with their Nilsson labels at ω=0. We shall use these labels to relate particular single–particle Routhians to deformed shell model states. The Nilsson labels provide a wealth of information about the interaction of valence orbitals in the particle–plus–rotor picture, which we use to interpret the interplay between collective rotation and single–particle motion. In addition to the Nilsson labels, we use the notation $\mathcal{N}_m$ to denote states that originate from shells with main quantum number $\mathcal{N}$. The index m in the sequence 6_1, 6_2, ... is used to label the lowest, second lowest, *etc.* state from the $\mathcal{N}$=6 shell. It is now accepted terminology to designate down–sloping states with high values of $\mathcal{N}$ as *intruders*, and the up–sloping states with lower $\mathcal{N}$ values as *extruders*.

An important feature of Fig. 2.3 is the occurrence of significant energy gaps in the single–particle spectrum, notably around the last occupied states for both neutrons and protons. One can notice that the intruder state 6_1 traverses the neutron gap at N=73, staying below the gap for all rotational frequencies exceeding $\hbar\omega \simeq$0.5 MeV. The gap above the last occupied state, including the intruder, becomes as large as 1 MeV around that frequency, and then becomes narrower as the state 6_2 approaches the Fermi level. The two intruders originate at $\hbar\omega$=0 MeV from the Nilsson state ($i_{13/2}$) [660]1/2, which, with its $\Omega = \frac{1}{2}$, has a significant signature splitting. The small value of Ω implies that a significant part of the $\frac{13}{2}$ =6.5 units of angular momentum is oriented nearly parallel to the y-axis around which the cranking takes place. As discussed in Section 2.2, the particle–plus–rotor model predicts that at low frequencies (*i.e.*, in the *deformation–aligned* limit) the slope of the single–particle Routhian for $\Omega = 1/2$ particle in the field of rotating prolate nuclear shapes is $\frac{a}{2}$. The slopes read from the Routhian diagram agree very well with this prediction. The opposite signs of the slopes show that the orientations of the spins for the pair of [660]1/2 neutrons are opposite to one another. As the rotational frequency increases, the 6_2 Routhian gradually changes its slope to negative and enters the N=73 gap from above with a slope nearly equal to that of its signature partner. In the *rotational–alignment limit*, which the band approaches at high frequencies, the value of $\left\langle \hat{j}_y \right\rangle$ approaches that of $j = 13/2$, so that the occupied 6_1 contributes about 6.5 units of angular momentum to that of the nucleus. As we can see from Fig. 2.3, the high–j low–Ω intruder states carry large intrinsic angular momenta, and their Routhians steeply decrease as functions of $\hbar\omega$. This means that the intruder states are usually responsible for the increase of total spin due to their alignment.

One can see that, besides the intruders, there are two more of the $\Omega = \frac{1}{2}$ neutron Nilsson states that exhibit signature splitting, although of much smaller magnitude : the [411]1/2 and [541]1/2. In the proton part of the diagram, such orbitals are the [550]1/2, and the [301]1/2, although they will be of lesser significance for our study.

In the cases when the values of Ω are large, the single–particle orbitals are deformation–aligned. The example is the proton $g_{9/2}$ [404]9/2 state, located immediately above the wide gap at Z=58. The large value of Ω implies that the single–particle angular momentum tends to be parallel to the symmetry axis. This leads to a very small signature splitting.

We shall return later to this way of reasoning based on the Nilsson model in order to understand the effects of occupation of individual nucleon orbitals. It is important to highlight the fact that the intruder and extruder orbitals play a significant role in the establishment of nuclear deformation, and that they are building blocks of nuclear angular momentum.

2.4.3 Level Crossings, Diabolic Points and Diabaticity

Some of the most important mechanisms for obtaining structural information involve the study of the locations and physical character of the single–particle level crossings, which are directly related to the interaction of bands built on configurations carrying the same quantum numbers.

The set of general parameters, *e.g.*, deformation parameters, cranking frequency, *etc.*, at which different configurations cross, are referred to as *diabolic points*. In a Nilsson diagram a *crossing* of two or more states will appear every time the trajectory passes through a diabolic point. When the external parameter is the cranking frequency, the crossing appears in the Routhian diagram as near–degeneracy of corresponding single–particle Routhians at a certain narrow range in cranking frequency.

In the cranking approximation, the self–consistent solution is obtained by minimizing the expectation value of the Routhian (2.25). The set(s) of density matrices, for which such solution(s) exist, provide approximate solution(s) of the cranked self–consistent problem, with the expectation value of $\hat{I}_y$ constrained to the specified good angular momentum, and the rotational frequency ω playing the role of a Lagrange multiplier. The studies of the validity and solvability of the cranking approximation indicate [149, 150, 151] that the minimization procedure fails to converge when the vacuum, *i.e.*, the stationary solution, becomes degenerate with respect to particle–hole excitations. This situation can occur at frequencies, referred to here as *crossing frequencies* $\omega^{(c)}$, for which crossings of occupied and unoccupied single–particle states occur in the Routhian diagram. The degeneracy of the vacuum implies that it becomes a mixture of wave packets with different angular–momentum distributions, so the identity of the band in the vicinity of $\omega^{(c)}$ is lost. The mixing of levels depends on the interaction between them — the separation of these wave packets can be achieved in principle by setting the interaction to zero [150]. The technique for dealing with this problem is rather procedural [152, 153] — it involves keeping track of the position of individual states recognizable by some of their characteristics and occupying the same level(s) before and after the crossing(s). The approach is often referred to as the *diabatic*, or *configuration–constrained* cranking model (CCCM).

In the case of the code HFODD, the levels at high spins are traced by either their angular momentum alignment, or intrinsic spin alignment, used as independent diabatic criteria. An example of an avoided level crossing in HFODD is shown in Fig. 2.4, where we compare the positive–parity configuration in ^{131}Ce with the one in which, instead of the lowest N=6 neutron intruder r=–i state, the state [402]5/2 with the same parity–signature quantum numbers is occupied. Note that the corresponding bands, although having the same occupation numbers ν[18,19,18,18], have different states as the 19–th occupied state in the (π,r)=(+,–i) block. The code is instructed to perform the iterative convergence process while keeping occupied that level, for which the occupation criterium value is chosen to be higher or lower.

In this and other examples involving intruder states (the occupation of which is likely also to cause a considerable shape–deformation effect), the intruder levels have high angular momentum alignment, and they are kept diabatically occupied by selecting higher alignment as a diabaticity criterium. In the "diabatic blocking" case of the 6_1 intruder crossing the [402]5/2 state in the (+,–i) parity–signature block, the code is instructed to occupy the orbital with the larger momentum alignment, if the intruder is to be occupied. In the actual HFODD calculation the minimization procedure leads to a change of the deformation around the level crossing, leading to a "jump" in the single–particle Routhians. When the points of the band's deformation path are combined together for the entire frequency interval, the points around the level crossing displaying irregular behavior are excluded and the diabatic levels show a discontinuity, as marked with the shaded area in Fig. 2.4. Note that such a deformation jump occurs only when the

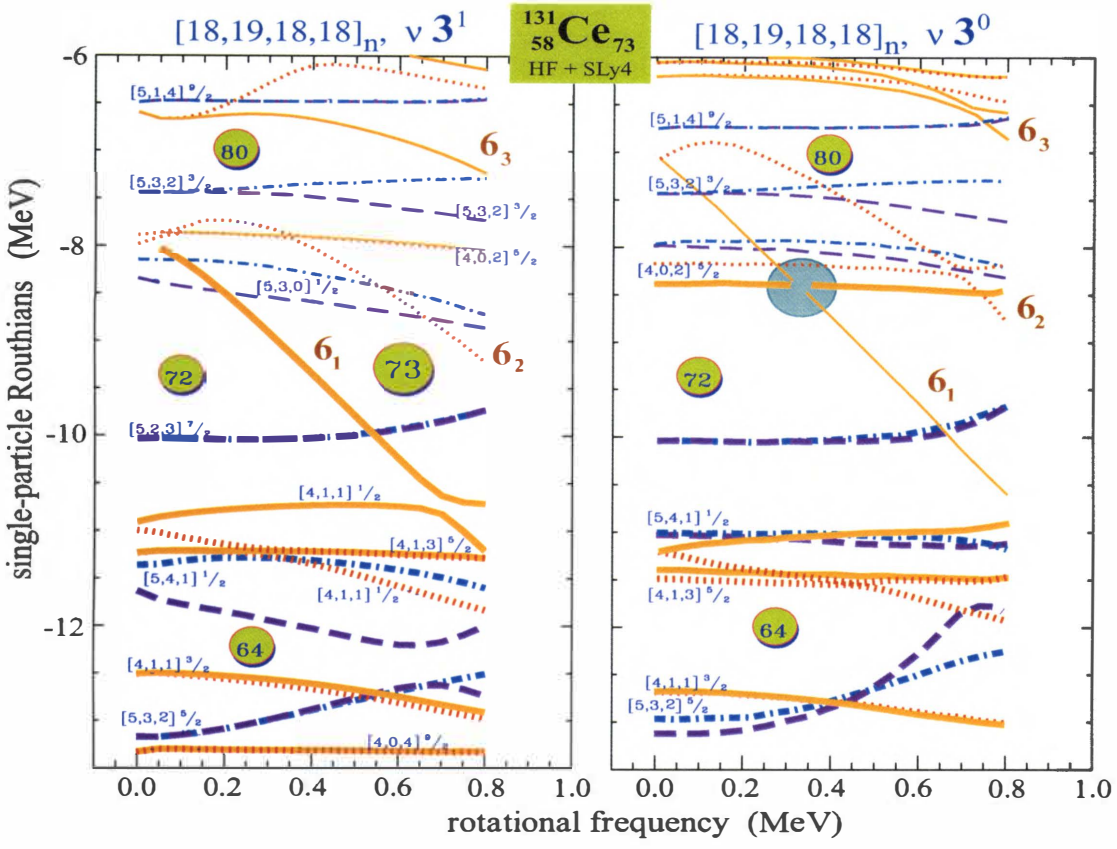

Figure 2.4: Single–neutron Routhians for ^{131}Ce calculated for the ν [18,19,18,18] configurations with (left) and without (right) the 6_1 intruder orbital. The shaded area marks the crossing of the 19-th and 20-th single–particle Routhians in the (+,–i) parity–signature block. The intruder configuration is more deformed (by about 0.6 eb), which causes the rearrangement of levels. See the text for interpretation and discussion.

crossing is between occupied and unoccupied states, when there is the possibility for the nucleon to occupy any one of the two or more states interacting and nearly degenerating at the crossing point. It does not happen when the crossing is between two or more states which are all either occupied or unoccupied simultaneously.

It is important to emphasize at this point, that the crossings between single–particle levels play a very significant role in models of large–amplitude nuclear motion, *e.g.*, shape coexistence, fission, fusion, and so forth, for which the time evolution of the collective coordinates can be treated via a physically well–defined collective velocity. In the cranking model, the diabatic traversing of the crossing point is done somewhat artificially, by means of a numeric procedure. For the sake of convenience in bookkeeping and analysis of the rotating configurations, all crossings have to be considered perfectly diabatic, the diabaticity being an artefact of the configuration–constrained model.

2.5 Jahn–Teller Mechanism of Core Polarization

The microscopic mechanism responsible for shape deformations is the Jahn–Teller effect. It is particularly relevant here because we are interested in the treatment of degrees of freedom on different time scales — the "fast" degrees of freedom of single–particle motion of individual nucleons, and the slower ones related to collective motion of the nucleus as a whole, characterized by rotational degrees of freedom.

The JT coupling Hamiltonian is a basic element in the analysis of nuclear collective modes and deformations [95]. As we mentioned before, depending on the geometrical properties of the individual valence nucleon (for example, the anisotropy of its wave function), the particle–vibration coupling can result in core polarization that can change its original deformation. In Bohr's picture, the vibronic coupling was represented by the interaction between the single-particle motion of valence nucleons and the collective excitations (multipole vibrations) of the core, known as *the particle-vibration (PV) coupling* :

$$H_{\rm PV} = -\sum_{\lambda\mu} \kappa_{\lambda\mu}\alpha_{\lambda\mu} \sum_i f(r_i)Y_{\lambda\mu}(\Omega_i), \tag{2.108}$$

where $\alpha_{\lambda\mu}$ is the amplitude of the nuclear deformation of the core, $f(r_i)Y_{\lambda\mu}(\Omega_i)$ is the multipole moment of the i-th valence nucleon, and $\kappa_{\lambda\mu}$ denotes the particle-vibration coupling strength.

The core polarization induced by the decoupled nucleons in highly–deformed shapes may be sufficiently large to mask or suppress the appearance of any pairing related odd–even energy staggering (OES). The "static" part of the shape–deformation polarization is assumed to originate from the mass multipole moments of the nucleon's density distribution. Besides that effect, the odd nucleon(s) can break rotational and especially time–reversal intrinsic invariance by adding non–negligible time–odd current and spin contributions to the rest of the system, leading to its current and spin polarization ("dynamical" polarization) [154, 155]. Their proper treatment requires deformed calculations with time–odd terms in the single–particle Hamiltonian, as it is elaborated in [133, 134, 154]. The change in energy caused by core polarization is dependent essentially on the time–odd spin and spin–isospin parts of the effective interaction, which have not been properly fitted yet (see [156, 157] and references therein). The role of the dynamic polarization effects in mean–field theories (of the kind used in this dissertation) has been subject to a notable attention in the last several years, with test case systematics carried out using both non–relativistic Skyrme Hartree–Fock [133, 158], and relativistic mean–field [154, 155] models.

For a comprehensive discussion of the Jahn–Teller mechanism in nuclear deformation and the stability condition refer to [75, 76].

2.6 Microscopic Origin of HD Rotational States

In order to illustrate the role played by the high–j intruder states, we refer to the example of a neighbor isotope to the ^{131}Ce core configuration shown in Fig. 2.3. The total Routhian surfaces for the lowest (π, r)=(+,1) (α=0) configuration of ^{132}Ce, calculated in the framework of the cranked Nilsson–Strutinsky model [159] is shown in Fig. 2.5 for two rotational frequencies differing by only 0.12 MeV. The results of a wide variety of similar models [41, 152] indicate that a second minimum in the total Routhian appears at $\beta_2 \sim 0.4$ for spins I exceeding 40 $\hbar$. For lower spins, the yrast deformation is $\beta_2 \sim 0.2$. The larger deformation is explained in terms of the 74-th neutron occupying the second $i_{13/2}$ intruder level at frequencies above 0.5 MeV (see the location of the 6_2 neutron Routhian in Fig. 2.3). Note the "softness" of the minima

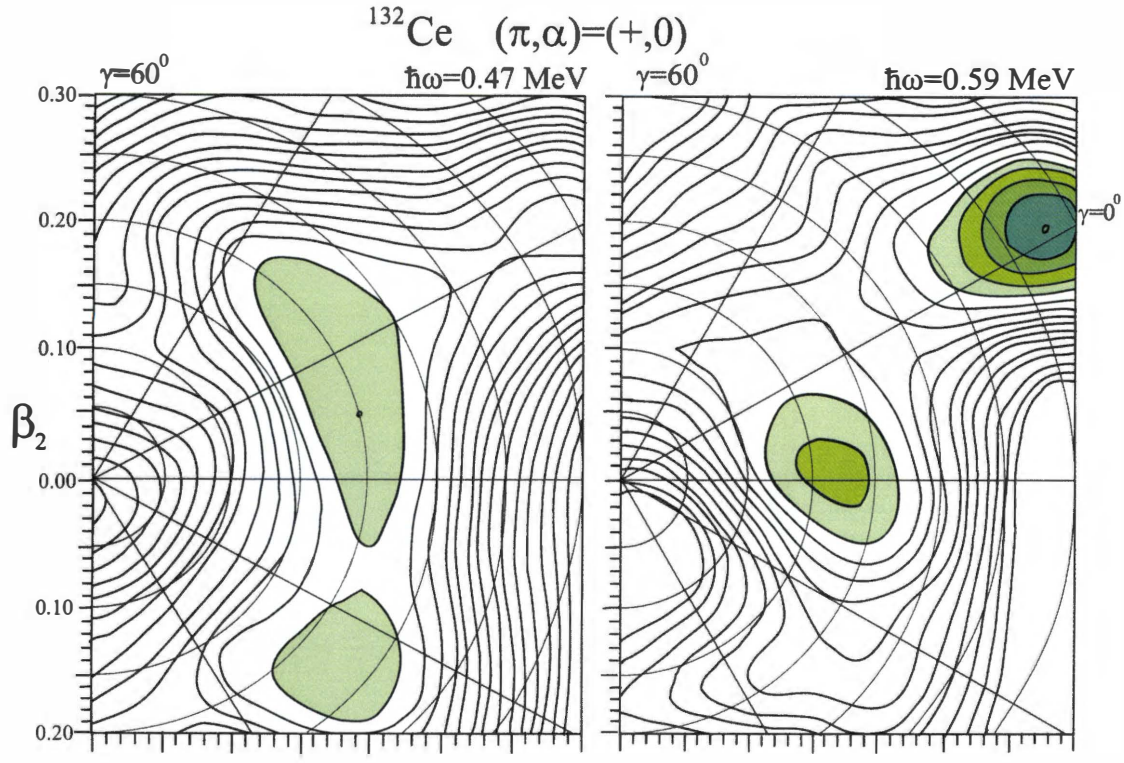

Figure 2.5: Total Routhian surfaces for ^{132}Ce configuration (π, r)=(+,1) in the (β, γ) plane at fixed values of the cranking frequency, for which the ν $i_{13/2}$ gets occupied. The spacing of the energy contours is 100 MeV, the shaded areas indicate the local minima, with the global minima marked by dots.
Source : R. Wyss, *et al.*, Phys. Lett. B **215**, 211 (1988).

with respect to γ–deformation of the nuclear shape, which allows for the occurrence of various degrees of triaxiality with rotation.

The first backbending in the A$\simeq$130 region is directly related to the alignment of the $i_{13/2}$ neutrons. The associated breaking of the pair(s) also reduces the pairing interaction in the system, which is observed as a decrease of the pairing gap with frequency. The rotational alignment of high–j states also modifies the quadrupole–like deformation of the nuclear surface, by having the aligned particle density distribution contribute to shape triaxiality [32] — this ability is strongly correlated with the chemical potential λ [67]. Indeed, the occupation of one of the lowest (highest) levels of a single–j ($j \gg 1$) leads to positive (negative) γ–deformation. For such a shell, states occupying the bottom of the shell tend to push the shape of the system towards $\gamma = 60°$, while those towards its top favor $\gamma = 120°$ [160]. For the proton–rich A$\simeq$130 nuclei, the nuclear triaxiality is driven by the balance of the effects of decoupling of the neutron $i_{13/2}$ states at the bottom of the shell (favoring positive values of γ), and that of the proton $h_{11/2}$ states (driving towards negative γ).

2.7 Phenomenology of Rotational Bands

The rotational effects of the Coriolis and centrifugal terms can be significant in the energy spectra of the nuclear system, so we need quantitative ways of extracting rotational characteristics from experimental data. In the cranking approach, the *Routhian* operator (2.25) acquires an extra term, proportional to $\hat{J}_x$, in which ω enters as a Lagrange multiplier [1]. The eigenenergies of the Routhian (2.25) are given by

$$E'(I) = E(I) - \hbar\omega\, I_x(I), \tag{2.109}$$

which define the rotational frequency as

$$\omega := \frac{1}{\hbar}\frac{dE(I)}{dI_x(I)}. \tag{2.110}$$

When the energy levels $E(I)$ are measured experimentally as a sequence of discrete values from γ-transitions forming a band, the angular momentum I changes in steps of $1\hbar$ or $2\hbar$ (Fig. 2.6). In the latter case, which also is most common for the type of shapes we study, we can use the classification scheme provided by the signature symmetry. The expression for ω (2.110) offers a way to evaluate the frequency $\omega(I)$ ascribed to each of the transitions by using a discrete approximation for the derivative :

$$\omega_{\mathrm{exp}}(I) := \frac{1}{\hbar}\left.\frac{\Delta E}{\Delta\sqrt{I(I+1)}}\right|_{I+1,I-1} = \frac{1}{\hbar}\frac{E(I+1)-E(I-1)}{I_x(I+1)-I_x(I-1)} = \frac{E_\gamma(I)}{\hbar(\Delta I_x)}. \tag{2.111}$$

The values of I_x can be calculated from the semiclassical geometric relation

$$I_x(I) = \sqrt{I(I+1)^2 - K^2} \approx \sqrt{(I+1/2)^2 - K^2}, \tag{2.112}$$

where K is the projection of the total angular momentum on the symmetry axis z (Fig. 2.2). The total Routhian at angular momentum I is given by

$$E'(I) = \frac{1}{2}\left[E(I+1) + E(I-1)\right] - \hbar\omega(I)\, I_x(I). \tag{2.113}$$

The further analysis requires a procedure for evaluating the moment of inertia for the band from the experimental γ-transition energies. Starting from the analogy with classical mechanics, we can define

$$\mathcal{J}^{(1)}(I) \stackrel{\mathrm{def}}{=} \hbar\frac{I_x(I)}{\omega(I)}, \tag{2.114}$$

commonly referred to as the *kinematic moment of inertia*. However, if we are interested in the dynamic changes of the moment of inertia along the band it is more informative to define the differential parameter

$$\mathcal{J}^{(2)} \stackrel{\mathrm{def}}{=} \hbar\frac{dI_x}{d\omega} = \frac{d\omega\mathcal{J}^{(1)}}{d\omega} = \mathcal{J}^{(1)} + \omega\frac{d\mathcal{J}^{(1)}}{d\omega}, \tag{2.115}$$

called the *dynamic moment of inertia*. Figure 2.7 illustrates these relations and shows their behavior at a band–crossing point. Using the discretization of the measured energy spectrum, $\mathcal{J}^{(2)}$ can be expressed as :

$$\mathcal{J}^{(2)}(I) := \hbar\left.\frac{\Delta I_x}{\Delta\omega}\right|_{I+1,I-1} = \hbar\frac{I_x(I+1)-I_x(I-1)}{\omega(I+1)-\omega(I-1)}, \tag{2.116}$$

[1] Let us recall that in the code HFODD the rotation is carried out around the y–axis instead of the x–, meaning that for the Skyrme calculations all cranking–related quantities use the index y instead of x.

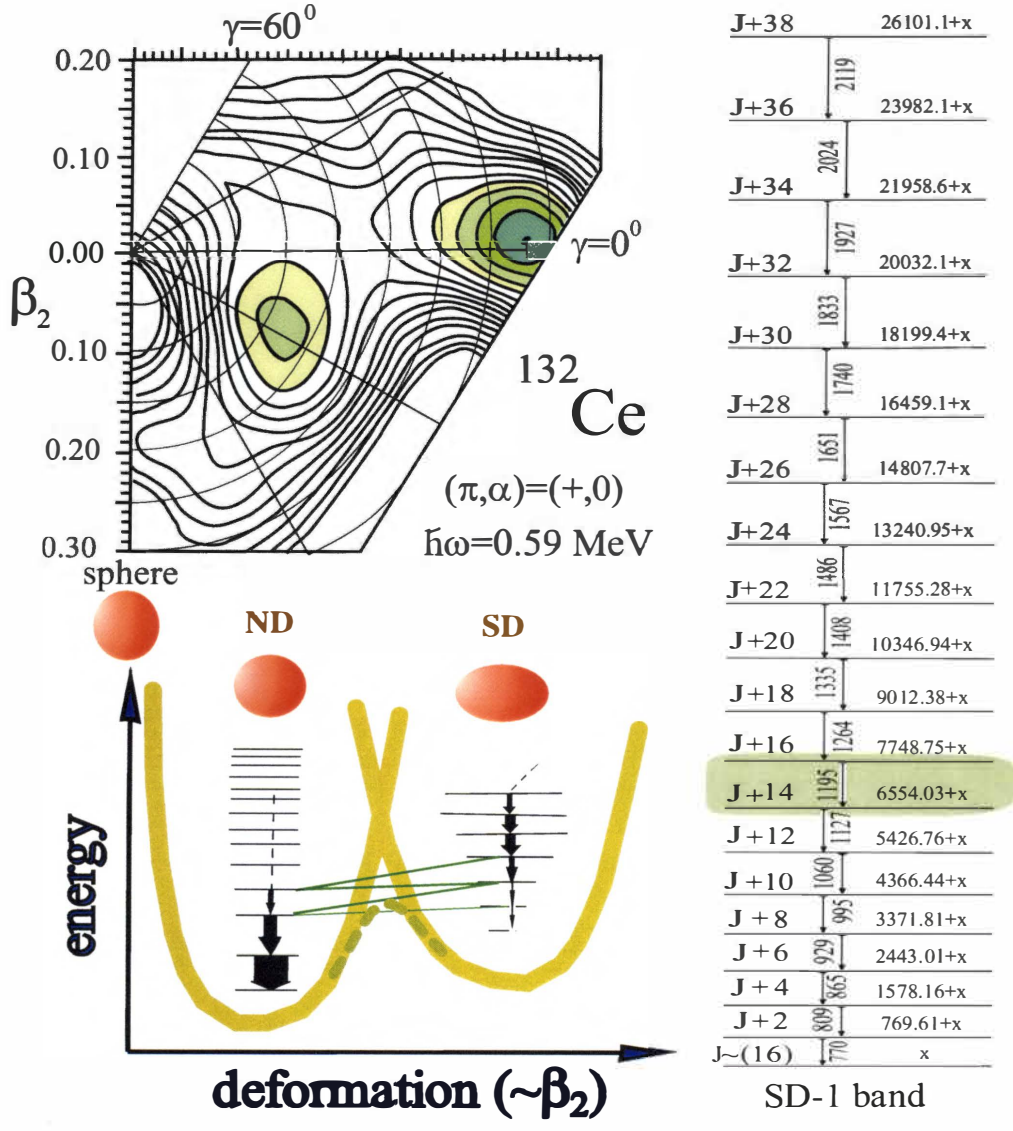

Figure 2.6: Schematic representation of a potential energy curve for ^{132}Ce illustrating the interplay between the normal deformation (ND) and superdeformed (SD) minima. For comparison we show the corresponding total Routhian surface (from [159]) at 0.59 MeV, in which the SD shape is favored. The energy profile is a function of distance along a trajectory in the (β, γ) plane traversing the saddle point, loosely associated with the prolate ellipsoid–like component of the quadrupole deformation. The right portion shows the observed superdeformed band SD–1 of ^{132}Ce [161, 148, 162, 163, 50].

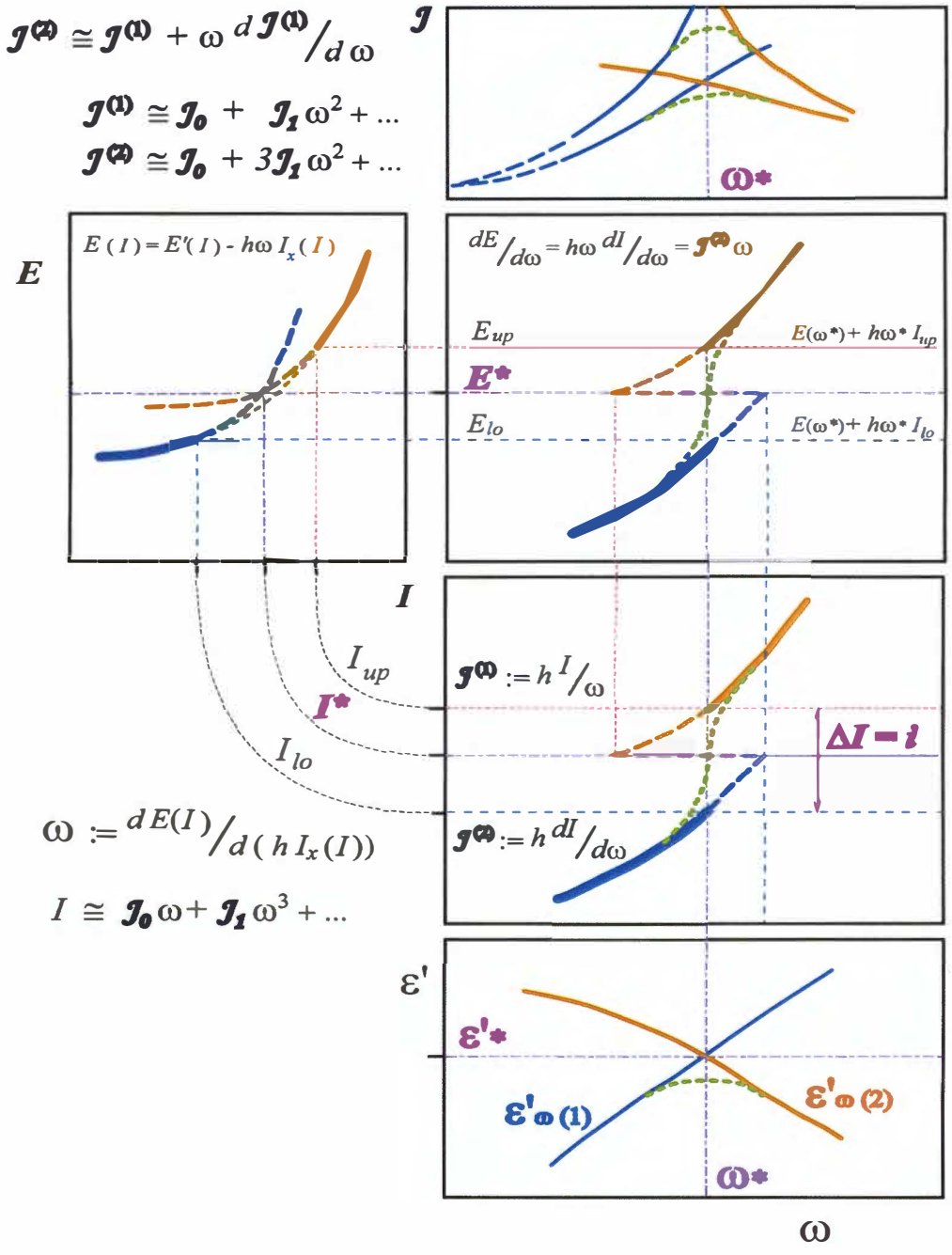

Figure 2.7: Schematic representation of the definitions of the phenomenological parameters of rotational bands and their behavior at a band crossing.

where $\omega(I \pm 1) = \frac{1}{2}(\omega(I) + \omega(I \pm 2))$.

In addition to these quantities, which provide the basic characterization of a rotational band, we can extract the valence–particle contributions i' of the total angular momentum

$$i'(\omega) \stackrel{\text{def}}{=} I_x(\omega) - I_x^{\text{ref}}(\omega), \tag{2.117}$$

where $I_x^{\text{ref}}(\omega)$ is a reference configuration given by

$$I_{\text{ref}}(\omega) = \frac{1}{\hbar}\mathcal{J}_{\text{ref}}^{(1)}\,\omega. \tag{2.118}$$

$\mathcal{J}_{\text{ref}}^{(1)}$ is usually parameterized in the form

$$\mathcal{J}_{\text{ref}}^{(1)} := \mathcal{J}_0 + \omega^2\mathcal{J}_1, \tag{2.119}$$

where the coefficients $\mathcal{J}_0$ and $\mathcal{J}_1$ are fitted to the reference–core configuration and are called *Harris' parameters* [164].

At high spins ($I \gg 1$) asymptotic expansions can be made :

$$\hbar\omega_{\text{exp}}(I-1) \simeq \frac{E_\gamma(I+2)}{2}, \tag{2.120}$$

$$\mathcal{J}^{(1)} = \hbar\frac{I_x}{\hbar\omega} \simeq \frac{2I_x}{E_\gamma}, \tag{2.121}$$

$$\mathcal{J}^{(2)} = \frac{4\hbar^2}{E_\gamma(I+2) - E_\gamma(I)}, \tag{2.122}$$

where $E_\gamma(I) \equiv E(I) - E(I-2)$.

2.7.1 End of Collective Rotation : Band Termination

As discussed in the previous Sections, a rotational band is characterized by its single–particle configuration, corresponding to a particular nucleonic arrangement. Although the deformation parameters and other bulk characteristics of the nuclear system may change continuously without major readjustments, the alignment of unpaired nucleons and their spatial redistribution closer to the equatorial plane of rotation makes possible more radical rearrangements, which underline band crossings and mixings with other bands.

The limit to extreme angular momentum from valence nucleons was first explored by Bohr and Mottelson [95] for the case of the s–d nucleus ^{20}Ne, where the closed shells, corresponding to ^{16}O, form a distinct core configuration. The maximal angular momentum is formed consequently by the spins of the valence $1d_{5/2}$ nucleons outside the core — two neutrons ($5/2 + 3/2$)$\hbar$ and two protons ($5/2 + 3/2$)$\hbar$ for a total of 8 units of angular momentum (experimentally confirmed in Ref. [165]). This limitation to rotational alignment is known as *band termination.* Ref. [95] also makes an estimate for the maximal available angular momentum (*"spin content"*) as a function of mass, which, for our SD mass range of interest (A$\sim$130–150), approaches 100 $\hbar$. The terminating configurations have been observed in some nuclei in the A$\sim$110 mass range with just a few nucleons outside the ^{100}Sn core; any excess of valence particles would disrupt the delicate balance of nucleon degrees of freedom by destroying the core, which would, in principle, remove any limitations on the total spin. The progress towards the termination point can be smooth or more abrupt, depending on the structural changes taking place. From a microscopic point of

view, the total angular momentum is a one–body operator, *i.e.*, it is a sum of contributions from all nucleons. At the initial stages of collective rotation, I_x consists of many small contributions from all of the nucleons. With the increase of cranking frequency some of the single–particle contributions rise in magnitude, eventually approaching and becoming comparable with the intrinsic angular momenta of the occupied orbitals. For a system with a well defined core, the angular momenta of the core nucleons would tend to compensate pair–wise, leaving only the contributions from the valence nucleons.

The total rotational alignment depends strongly on the number of valence nucleons. For a terminating band, the angular momentum reaches a saturation value, which can not be exceeded unless a significant single–particle structural rearrangement occurs. Such saturation can be reached for some bands at the highest–frequency end of the given cranked structure, and it usually corresponds to a rotationally–aligned, non-collectively rotating configuration. The total momentum of the band configuration at and beyond the termination point can therefore be predicted as the sum of the aligned spins of valence nucleons. Examples of band termination have been observed in a number of nuclei across the periodic table [166].

A general characteristic of terminating bands is their decreasing static, and respectively their dynamic moments of inertia, at the approach to termination. This is directly related to the increased energy cost to the softened nuclear system for generating the next two units of angular momentum required for an extra quadrupole γ–transition. It is worth mentioning in this context that the higher energy cost is not always clearly seen in the spectrum — for example, in the simplest case of ^{20}Ne, the γ–transition (from 6 to 8 units) is higher, in fact, in its energy expense than the previous in the sequence (from 4 to 6). The situation in every case depends on the relative energetic preference for the system populating a state $2\hbar$ in angular momentum *vs* undergoing a configuration/shape change, with the behavior of the energy cost in some cases imitating that of the more "rigid" shape.

The effects of rotational alignment in the regime closest to termination imply the transition from prolate (γ=0°) via most triaxial (γ=30°) to oblate shapes with $\gamma \simeq 60°$, which results in the decrease in the moments of inertia. This is combined with a significant drop in transition matrix elements B(E2), due to the decrease in rotational collectivity.

Let us consider, for example, the calculated yrast band of ^{30}Ne (Fig. 2.8). The (β,γ) diagram in the top right corner shows the trajectory of the nuclear shape with the increase of cranking frequency $\hbar\omega$ to 2 MeV. Starting with a well–deformed prolate shape ($\beta_2 \simeq 0.32$) and rotating around an axis perpendicular to the symmetry axis, the nuclear system proceeds smoothly towards a weakly–deformed oblate shape (γ =60°). As this happens, the paired nucleons make the transition from a strongly–coupled (deformation–aligned) to a weakly–coupled (rotation–aligned) scheme under the influence of the Coriolis terms in the Hamiltonian. From a collective rotation regime at low frequencies, the system gradually switches to a non–collective rotation with an oblate shape with the rotational axis coincident with the symmetry axis. The full alignment of the valence nucleons is observed beyond the termination frequency of $\hbar\omega \approx 1.35$ MeV, where the total spin reaches its maximal value of $12\hbar$, composed as a sum of the neutron ($8\hbar$) and proton ($4\hbar$) angular momenta. As seen from the single–particle Routhian diagram, the terminating state is made of the aligned $\nu(1f_{7/2})^2$ ($5/2 + 7/2$)$\hbar$, $\nu(1d_{3/2})^2$ ($3/2 + 1/2$)$\hbar$ neutrons and the aligned π $(1d_{5/2})^2$ ($3/2 + 5/2$)$\hbar$ protons. The change in shape has the well–recognizable effect on the values of the moments of inertia (*cf.* Fig. 2.7). The static moment of inertia decreases linearly, and the dynamic moment of inertia drops down to zero. More examples of terminating bands are shown in Chapter 4.

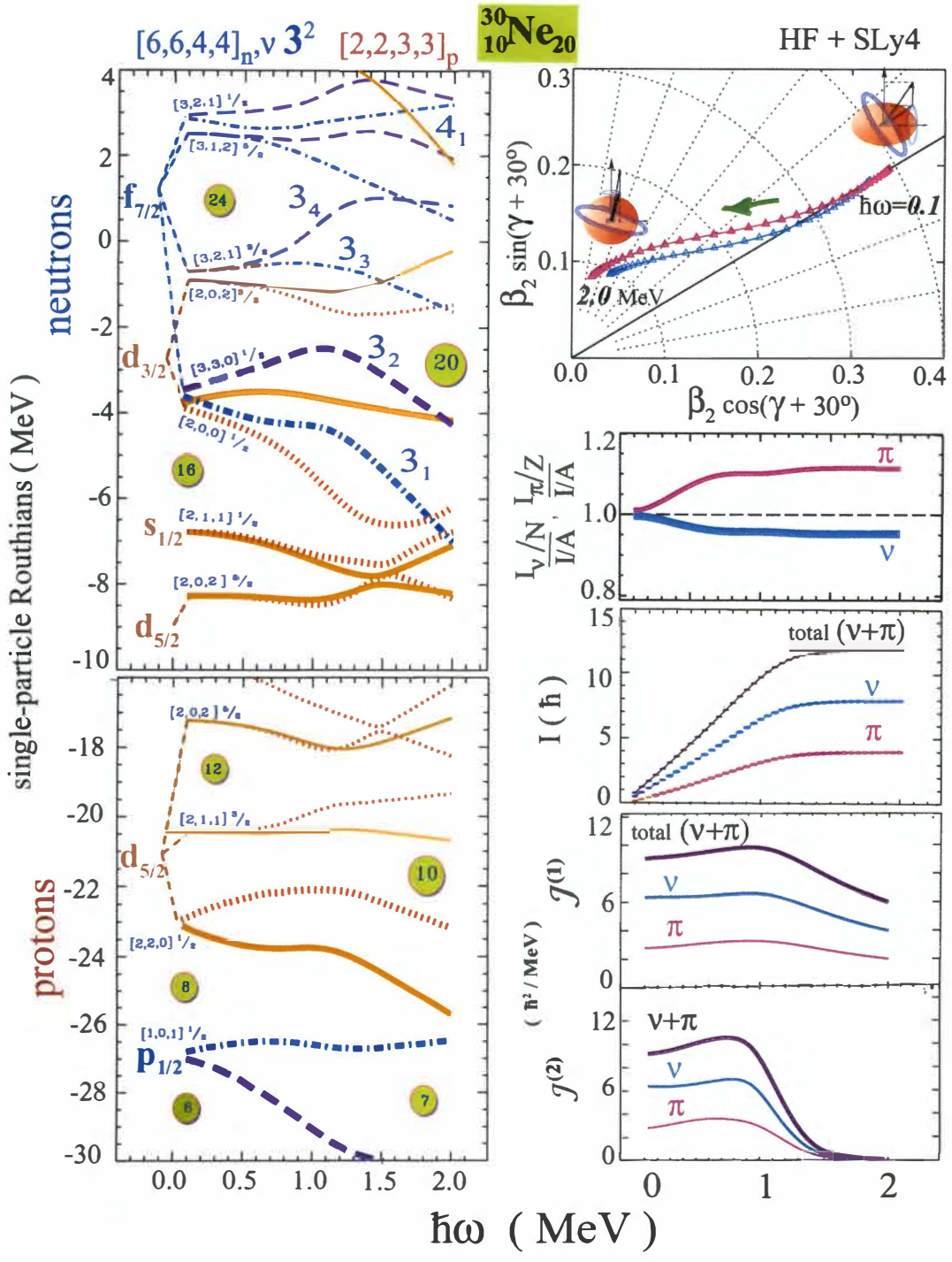

Figure 2.8: Calculated rotational band in ^{30}Ne, an example of band termination. See text for details and discussion in Chapter 4.

2.7.2 Deformation of High–Spin Bands

The components of the quadrupole moment $Q_{2\mu}$ are the lowest-order electrostatic quantities which measure the displacement of electric charge inside the nucleus and, therefore, can provide information about the proton distribution. The operator of the electric quadrupole moment

$$\widehat{Q}_{20} = 2z^2 - x^2 - y^2 \tag{2.123}$$

can be used to calculate its observable value when we introduce the corresponding equivalent for the electric charge density :

$$Q_0 \equiv Q_{20} = \left\langle \widehat{Q}_{20} \right\rangle \Big|_{\text{charges}} . \tag{2.124}$$

The *microscopic* quadrupole moment can be calculated by summing–up the single–proton contributions :

$$Q^{\text{micro}} = e \sum_{i=1}^{Z} \langle i | \left(2z^2 - \rho^2\right) | i \rangle . \tag{2.125}$$

The neutrons, having zero charge, do not appear in the sum, but their presence and deformation changes, hence they also impact, albeit indirectly, the quadrupole moment.

2.7.3 Definitions

In the limit of high angular momentum [167] the electric quadrupole operators $\widehat{Q}_{\Delta I}$ of $E2$ transitions between yrast line levels can be expressed through the components of the quadrupole deformation of the rotating core in its intrinsic system, $Q_{20} = q \sin\gamma$ and $(-\sqrt{2})Q_{22} = q\cos\gamma$ as follows :

$$\widehat{Q}_0 = -\left(\frac{1}{2}Q_{20} + \frac{\sqrt{3}}{2}(-\sqrt{2}Q_{22})\right) = -q\sin\left(\gamma + 30^\circ\right), \tag{2.126}$$

and

$$\widehat{Q}_{\pm 2} = -\left(\sqrt{\frac{3}{8}}Q_{20} + \frac{1}{2}Q_{22})\right) = -\frac{q}{\sqrt{2}}\cos\left(\gamma + 30^\circ\right) \tag{2.127}$$

where $q = Q_0 = \frac{4}{5}ZeR_0^2\beta_2 = \sqrt{Q_{20}^2 + 2Q_{22}^2}$. The transition quadrupole moment Q_t (related to experimental lifetime) is given by

$$Q_t = q\frac{\cos\left(\gamma + 30^\circ\right)}{\cos 30^\circ} = |Q_{20}| - \sqrt{\frac{2}{3}}Q_{22}. \tag{2.128}$$

It is important to remember here that in the Skyrme code HFODD the rotation axis is y instead of x, therefore the sign of Q_{22} is inverted, and $\cos(\gamma + 30^\circ)$ becomes $\cos(\gamma - 30^\circ)$. We have to keep in mind that the value of Q_{22} is redefined to absorb the factor of $\sqrt{2}$, which leads us to the following relation, specific to HFODD :

$$Q_t = Q_{20} - \sqrt{\frac{1}{3}}Q_{22}, \quad \text{and} \quad q = \sqrt{Q_{20}^2 + Q_{22}^2}. \tag{2.129}$$

A non-zero value for Q_{22} does not necessarily imply that the core is γ-deformed (non-axial), because small anharmonic shape vibrations around the axially–symmetric shape can also lead

to effective non-zero values of γ. From the components of the quadrupole moment, $Q_{20}^{(\tau)}$ and $Q_{22}^{(\tau)}$, and the root–mean–squared proton and neutron radii $\langle r^2 \rangle_\tau$, one can extract the Bohr quadrupole deformation parameters β_2 and γ [110], in cases in which they are different (as is the case in drip–line and halo nuclei) :

$$\beta_2^{(\tau)} \equiv \sqrt{\frac{\pi}{5}} \frac{\sqrt{\left(Q_{20}^{(\tau)}\right)^2 + \left(Q_{22}^{(\tau)}\right)^2}}{N_\tau \langle r^2 \rangle_\tau} \tag{2.130}$$

$$\tan \gamma^{(\tau)} \equiv \frac{Q_{22}^{(\tau)}}{Q_{20}^{(\tau)}}, \tag{2.131}$$

where $N_{\tau=1} \equiv$N and $N_{\tau=-1} \equiv$Z.

2.8 Additivity in Superdeformed Bands

One of the many reasons for our interest in superdeformed bands is that there is compelling evidence for the reduction of pairing. This makes it possible to apply theoretical methods based on the analysis of one–body operators and single–particle expectation values.

In this Section we present some of the theoretical reasoning behind the concept of additivity, as it is applied to the superdeformed regions on the proton–rich side of the chart of the nuclides (Fig. 1.2).

2.8.1 The Case for Additivity

The statistical analysis of G. De France, *et al.* [168] in the A$\sim$130, 150, 190 mass regions clearly demonstrated that the so–called phenomenon of band twinning (or identical bands, IB's) is more likely to occur in superdeformed than in normally–deformed bands. Following the reasoning of the authors, if the distributions of the moments of inertia are recognizably different among ND and HD/SD configurations, then this difference should be traceable down to structural differences in their nucleonic mean field, and be associated with causes like shell effects or reduced residual interactions. This hypothesis led to startling observations in the distributions of fractional changes of the dynamic moments of inertia $\mathcal{J}^{(2)}$ [168]; these results indeed confirmed that a necessary condition for the occurrence of IB's higher deformation was the presence of the same number of high–$\mathcal{N}$ orbitals. The analysis in the A$\sim$190 region yielded further evidence that the presence of larger residual interactions would reduce the quality of the fit by effectively smoothing out the effect of the intruders. The results of Ref. [168] give strong support for the notion that in high–spin SD configurations the shell structure and the presence of intruders are arguably much more important than the pairing effects.

The first quantitative discussion of shape polarization in SD bands was given in the HF study of Ref. [77]. Later on, this was followed by less microscopic studies of [169, 170, 171].

The mean–field description of the quadrupole moments of the SD nuclei around ^{152}Dy shows [77] that the variations of the nuclear shape from band to band and from nucleus to nucleus are consistent with the measured values. The SD configuration in ^{152}Dy is the logical choice for a doubly–magic SD core; consequently, effective single–particle quadrupole moments q_α^{eff} can be introduced for the single–particle states around the Fermi level.

$$Q = Q^{\text{core}} + \sum_{\alpha=\text{particles}} q_\alpha^{\text{eff}} - \sum_{\alpha=\text{holes}} q_\alpha^{\text{eff}}, \tag{2.132}$$

In this equation α is a running index enumerating the particle and hole states for both protons and neutrons. The values of q_α^{eff} can be calculated by proceeding step by step from the core configuration to the neighbouring ones (*i.e.* configurations differing from the core by one particle/hole), then to configurations farther away, and so forth, until a large enough data set is built, which could provide sufficient statistics for each one of the q_α^{eff} to be determined with appreciable precision.

2.8.2 Additivity Assumptions and Procedure

The systematics of the remarkable results in the A$\simeq$150 SD mass region has led to the introduction of the concept of additivity [77] for the 1-body quantities characterizing the rotational states. The authors were able to demonstrate that the strong shell effects in this superdeformed region (with ^{152}Dy as a doubly–magic deformed core) encompass a wide interval of deformations and are explained with the individual contributions from orbitals close to the Fermi level. One of the results from this study was the evaluation of a chosen set of relative intrinsic multipole moments $Q_{\lambda\mu}$ (for λ=2,4) as an additive function of the effective values for these moments for the orbitals involved (see Eq. (2.132)). This allowed for the estimates for the effective moments for 20 orbitals including the intruder ν $\mathcal{N}$=7 and π $\mathcal{N}$=6 states.

Following the accepted shell–model understanding of the one–body effective moments $q_{\lambda\mu}^{\text{eff}}$, their values deviate from their corresponding bare values $q_{\lambda\mu}^{\text{bare}}$ by certain amounts q^{pol} contributed by the polarization of the core :

$$q_\alpha^{\text{eff}} = q_\alpha^{\text{bare}} + q_\alpha^{\text{pol}}. \tag{2.133}$$

In particular, for neutrons q^{bare}=0, therefore the non–zero values of q^{eff} originate entirely from the core polarization effect introduced through the self-consistency of the mean field. The results of Ref. [77] showed a remarkable agreement with experiment and have lent credibility to the mean field mechanisms for the explanation of superdeformation in this region.

In our study, presented in Chapter 3, we performed a systematic analysis of the single–particle quadrupole moments and alignments for the configurations around ^{131}Ce. According to [77], intrinsic quadrupole moments are robust enough to be used as fingerprints for configuration assignments. Unlike the moments of inertia, quadrupole moments do not get disturbed easily by small changes of single-particle energies, band crossings *etc.*

As mentioned above, the quantities of interest in this study were the components of the total intrinsic charge quadrupole moment, Q_{20}^π and Q_{22}^π, (the superscript π stands for protons) as well as the total angular momentum I. Once the core configuration had been chosen — in our case it was the SD-1 band in ^{131}Ce (Z=58, N=73), the *relative variations* δQ_{20}^π and δQ_{22}^π with respect to those for the core were calculated and fitted using an additivity scheme to determine the q_α^{eff} for the single-particle/hole states. Assuming that the SD configurations are characterized by undisturbed single-particle motion without pairing, the relative multipole moments δQ_{20}^π and δQ_{22}^π, obtained in the self–consistent mean–field calculations, can be expressed as sums of the individual corresponding moments q_α^{eff} according to Eq. (2.132) :

$$Q_{20}^\pi(k) - Q_{20}^{\pi(\text{core})} = \delta Q_{20}^\pi(k) \quad = \quad \sum_\alpha c_\alpha(k) q_{20,\alpha}^{\text{eff}}, \tag{2.134}$$

$$Q_{22}^\pi(k) - Q_{22}^{\pi(\text{core})} = \delta Q_{22}^\pi(k) \quad = \quad \sum_\alpha c_\alpha(k) q_{22,\alpha}^{\text{eff}}, \tag{2.135}$$

$$I(k) - I^{(\text{core})} = \delta i(k) \quad = \quad \sum_{\alpha} c_\alpha(k) i_\alpha^{\text{eff}}, \tag{2.136}$$

where the coefficients c_α reflect the single-particle/hole content of the configuration k with respect to the core configuration. Namely, $c_\alpha(k) = 0$ if the state α is not present in either of these two configurations, $c_\alpha(k) = 1$ if state α is a *particle* in addition to the core, and $c_\alpha(k) = -1$ if state α is a *hole* with respect to the core. Therefore, we can label our configuration k with the set of coefficients $C(k) = \{c_\alpha(k), \alpha = 1, \ldots, m\}$. The assumptions of eqs. (2.134)–(2.136) are commonly referred to as *"additivity model"* [77].

Once the configurations $C(k)$ are determined for the calculated theoretical configurations, the problem of finding the components of the effective quadrupole moments the least–square fitting procedure, discussed in the following.

The solution for the additive decomposition of the eigenvalues $\delta F = (\delta F(k), k = 1, \ldots, N_c)$, N_c being the total number of configurations/bands included, of the 1–body operator quantity $F - F_{(\text{core})}$ as a sum of m single–state quantities $f = \{f_\alpha, \alpha = 1, \ldots, m\}$

$$\delta F(k) = F(k) - F^{(\text{core})}(k) = \sum_{\alpha} c_\alpha(k) f_\alpha \tag{2.137}$$

is obtained as a multivariate least–square fit by minimizing the function

$$\sum_k (\epsilon_F(k))^2 = \sum_k \left(\delta F(k) - \sum_\alpha f_\alpha c_\alpha(k) \right)^2 \tag{2.138}$$

where we introduced $\epsilon_F(k)$ by the relation $\delta F(k) = \sum_\alpha c_\alpha(k) f_\alpha + \epsilon_F(k)$. The problem is only meaningful for $N_c > m$. Following the general concept of the least-square method (see [172], [173],pp. 67-73), the partial differentiation with respect to the minimization variables yields

$$0 \quad = \quad \frac{1}{2} \frac{\partial}{\partial f^\alpha} \left(\Delta(\delta F)^2 \right) \tag{2.139}$$

$$= \quad \sum_{\alpha'} \sum_k c_\alpha(k) c_{\alpha'}(k) f_{\alpha'} \sum_k \delta F(k) c_\alpha(k) \tag{2.140}$$

$$= \quad (Bf - a)_\alpha, \tag{2.141}$$

where $a_\alpha = \sum_k \delta F(k) c_\alpha(k) = c^T \delta F$, and $B = \|B_{\alpha\alpha'}\| = \| \left(\sum_k c_\alpha(k) c_{\alpha'}(k) \right) \| = c^T c$. Solving this equation by inverting the non-singular matrix B gives the solution to the multivariate regression problem as

$$\widehat{f} = B^{-1} a = (c^T c)^{-1} c^T \delta F. \tag{2.142}$$

The fact that B is positive-definite guarantees that the solution $\widehat{f}$ corresponds to a minimum of $\sum_k (\epsilon_F(k))^2$. If in order to estimate the variances in this problem we assume that the first statistical moment of $\epsilon_F(k)$ is zero for all $k = 1, \ldots, N_c$, then $\widehat{f}$ can be considered an unbiased estimate of f. Furthermore, under the assumptions that

$$var(\epsilon_F(k)) = \sigma^2 \tag{2.143}$$

for all $k = 1, \ldots, N_c$, and

$$cov(\epsilon_F(k), \epsilon_F(k')) = 0 \tag{2.144}$$

for all $\{k, k' = 1, \ldots, N_c \mid k \neq k'\}$, one can define the variance–covariance matrix as $\sigma^2 B^{-1} = \sigma^2 (c^T c)^{-1}$, for which the unbiased estimate for σ^2 is given by

$$\widehat{\sigma}^2 = \frac{1}{N_c - m} \sum_{k=1}^{N_c} \epsilon_F(k)^2. \tag{2.145}$$

Finally, the unbiased estimate for the variance–covariance matrix for $\widehat{f}$ is given by $B^{-1}\sigma^2$.

In our study, the calculated single–state quantities f_α are the quantities $\{(q_{20,\alpha}, q_{20,\alpha}, i_\alpha), \alpha = 1, m\}$ which were obtained by applying the fitting procedure described above independently for $F = \{F(k), k = 1, \ldots, m\} = \{(Q^\pi_{20}(k) - Q^\pi_{20}(\text{core}), (Q^\pi_{22}(k) - Q^\pi_{22}(\text{core}), (I(k) - I(\text{core})), k = 1, \ldots, m\}$.

Having presented the theoretical framework for our study in the superdeformed A$\simeq$130 mass region [174], we are now ready to proceed with the comparative analysis of the two self–consistent models for high–spin superdeformation.

Chapter 3

Superdeformation in the A$\simeq$130 Nuclear Mass Region

"All things come into being by conflict of opposites,
and the sum of things flows like a stream."

— Heraclitus the Riddler (c.535–c.475 B.C.)
Diogenes Laertius Book IX, Sec. 8,9 [175]

In the previous Chapter we introduced the basic concepts of the nuclear mean–field approach and described how the underlying single–particle structures can be calculated and extracted from the data. The primary purpose of this Chapter is *(i)* to point at the existence of theoretical evidence for undisturbed single–particle motion in the nuclear mean field, *(ii)* to illustrate that a wealth of structural information can be extracted from the superdeformed spectra and lifetime measurements, and *(iii)* to make a comprehensive analysis and comparison of the results of the two different self–consistent mean field models.

The published results, part of which are shown in Fig. 1.3, offer compelling evidence for the soundness of the additivity approach in superdeformed high–spin rotational bands, as it was previously applied in the A$\sim$150 mass region [77]. Our ambition of extending this analysis to the neighboring A$\sim$130–140 mass range has been the main direction for my work through this Chapter, with practical results in the improvement of the computational methods (software, written in IDL and Fortran 77/90 for additivity analysis, interpretation of experimental band data, databases of SD bands, and many others), extra instrumentation for the interpretation of band numerics and structural insight (software packages in IDL and Fortran 77/90 for creating Routhian and Nilsson diagrams, nucleon density, generation of input and output file interpretation for `HFODD`, *etc.*), as well as the new possibility of comparing the results of different self–consistent approaches with experimental data. As an analytical way of illustrating that the nucleons move in an averaged mean field with small residual interaction effects, we show that it is possible to extract effective additive quantities for the individual nucleon orbitals with remarkable accuracy, and then demonstrate that the resulting band assignments can serve as a guideline for spectroscopic measurements and interpretation, including deformations, angular

momenta, parity–signature labeling, *etc.*

3.1 Overview of Superdeformed A∼130 Region

Historically, rotational sequences suggesting prolate shapes ($\beta_2 \sim 0.30$–0.40) in the proton–rich A≈135 nuclei of the rare–earth La–Sm region have been known since the early 1970's [176]. Such observations were consistent with nuclear shapes considerably better deformed than those of the ground states, for which the typical β_2 does not exceed 0.2. Early on, calculations unambiguously confirmed, using different theoretical approaches [43, 41, 177], that secondary minima are to be expected at large deformations. Experimental measurements of the collective $\mathcal{J}^{(2)}$ moments of inertia in the region were soon to confirm these expectations at high frequencies [178].

3.1.1 Typical Features of the Superdeformed Bands

A rotational SD band is characterized by a "picket–fence like" sequence of equally–spaced in energy γ–rays, with the spacing for our mass region being around 70 keV (50 keV for A∼150). In most of the practical cases, experimental $\mathcal{J}^{(1)}$ is unknown, because the spins of the SD states involved in the transition sequence at best are known only vaguely from the data set. Furthermore, the SD states, being highly collective, are characterized by their very strong enhancement of the *E2* transition probabilities — more than 2000–3000 Weisskopf units (W.u.). Measurements of lifetimes give us information on transition quadrupole moments. Another property of enhanced or superdeformed bands is their low population, which makes detecting them a technical challenge. The cross–section is normally of the order of a few percent of that of the producing reaction, but in the A∼130 region, it is somewhat higher, 5–10 %, with the most favorable cases in ^{133}Nd reaching as high as 20 %. The populated bands decay by rapidly losing intensity over only a few transitions, making the transitions, linking the SD to ND configurations, very difficult to observe. In most of the cases, the SD bands are fed at the high end of the frequency range through very narrow spin "windows", and generally at lower energies than the ND sequences.

3.1.2 SD Bands in the A∼130 Mass Region

The discovery of the first SD band in ^{152}Dy in 1984, while validating the concepts and confirming the expectations, led to a feverish search for highly–elongated configurations in neighboring nuclei. This also followed the extensive studies in the transitional region of proton–rich nuclei ranging all the way from La (Z=57) to Gd (Z=64) and beyond. In 1987, the presence of the deformed secondary minima in the A∼130 region was confirmed by lifetime measurements in ^{132}Ce [50], thus firmly establishing the experimental existence of what we now commonly refer to as *the A≃130 superdeformed region.* The experimental value for the quadrupole moment Q_0=8.8 *e*b, corresponding to $\beta \sim 0.50$, was fully consistent with theoretical expectations, and is typical for these nuclei. Immediately after that, SD bands were discovered in several Nd isotopes [179, 180, 181], and in ^{137}Sm [182].

The role played by high–j intruder orbitals has always been considered of critical importance for the occurrence of shapes with high prolate deformation. In order to demonstrate the expected effects of the occupation of these states we refer to the Nilsson diagrams of the kind shown in Fig. 2.1.

Figure 3.1 presents the Nilsson diagram for the A∼130 region, calculated in the framework of our Skyrme HF model with SLy4 interaction. Their fast variations with the proton quadrupole

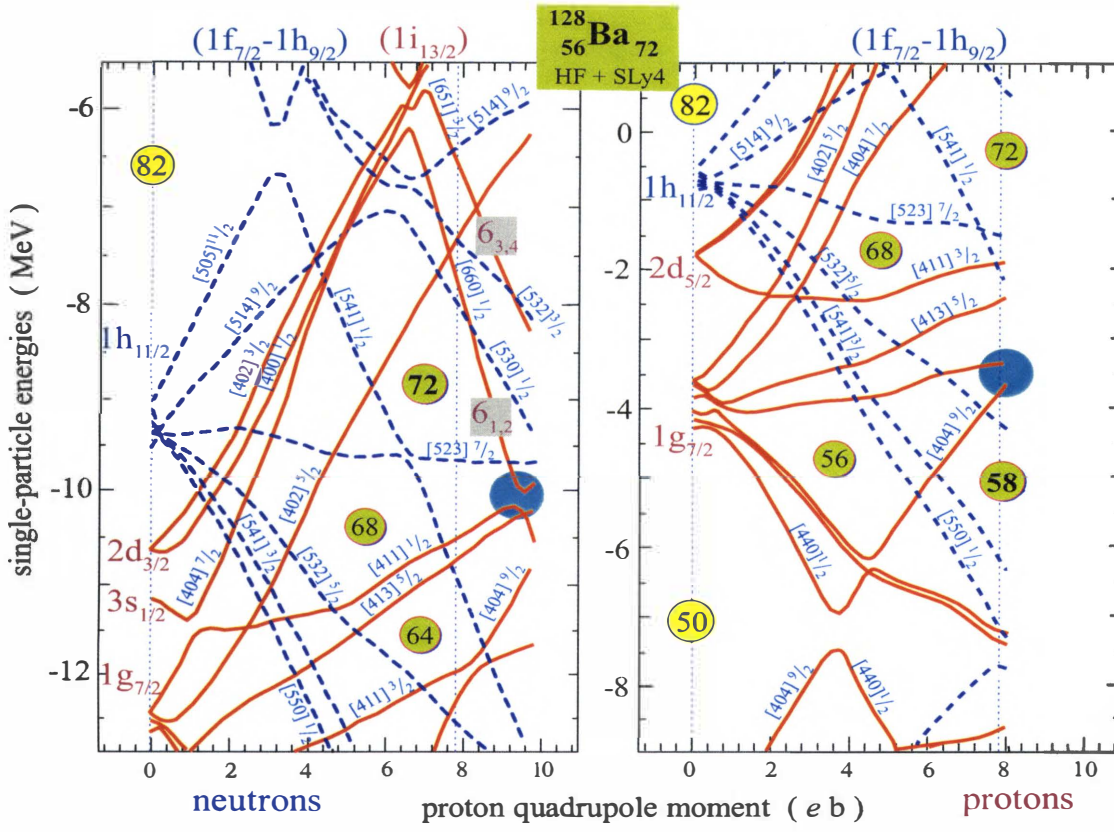

Figure 3.1: Nilsson diagram for the superdeformed rotating configurations in the Skyrme CHF calculations, showing the deformed region of interest, and the locations of the intruder and extruder orbitals.

moment is an indication of their high sensitivity to change in quadrupole deformation. A neutron placed in the [660]1/2 orbit (ν 6_1 in our notation) has a strong prolate–driving effect. In a similar fashion, the proton extruder state [404]9/2 is steeply up–sloping, thereby, when occupied, favoring less elongated shapes.

The low–Ω Nilsson orbitals originating from the Ω in $g_{9/2}$, $h_{11/2}$, and $i_{13/2}$, $j_{15/2}$ major shells "carry" large quadrupole moments. It is therefore understood that it is of primary importance for the investigation of deformed bands to study these single–particle/hole states.

In the early theoretical studies in the A$\simeq$130 region, it was generally assumed that the involvement of at least one occupied intruder orbital was mandatory for the development of highly–deformed configurations [159]. Their importance is especially significant when the level density for the valence nucleons is low, that is, in the proximity of deformed single–particle shell gaps. The strongest polarization effects are caused by the ν ($i_{13/2}$) [660]1/2 intruder from the $\mathcal{N}$=6 shell, the $\mathcal{N}$=4 extruder π ($g_{9/2}$) [404]9/2, and the mixed ν ($h_{9/2}\oplus f_{7/2}$) [541]1/2 orbital.

In the proton part of the Nilsson diagram, the particularly strongly favored region is Z=58–62, with the lower bound marking the best candidate for a core nucleus for our analysis — ^{130}Ce. The SD band was observed in ^{131}Ce in 1987 [183], and has led to the expansion of SD studies

to the neighboring nuclei since then. A wide variety of superdeformed states in the region have been observed experimentally so far. Their systematics [51, 52, 53] provide solid evidence for the presence of highly–deformed orbitals and microscopic shell effects.

Experimental studies in the middle of the 1990's demonstrated that partial de-occupation of the extruder $g_{9/2}$ proton orbital [404]9/2 in rotational bands for Z=59 (Pr) [184, 185, 186], and Z=61 (Pm) [187] isotopes can appear also in the range of deformation characteristic for SD bands. [188] It turned out also (see the single–particle diagrams in [159, 188]) that for nuclear systems lighter than N=73 with the ν $i_{13/2}$ orbitals unoccupied (they are shifted upwards), the more highly–prolated deformations can be observed when the bands involve the occupation of the [541]1/2 orbital (Fig. 3.1) from the $f_{7/2}\oplus$ $h_{9/2}$ shell [189, 190, 191].

Recently, a large–scale lifetime measurement was carried out by a collaboration at GAMMASPHERE, which has resulted in a preliminary analysis of shape polarization effects in A$\sim$130 nuclei [2]. The idea of doing "differential" lifetime measurements has been exploited in the A=80 [192], and A=130–135 [193, 148], A=150 [194], and A=190 [195] superdeformed regions.

The bands with highest deformation in the GAMMASPHERE study were observed in the N=73 Neodymium and Samarium isotones, with ^{133}Nd reaching Q_0=6.5(2) eb [196] and ^{135}Sm — 6.4(5) eb. For the N=75 Nd, Pm, Sm isotones, the deformation gradually decreases with Z from 5.8(2)eb in ^{135}Nd bands [196], down to 4.8(4)eb in ^{137}Sm. The trend lines also were found to be in agreement with total Routhian surface and cranked calculations — with pairing [197, 198], or without [188]. These results illustrate an other important trend, for the highly–deformed bands built upon the proton $g_{9/2}$ [404]9/2$^+$ orbital in ^{130,131}Pr and ^{133}Pm [184, 187, 199]. The values Q_0 are comparable to the N=75 isotones with non–zero ν $i_{13/2}$ content, but they are somewhat lower than those for the N=73 isotones, which confirms the expected significant role of the partial or full de–occupation of the [404]9/2 for the occurrence of highly–deformed structures in the region. This correlates well with the fact that the deformations are highest for the Ce isotopes with Z=58, where the gap is just above the Fermi surface [188].

As the Nilsson diagram illustrates, it is of considerable interest to extract the deformation effect of the neutron [541]1/2 downsloping orbitals from the mixed $f_{7/2}\oplus$ $h_{9/2}$ shells, which are included in several bands observed in ^{130}Pr [186, 190, 200], the N=73 isotones of ^{132}Pr [201, 202], ^{133}Nd [203, 204], and ^{134}Pm [205]. Their Q_0 values, which are intermediate between the highly–deformed intruder/extruder configurations and the ND bands, also seem to indicate somewhat decreasing values with Z. Since the neutron structure of nuclei with N$\leq$73 does not favor the occupation of the $i_{13/2}$ intruder, the down–sloping [541]1/2 orbital may lead also to polarization of the core. [189, 190] The experimental playground for studying the $f_{7/2}\oplus$ $h_{9/2}$ orbitals includes several bands in ^{130}Pr [200, 186, 190] and the N=73 isotones of ^{132}Pr [202, 201], ^{133}Nd [206, 203, 204], and ^{134}Pm [205].

For the nuclei in the A$\simeq$130 region, the yrast line at low spin is dominated by normally–deformed configurations. However, when the total spin increases above 10–20 $\hbar$ these structures are predicted to be very γ–soft. This implies that the additivity concept is likely to meet its limits for ND shapes. This caution is particularly relevant when we observe the general trend of the ND–HD separation in Q_0 to decrease with Z or N from the lightest to the heaviest nuclei in the region — a behavior that can be associated with the softening of the core. One would expect such a tendency to be present until another neutron/proton particle number corresponding to a deformed gap is reached. In our case, such change seemingly occurs around the Z=58, N=74 gaps (^{132}Ce), and the trend is followed until around Z=62, N=80 (^{142}Sm). Beyond these nucleon numbers, the values of Q_0 appear to take a jump, which can be associated with the occupation of the next intruder orbitals, namely $\mathcal{N}$=7 neutrons and (later) $\mathcal{N}$=6 protons.

3.2 HFODD Calculations — Convergence and Accuracy

The issues of accuracy, robustness, and reliability of the Skyrme Hartree–Fock method have been addressed by a considerable body of research. Several deformed Hartree–Fock codes allowing for triaxial nuclear deformations have been in use since the mid–1980's [121, 111, 113, 114, 115]. The code HFODD, being the first one of this kind available in the public domain, has been subject to relatively more extensive testing, and the accuracy of the Skyrme Hartree-Fock equations in the Cartesian harmonic oscillator (HO) basis has undergone studies by the authors of the code HFODD [110], who have applied it in different regions of the periodic chart [130].

3.2.1 Convergence of HFODD versus the HO Basis Deformation

The accuracy of the harmonic oscillator expansion depends on the three parameters of the oscillator wave functions, the frequencies ($\hbar\omega_x$, $\hbar\omega_y$, and $\hbar\omega_z$) and the number of HO states included in the basis set (M). The basis set is defined to include the lowest M states with energies given by

$$\varepsilon_{n_x,n_y,n_z} = \hbar\omega_x(n_x + \frac{1}{2}) + \hbar\omega_y(n_y + \frac{1}{2}) + \hbar\omega_z(n_z + \frac{1}{2}), \tag{3.1}$$

with n_x,n_y,$n_z < \mathcal{N}_0$, where $\mathcal{N}_0$ is the maximum number of harmonic oscillator quanta. Both M and $\mathcal{N}_0$ have to be chosen in advance for the basis to be determined. When $\mathcal{N}_0$ is chosen to be sufficiently large, the accuracy of the Hartree–Fock calculations depends only on the choice of M.

In the present study, the results have been obtained with an axially–deformed basis, *i.e.* one with $\omega_\perp = \omega_x = \omega_y$, where the frequencies are defined as in (2.11). The deformation of the basis is given using the standard parameterization (2.15),

$$q = \omega_\perp/\omega_z \equiv \zeta \quad \text{and} \quad \omega_0 = (\omega_\perp^2\omega_z)^{1/3}. \tag{3.2}$$

The dependence of the results on the size of the basis has been tested systematically from small bases ($\mathcal{N}_0 \leq$10 in the early implementations of the method [207]) to $\mathcal{N}_0$ ~26 and higher. The conclusions from calculations with small values of $\mathcal{N}_0$ suggest that the deformation of the basis (ω_0 and $q \equiv \zeta$ in our case) can be tuned for the specified values of M and $\mathcal{N}_0$ by minimizing the total Hartree–Fock energy. It remains questionable whether such an optimization would guarantee the optimal regime of the variational calculations for other quantities of interest. In the middle of the 1970's, when the values of $\mathcal{N}_0$ ~10 were pushing the limits of the available computational facilities, such optimization was worthwhile, even at the cost of expensive preliminary calculations in search for a trustable physical solution. It is instructive to see the Skyrme HF method in this early work applied to the test cases of ^{126,134}Ce, which are very close to our A~130 core configuration. The results with $\mathcal{N} \leq 10$, (particularly Figs. 6,9,11, and 12 of [207]), give strong indications that the variation of $q \equiv \zeta$ has non–negligible effects on the total energy, deformation profile, and the positions of the minima in the energy landscape.

Since these early attempts, it has been possible to perform calculations with basis sizes sufficiently large to allow the elimination of the basis deformation parameters. When the value of $\mathcal{N}_0$ becomes large, the uncertainties of the HF solution can be made sufficiently small, and kept under control. The studies of [130] show convincingly that, under these conditions, the optimization of basis deformation parameters does not yield any significant improvement of the precision.

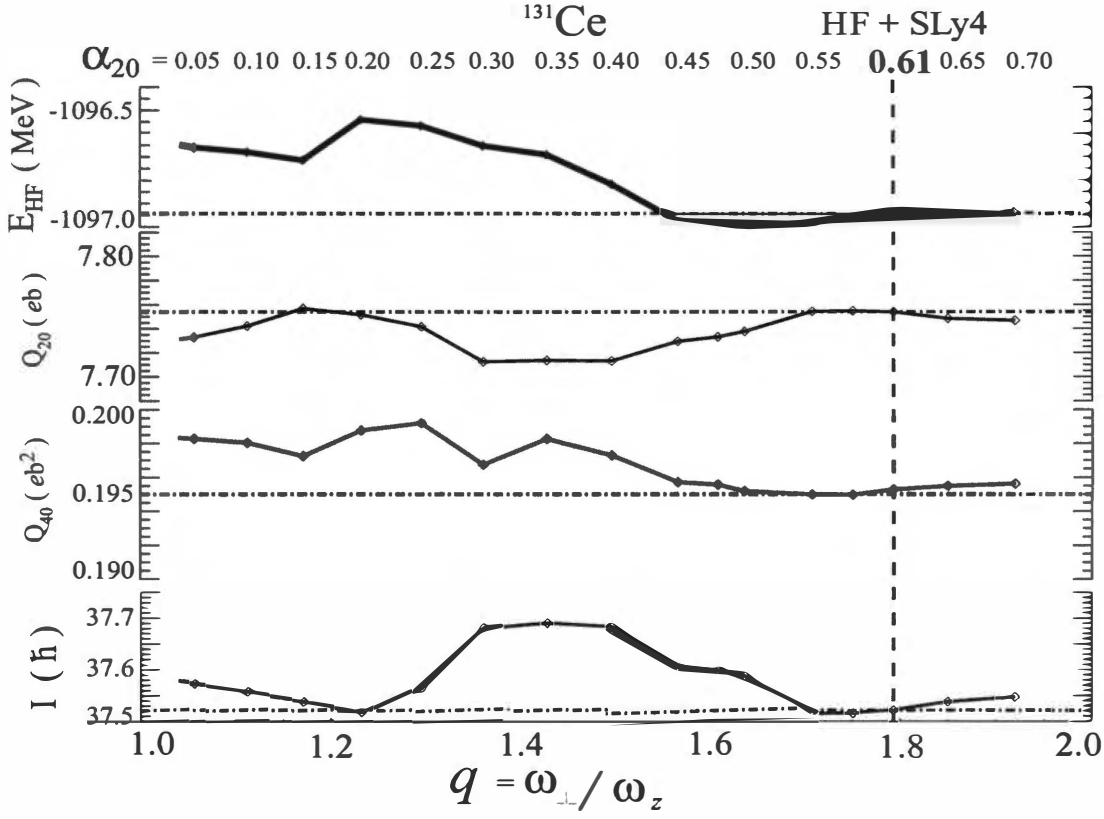

Figure 3.2: Convergence of the ^{131}Ce core configuration as a function of the deformation of the basis q. The value used in the calculations is indicated by a dashed line.

In all of our calculations the value of M was set to 296 [130]. The Hartree–Fock solution was tested by expanding in a basis of HO wave functions of the lowest superdeformed band in ^{131}Ce (Fig 2.3). The value of the frequency ω_0 is obtained from (2.10),

$$\hbar\omega_0 = 41.(\text{MeV}) \times A^{-1/3} = 9.6874 \text{ MeV}. \tag{3.3}$$

For the superdeformed region, a typical value for q is around 0.6, corresponding to $\hbar\omega_\perp$ =11.7688 MeV and $\hbar\omega_z$=6.5638 MeV. The value of q was then varied in the interval from 1.0 to 1.92, and the resulting values of several physical quantities relevant to our work are shown in Fig. 3.2. It is evident that the variations over the entire interval are significantly smaller than the experimental uncertainties. The data points for q=1.0 (spherical basis) were excluded — the deformed solution, being anisotropic, is not meaningful when expanded in a spherical basis. As soon as the basis gets slightly deformed, the quantities for the Hartree–Fock solution stay within fractions of the percent around the accepted value ($q \approx 1.9$). It is interesting to compare these results with Figs. 3,4 of Ref. [130]. Refer to the latter reference for a more detailed discussion of the convergence accuracy of the Skyrme Hartree–Fock method used in our work.

3.2.2 Accuracy and Precision of the Additivity Analysis

In this work we calculated rotational bands based on a number of single–particle configurations corresponding to the known highly–deformed rotating structures, including some expected structures, which have not been observed yet. The Skyrme Hartree–Fock calculations with the code `HFODD (v1.75)` [110, 130] with interaction SLy4 [109] used in the particle–hole channel, was carried out by the author, for a set of more than 200 single–particle configurations, which, after removing some of the ambiguous cases (due to crossings, convergence difficulties, *etc.*) was reduced to 183 to form a base set used in the additivity analysis.

In a similar fashion, a set of 105 configurations was calculated by our collaborators, G. A. Lalazissis and A. Afanasjev from Technische Universität in Münich, using their version of the Relativistic Mean Field cranking code with a basis of an anisotropic three-dimensional harmonic oscillator with $\beta_0 = 0.4$ in Cartesian coordinates, as described in Chapter 2 [208, 209, 210, 211]). All fermionic states below the energy cutoff $E_F^{\text{cut-off}} \leq 11.5\hbar\omega_0^F$ and all bosonic states below the energy cutoff $E_B^{\text{cut-off}} \leq 16.5\hbar\omega_0^B$ were used in the diagonalization and the matrix inversion.

The results for the values of the quantities of interest, the proton quadrupole moments Q_{20}^{π}, and Q_{22}^{π} in units of eb, the total angular momenta I, the total energies, and the total Routhian energies, along with additional bookkeeping information were stored in files to be used for the additivity analysis. Every configuration was labeled using the standard notation in terms of parity–signature blocks $[N_{+,+i}, N_{+,-i}, N_{-,+i}, N_{-,-i}]$, but, since these labels are not unique due to diabatic crossings, each configuration could only be identified by specifying its Nilsson orbital "content", that is, the Nilsson labels of the orbitals at zero frequency. The assignment of the Nilsson content to a given band is relatively easy to do when the Nilsson orbitals do not get mixed in the vicinity of level crossings. However, when such crossings occur, we chose the component with the highest probability in the decomposition. In a few cases such assignment was difficult to do because there were several orbitals with similar weights; those cases were excluded from the set.

Clearly, the likelihood of the occurrence of such ambiguous cases is reduced when the level density is smaller, for example in the vicinity of shell gaps. For the additivity analysis we needed to choose as a core configuration the one with the least ambiguous assignment of occupied Nilsson orbitals. The optimal conditions were found in the SD-1 configuration of ^{131}Ce.

We decided to conduct the additivity analysis at an angular frequency of $\hbar\omega$=0.65 MeV because it is high enough for the pairing effects in a highly–deformed band to be quenched, and because in a relatively wider interval (as compared with the vicinities of other frequency values) there are practically no level crossings. At $\hbar\omega$=0.65 MeV, the lowest $i_{13/2}$ intruder orbital already appears just below the N=73 neutron gap (Fig. 2.3). Therefore, at this frequency it is better to choose an odd–even core, a preference without negative consequences for the additivity scheme, which is insensitive to the selection of the core.

In some cases, we needed to calculate the entire band, down to very small frequencies, to be able to trace a given orbital down to its Nilsson scheme original. The Nilsson orbital content of a band is given in terms of particle and hole excitations with respect to the core configuration through the action of particle/hole operators with quantum labels corresponding to the occupied or emptied Nilsson orbitals. The core configuration ($[18,19,18,18]_n$, $[14,14,15,15]_p$) plays the role of a shell–model "*vacuum*"; it is given by

$$|\mathbf{core}\rangle = |\mathbf{core}\rangle_\nu \quad \otimes \quad |\mathbf{core}\rangle_\pi \equiv$$

$$
\begin{array}{r}
(\nu(1i_{13/2})\mathbf{6}_1^{-i}) \\
(\nu(1h_{11/2})[523]7/2^{\pm i})^2 \\
(\nu(2d_{3/2})[411]1/2^{\pm i})^2 \\
(\nu(1g_{7/2})[413]5/2^{\pm i})^2 \\
(\nu(2f_{7/2})[541]1/2^{\pm i})^2 \\
(\nu(2d_{5/2})[411]3/2^{\pm i})^2 \\
(\nu(1h_{11/2})[532]5/2^{\pm i})^2 \\
(\nu(1g_{9/2})[404]9/2^{\pm i})^2 \\
(\ \cdots\ )\,|0\rangle_\nu
\end{array}
\quad\otimes\quad
\begin{array}{r}
(\pi(1g_{9/2})[404]9/2^{\pm i})^2 \\
(\pi(1h_{11/2})[541]3/2^{\pm i})^2 \\
(\pi(1g_{7/2})[420]1/2^{\pm i})^2 \\
(\pi(2d_{5/2})[422]3/2^{\pm i})^2 \\
(\pi(1h_{11/2})[550]1/2^{\pm i})^2 \\
(\pi[301]1/2^{\pm i})^2 \\
(\ \cdots\ )\,|0\rangle_\pi
\end{array}
\ , \tag{3.4}
$$

where $|0\rangle_\nu$ and $|0\rangle_\pi$ are the neutron and proton particle *vacua*, respectively. In (3.4) we have limited ourselves to writing out explicitly only the orbitals shown in Fig. 2.3.

As an example let us consider the neutron configurations of Fig. 2.4. Although having the same parity–signature configurations, ν [18,19,18,18], they have different numbers of $i_{13/2}$ intruders occupied — the 6_1^{-i} Routhian, occupied in the left diagram, has been emptied in the right diagram. The former neutron diagram corresponds to the core configuration, and the latter part can be obtained from it by the operators creating a hole in ν 6_1 and a particle in $[402]5/2^{-i}$, which can be written as

$$
(\nu\mathbf{6}_1-)^{-1}(\nu[402]5/2-)\,|\mathbf{core}\rangle_\nu \otimes |\mathbf{core}\rangle_\pi \equiv (\nu\mathbf{6}_1-)^{-1}(\nu[402]5/2-)\,|\mathbf{core}\rangle \tag{3.5}
$$

Note that the signs appearing after the state's Nilsson label are the signature quantum numbers : "–" represents r=–i (α=+1/2), and "+" signifies r=i (α=–1/2).

Upon reading the input file with band configurations, the additivity analysis program generates the matrix $\{c_\alpha(k)\}$, filling it with the values +1, –1, or 0, depending, respectively, on whether state α is a particle, a hole, or not–present in configuration k. One of the main results of the analysis is the set of effective single–particle values for $q_{20,\alpha}$, $q_{22,\alpha}$, and i_α. The quality of the additivity model then can be estimated from the values of the deviations from the fitted values, namely the quantities

$$
\sum_\alpha c_\alpha(k)q_{20,\alpha} - \delta Q_{20}^\pi(k) \;=\; \sum_\alpha c_\alpha(k)q_{20,\alpha} - \left(Q_{20}^\pi(k) - Q_{20}^{\pi(\mathrm{core})}\right) \tag{3.6}
$$

$$
\sum_\alpha c_\alpha(k)q_{22,\alpha} - \delta Q_{22}^\pi(k) \;=\; \sum_\alpha c_\alpha(k)q_{22,\alpha} - \left(Q_{22}^\pi(k) - Q_{22}^{\pi(\mathrm{core})}\right) \tag{3.7}
$$

$$
\sum_\alpha c_\alpha(k)i_\alpha - \delta i(k) \;=\; \sum_\alpha c_\alpha(k)i_\alpha - \left(I(k) - I^{(\mathrm{core})}\right). \tag{3.8}
$$

In the following Figs. 3.3, and 3.4 we show the distribution of the values of these deviations around zero.

Let us look first at the quality of the additivity assumption for the fitted values of Q_{20}^π and I for both self–consistent models in our study (Fig. 3.3, top). The majority of the deviations (more than 97.8% of the total number) fit comfortably within an interval of ±0.1 eb. Having in mind, that the total value of Q_{20}^π for the core configuration is 7.754 eb, the deviation is around 1.3%. The distribution is even narrower for the relativistic mean–field calculations, with more than 90% of the deviations fitting within a ±0.05 eb interval, or less than 0.7% of the total value. We interpret these results as good indications that the additivity assumption works.

Our results for the total angular momenta (Fig. 3.3, bottom) appear further to confirm this observation. The deviations from the additivity ansatz in the RMF is very narrow, with only 10% of the cases differing by more than $\pm\hbar/2$. A majority of cases lies within half of this

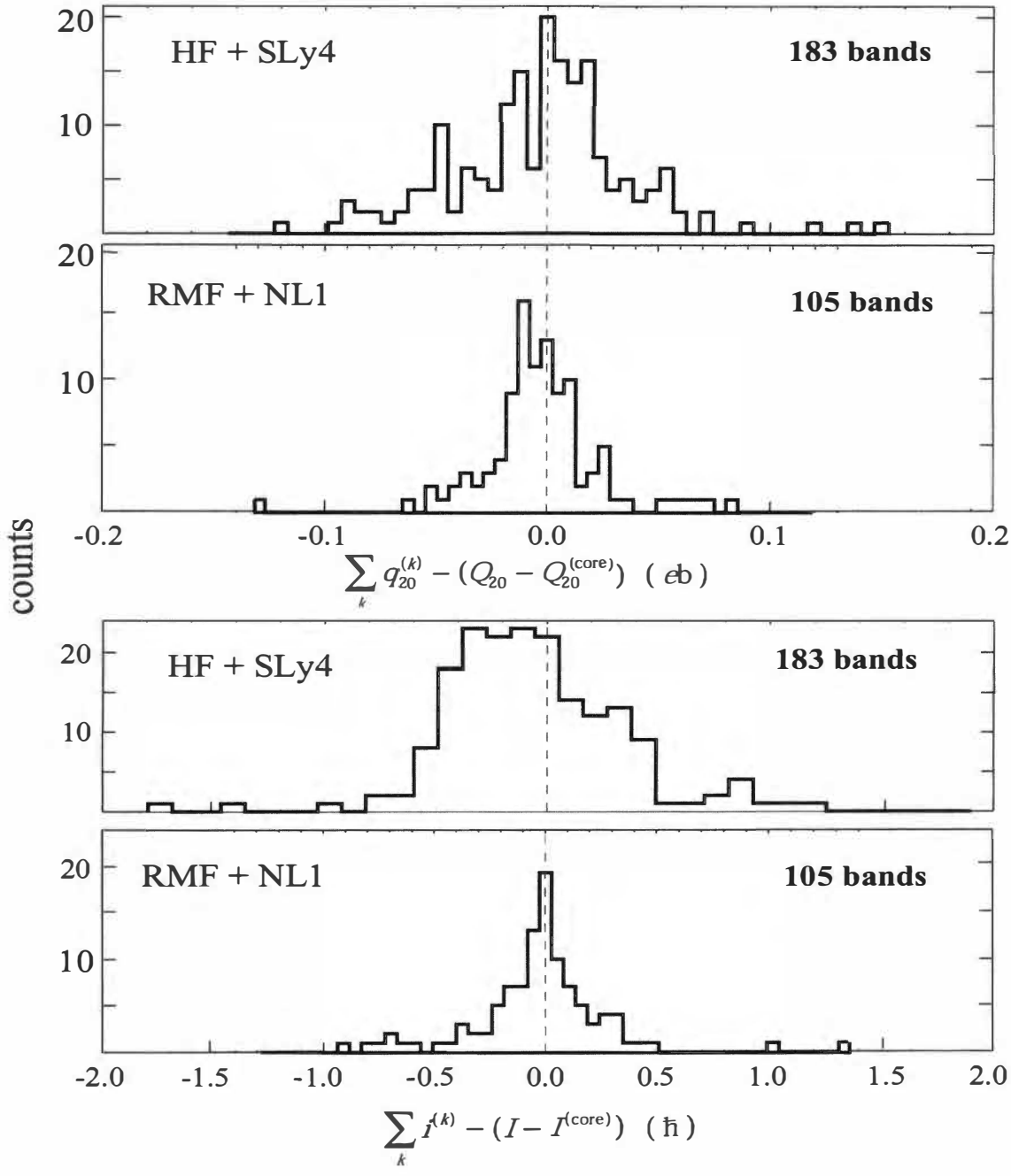

Figure 3.3: Side–by–side comparisons of the deviation distributions of the additive–fitted values for the quadrupole moment Q_{20}^{π}, and the total angular momentum I from their calculated values. The data is represented on the same scale for both models.

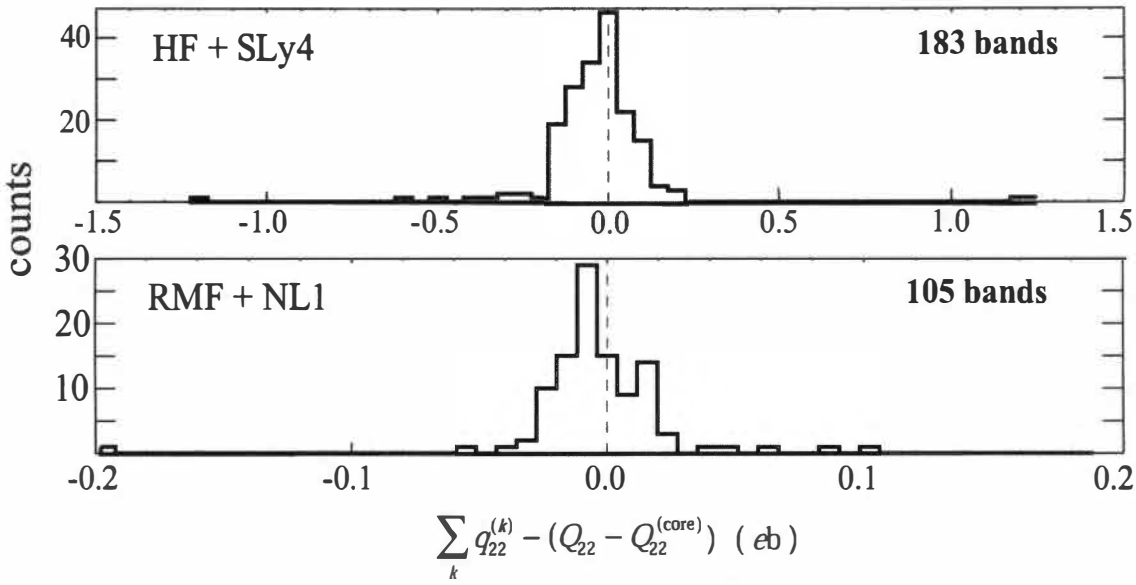

Figure 3.4: Similar to Fig. 3.3, but for Q_{22}^{π}. Note the difference in scale.

width, and is sharply centered around 0 $\hbar$. The corresponding histogram for the Skyrme model, with its 183 bands, is somewhat wider, but again — the majority of more than 90% of the angular momentum deviations falls within a $\pm\hbar/2$ interval. Taking into consideration that the experimental angular momenta assigned with uncertainties that are multiples of $\hbar$, our results should give some encouragement for theoretical interpretations based on the single–particle alignments obtained from self–consistent calculations.

The results for the deviations in Q_{22}^{π}, Fig. 3.4, have to be interpreted separately. In both Skyrme HF and RMF cases, the distributions are relatively narrow. Again, nearly 95% of the deviations for RMF (bottom part) are within ± 0.025 eb, and 98% are within ± 0.1 eb. The distribution of the deviations in the Skyrme model calculations is somewhat wider, with more than a 90% majority falling within ± 0.2 eb of zero.

Clearly, the quality of the Q_{22} fit deserves special attention in our further analysis. We recall at this point that the potential energy surface in these nuclei has relatively shallow minima allowing for shape instability with respect to the γ–deformation degree of freedom, allowing for the appearance of triaxially–deformed shapes. Our results add credibility to the assumption, that the nuclei in this region show a certain "softness" of shape with respect to the γ degree of freedom, which is not observed to the same degree in the β direction. The nuclear shape parameterization in the basis of Q_{20} and Q_{22} offers a possibility of separating out the two components, and evaluating the two terms in the definition of Q_t (2.129), respectively calculating q_t. We shall return to this question in the next Section.

3.3 The Core and Excited Configurations in ^{131}Ce

The lowest superdeformed configuration SD-1 of ^{131}Ce was introduced in Chapter 2 (Fig. 2.3); in the parity-signature classification scheme it is labeled as ν [18, 19, 18, 18], π [14, 14, 15, 15], with total parity $P = +1$ and signature $R = -i$. Its choice as the core for our additivity analysis was facilitated to a great extent by the fact that it was the first known experimentally to have occupied the lowest neutron $i_{13/2}$ intruder state [147], along with its identical band SD-1 in ^{132}Ce [50]. These studies also provided experimental indications for the existence of the energy gaps at Z=58 and N=72,73, which have been subject to further studies throughout the 1990's (see [148, 161], and references therein).

Figure 3.5 shows the neutron part of the Routhian diagram aligned in frequency with the latest data for band SD-1 [53]. The core parameters calculated in CHF at $\hbar\omega$=0.65 MeV are as follows : $Q_{20}^{\pi(\text{core})}$=7.75 eb, $Q_{22}^{\pi(\text{core})}$=0.19 eb, and $I^{(\text{core})}$=37.5210 $\hbar$. The corresponding parameter values for the CRMF are 7.57 eb, 0.12 eb, and 37.33 $\hbar$, respectively. The experimental frequencies have been calculated using the phenomenological formula (2.120). The spectroscopic analysis infers for the bandhead an angular momentum of $J \simeq 29/2$, so the E2 γ-transition, corresponding to frequency $\hbar\omega$=0.65 MeV with $E_\gamma(J+22 \rightarrow J+20)$=1.301 MeV, would occur when the rotating system has an angular momentum of 14.5 + 21 = 35.5 $\hbar$, which puts it almost exactly 2 units below the calculated value. Our result would therefore suggest angular momentum of 33/2 $\hbar$ for the bandhead.

This comparison allows us to make further interpretations of the physical information for this band. Figure 3.6 shows the SD-1 band along with the best candidate for the first excited structure, band SD-2 [148, 161]. The upper right panel displays a (β_2,γ) trajectory for neutrons and protons. The band starts with a pure prolate deformation, but with increased ω, β decreases, and the system develops positive–γ triaxiality. The shape change is minor and the system is very far from full alignment. The bottom–right panel offers a comparison of the dynamic moments of inertia with the experimental results. At high frequencies, the dynamic moments of inertia show a gradual decrease, which is associated with the decrease in the prolate deformation. The differences between the theoretical curves and the experimental points at low frequencies can be explained by the activation of pairing correlations [159].

Table 3.1 displays the lowest SD bands in ^{131}Ce calculated in the HF model, sorted by parity–signature blocks and listed in ascending order by Routhian from the bottom up. It is the basis for Table 3.2, in which the most relevant of them are analyzed for assignment to the known experimental bands.

Table 3.2 shows our candidates for experimental band SD-2, labeled $|\mathbf{SD\text{-}2}_a\rangle$, and $|\mathbf{SD\text{-}2}_a\rangle$ (for both signatures) and Figure 3.6 places the one lower in energy alongside SD-1 for comparison. The difference in energy between the two bands is obtained from the excitation energy between the core and the excited band at frequency $\hbar\omega$=0.65 MeV.

3.4 Results of the Additivity Analysis

We are now ready to discuss the results of the additivity analysis in the whole superdeformed A$\sim$130 region. In particular, the polarizing effects of specific orbitals on equilibrium shapes and predictions are made for yet–unobserved structures.

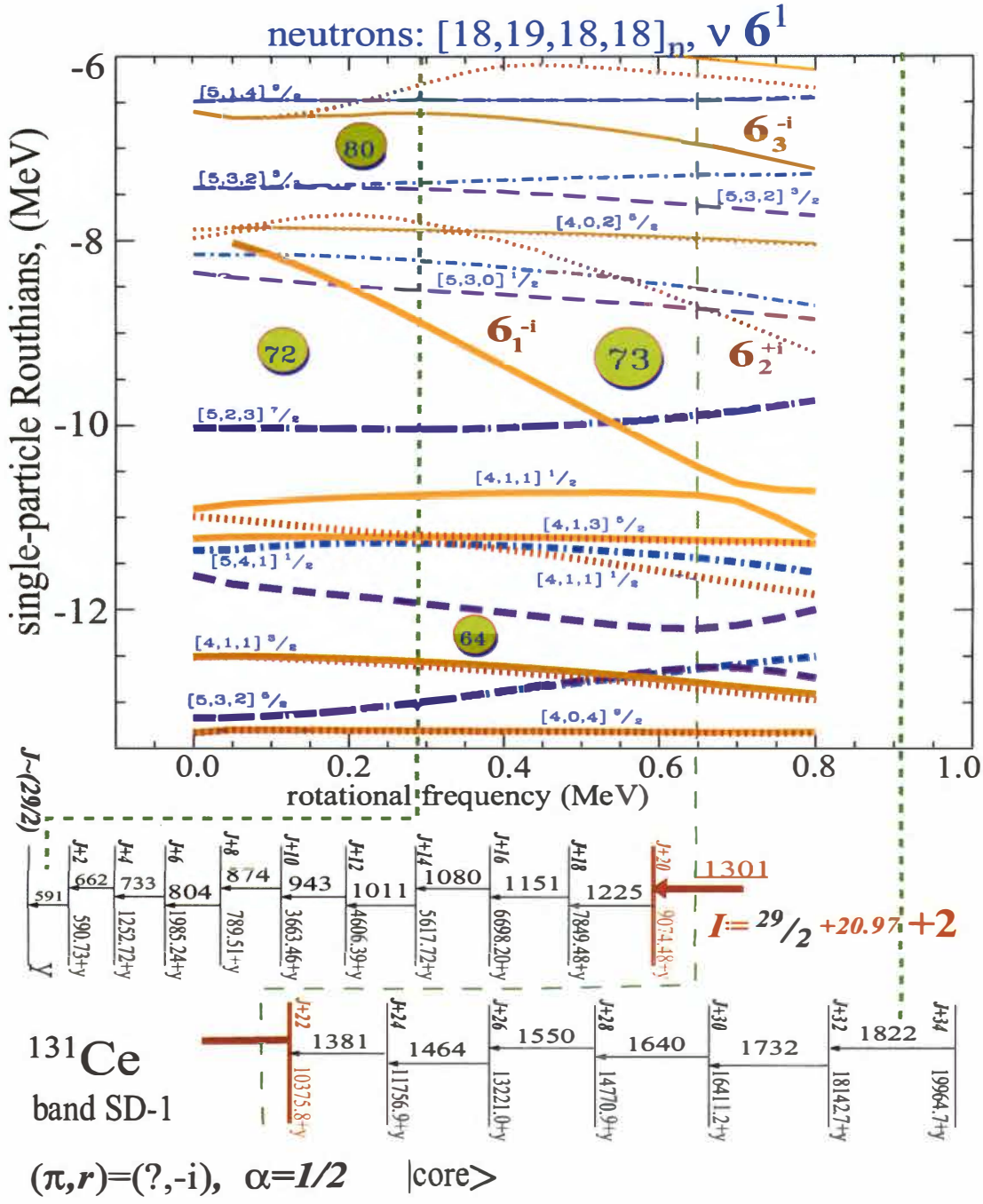

Figure 3.5: Neutron single–particle Routhian diagram for the ^{131}Ce core configuration aligned in frequency with the observed level sequence in the superdeformed band SD-1. Experimental data in all cases henceforth taken from [53], unless explicitly stated otherwise.

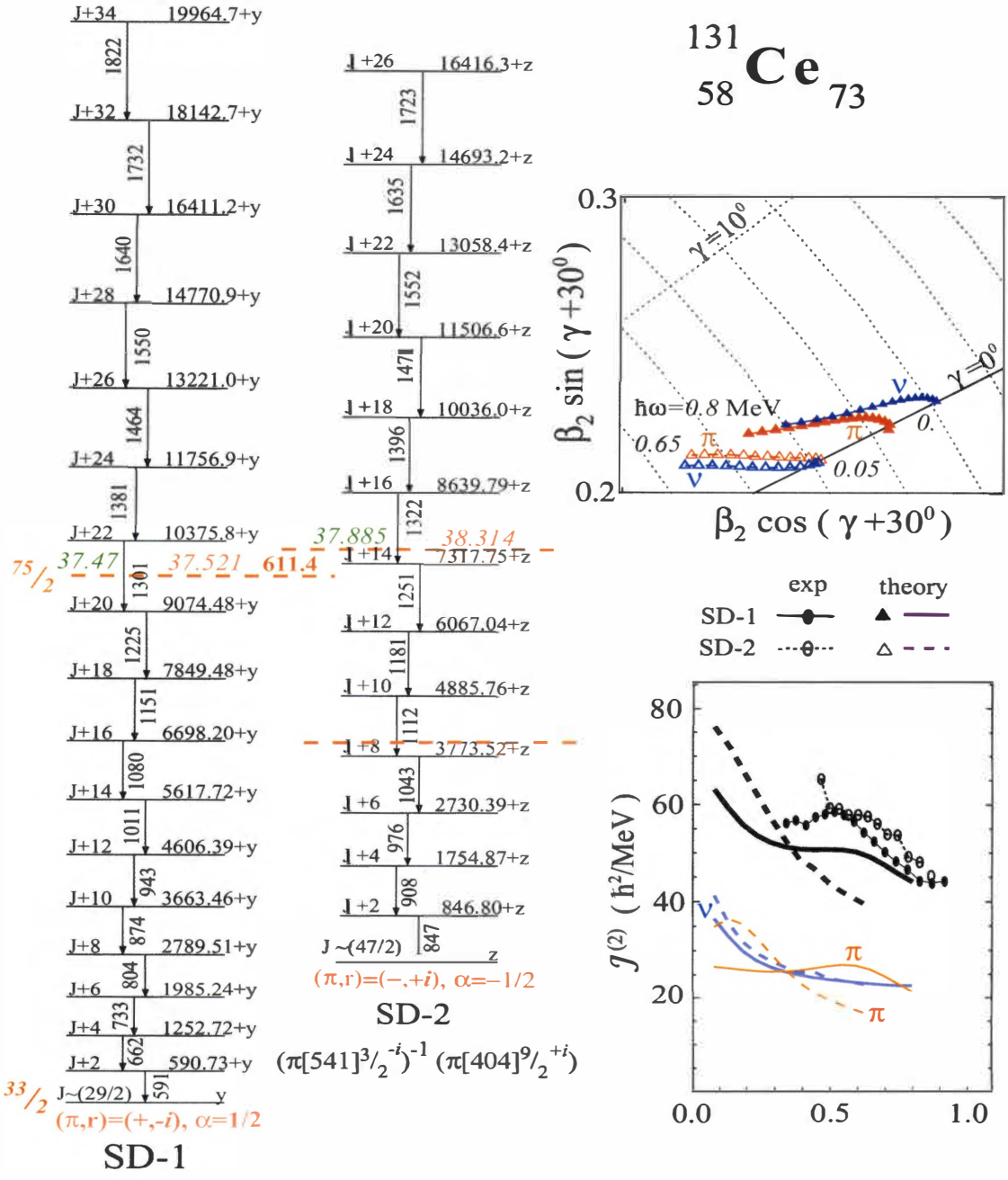

Figure 3.6: Assignments for the two experimentally–observed SD bands in ^{131}Ce and comparison between their spectroscopic parameters and the corresponding Skyrme HF results. The level energies (left) have been shifted in energy by an amount obtained from the total Routhian difference at $\hbar\omega$=0.65 NeV. Experimental data were taken from [53].

Table 3.1: Band configurations in low–lying SD bands in ^{131}Ce, calculated in the CHF+SLy4 model.

$E_\omega - E_\omega^{\rm core}$ (MeV)	$[N_{+,+i}, N_{+,-i}, N_{-,+i}, N_{-,-i}]$	Q_{20}^π (eb)	Q_{22}^π (eb)	I ($\hbar$)	Band configiration w/respect to $\|$**core**$\rangle$
		^{131}**Ce**			
	(π, r)=(+, i)				
2.78	$[19,19,17,18]_n[14,15,14,15]_p$	6.54	0.410	37.96	$(\nu[523]7/2+)^{-1}$ $(\nu[402]5/2+)$ $(\pi[404]9/2-)$ $(\pi[541]3/2+)^{-1}$
2.24	$[18,18,19,18]_n[14,15,15,14]_p$	6.78	0.05	33.96	$(\nu\mathbf{6}_1-)^{-1}(\nu[530]1/2+)$ $(\pi[404]9/2-)$ $(\pi[541]3/2-)^{-1}$
1.62	$[19,18,18,18]_n[14,14,15,15]_p$	8.25	0.15	40.22	$(\nu\mathbf{6}_2+)(\nu[411]1/2-)^{-1}$
	(π, r)=(–,–i)				
1.83	$[18,18,18,19]_n[14,14,15,15]_p$	7.54	0.09	33.95	$(\nu\mathbf{6}_1-)^{-1}(\nu[530]1/2-)$
0.90	$[19,19,17,18]_n[14,14,15,15]_p$	8.15	0.18	40.93	$(\nu\mathbf{6}_2+)(\nu[523]7/2+)^{-1}$
0.61	$[18,19,18,18]_n[14,15,15,14]_p$	6.85	0.31	38.30	$(\pi[404]9/2-)$ $(\pi[541]3/2-)^{-1}$
	(π, r)=(–, i)				
1.73	$[18,18,19,18]_n[14,14,15,15]_p$	7.59	-0.05	34.03	$(\nu\mathbf{6}_1-)^{-1}(\nu[530]1/2+)$
0.61	$[18,19,18,18]_n[15,14,15,14]_p$	6.85	0.32	38.31	$(\pi[541]3/2-)^{-1}$ $(\pi[404]9/2+)$
	(π, r)=(+,–i)				
2.65	$[19,19,18,17]_n[14,15,14,15]_p$	6.54	0.39	38.23	$(\nu[402]5/2+)$ $(\nu[523]7/2-)^{-1}$ $(\pi[404]9/2-)$ $(\pi[541]3/2+)^{-1}$
2.30	$[18,18,18,19]_n[14,15,15,14]_p$	6.71	0.20	33.82	$(\nu\mathbf{6}_1-)^{-1}(\nu[530]1/2-)$ $(\pi[404]9/2-)$ $(\pi[541]3/2-)^{-1}$
0.00 **(-1096.9)**	$[18,19,18,18]_n[14,14,15,15]_p$	**7.75**	**0.19**	**37.52**	$\|$**core**$\rangle \equiv$ **SD-1**

Table 3.2: The CHF+SLy4 assigned configurations in ^{131}Ce.

E' (MeV)	parity–signature blocks	Q_t (eb)	I ($\hbar$)	Band configiration w/respect to $\|$**core**$\rangle$
		$\boxed{^{131}\mathbf{Ce}}$		
1.62		+0.524	+2.701	
	$[19,18,18,18]_n$			$(\nu\ \mathbf{6_2}+)$ $(\nu\ [411]1/2\text{-})^{-1}$ $\|\mathbf{core}\rangle_\nu$
				$\otimes$
	$[14,14,15,15]_p$			$\|\mathbf{core}\rangle_\pi$
0.61		-0.968	+0.777	$\|\mathbf{SD\text{-}2}_b\rangle :=$
	$[18,19,18,18]_n$			$\|\mathbf{core}\rangle_\nu$
				$\otimes$
	$[14,15,15,14]_p$			$(\pi\ [541]3/2\text{-})^{-1}$ $(\pi\ [404]9/2\text{-})$ $\|\mathbf{core}\rangle_\pi$
0.61		-0.973	+0.793	$\|\mathbf{SD\text{-}2}_a\rangle :=$
	$[18,19,18,18]_n$			$\|\mathbf{core}\rangle_\nu$
				$\otimes$
	$[15,14,15,14]_p$	-0.635 -0.379	+0.540 -0.719	$(\pi\ [541]3/2\text{-})^{-1}$ $(\pi\ [404]9/2+)$ $\|\mathbf{core}\rangle_\pi$
0	$\|\mathbf{core}\rangle$	**0**	**0**	$\|\mathbf{SD\text{-}1}\rangle :=$
	$[18,19,18,18]_n$	**(7.64)**	**(37.52)**	$\|\mathbf{core}\rangle_\nu \otimes$
	$[14,14,15,15]_p$			$\|\mathbf{core}\rangle_\pi$

3.4.1 Effective Quadrupole Moments for the Nilsson Orbitals

Table 3.3 presents in a concise way the values of $q_{20}^{\rm eff}$ for a number of single–particle orbitals and allows for a comparison of its values with the corresponding ones, obtained as part of the similar analysis [77] in the A$\sim$150 superdeformed mass region. The Table is best interpreted along with the illustrative Figs. 3.7 and 3.8 for neutron and proton states, respectively, where the shape polarization effects of particular orbitals can be compared directly with their behaviors in the Nilsson diagrams. [1].

The Table includes a good deal of information for comparison between the different self–consistent models used in the additivity studies. One can notice immediately the overall excellent agreement between the q_{20} results for the two mean–field models employed in this study. In a majority of the cases, the uncertainties are small enough to give us two correct significant digits. The two lowest intruder states experience significant signature splitting, and their effective quadrupole moment contributions differ by more than 5%.

The extracted values confirm the expectations for the role of the intruder and extruder states. The neutron $i_{13/2}$ orbitals $\mathbf{6}_1^{-i}$ and $\mathbf{6}_2^{+i}$ both carry prolate $q_{20} \simeq 0.37$ eb, which illustrates their significant prolate–polarizing effect on the core. The third intruder orbital, $\mathbf{6}_3^{-i}$, although calculated with relatively poor statistics, confirms this trend.

The proton π [404]9/2 extruder states have large negative values of q_{20}, which confirms the hypothesis that emptying them would drive the nuclear system towards more prolate–deformed shapes. Interestingly, their q_{20} values of around –0.31 eb are close in magnitude to those of $\mathcal{N}$=6 neutron intruders. They have practically zero signature splitting, and their values of q_{20} are practically indistinguishable within the error bars.

It is of considerable interest for our studies of highly deformed shapes in this region to pay attention to the role of the proton $h_{11/2}$ states, notably the two π [541]$3/2^{\pm i}$ levels. Table 3.3 attributes to them prolate quadrupole moments in excess of 0.45 eb, very significant values compared with other states listed. These two states lie immediately below the N=58 energy gap, and their emptying in the Lantanum and Barium isotopes leads to a rapid loss of deformation. In view of the comparison with the intruder and extruder, it would not be an overstatement to conclude that these two states have a significant role to play in the existence of this island of high deformation. Similar is the effect of the π [532]$5/2^{\pm i}$ orbital from the same shell, appearing immediately above the proton Z=58 gap.

The downsloping orbitals [541]$1/2^{\pm i}$ originating from neutron ($f_{7/2} \oplus h_{9/2}$) shells carry large quadrupole moments (more than 0.3 eb). Although one could expect them to play a role in the formation of large prolate deformations, these states appear perhaps a little too low in energy and would therefore always stay occupied.

The results presented in Table 3.3 other sets of cranked Hartree–Fock models and interactions on the market. The columns on the left side of the Table show an overall reasonable quantitative agreement with the additivity results from the previous study in the A$\simeq$150 superdeformed mass region [77]. Note that some of our particle states appear as hole states in the heavier mass region, in which cases we had to invert the signs of their effective q_{20}. It gives reasons for optimism in favor of the agenda to eventually combine the two regions into a wider systematic study, and interpret the entire area of highly–deformed rotational states from the mass range A $\sim$ 128–160 on the same theoretical platform. The virtual independence of the effective quadrupole

[1] One should keep in mind that the Nilsson diagram has been calculated for ^{128}Ba, not for the core configuration in ^{131}Ce, so there are small differences between the positions of the single–particle states in the Nilsson diagrams and the corresponding states in the Routhian diagram at zero frequency. This should not be a problem, since we are interested mainly in the slopes of energy levels, and relative excitation energies.

Table 3.3: Effective quadrupole moments $q_{20} \equiv q_{20}^{\rm eff}$ calculated in CHF and CRMF models. The SkP and SkM* results are from Ref. [77].

State		CHF+SkP	CHF+SkM*		CHF+SLy4		CRMF+NL1
$[\mathcal{N}n_z\Lambda]\Omega^r$	p/h	q_{20}	q_{20}	p/h	$\langle\hat{q}_{20}\rangle$	q_{20}	q_{20}
$\nu\ [402]\frac{5}{2}^{+i}$	p	−0.44	−0.38	p	−0.134	−0.347 ±0.013	−0.259 ±0.014
$\nu\ [402]\frac{5}{2}^{-i}$	p	−0.44	−0.38	p	−0.134	−0.340 ±0.018	−0.257 ±0.024
$\nu\ [411]\frac{1}{2}^{+i}$	h	−0.18		h	0.045	−0.147 ±0.022	−0.109 ±0.015
$\nu\ [411]\frac{1}{2}^{-i}$	h	−0.15		h	0.105	−0.123 ±0.014	−0.056 ±0.015
$\nu\ [411]\frac{3}{2}^{+i}$	h	−0.18		h	0.052	−0.145 ±0.042	−0.127 ±0.027
$\nu\ [411]\frac{3}{2}^{-i}$	h	−0.15		h	0.050	−0.109 ±0.051	−0.115 ±0.027
$\nu\ [413]\frac{5}{2}^{+i}$	h		−0.16	h	0.042	−0.130 ±0.021	−0.127 ±0.025
$\nu\ [413]\frac{5}{2}^{-i}$	h		−0.13	h	0.044	−0.121 ±0.027	−0.114 ±0.024
$\nu\ [523]\frac{7}{2}^{+i}$				h	0.150	0.031 ±0.009	0.046 ±0.011
$\nu\ [523]\frac{7}{2}^{-i}$				h	0.153	0.042 ±0.010	0.009 ±0.017
$\nu\ [530]\frac{1}{2}^{+i}$				p	0.314	0.220 ±0.010	0.170 ±0.008
$\nu\ [530]\frac{1}{2}^{-i}$				p	0.315	0.168 ±0.010	0.189 ±0.009
$\nu\ [532]\frac{3}{2}^{+i}$				p	0.313	0.209 ±0.027	—
$\nu\ [532]\frac{3}{2}^{-i}$				p	0.286	0.167 ±0.027	—
$\nu\ [532]\frac{5}{2}^{+i}$				h	0.278	0.189 ±0.027	0.169 ±0.027
$\nu\ [532]\frac{5}{2}^{-i}$				h	0.353	0.244 ±0.027	0.382 ±0.027
$\nu\ [541]\frac{1}{2}^{+i}$				h	0.437	0.353 ±0.028	0.349 ±0.022
$\nu\ [541]\frac{1}{2}^{-i}$				h	0.387	0.372 ±0.028	0.327 ±0.025
$\nu\ \mathbf{6}_1^{-i}$				h	0.412	0.382 ±0.007	0.396 ±0.007
$\nu\ \mathbf{6}_2^{+i}$				p	0.425	0.361 ±0.009	0.363 ±0.009
$\nu\ \mathbf{6}_3^{-i}$	h	0.43	0.30	p	0.394	0.345 ±0.045	—
$\pi\ [301]\frac{1}{2}^{+i}$	h	−0.15	−0.13	h	−0.081	0.513 ±0.049	—
$\pi\ [404]\frac{9}{2}^{+i}$	p	−0.30	−0.28	p	−0.132	−0.318 ±0.008	−0.372 ±0.008
$\pi\ [404]\frac{9}{2}^{-i}$	p	−0.30	−0.28	p	−0.132	−0.315 ±0.008	−0.372 ±0.008
$\pi\ [411]\frac{3}{2}^{+i}$	p	0.11	0.10	p	0.061	−0.048 ±0.016	—
$\pi\ [411]\frac{3}{2}^{-i}$	p	0.11	0.10	p	0.059	−0.002 ±0.014	—
$\pi\ [413]\frac{5}{2}^{-i}$				p	0.059	0.284 ±0.048	—
$\pi\ [422]\frac{3}{2}^{+i}$				h	0.200	0.326 ±0.022	0.326 ±0.025
$\pi\ [422]\frac{3}{2}^{-i}$				h	0.223	0.337 ±0.021	0.281 ±0.022
$\pi\ [532]\frac{5}{2}^{+i}$				p	0.276	0.425 ±0.011	0.410 ±0.015
$\pi\ [532]\frac{5}{2}^{-i}$				p	0.362	0.560 ±0.018	0.541 ±0.034
$\pi\ [541]\frac{1}{2}^{-i}$				p	0.396	0.581 ±0.021	—
$\pi\ [541]\frac{3}{2}^{+i}$				h	0.342	0.497 ±0.012	0.479 ±0.010
$\pi\ [541]\frac{3}{2}^{-i}$				h	0.386	0.568 ±0.009	0.504 ±0.010
$\pi\ [550]\frac{1}{2}^{-i}$				h	0.302	0.489 ±0.047	0.465 ±0.036

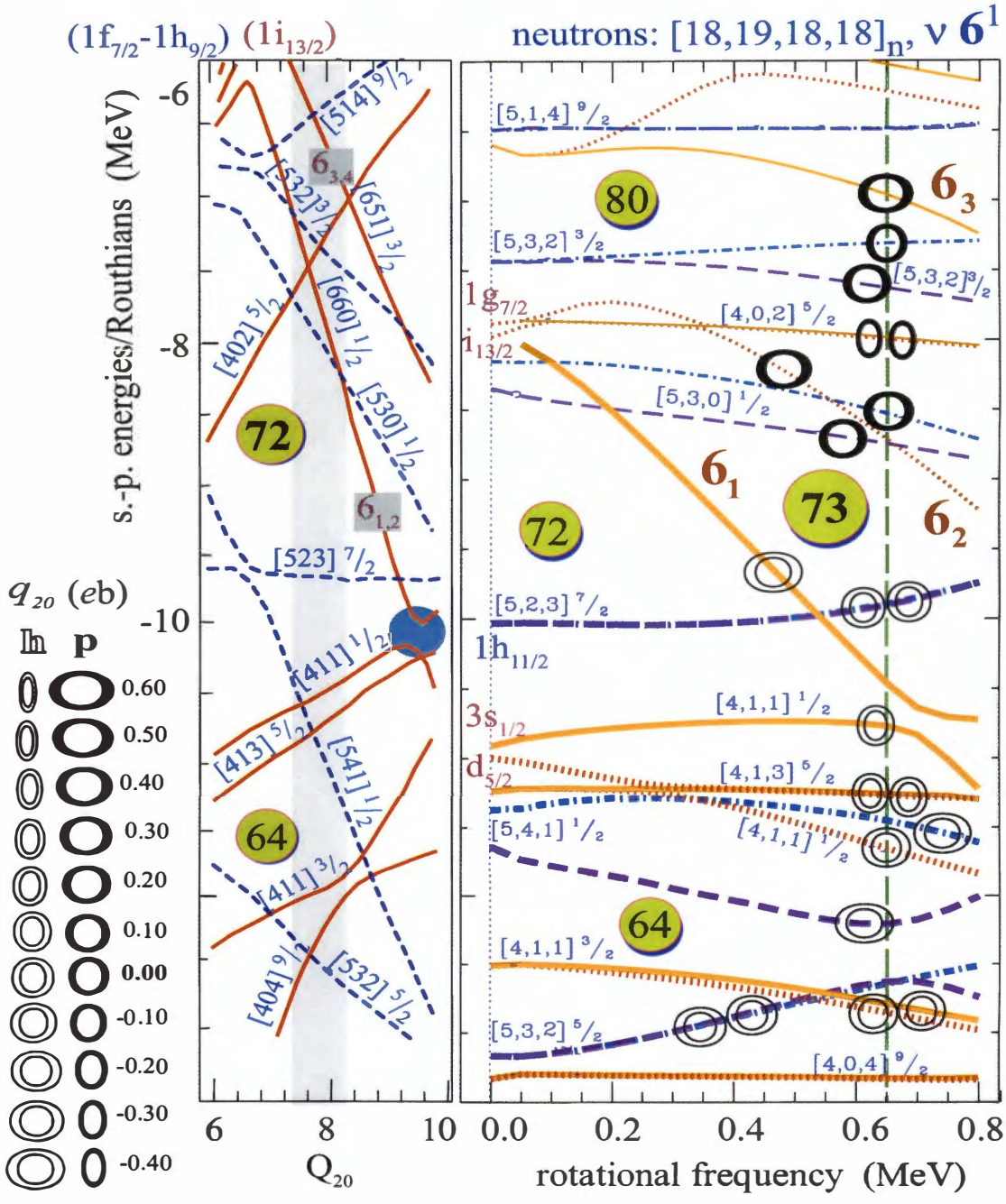

Figure 3.7: Nilsson and Routhian diagram of the core configuration with the calculated effective neutron quadrupole moments q_{20}. The ovals are schematic representations of q_{20} with respect to the horizontal symmetry axis.

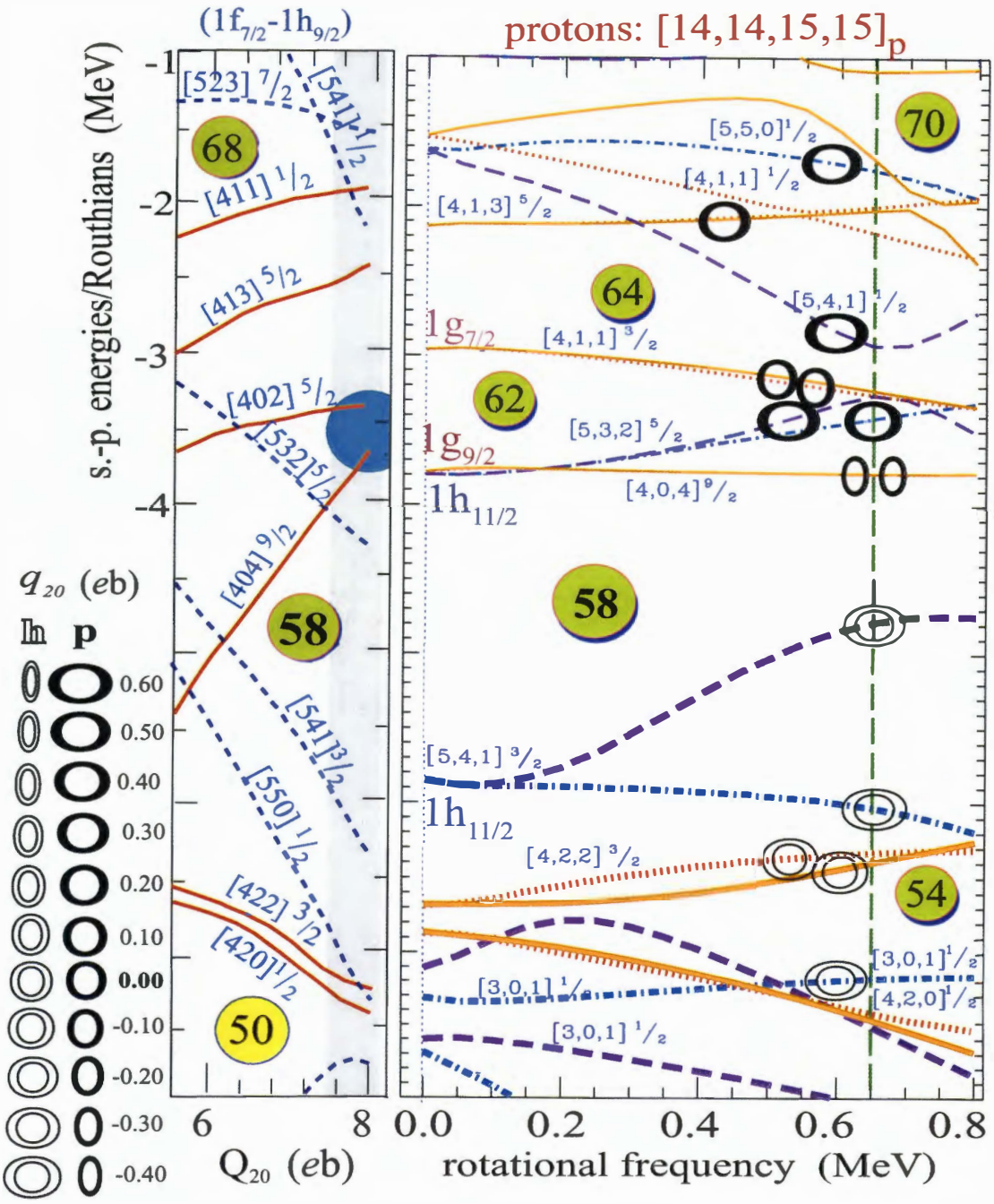

Figure 3.8: Similar as in Fig. 3.7 but for protons.

moments gives credence to the applicability of this approach as well as to the validity of the additivity model in these regions, and the mean–field concepts, on which it is based. It would be interesting to look into the trends of change of the effective values with nucleon number in these regions.

An important part of this analysis is the comparison between the effective values of q_{20} and the corresponding expectation values $\langle \hat{q}_{20} \rangle$ in the sense of (2.133) :

$$q^{\text{eff}}_{20,\alpha} = q^{\text{bare}}_{20,\alpha} + q^{\text{pol}}_{20,\alpha} \tag{3.9}$$

This decomposition obviates the difference between the roles played by the two components q_{20} and q_{22} for every band. If the shape polarization effects did not exist, we would have :

$$q^{\text{eff}}_{20,\alpha} = q^{\text{bare}}_{20,\alpha} \tag{3.10}$$

and therefore for protons we obtain $q^{\text{eff}}_{20,\alpha} = \langle q_{20,\alpha} \rangle$, and for neutrons $q^{\text{eff}}_{20,\alpha} = 0$. The existence of shape polarization terms changes the single–particle quadrupole moments dramatically. Having in mind that effective values take into consideration the presence of other nucleons in the vicinity of the nucleon orbital's space distribution, the systematics allow us to investigate further the effects of interaction terms on the given orbital. The values of $q^{\text{eff}}_{20,\alpha}$ are generally very different from $q^{\text{bare}}_{20,\alpha} = \langle q_{20,\alpha} \rangle$. In clear–cut cases, like the neutron intruder orbitals with $\mathcal{N}$=6, the differences between the effective mean values are small, in spite of the fact that these are very different quantities, while for some of the states with $\mathcal{N}$=5 the effect becomes significant. In the most interesting cases, like the neutron states [411]3/2, [411]1/2, and [413]5/2, the two values have opposite signs, *i.e.*, although the Hartree–Fock mean value would normally imply that these hole orbitals, when occupied, would lead to slightly higher prolate deformations, the effective moments indicate that their deformation effect is in fact favoring less elongated nuclear shapes ! This observation makes it even more interesting because in the cases of the $i_{13/2}$ intruders, the values of these two quantities are rather similar. A full understanding of the reasons for such closeness may require deeper analysis of the causes for shape polarization. These examples agree very well with the calculated values with other Skyrme forces in the A$\simeq$150 mass region.

3.4.2 Effective Transition Moments q_t and q_{22} Corrections

The additivity model provides many insights into the influence of the single–particle structure on deformation properties of rotating nuclei. In order to relate them to the data, we need to convert them to effective transition quadrupole moments q_t, using a definition analogous to (2.129) :

$$q_t = q_{20} - \frac{1}{\sqrt{3}} q_{22}. \tag{3.11}$$

With the resulting set of such numerical parameters for the single–particle/hole states, the experimentalists could easily calculate the expected values for Q_t for any configurations of interest in the A$\simeq$130 region.

Table 3.4 presents the calculated values of the effective single–particle transition moments. While the values of q_{20}, discussed in the previous subsection, have sufficiently small error bars, the uncertainties of q_{22} appear to be larger. We recall at this point that the distribution of the deviations of the additivity–model–calculated estimated values of Q_{22} from the Hartree–Fock values was relatively wide, casting a shadow of doubt over how meaningful the use of q_{22} can be. Although the numerical values are generally smaller than q_{20}, and are attenuated by a

Table 3.4: Effective quadrupole moments q_t calculated in the framework of the Cranked Hartree-Fock with the Skyrme SLy4 and the Cranked Relativistic Mean Field.

State	CSHF + SLy4			CRMF + NL1		
$[\mathcal{N}n_z\Lambda]\Omega^r$	q_{20} (eb)	q_{22} (eb)	q_t (eb)	q_{20} (eb)	q_{22} (eb)	q_t (eb)
$\nu[402]\frac{5}{2}^{+i}$	−0.35±0.02	0.14±0.06	−0.04±0.04	−0.26±0.02	−0.02±0.01	−0.25±0.02
$\nu[402]\frac{5}{2}^{-i}$	−0.34±0.02	0.08±0.08	−0.38±0.05	−0.26±0.03	−0.07±0.02	−0.22±0.03
$\nu[411]\frac{1}{2}^{+i}$	−0.15±0.03	−0.24±0.10	−0.01±0.06	−0.11±0.02	0.09±0.02	−0.16±0.02
$\nu[411]\frac{1}{2}^{-i}$	−0.12±0.02	0.06±0.06	−0.16±0.04	−0.06±0.02	−0.17±0.02	0.04±0.02
$\nu[411]\frac{3}{2}^{+i}$	−0.14±0.04	0.20±0.20	−0.26±0.12	−0.13±0.03	−0.02±0.03	−0.11±0.03
$\nu[411]\frac{3}{2}^{-i}$	−0.11±0.05	−0.05±0.24	−0.08±0.15	−0.11±0.03	0.02±0.03	−0.12±0.03
$\nu[413]\frac{5}{2}^{+i}$	−0.13±0.02	−0.05±0.10	−0.10±0.06	−0.13±0.03	−0.04±0.03	−0.10±0.03
$\nu[413]\frac{5}{2}^{-i}$	−0.12±0.03	−0.12±0.13	−0.05±0.08	−0.11±0.03	0.15±0.03	−0.20±0.03
$\nu[523]\frac{7}{2}^{+i}$	0.03±0.01	−0.00±0.05	0.03±0.03	0.05±0.01	0.00±0.01	0.04±0.01
$\nu[523]\frac{7}{2}^{-i}$	0.04±0.01	−0.01±0.05	0.05±0.03	0.01±0.02	−0.00±0.02	0.01±0.02
$\nu[530]\frac{1}{2}^{+i}$	0.22±0.01	−0.21±0.05	0.34±0.03	0.17±0.01	−0.09±0.01	0.22±0.01
$\nu[530]\frac{1}{2}^{-i}$	0.17±0.01	−0.01±0.05	0.18±0.03	0.19±0.01	0.10±0.01	0.13±0.01
$\nu[532]\frac{3}{2}^{+i}$	0.21±0.03	0.21±0.13	0.09±0.08	—	—	—
$\nu[532]\frac{3}{2}^{-i}$	0.17±0.03	0.03±0.13	0.15±0.08	—	—	—
$\nu[532]\frac{5}{2}^{+i}$	0.19±0.04	−0.08±0.20	0.24±0.12	0.17±0.03	−0.02±0.03	0.18±0.03
$\nu[532]\frac{5}{2}^{-i}$	0.24±0.04	−0.01±0.20	0.25±0.12	0.38±0.03	0.00±0.03	0.38±0.03
$\nu[541]\frac{1}{2}^{+i}$	0.35±0.03	−0.04±0.13	0.38±0.08	0.35±0.02	−0.00±0.02	0.35±0.03
$\nu[541]\frac{1}{2}^{-i}$	0.37±0.03	0.01±0.14	0.36±0.08	0.33±0.03	0.04±0.03	0.30±0.03
$\nu\ \mathbf{6}_1^{-i}$	0.38±0.01	0.21±0.03	0.26±0.02	0.40±0.01	0.12±0.01	0.33±0.01
$\nu\ \mathbf{6}_2^{+i}$	0.36±0.01	−0.01±0.04	0.37±0.03	0.36±0.01	−0.01±0.01	0.37±0.01
$\nu\ \mathbf{6}_3^{-i}$	0.34±0.05	−0.06±0.22	0.38±0.13	—	—	—
$\pi[301]\frac{1}{2}^{+i}$	0.51±0.05	−0.10±0.24	0.57±0.14	—	—	—
$\pi[404]\frac{9}{2}^{+i}$	−0.32±0.01	0.10±0.04	−0.38±0.02	−0.37±0.01	0.02±0.01	−0.38±0.01
$\pi[404]\frac{9}{2}^{-i}$	−0.31±0.01	0.09±0.04	−0.37±0.02	−0.37±0.01	0.02±0.01	−0.38±0.01
$\pi[411]\frac{3}{2}^{+i}$	−0.05±0.02	0.10±0.07	−0.10±0.05	—	—	—
$\pi[411]\frac{3}{2}^{-i}$	0.00±0.02	−0.22±0.07	0.12±0.04	—	—	—
$\pi[422]\frac{3}{2}^{+i}$	0.33±0.02	−0.27±0.10	0.48±0.06	0.33±0.03	−0.13±0.02	0.40±0.03
$\pi[422]\frac{3}{2}^{-i}$	0.34±0.02	0.14±0.10	0.25±0.06	0.28±0.02	0.16±0.02	0.19±0.02
$\pi[532]\frac{5}{2}^{+i}$	0.42±0.01	−0.05±0.05	−0.46±0.03	0.41±0.02	−0.04±0.01	0.43±0.02
$\pi[532]\frac{5}{2}^{-i}$	0.56±0.02	−0.07±0.09	0.60±0.05	0.54±0.04	0.05±0.03	0.51±0.04
$\pi[541]\frac{1}{2}^{-i}$	0.58±0.02	−0.01±0.10	0.59±0.06	—	—	—
$\pi[541]\frac{3}{2}^{+i}$	0.50±0.01	−0.05±0.06	0.52±0.04	0.48±0.01	−0.10±0.01	0.54±0.01
$\pi[541]\frac{3}{2}^{-i}$	0.57±0.01	−0.12±0.04	0.63±0.03	0.50±0.01	−0.10±0.01	0.56±0.01
$\pi[550]\frac{1}{2}^{-i}$	0.49±0.05	−0.06±0.22	0.52±0.14	0.46±0.04	−0.02±0.04	0.48±0.04

factor of $\frac{1}{\sqrt{3}}$, their lack of precision in some cases can be bad enough to seriously deteriorate the quality of q_t. With all these words of caution in mind, we can proceed with looking into the quantitative estimates for q_t, especially in light of the fact that in many cases the q_{22} can be viewed as smaller than the experimental error bars and thus irrelevant for direct comparison with current spectroscopic data.

One of the important features of Table 3.4 is the side–by–side comparison between the Skyrme HF and the Relativistic model.

3.4.3 Effective Angular Momenta of the Orbitals

The next stage in the analysis involves the evaluation and interpretation of the effective additive contributions to the total angular momentum. Table 3.5 shows effective single–particle angular momenta $i_\alpha^{\rm eff}$ of the Nilsson orbitals in our comparative analysis for both of the self–consistent models side by side.

A quick look at the values reveals the highest positive contributions, stemming from the neutron intruder states (several times higher then the others), the states ν [530]1/2 (both signatures), [411]$3/2^{+i}$, and π [541]$1/2^{-i}$, [541]$3/2^{+i}$. The biggest negative contributions come from the occupation of ν [523]7/2 (both signatures) and π [532]5/2 orbitals.

Table 3.5 displays the comparison of CHF mean values $\langle \hat{i} \rangle$ with their effective counterparts. The differences in these single–orbital contributions can be attributed to the presence of shape polarization effects, as in

$$i^{\rm eff} = i^{\rm bare} + i^{\rm pol}. \tag{3.12}$$

It is clear from the Table that the standard cranked shell model analysis, which is based on expectation values $\langle \hat{i} \rangle$ can often be quite misleading. Table 3.5 provides very valuable information for the analysis of experimental angular momentum alignments. The larger values of $i^{\rm pol}$ are unambiguous evidence that the use of $i^{\rm bare} = \langle i \rangle$ (for example derived from the slopes versus frequency of the single–particle Routhians) instead of $i^{\rm eff}$ can be very misleading indeed. Further analysis of the origins of $i^{\rm pol}$ would be in order, but this objective is outside the scope of this dissertation.

3.4.4 Comparison With ^{142}Sm — HF Consistency Across the Region

Our CHF calculations can be checked for consistency if we look at the region's borderline case of ^{142}Sm, a nuclide from the edge of the A$\simeq$150 superdeformation region. The additivity study in this heavier region [77], the results of which we compared with ours side by side in Table 3.3, although utilizing older versions of the Skyrme interaction, SkM* and SkP, are supposed to be compatible with ours.

Two highly–deformed bands in this nucleus have been observed so far : the *yrast* SD-1 (A) [212], and an excited SD-2 (B) [213]. The quadrupole moments in these bands have also been measured [214]. The study of ^{142}Sm is facilitated considerably (Fig. 3.9) by the closing of the neutron shell for N=80, which suggests that differences in superdeformed bands can be contributed to the occupation of proton orbitals. The assignment of the bands is with respect to the well–studied superdeformed band in the isotone ^{143}Eu [215], with intruder structure

$$|{\rm SD}(^{143}{\rm Eu})\rangle = \left(\nu 7^0 6^2_{\Omega=3/2}\right)\left(\pi 6^1_1\right). \tag{3.13}$$

Experimental evidence [212] suggests that in SD-1 (A) of ^{142}Sm the orbital π [541]1/2 with (π,r)=(−,+i) has a hole character.

Table 3.5: Effective single–particle angular momenta i^{eff} calculated in CHF and CRMF.

State $[\mathcal{N}n_z\Lambda]\Omega^r$	CHF+SLy4 $\langle\hat{i}\rangle$ ($\hbar$)	CHF+SLy4 i^{eff} ($\hbar$)	CRMF+NL1 i^{eff} ($\hbar$)
$\nu\ [402]\frac{5}{2}^{+i}$	–0.528	0.58 ±0.14	0.47 ±0.15
$\nu\ [402]\frac{5}{2}^{-i}$	–0.493	0.51 ±0.20	0.38 ±0.26
$\nu\ [411]\frac{1}{2}^{+i}$	0.411	0.67 ±0.24	0.64 ±0.17
$\nu\ [411]\frac{1}{2}^{-i}$	0.380	0.40 ±0.15	0.09 ±0.16
$\nu\ [411]\frac{3}{2}^{+i}$	–0.092	1.72 ±0.46	1.35 ±0.29
$\nu\ [411]\frac{3}{2}^{-i}$	0.077	0.56 ±0.57	1.08 ±0.29
$\nu\ [413]\frac{5}{2}^{+i}$	–0.316	–0.10 ±0.23	0.44 ±0.27
$\nu\ [413]\frac{5}{2}^{-i}$	–0.428	0.12 ±0.30	0.14 ±0.26
$\nu\ [523]\frac{7}{2}^{+i}$	–0.908	–1.10 ±0.10	–1.24 ±0.12
$\nu\ [523]\frac{7}{2}^{-i}$	–0.974	–1.19 ±0.12	–0.92 ±0.18
$\nu\ [530]\frac{1}{2}^{+i}$	1.548	1.19 ±0.11	1.86 ±0.09
$\nu\ [530]\frac{1}{2}^{-i}$	0.564	0.88 ±0.11	0.93 ±0.10
$\nu\ [532]\frac{3}{2}^{+i}$	0.171	–0.34 ±0.30	—
$\nu\ [532]\frac{3}{2}^{-i}$	0.835	0.44 ±0.31	—
$\nu\ [532]\frac{5}{2}^{+i}$	–0.331	–0.89 ±0.46	–0.95 ±0.29
$\nu\ [532]\frac{5}{2}^{-i}$	0.417	–1.06 ±0.46	–1.29 ±0.30
$\nu\ [541]\frac{1}{2}^{+i}$	1.793	0.92 ±0.31	0.95 ±0.25
$\nu\ [541]\frac{1}{2}^{-i}$	0.466	0.89 ±0.32	–0.34 ±0.28
$\nu\ \mathbf{6}_1^{-i}$	4.840	4.78 ±0.08	4.59 ±0.08
$\nu\ \mathbf{6}_2^{+i}$	4.031	3.42 ±0.11	3.15 ±0.10
$\nu\ \mathbf{6}_3^{-i}$	2.662	0.77 ±0.50	—
$\pi\ [301]\frac{1}{2}^{+i}$	–0.432	1.23 ±0.55	—
$\pi\ [404]\frac{9}{2}^{+i}$	–0.719	–0.00 ±0.09	0.09 ±0.09
$\pi\ [404]\frac{9}{2}^{-i}$	–0.719	–0.00 ±0.09	0.11 ±0.09
$\pi\ [411]\frac{3}{2}^{+i}$	–0.249	0.81 ±0.18	—
$\pi\ [411]\frac{3}{2}^{-i}$	–0.062	0.65 ±0.16	—
$\pi\ [413]\frac{5}{2}^{-i}$	–0.539	–1.52 ±0.53	—
$\pi\ [422]\frac{3}{2}^{+i}$	–0.315	–0.19 ±0.25	–0.21 ±0.27
$\pi\ [422]\frac{3}{2}^{-i}$	0.510	–0.84 ±0.23	–0.38 ±0.24
$\pi\ [532]\frac{5}{2}^{+i}$	–0.253	–0.90 ±0.13	–1.11 ±0.16
$\pi\ [532]\frac{5}{2}^{-i}$	–0.022	–0.67 ±0.20	–3.25 ±0.38
$\pi\ [541]\frac{1}{2}^{-i}$	0.944	1.75 ±0.23	—
$\pi\ [541]\frac{3}{2}^{+i}$	1.743	1.57 ±0.13	1.18 ±0.11
$\pi\ [541]\frac{3}{2}^{-i}$	–0.057	–0.54 ±0.10	–0.48 ±0.11
$\pi\ [550]\frac{1}{2}^{-i}$	2.819	2.99 ±0.52	2.86 ±0.40

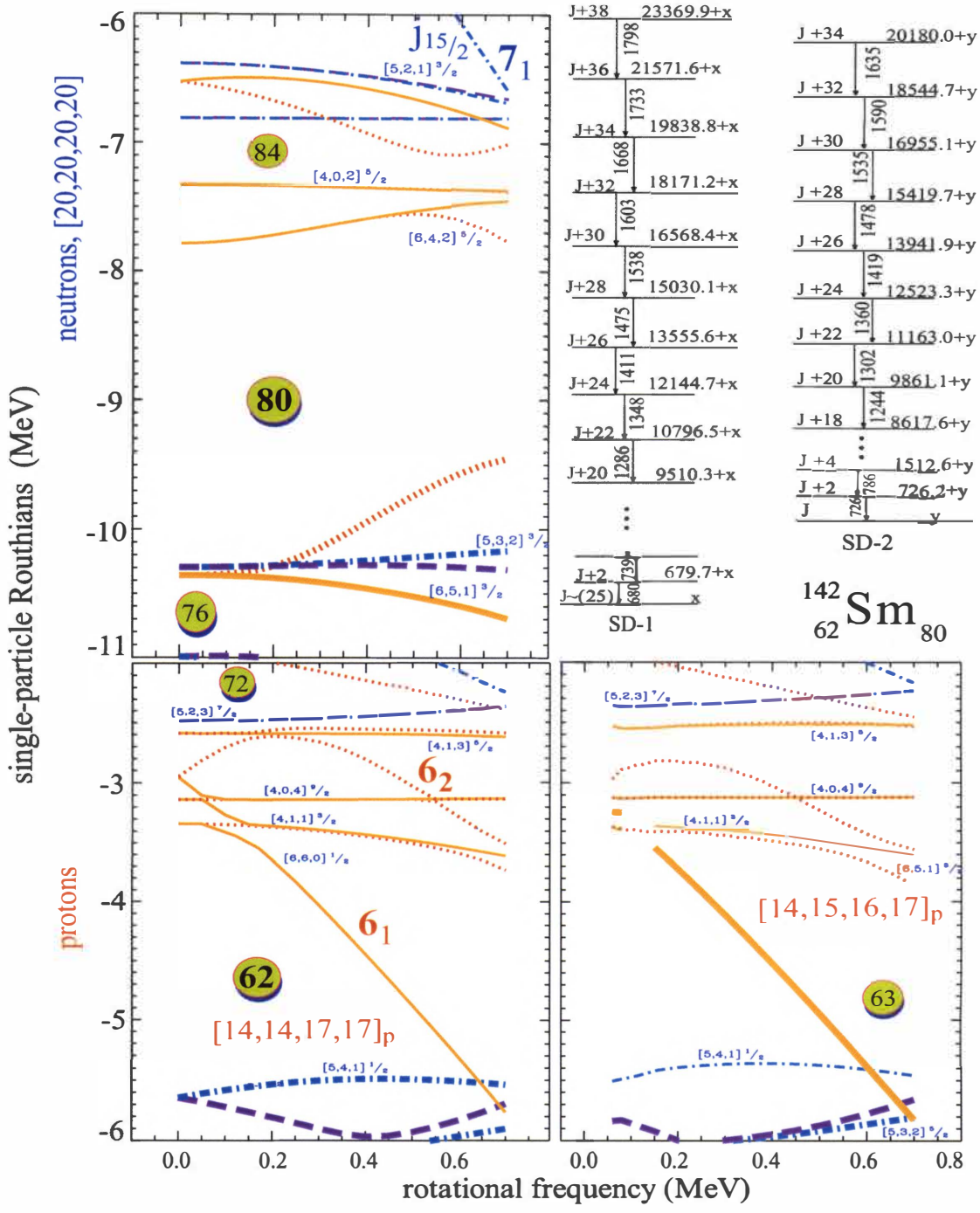

Figure 3.9: Routhian diagrams for superdeformed bands SD-1,2 in ^{142}Sm. The bands are offset in energy by the difference in their total Routhians at $\hbar\omega$=0.65 MeV.

The total angular momentum of band SD-1 (A) at $\hbar\omega$=0.65 MeV is predicted to be I=43.25 $\hbar$. Experimentally, $I = I_0 + 21.45\ \hbar$, where I_0 has the suggested value of 25 $\hbar$. This gives a total of 46.454 units at frequency 0.65 MeV. Similarly, for band SD-2 (B) our calculations yield 47.28 $\hbar$ at 0.65 MeV, thus suggesting that it is reasonable to assume the bandhead to have approximately 26 $\hbar$.

The main reason for our interest in ^{142}Sm is the comparison with its transition quadrupole moment within the additivity model. The inset of Fig. 1.3 illustrates that both of the assigned superdeformed bands in this nucleus are very close to the experimental best estimates, being within (or just outside) the error bars. Our result for configuration A is Q^{π}_{20}=12.12 eb, which compares well with the experimentally–measured value of (11.7±0.1) eb [214]. The corresponding value for configuration B at 12.07 eb is visibly lower than the measured value of ($13.2^{+0.8}_{-0.7}$) eb, but the difference is comparable with the error bar.

The comparison lends credibility to the validity of our CHF framework and indicates that the model could be applied easily to the study of heavier superdeformed systems.

3.5 Example Cases of SD Bands

In this Section we analyze in more detail some of the experimentally–observed superdeformed bands in the A≃130 region. The existence of energy gaps for particle numbers Z=58 and N=72, 73 make the nuclei with fewest differences from our core case of ^{131}Ce convenient starting points for studying the effects of the levels immediately below and above the gaps.

The Cerium Isotopes

The Cerium isotopes are the perfect study platform for the investigation of the relative effects of the first neutron $\mathcal{N}$=6 intruder orbital in comparison with the other states around the N=72 gap, which turns into the, from our perspective, more significant gap of N=73 for frequencies above 0.3 MeV.

In the proton sector, the wide energy separation in energy between the π ($h_{11/2}$) [541]3/2 (with r=–i), and the unsplit pair of ($g_{9/2}$) [404]9/2 extruder states, which stabilizes the Cerium proton configurations at low frequencies, gradually decreases down to less than 1 MeV around the rotational frequency region of interest of 0.65 MeV. This implies that excitations across this gap must be considered in addition to the neutron excitations. In the highest frequency range, the π ($h_{9/2}$) [541]1/2 (r=–i) state is in the immediate vicinity of the core's Fermi level, and above $\hbar\omega$ ≃1.1 MeV we see the appearance of the first proton $\mathcal{N}$=6 intruder. These proton Routhian structures are very important, but they occur at frequencies perhaps too high above the bands seen experimentally, and we exclude them for the purposes of this study. The most of what we can see is a hint of the interaction in the (–,–i) parity–signature block between the proton [541] states from the $h_{11/2}$ and $h_{9/2}$ Nilsson levels with Ω=3/2 and 1/2, respectively, which changes the rotational slope of the occupied orbital.

^{130}Ce

The experimental studies of the rotational bands of the Cerium isotope with N=72 have resulted in the discovery of four highly–deformed bands [216, 217], referred to in the present nomenclature as SD-1 (1a), [2] SD-2 (2a), SD-3 (1b), and SD-4 (2b) [51, 53].

[2] The notations in the parentheses are according to the older of the two systematics.

Table 3.6: Some of the CHF+SLy4 configurations in ^{130}Ce.

$E_\omega - E_\omega^{\min}$ (MeV)	$[N_{+,+i}, N_{+,-i}, N_{-,+i}, N_{-,-i}]$	Q_{20}^{π} (eb)	Q_{22}^{π} (eb)	I ($\hbar$)	Band configiration w/respect to $\|\mathbf{core}\rangle$
		$\boxed{^{130}\mathrm{Ce}}$			
	(π,r)=(+,−1)				
1.31	$[17,19,18,18]_n[14,14,15,15]_p$	7.89	0.25	37.26	$(\nu[411]1/2+)^{-1}$
0.68	$[18,19,17,18]_n[14,15,15,14]_p$	6.82	0.30	39.28	$(\nu[523]7/2+)^{-1}$ $(\pi[404]9/2-)(\pi[541]3/2-)^{-1}$
0.65	$[18,19,18,17]_n[15,14,15,14]_p$	6.81	0.30	39.49	$(\nu[523]7/2-)^{-1}$ $(\pi[404]9/2+)(\pi[541]3/2-)^{-1}$
	(π,r)=(+, 1)				
0.56	$[18,19,17,18]_n[15,14,15,14]_p$	6.81	0.31	39.49	$(\nu[523]7/2+)^{-1}$ $(\pi[404]9/2+)(\pi[541]3/2-)^{-1}$
0.53	$[18,19,18,17]_n[14,15,15,14]_p$	6.81	0.30	39.68	$(\nu[523]7/2-)^{-1}$ $(\pi[404]9/2-)(\pi[541]3/2-)^{-1}$
0.47	$[18,18,18,18]_n[14,14,15,15]_p$	7.35	0.07	32.86	$(\nu\mathbf{6}_1-)^{-1}$
	(π,r)=(−,+1)				
0.60	$[18,18,18,18]_n[14,15,15,14]_p$	6.53	0.18	32.84	$(\nu\mathbf{6}_1-)^{-1}$ $(\pi[404]9/2-)(\pi[541]3/2-)^{-1}$
0.01	$[18,19,18,17]_n[14,14,15,15]_p$	7.76	0.19	37.74	$(\nu[523]7/2-)^{-1}$
	(π,r)=(−,−1)				
1.36	$[18,19,18,17]_n[14,14,16,14]_p$	7.52	0.21	38.70	$(\nu[523]7/2-)^{-1}$ $(\pi[532]5/2+)(\pi[541]3/2-)^{-1}$
0.00	$[18,19,17,18]_n[14,14,15,15]_p$	7.74	0.20	38.31	$(\nu[523]7/2+)^{-1}$

The Total Routhian Sirface (TRS) calculations [218, 159, 219] for the positive parity r=1 configurations of this isotope show a relatively soft, low–frequency second minimum for quadrupole deformations of $\beta_2 \simeq 0.35$ without any $\mathcal{N}$=6 neutrons. The appearance of the intruder, at higher frequencies leads to a small increase in β to about 0.37, making its occupation energetically favorable, which justifies the assignment of the observed bands to yrast ν 6_1 structures [217]. The experimental results indicated that bands SD-1 (1a) and SD-3 (1b) are most likely signature partners with two–quasiparticle configurations $\nu 6^1 \otimes [411]1/2$ ($r = \pm 1$).

Table 3.6 shows some of the lowest configurations in each of the parity–signature blocks for this nucleus. Band SD-1 is most likely built on the nucleonic configuration with r=+1, corresponding in our notations to $|\mathbf{SD\text{-}1}\rangle = (\nu(2d_{3/2})[411]1/2^{-i})^{-1}\,|\mathbf{core}\rangle$, and its partner with r=−1 is : $|\mathbf{SD\text{-}3}\rangle = (\nu(2d_{3/2})[411]1/2^{+i})^{-1}\,|\mathbf{core}\rangle$. The latter of them is shown in Fig. 3.10, next to the single–neutron Routhian diagram. The de–occupied state ν [411]1/2, 18-th in the (+,+i) parity–signature block, is shifted upwards in energy, which reduces its interaction with the underlying 17-th state [413]5/2, which remains parallel to it without crossing at lower frequency. The total angular momentum at cranking frequency $\hbar\omega$=0.65 MeV for SD-3 is 37.26

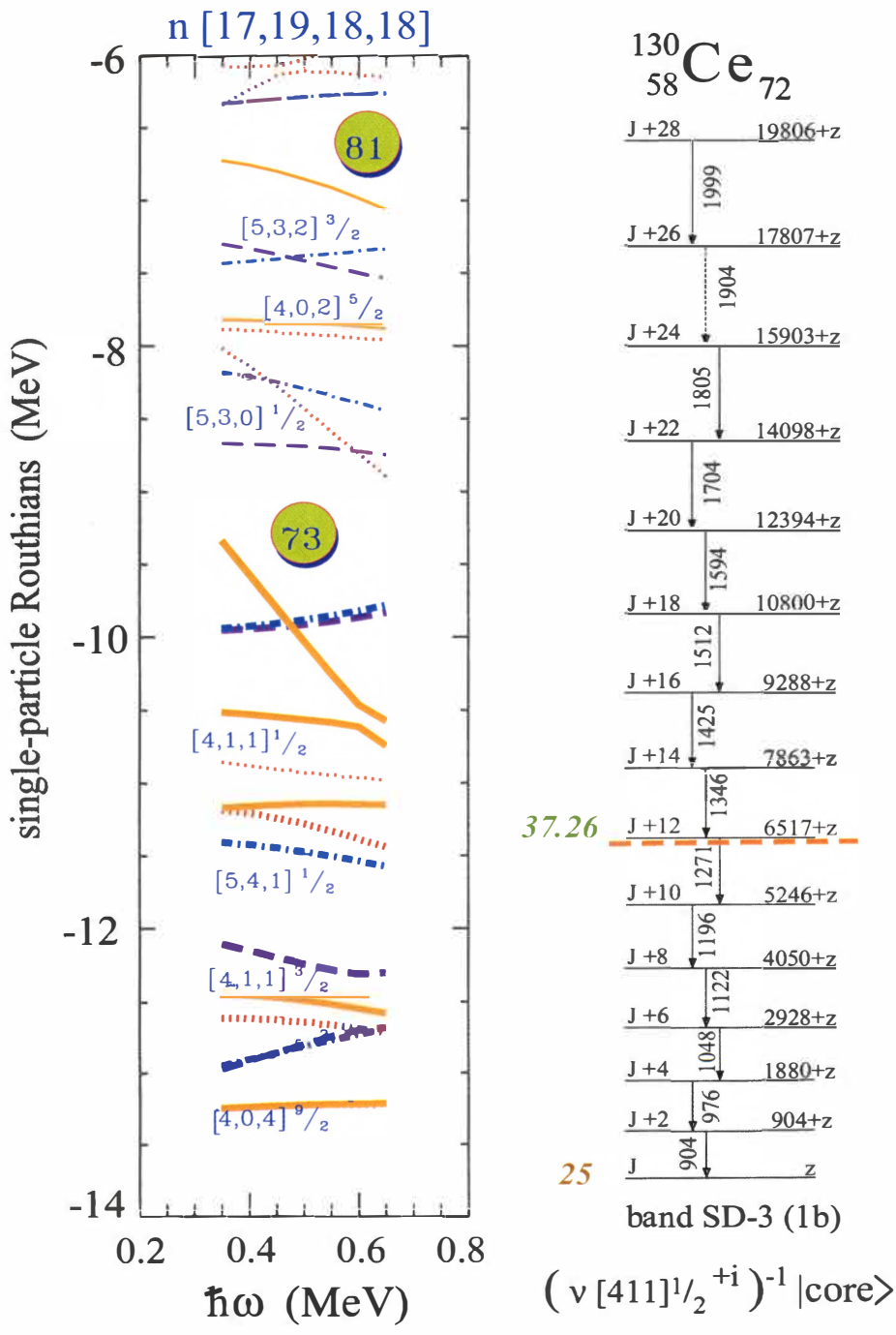

Figure 3.10: Neutron Routhians corresponding to band SD-3 in ^{130}Ce.

$\hbar$, suggesting 25 units for the bandhead. The signature partner (SD-1) of this band has a level crossing in the (+,–i) parity–signature block at frequency 0.65 MeV, so it had to be excluded from the additivity analysis.

The other two superdeformed bands in this isotope, SD-2 (2a) and SD-4 (2b), are also assumed to be signature partners, built on the 2–quasiparticle configurations $|\mathbf{SD\text{-}3}\rangle = (\nu(1h_{11/2})$ $[523]1/2^{\pm i})^{-1}\,|\mathbf{core}\rangle$. In our calculations these negative–parity bands are degenerate, and appear to be the lowest in total Routhians among all the other bands. Figure 3.11 shows the calculated Routhian diagrams for the partner with hole in the ν $[523]7/2^{-i}$ orbital. The two candidates lowest in total Routhian involve the proton core (part a.), and the proton configuration with a particle–hole across the vanishing Z=58 gap to one of the [404]9/2 extruder orbitals (part b.). The de–occupation of π $[541]3/2^{-i}$ and the occupation of the extruder instead leads to an overall *decrease* of the quadrupole deformation, which is sufficient for considerable rearrangements of the neutron orbitals. The less–prolate nuclear shape pushes upwards the ν [530]1/2 levels and lowers the [402]5/2 ones (*cf.* Figs. 3.7,3.8), leading to their interchange. The intruder 6_2 shifts higher above the N=73 gap, becoming less accessible for particle–hole excitations, and the occupied states ν [541]1/2 rise closer to the Fermi level.

The excited configuration is only about 0.5 MeV higher than the lowest, so it must be taken into consideration in the interpretation of the bands SD-2,4. From Table 3.6 we obtain the total angular momenta for the two partners at frequency $\hbar\omega$=0.65 MeV. For $(\nu(1h_{11/2})[523]1/2^{-i})^{-1}$ $|\mathbf{core}\rangle$ it is 37.74 $\hbar$, and for its partner 38.31 $\hbar$, while the proton excitation increases them by nearly 2 units. The calculation of the phenomenological frequencies places the bandhead 14 units below these values, suggesting for SD-2 a bandhead angular momentum of 13.7 for the r=–i two–quasiparticle hole.

The following Tables 3.7–3.15 present the other calculated configurations in the region.

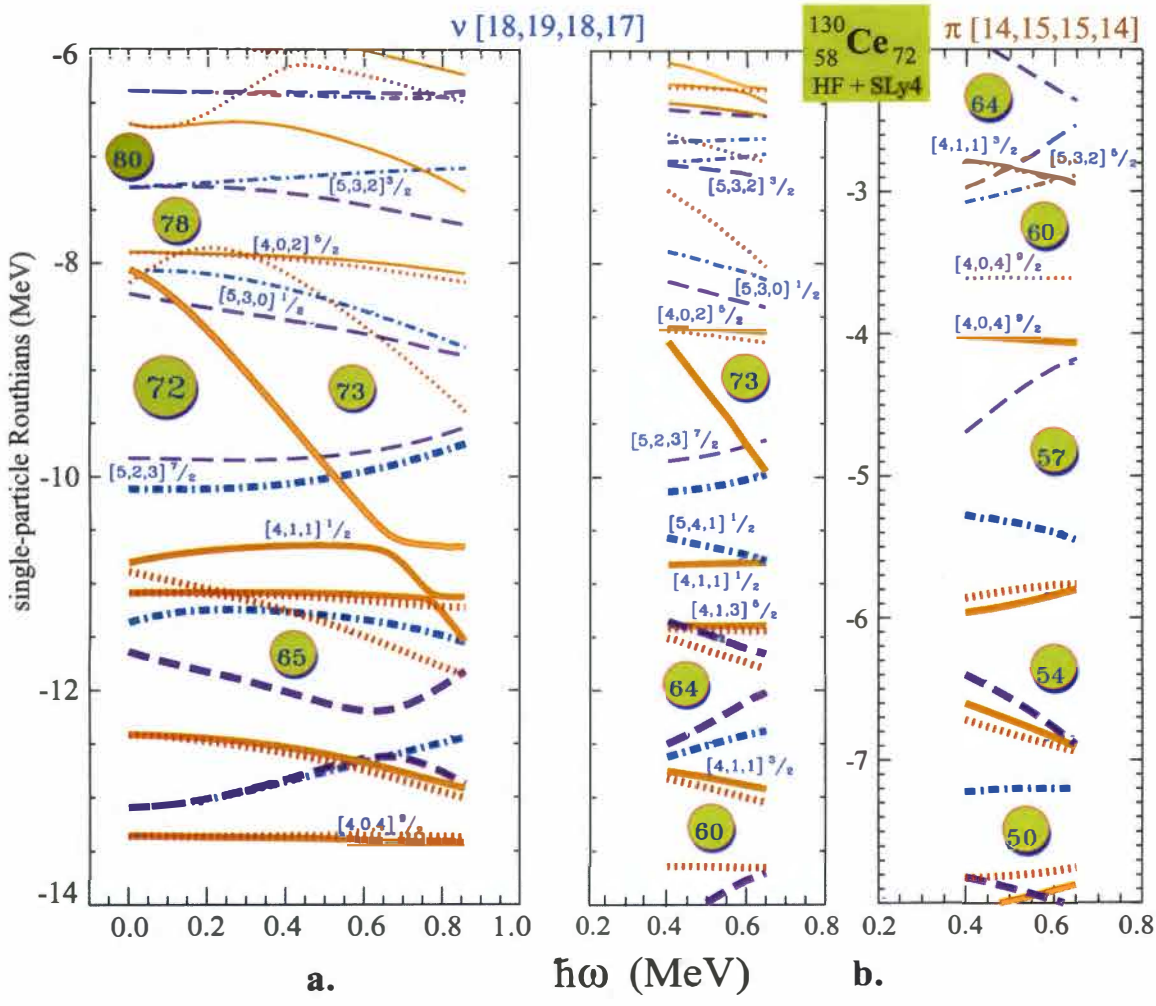

Figure 3.11: Single–particle Routhians of the two lowest candidates for the r=1 bands SD-2,4 in ^{130}Ce. Part **a.** shows the neutron sector of the configuration compared with one involving a proton p–h excitation to a $g_{9/2}$ extruder state (part **b.**).

Table 3.7: The CHF+SLy4 configurations in ^{132,134}Ce.

$E_\omega - E_\omega^{\text{core}}$ (MeV)	$[N_{+,+i}, N_{+,-i}, N_{-,+i}, N_{-,-i}]$	Q_{20}^π (eb)	Q_{22}^π (eb)	I ($\hbar$)	Band configiration w/respect to $\lvert$**core**$\rangle$
		^{132}Ce			
	(π,r)=(+,-1), α= 1				
3.53	$[19,18,18,19]_n[14,15,14,15]_p$	6.42	0.21	32.56	$(\nu\mathbf{6}_1\text{-})^{-1}$ $(\nu[402]5/2+)$ $(\nu[530]1/2\text{-})$ $(\pi[404]9/2\text{-})$ $(\pi[541]3/2+)^{-1}$
	(π,r)=(–, 1), α= 0				
1.30	$[19,19,18,18]_n[14,15,15,14]_p$	7.18	0.29	41.81	$(\nu\mathbf{6}_2+)$ $(\pi[541]3/2\text{-})^{-1}$ $(\pi[404]9/2\text{-})$
0.19	$[18,19,19,18]_n[14,14,15,15]_p$	7.97	0.07	38.69	$(\nu[530]1/2+)$
	(π,r)=(–,–1), α= –1				
1.44	$[19,18,19,18]_n[14,14,15,15]_p$	8.46	-0.15	41.56	$(\nu\mathbf{6}_2+)(\nu[530]1/2+)$ $(\nu[411]1/2\text{-})^{-1}$
0.10	$[18,19,18,19]_n[14,14,15,15]_p$	7.92	0.27	38.29	$(\nu[530]1/2\text{-})$
	(π,r)=(+, 1), α= 0				
3.64	$[19,18,19,18]_n[14,15,14,15]_p$	6.48	0.06	32.77	$(\nu\mathbf{6}_1\text{-})^{-1}(\nu[530]1/2+)$ $(\nu[402]5/2+)(\pi[404]9/2\text{-})$ $([541]3/2+)^{-1}$
1.97	$[18,18,19,19]_n[14,14,15,15]_p$	7.79	-0.09	35.32	$(\nu\mathbf{6}_1\text{-})^{-1}$ $(\nu[530]1/2\text{-})(\nu[530]1/2+)$
0.90	$[19,19,18,18]_n[14,14,15,15]_p$	8.29	0.26	41.77	$(\nu\mathbf{6}_2+)(\nu[523]7/2\text{-})^{-1}$ $(\nu[530]1/2\text{-})$
0.00	$[19,19,18,18]_n[14,14,15,15]_p$	8.15	0.18	40.40	$(\nu\mathbf{6}_2+)$
		^{134}Ce			
	(π,r)=(–, 1), α= 0				
1.53	$[18,19,20,19]_n[14,14,15,15]_p$	8.35	0.23	39.33	$(\nu[530]1/2+)(\nu[530]1/2\text{-})$ $(\nu[532]3/2+)$
	(π,r)=(–,–1), α= 1				
1.18	$[18,19,19,20]_n[14,14,15,15]_p$	8.31	0.06	40.19	$(\nu[530]1/2+)(\nu[530]1/2\text{-})$ $(\nu[532]3/2\text{-})$
	(π,r)=(+,–1), α= 1				
1.46	$[19,19,20,18]_n[14,14,15,15]_p$	8.55	0.15	41.50	$(\nu\mathbf{6}_2+)(\nu[530]1/2+)$ $(\nu[532]3/2+)$
1.11	$[19,19,18,20]_n[14,14,15,15]_p$	8.46	0.17	41.95	$(\nu\mathbf{6}_2+)(\nu[530]1/2\text{-})$ $(\nu[532]3/2\text{-})$
	(π,r)=(+, 1), α= 0				
1.56	$[19,19,19,19]_n[14,14,15,15]_p$	8.46	0.15	45.76	$(\nu\mathbf{6}_2+)$ $(\nu[530]1/2\text{-})(\nu[530]1/2+)$ $(\pi[541]3/2\text{-})^{-1}(\pi[541]1/2\text{-})$
0.00	$[19,19,19,19]_n[14,14,15,15]_p$	8.49	0.10	42.53	$(\nu\mathbf{6}_2+)$ $(\nu[530]1/2\text{-})(\nu[530]1/2+)$

Table 3.8: The CHF+SLy4 configurations in ^{133}Ce.

$E_\omega - E_\omega^{\rm core}$ (MeV)	$[N_{+,+i}, N_{+,-i}, N_{-,+i}, N_{-,-i}]$	Q_{20}^π (eb)	Q_{22}^π (eb)	I ($\hbar$)	Band configiration w/respect to |core⟩
		$\boxed{^{133}\mathbf{Ce}}$			
	(π, r)=(+,+i), α= −1/2				
1.64	$[18,19,20,18]_n[14,14,15,15]_p$	8.17	0.17	38.56	(ν[530]1/2+)(ν[532]3/2+)
1.61	$[19,19,19,18]_n[14,15,15,14]_p$	7.40	0.14	43.04	($\nu\mathbf{6}_2$+)(ν[530]1/2+) (π[541]3/2-)$^{-1}$(π[404]9/2-)
1.15	$[18,19,18,20]_n[14,14,15,15]_p$	8.08	0.18	38.99	(ν[530]1/2-)(ν[532]3/2-)
	(π, r)=(+,−i), α= 1/2				
1.61	$[19,19,19,18]_n[15,14,15,14]_p$	7.40	0.14	43.05	($\nu\mathbf{6}_2$+)(ν[530]1/2+) (π[541]3/2-)$^{-1}$(π[404]9/2+)
1.57	$[19,19,18,19]_n[14,15,15,14]_p$	7.30	0.39	42.62	($\nu\mathbf{6}_2$+)(ν[530]1/2-) (π[541]3/2-)$^{-1}$(π[404]9/2-)
1.51	$[19,20,18,18]_n[14,14,15,15]_p$	8.46	0.13	41.71	($\nu\mathbf{6}_2$+)($\nu\mathbf{6}_3$-)
0.32	$[18,19,19,19]_n[14,14,15,15]_p$	8.14	0.10	39.48	(ν[530]1/2+)(ν[530]1/2-)
	(π, r)=(−,−i), α= 1/2				
1.68	$[19,19,18,19]_n[14,14,15,15]_p$	8.27	0.33	44.83	($\nu\mathbf{6}_2$+)(ν[530]1/2-) (π[541]3/2-)$^{-1}$(π[541]1/2-)
1.66	$[19,19,18,19]_n[14,14,15,15]_p$	8.07	0.28	41.74	($\nu\mathbf{6}_2$+)(ν[530]1/2-) (π[541]3/2-)$^{-1}$(π[532]5/2+)
1.66	$[19,19,19,18]_n[14,14,16,14]_p$	8.12	0.04	42.15	($\nu\mathbf{6}_2$+)(ν[530]1/2+) (π[541]3/2-)$^{-1}$(π[532]5/2+)
0.02	$[19,19,18,19]_n[14,14,15,15]_p$	8.29	0.26	41.23	($\nu\mathbf{6}_2$+)(ν[530]1/2-)
	(π, r)=(−, i), α= −1/2				
1.62	$[19,19,19,18]_n[14,14,15,15]_p$	8.29	0.07	44.48	($\nu\mathbf{6}_2$+)(ν[530]1/2+) (π[541]3/2-)$^{-1}$(π[541]1/2-)
0.00	$[19,19,19,18]_n[14,14,15,15]_p$	8.34	0.05	41.74	($\nu\mathbf{6}_2$+)(ν[530]1/2+)

Table 3.9: The CHF+SLy4 configurations in ^{130,131}Pr.

$E_\omega - E_\omega^{\text{core}}$ (MeV)	$[N_{+,+i},N_{+,-i},N_{-,+i},N_{-,-i}]$	Q_{20}^{π} (eb)	Q_{22}^{π} (eb)	I ($\hbar$)	Band configiration w/respect to $\|\mathbf{core}\rangle$
		^{130}Pr			
	(π,r)=(+,−1), α= 1				
1.17	$[18,17,18,18]_n[15,14,15,15]_p$	7.14	0.17	32.66	$(\nu\mathbf{6}_1\text{-})^{-1}(\nu[411]1/2\text{-})^{-1}$ $(\pi[404]9/\mathbf{2}+)$
	(π,r)=(−,−1), α= 1				
1.22	$[18,17,18,18]_n[15,15,15,14]_p$	6.27	0.47	33.22	$(\nu\mathbf{6}_1\text{-})^{-1}(\nu[411]1/2\text{-})^{-1}$ $(\pi[404]9/2+)(\pi[404]\mathbf{9}/2\text{-})$ $(\pi[541]3/2\text{-})^{-1}$
0.12	$[18,18,18,17]_n[15,14,15,15]_p$	7.00	0.09	33.93	$(\nu\mathbf{6}_1\text{-})^{-1}(\nu[523]7/2\text{-})^{-1}$ $(\pi[404]9/2+)$
0.12	$[18,18,17,18]_n[14,15,15,15]_p$	7.01	0.10	33.75	$(\nu\mathbf{6}_1\text{-})^{-1}(\nu[523]7/2+)^{-1}$ $(\pi[404]9/2\text{-})$
	(π,r)=(−,+1), α= 0				
0.01	$[18,18,18,17]_n[14,15,15,15]_p$	6.99	0.09	34.10	$(\nu\mathbf{6}_1\text{-})^{-1}(\nu[523]7/2\text{-})^{-1}$ $(\pi[404]9/2\text{-})$
0.00	$[18,18,17,18]_n[15,14,15,15]_p$	7.00	0.10	33.99	$(\nu\mathbf{6}_1\text{-})^{-1}(\nu[523]7/2+)^{-1}$ $(\pi[404]9/2+)$
		^{131}Pr			
	(π,r)=(+,−i), α= 1/2				
0.39	$[18,18,18,18]_n[14,15,15,15]_p$	7.04	0.08	32.73	$(\nu\mathbf{6}_1\text{-})^{-1}(\pi[404]9/2\text{-})$
	(π,r)=(+,+i), α=−1/2				
2.90	$[19,17,18,18]_n[14,15,15,15]_p$	7.50	0.00	35.97	$(\nu\mathbf{6}_1\text{-})^{-1}(\nu\mathbf{6}_2+)$ $(\nu[411]1/2\text{-})^{-1}(\pi[404]9/2\text{-})$
0.39	$[18,18,18,18]_n[15,14,15,15]_p$	7.04	0.08	32.75	$(\nu\mathbf{6}_1\text{-})^{-1}(\pi[404]9/2+)$
	(π,r)=(−,+i), α=−1/2				
2.84	$[19,17,18,18]_n[14,14,15,16]_p$	8.99	0.10	41.94	$(\nu\mathbf{6}_2+)(\nu[411]1/2\text{-})^{-1}$ $(\nu[413]5/2\text{-})^{-1}(\pi[541]1/2\text{-})$
1.96	$[19,17,18,18]_n[14,14,15,16]_p$	8.47	0.19	38.27	$(\nu[413]5/2+)^{-1}(\pi[532]5/2\text{-})$
1.52	$[19,17,18,18]_n[14,14,15,16]_p$	7.59	0.32	37.20	$(\nu[413]5/2+)^{-1}(\pi[404]9/2\text{-})$
1.24	$[18,18,18,18]_n[14,14,16,15]_p$	7.78	0.01	32.16	$(\nu\mathbf{6}_1\text{-})^{-1}(\pi[532]5/2+)$
0.38	$[18,18,18,18]_n[15,15,15,14]_p$	6.22	0.23	32.89	$(\nu\mathbf{6}_1\text{-})^{-1}(\pi[541]3/2\text{-})^{-1}$ $(\nu[404]9/2\text{-})(\pi[404]9/2+)$
	(π,r)=(−,−i), α= 1/2				
1.56	$[18,18,18,18]_n[15,15,14,15]_p$	6.22	0.22	31.48	$(\nu\mathbf{6}_1\text{-})(\pi[541]3/2+)^{-1}$ $(\nu[404]9/2\text{-})(\pi[404]\mathbf{9}/2+)$
0.00	$[18,19,17,18]_n[15,14,15,15]_p$	7.43	0.24	38.49	$(\nu[523]7/2+)^{-1}(\pi[404]9/2+)$

Table 3.10: The CHF+SLy4 configurations in ^{132,133}Pr.

$E_\omega - E_\omega^{\text{core}}$ (MeV)	$[N_{+,+i}, N_{+,-i}, N_{-,+i}, N_{-,-i}]$	Q_{20}^{π} (eb)	Q_{22}^{π} (eb)	I ($\hbar$)	Band configiration w/respect to $\|\mathbf{core}\rangle$
		^{132}Pr			
	(π,r)=(–,–1), α= 1				
1.87	$[18,18,18,19]_n[14,15,15,15]_p$	7.22	0.10	33.65	$(\nu\mathbf{6}_1\text{-})^{-1}(\nu[530]1/2\text{-})$ $(\pi[404]9/2\text{-})$
1.72	$[18,18,19,18]_n[15,14,15,15]_p$	7.27	-0.05	33.88	$(\nu\mathbf{6}_1\text{-})^{-1}(\nu[530]1/2\text{+})$ $(\pi[404]9/2\text{+})$
	(π,r)=(–, 1), α= 0				
1.87	$[18,18,18,19]_n[15,14,15,15]_p$	7.22	0.09	33.67	$(\nu\mathbf{6}_1\text{-})^{-1}(\nu[530]1/2\text{-})$ $(\pi[404]9/2\text{+})$
1.73	$[18,18,19,18]_n[14,15,15,15]_p$	7.27	-0.05	33.88	$(\nu\mathbf{6}_1\text{-})^{-1}(\nu[530]1/2\text{+})$ $(\pi[404]9/2\text{-})$
1.02	$[19,19,17,18]_n[15,14,15,15]_p$	7.84	0.22	41.18	$(\nu\mathbf{6}_2\text{+})(\nu[523]7/2\text{+})^{-1}$ $(\pi[404]9/2\text{+})$
	(π,r)=(+,–1), α= 1				
1.39	$[19,18,18,18]_n[15,14,15,15]_p$	6.72	0.08	33.04	$(\nu\mathbf{6}_1\text{-})^{-1}(\nu[402]5/2\text{+})$ $(\pi[404]9/2\text{+})$
0.00	$[18,19,18,18]_n[14,15,15,15]_p$	7.45	0.23	37.53	$(\pi[404]9/2\text{-})$
	(π,r)=(+,+1), α= 0				
1.39	$[19,18,18,18]_n[14,15,15,15]_p$	6.73	0.08	33.01	$(\nu\mathbf{6}_1\text{-})^{-1}(\nu[402]5/2\text{+})$ $(\pi[404]9/2\text{-})$
0.00	$[18,19,18,18]_n[15,14,15,15]_p$	7.45	0.23	37.53	$(\pi[404]9/2\text{+})$
		^{133}Pr			
	(π,r)=(+, i), α=–1/2				
0.31	$[18,19,19,18]_n[14,14,16,15]_p$	8.39	0.02	37.99	$(\nu[530]1/2\text{+})(\pi[532]5/2\text{+})$
	(π,r)=(–, i), α=–1/2				
0.16	$[19,19,18,18]_n[14,14,16,15]_p$	8.58	0.14	39.66	$(\nu\mathbf{6}_2\text{+})(\pi[532]5/2\text{+})$
0.08	$[18,19,18,19]_n[14,15,15,15]_p$	7.62	0.31	38.30	$(\nu[530]1/2\text{-})(\pi[404]9/2\text{-})$
	(π,r)=(–,–i), α= 1/2				
0.16	$[18,19,19,18]_n[14,15,15,15]_p$	7.67	0.08	38.72	$(\nu[530]1/2\text{+})(\pi[404]9/2\text{-})$
0.07	$[19,19,18,18]_n[14,14,15,16]_p$	8.73	0.12	41.97	$(\nu\mathbf{6}_2\text{+})(\pi[532]5/2\text{-})$
	(π,r)=(+,–i), α= 1/2				
1.12	$[19,19,18,18]_n[14,15,15,15]_p$	6.41	0.07	33.49	$(\nu\mathbf{6}_1\text{-})^{-1}(\pi[404]9/2\text{-})$ $(\nu[402]5/2\text{+})(\pi[402]5/2\text{-})$
0.25	$[18,19,18,19]_n[14,14,16,15]_p$	8.35	0.24	37.39	$(\nu[530]1/2\text{-})(\pi[532]5/2\text{+})$
0.06	$[19,19,18,18]_n[14,15,15,15]_p$	7.12	0.30	37.95	$(\nu[402]5/2\text{+})(\pi[404]9/2\text{-})$
0.05	$[19,19,18,18]_n[14,15,15,15]_p$	7.12	0.30	37.97	$(\nu[402]5/2\text{+})(\pi[404]9/2\text{+})$
0.00	$[19,19,18,18]_n[14,15,15,15]_p$	7.84	0.21	40.46	$(\nu\mathbf{6}_2\text{+})(\pi[404]9/2\text{-})$

Table 3.11: The CHF+SLy4 configurations in ^{132,133}Nd.

$E_\omega - E_\omega^{\text{core}}$ (MeV)	$[N_{+,+i}, N_{+,-i}, N_{-,+i}, N_{-,-i}]$	Q_{20}^{π} (eb)	Q_{22}^{π} (eb)	I ($\hbar$)	Band configiration w/respect to $\|\mathbf{core}\rangle$
		^{132}Nd			
	(π,r)=(+,–1), α= 1				
1.37	$[18,18,18,18]_n[15,15,16,14]_p$	6.60	0.14	32.25	$(\nu\mathbf{6}_1\text{-})^{-1}$ $(\pi[532]5/2+)(\pi[541]3/2\text{-})^{-1}$ $(\pi[404]9/2+)(\pi[404]9/2\text{-})$
	(π,r)=(+, 1), α= 0				
0.20	$[18,18,18,18]_n[15,15,15,15]_p$	6.72	0.11	32.78	$(\nu\mathbf{6}_1\text{-})^{-1}$ $(\pi[404]9/2+)(\pi[404]9/2\text{-})$
	(π,r)=(–,–1), α= 1				
0.00	$[18,19,17,18]_n[15,15,15,15]_p$	7.12	0.29	38.56	$(\nu[523]7/2+)^{-1}$ $(\pi[404]9/2+)(\pi[404]9/2\text{-})$
		^{133}Nd			
	(π,r)=(–,–i), α= 1/2				
1.89	$[18,18,18,19]_n[15,15,15,15]_p$	6.89	0.12	33.71	$(\nu\mathbf{6}_1\text{-})^{-1}(\nu[530]1/2\text{-})$ $(\pi[404]9/2+)(\pi[404]9/2\text{-})$
	(π,r)=(–, i), α=–1/2				
1.72	$[18,18,19,18]_n[15,15,15,15]_p$	6.95	-0.04	33.97	$(\nu\mathbf{6}_1\text{-})^{-1}(\nu[530]1/2+)$ $(\pi[404]9/2+)(\pi[404]9/2\text{-})$
1.21	$[19,18,18,18]_n[15,16,15,14]_p$	5.91	0.21	33.62	$(\nu\mathbf{6}_1\text{-})^{-1}(\nu[402]5/2+)$ $(\pi[541]3/2\text{-})^{-1}(\pi[411]3/2\text{-})$ $(\pi[404]9/2+)(\pi[404]9/2\text{-})$
	(π,r)=(+,–i), α= 1/2				
1.16	$[19,20,18,18]_n[15,15,15,15]_p$	5.89	0.27	33.77	$(\nu\mathbf{6}_1\text{-})^{-1}(\nu[402]5/2\text{-})$ $(\pi[541]3/2\text{-})^{-1}(\pi[411]3/2\text{-})$ $(\pi[404]9/2+)(\pi[404]9/2\text{-})$
0.00	$[18,19,18,18]_n[15,15,15,15]_p$	7.13	0.29	37.67	$(\pi[404]9/2+)(\pi[404]9/2\text{-})$

Table 3.12: The CHF+SLy4 configurations in ^{134,135}Nd.

$E_\omega - E_\omega^{\text{core}}$ (MeV)	$[N_{+,+i}, N_{+,-i}, N_{-,+i}, N_{-,-i}]$	Q_{20}^π (eb)	Q_{22}^π (eb)	I ($\hbar$)	Band configiration w/respect to $\|\mathbf{core}\rangle$
		^{134}Nd			
	(π, r)=(–, 1), α= 0				
0.47	[18,19,19,18]$_n$[14,14,16,16]$_p$	9.01	-0.03	39.08	(ν[530]1/2+) (π[532]5/2+)(π[541]1/2-)
	(π, r)=(–,–1), α= 1				
0.06	[18,19,18,19]$_n$[15,15,15,15]$_p$	7.30	0.38	38.51	(ν[530]1/2-) (π[404]9/2+)(π[404]9/2-)
	(π, r)=(+, 1), α= 0				
1.94	[18,18,19,19]$_n$[15,15,15,15]$_p$	7.13	-0.09	34.95	($\nu\mathbf{6}_1$-)$^{-1}$ (ν[530]1/2-)(ν[530]1/2+) (π[404]9/2+)(π[404]9/2-)
0.17	[19,19,18,18]$_n$[14,14,16,16]$_p$	9.19	0.07	41.27	($\nu\mathbf{6}_2$+) (π[532]5/2+)(π[541]1/2-)
0.00	[19,19,18,18]$_n$[15,15,15,15]$_p$	7.52	0.27	40.67	($\nu\mathbf{6}_2$+) (π[404]9/2+)(π[404]9/2-)
		^{135}Nd			
	(π, r)=(–, i), α=–1/2				
1.17	[19,19,19,18]$_n$[15,15,15,15]$_p$	7.73	0.10	42.06	($\nu\mathbf{6}_2$+)(ν[530]1/2+) (π[404]9/2+)(π[404]9/2-)
	(π, r)=(+,–i), α= 1/2				
0.00	[19,20,18,18]$_n$[15,15,15,15]$_p$	6.43	0.65	39.01	(ν[402]5/2+)(ν[402]5/2-) (π[404]9/2+)(π[404]9/2-)

Table 3.13: The CHF+SLy4 configurations in ^{133,134}Pm.

$E_\omega - E_\omega^{\text{core}}$ (MeV)	$[N_{+,+i}, N_{+,-i}, N_{-,+i}, N_{-,-i}]$	Q_{20}^{π} (eb)	Q_{22}^{π} (eb)	I ($\hbar$)	Band configiration w/respect to $\|\mathbf{core}\rangle$
		^{133}Pm			
	(π, r)=(–,–i), α= 1/2				
0.78	$[18,18,18,18]_n[15,15,15,16]_p$	7.32	0.09	31.26	$(\nu\mathbf{6}_1\text{-})^{-1}(\pi[532]5/2\text{-})$ $(\pi[404]9/2\text{+})(\pi[404]9/2\text{-})$
	(π, r)=(–,–i), α= 1/2				
0.54	$[18,19,17,18]_n[15,16,15,15]_p$	6.31	0.14	35.45	$(\nu\mathbf{6}_1\text{-})^{-1}(\nu[523]7/2\text{+})^{-1}$ $(\nu[402]5/2\text{+})(\pi[411]3/2\text{-})$ $(\pi[404]9/2\text{+})(\pi[404]9/2\text{-})$
	(π, r)=(–, i), α=–1/2				
0.42	$[18,18,18,18]_n[15,15,16,15]_p$	7.13	0.03	31.95	$(\nu\mathbf{6}_1\text{-})^{-1}(\pi[532]5/2\text{+})$ $(\pi[404]9/2\text{+})(\pi[404]9/2\text{-})$
0.10	$[18,19,17,18]_n[15,16,15,15]_p$	7.08	0.28	39.45	$(\nu[523]7/2\text{+})^{-1}(\pi[411]3/2\text{-})$ $(\pi[404]9/2\text{+})(\pi[404]9/2\text{-})$
	(π, r)=(+, i), α=–1/2				
0.05	$[18,18,18,18]_n[16,15,15,15]_p$	6.70	0.17	33.35	$(\nu\mathbf{6}_1\text{-})^{-1}(\pi[411]3/2\text{+})$ $(\pi[404]9/2\text{+})(\pi[404]9/2\text{-})$
	(π, r)=(+,–i), α= 1/2				
0.00	$[18,18,18,18]_n[15,16,15,15]_p$	6.68	0.08	33.59	$(\nu\mathbf{6}_1\text{-})^{-1}(\pi[411]3/2\text{-})$ $(\pi[404]9/2\text{+})(\pi[404]9/2\text{-})$
		^{134}Pm			
	(π, r)=(–, 1), α= 0				
0.98	$[18,19,18,18]_n[16,16,15,14]_p$	5.87	0.53	34.18	$(\nu\mathbf{6}_1\text{-})^{-1}(\nu[402]5/2\text{-})$ $(\pi[404]9/2\text{+})(\pi[404]9/2\text{-})$ $(\pi[411]3/2\text{+})(\pi[411]3/2\text{-})$ $(\pi[541]3/2\text{-})^{-1}$
	(π, r)=(+,–1), α= 1				
0.58	$[18,19,18,18]_n[15,16,15,15]_p$	6.36	0.12	34.01	$(\nu\mathbf{6}_1\text{-})^{-1}(\nu[402]5/2\text{-})$ $(\pi[404]9/2\text{+})(\pi[404]9/2\text{-})$ $(\pi[411]3/2\text{-})$
0.08	$[18,19,18,18]_n[15,16,15,15]_p$	7.10	0.27	38.46	$(\pi[404]9/2\text{+})(\pi[404]9/2\text{-})$ $(\pi[411]3/2\text{-})$
	(π, r)=(+, 1), α= 0				
0.00	$[18,19,18,18]_n[16,15,15,15]_p$	7.07	0.55	38.51	$(\pi[404]9/2\text{+})(\pi[404]9/2\text{-})$ $(\pi[411]3/2\text{+})$

Table 3.14: The CHF+SLy4 configurations in ^{135,136}Pm.

$E_\omega - E_\omega^{\text{core}}$ (MeV)	$[N_{+,+i}, N_{+,-i}, N_{-,+i}, N_{-,-i}]$	Q_{20}^{π} (eb)	Q_{22}^{π} (eb)	I ($\hbar$)	Band configiration w/respect to $\|\mathbf{core}\rangle$
		^{135}Pm			
	(π, r)=(+,−i), α= 1/2				
0.06	$[19,19,18,18]_n[15,16,15,15]_p$	6.03	0.10	34.47	$(\nu\mathbf{6}_1\text{-})^{-1}(\pi[411]3/2\text{-})$ $(\nu[402]5/2+)(\nu[402]5/2\text{-})$ $(\pi[404]9/2+)(\pi[404]9/2\text{-})$
	(π, r)=(+, i), α=−1/2				
0.00	$[19,19,18,18]_n[16,15,15,15]_p$	5.99	0.99	34.50	$(\nu\mathbf{6}_1\text{-})^{-1}(\pi[411]3/2+)$ $(\nu[402]5/2+)(\nu[402]5/2\text{-})$ $(\pi[404]9/2+)(\pi[404]9/2\text{-})$
		^{136}Pm			
	(π, r)=(−,−1), α= 1				
1.23	$[19,20,18,18]_n[15,15,15,16]_p$	7.01	0.66	38.02	$(\nu[402]5/2+)(\nu[402]5/2\text{-})$ $(\pi[404]9/2+)(\pi[404]9/2\text{-})$ $(\pi[532]5/2\text{-})$
	(π, r)=(−, 1), α= 0				
1.04	$[19,20,18,18]_n[15,15,16,15]_p$	6.87	0.50	37.93	$(\nu[402]5/2+)(\nu[402]5/2\text{-})$ $(\pi[404]9/2+)(\pi[404]9/2\text{-})$ $(\pi[532]5/2+)$
	(π, r)=(+,−1), α= 1				
0.53	$[19,20,18,18]_n[15,16,15,15]_p$	6.40	0.51	39.68	$(\nu[402]5/2+)(\nu[402]5/2\text{-})$ $(\pi[404]9/2+)(\pi[404]9/2\text{-})$ $(\pi[411]3/2\text{-})$
	(π, r)=(+,−1), α= 1				
0.00	$[19,20,18,18]_n[16,15,15,15]_p$	6.24	1.29	40.37	$(\nu[402]5/2+)(\nu[402]5/2\text{-})$ $(\pi[404]9/2+)(\pi[404]9/2\text{-})$ $(\pi[411]3/2+)$

Table 3.15: The CHF+SLy4 configurations in ^{135,136,137}Sm.

$E_\omega - E_\omega^{\text{core}}$ (MeV)	$[N_{+,+i}, N_{+,-i}, N_{-,+i}, N_{-,-i}]$	Q_{20}^π (eb)	Q_{22}^π (eb)	I ($\hbar$)	Band configiration w/respect to $\|\mathbf{core}\rangle$
		^{135}Sm			
	(π, r)=(−,−i), α= 1/2				
0.19	$[18,19,18,18]_n[15,16,16,15]_p$	7.53	0.22	37.61	(π[411]3/2-)(π[532]5/2+) (π[404]9/2+)(π[404]9/2-)
	(π, r)=(−, i), α=−1/2				
0.10	$[18,19,18,18]_n[16,15,16,15]_p$	7.52	0.45	37.47	(π[411]3/2+)(π[532]5/2+) (π[404]9/2+)(π[404]9/2-)
	(π, r)=(+,−i), α= 1/2				
0.41	$[18,19,18,18]_n[16,16,15,15]_p$	6.36	-0.09	34.57	($\nu\mathbf{6}_1$-)$^{-1}$(ν[402]5/2-) (π[411]3/2+)(π[411]3/2-) (π[404]9/2+)(π[404]9/2-)
0.00	$[18,19,18,18]_n[16,16,15,15]_p$	7.04	0.60	39.30	(π[411]3/2+)(π[411]3/2-) (π[404]9/2+)(π[404]9/2-)
		^{136}Sm			
	(π, r)=(+, 1), α= 0				
3.39	$[18,18,19,19]_n[16,16,15,15]_p$	6.98	-1.39	36.16	($\nu\mathbf{6}_1$-)$^{-1}$(ν[402]5/2-) (ν[530]1/2+)(ν[530]1/2-) (ν[411]1/2-)$^{-1}$ (π[411]3/2+)(π[411]3/2-) (π[404]9/2+)(π[404]9/2-)
0.00	$[19,19,18,18]_n[16,16,15,15]_p$	6.08	-0.96	34.83	($\nu\mathbf{6}_1$-)$^{-1}$ (ν[402]5/2+)(ν[402]5/2-) (π[411]3/2+)(π[411]3/2-) (π[404]9/2+)(π[404]9/2-)
		^{137}Sm			
	(π, r)=(+,−i), α= 1/2				
0.00	$[19,20,18,18]_n[16,16,15,15]_p$	6.23	1.64	40.19	(ν[402]5/2+)(ν[402]5/2-) (π[411]3/2+)(π[411]3/2-) (π[404]9/2+)(π[404]9/2-)

Chapter 4

High–Spin States in Light Neutron–Rich Nuclei

4.1 Properties of Exotic Neutron–Rich Nuclei

As demonstrated in the previous Chapter, the excursion away from the line of beta stability towards nuclei with large proton excess has led to the discovery of highly–deformed shapes and to a better understanding of nuclear shell structure. The improved experimental tools have made the field of exotic nuclei one of the fastest growing in low–energy nuclear physics, allowing for the exploration of previously unaccessible regions of the nuclear landscape. Nuclei far from stability have never been so accessible for study experimentally as they are now, thanks to the existence of radioactive nuclear beam (RNB) facilities [220, 221].

The possibilities of studying new physical phenomena in very neutron–rich nuclei have been of considerable interest. There are many new phenomena expected to occur around the neutron drip line : neutron emission, variations in cross-sections [222, 223], possible soft collective modes and low–lying transition strengths [224, 225, 226, 227, 228, 229], changes in shell structure [230, 231, 232], and many others. For medium–mass and heavy nuclear systems, the areas of the proton and neutron drip lines are accessible using reactions via compound nucleus formation [233, 234, 235]. Such experimental studies for the neutron–rich side are facilitated for the medium–mass regions by the ease of their production as fission fragments, however, this method is practically unusable for light nuclei in view of the low yield. The neutron drip line has been explored experimentally only up to oxygen, but new advantages of the RNB technology have promised to push those limits even further [236]. Studies of extreme N/Z ratios, both theoretical and experimental, have revealed new conceptual aspects, shedding new light on the nuclear many–body problem. In this context, one should mention the indications for the existence of halo nuclei, and the so–called Borromean nuclei [240] along the edges of the nucleon drip line (Fig. 4.1).

One of the very interesting effects in nuclear systems far from stability is the observed increase in radial size with the decrease in binding energy [241, 242, 243, 244]. This can lead to the creation of a nucleon skin or a nucleon halo. These effects are observable in loosely–bound systems, usually with extreme isospin values [245]. Drawing the distinction line between skin and halo is pretty much a matter of convention [246], but there are clear indications that their formation mechanisms are different at the microscopic level. The halo terminology was

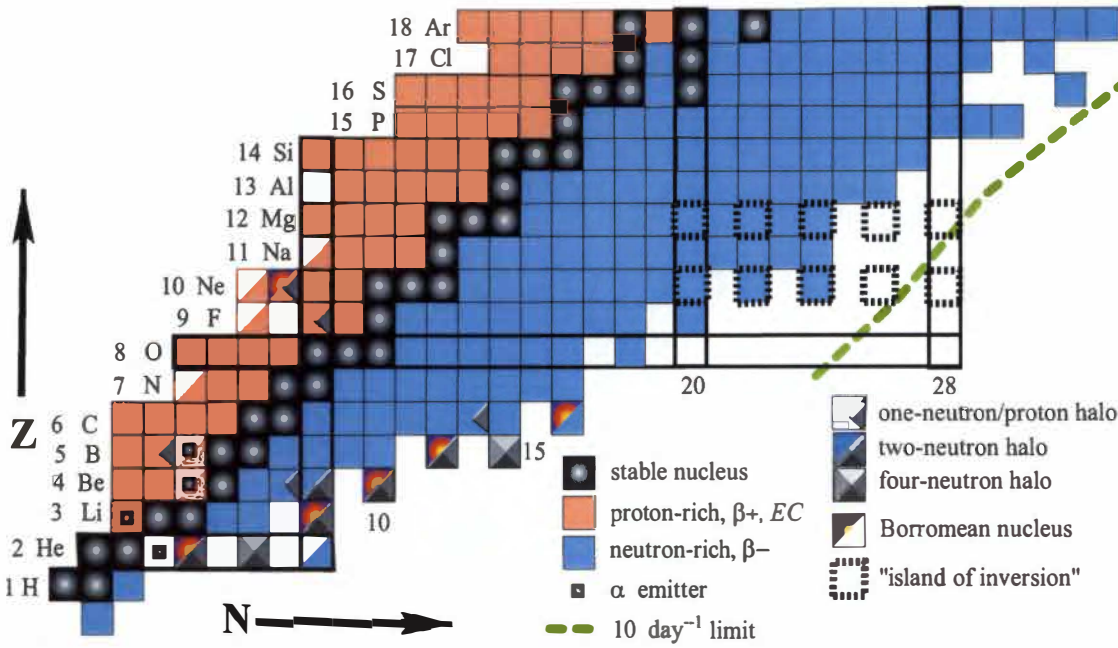

Figure 4.1: Part of the nuclear landscape showing halo nuclei and some of the structures far from stability. The deformed "island of inversion" in the heavy even–even Ne and Mg nuclei studied in this Chapter is marked. The information about halo/Borromean nuclei comes from Refs. [237, 238]. The dashed line shows the production limit of 10 nuclei/day on the K500–K1200 facility at NCSL [239], a reasonable practical experimental limitation.

introduced historically at the time when the same nuclei exhibited interaction cross–sections [247, 248], which appeared to be large compared with the calculated reaction cross–sections. When single–particle densities were fitted to the data using Glauber's model [249], halo nuclei were identified as those with root–mean–square radii "much larger" than 1.1 $A^{1/3}$ fm. While the halo can be created by one or few weakly–bound nucleons outside the core, which occupy single–particle states with low angular momenta [241], the nucleonic skin is not subject to such a restriction, and involves pairing interactions, polarization of the core and other features usually associated with heavier systems. The *neutron halo* [250, 241], for example, is likely to be seen in systems with nearly three times as many neutrons as protons; such structures have been observed in a variety of nuclei (see *e.g.* [238, 251] and references therein). The outermost part of the neutron density in such systems is essentially determined by quantum effects, since the halo nucleons spend most of their time in the classically–forbidden region. The proximity of the continuum states requires non-standard techniques involving the explicit description of few-body dynamic effects [235]. It is no wonder that skin/halo studies are some of the most vigorously developing in low–energy nuclear structure physics — both theoretically and experimentally.

The presence of a *neutron skin* [252] is often considered characteristic of heavy neutron–rich nuclear systems. The valence neutrons in such nuclei are likely to form a neutron skin "outside" of the "surface" defined by a well–bound proton structure [246]. In some cases it may be possible to see evidence for both a neutron skin *and* halo. Indeed, in nuclei closer to the valley of stability, the root–mean–square radii of neutrons do not exceed those of protons

by more than $\Delta R_{np} = 0.2$ fm [253, 254, 255, 232, 246]. This value increases rapidly when the neutron excess becomes higher, the effect likely being caused by both halo and skin effects. Information about the difference ΔR_{np} has been obtained experimentally ([232] and references therein, [256, 257, 258, 259, 260, 261]). Experimental results on neutron/proton radii have stimulated an impressive theoretical activity ([246] and references therein), especially focusing on features of the nuclear surface and details of the nucleon distribution. In particular, it has been demonstrated that the diffraction radii of nuclear systems, defined in the framework of electron–scattering measurements [262, 263, 264], are mostly sensitive to the surface nucleon distribution and do not depend significantly on the shell structure in the interior [265, 266, 267, 268, 269]; hence they can be used to determine the neutron skin. The experimental information is usually limited to charge densities of stable nuclei, however, some recent developments indicate that new possibilities in intermediate–energy proton scattering [270] and parity–violating elastic electron scattering [271, 272, 273, 274, 275, 276] may provide data on neutron density form–factors as well.

In this Chapter, we look at a region of Ne and Mg nuclei in the vicinity of the neutron drip line (Fig. 4.1). It has been noted that a number of nuclei between neutron numbers N=20 and 28 exhibit features typical of well–deformed systems. (A general review of shape coexistence in light and heavy nuclei can be found in [277, 39], and references therein.) We start the following Section with a general discussion of the Ne–Mg region. Then we look at properties of single–particle states in the vicinity of the Fermi level, their effects on deformation and angular momentum, and other structural information. Theoretical studies of such nuclei indicate that considerable modification of our usual understanding of shell structure may be necessary [278, 244]. The mean field concept may have to be carefully reconsidered, and we need further insights into how well the traditional mechanisms can explain properties of nuclear matter so far away from the beta-stability line [235, 230, 231, 232].

Rotational structures in very neutron–rich nuclei have been analyzed experimentally using nucleon transfer reactions [279, 280], incomplete fusion [281], neutron-induced fission [282, 283], proton inelastic scattering [284, 285], deep inelastic reactions [286, 287], nucleon knockout reactions [288, 289], projectile fragmentation reactions [290, 291, 292, 293], and Coulomb excitation at intermediate energies [294, 295, 296, 297, 298, 299, 293]. The latter methods, for example, provided information on the collectivity of the lowest 2^+ and 4^+ states in ^{32,34}Mg [294, 299, 293], the new data supporting the conjecture that quenching of spherical magic gaps at N=20 and N=28 brings the deformed configurations lower in excitation energy, therefore increasing the likelihood of shape transitions.

4.2 Neutron Drip–Line Nuclei in the Ne–Mg Region

The structure of nuclei in the neutron–rich region with Z=8–12 has been a matter of significant interest since the first observations of a trend towards over–binding in very neutron–rich Na nuclei by Thibault *et al.* in 1975 [300], and then of an anomalously high isotope shift in ^{31}Na [301], along with a decrease in the two–neutron separation energy S_{2n} for ^{30}Ne and ^{31,33,35}Na [300, 301]. It hinted at the existence of a so–called *"island of inversion"* [302] beyond the N=20 shell closure — the occurrence of prolate deformations, rather than the expected spherical behavior, accompanied by a strong decrease in binding energy ([303] and references therein). Such behavior was interpreted as an indication that the spherical magic N=20 gap vanishes in the neutron rich region [304, 305] (see Fig. 2.1).

The unexpectedly low first 2^+ state in ^{32}Mg was determined experimentally in 1979 [306],

marking the beginning of the spectroscopic studies in this region and making this nuclide a benchmark case for explorations. The transition probability $B(E2; 2_1^+ \rightarrow 0_1^+)$ [307, 308] was re-measured recently [294] and confirmed to be very large, an indication for a well-deformed prolate shape with $\beta_2 \approx 0.52$. This significant quadrupole collectivity evidences the closure of the N=20 spherical gap when approaching the neutron drip line. Being model-dependent, the deduction of shape deformation from the $B(E2)$ data required more comprehensive studies, involving other excited levels and analysis of the $E(4^+)/E(2^+)$ ratio in particular [1]. The measurements in Ref. [290] gave $E_x(4_1^+)/E_x(2_1^+) \approx 2.5$, later confirmed by the Monte-Carlo Shell Model (MCSM) calculations in the s-*d* and *p*-*f* shell model space [310, 311]. The measurement of Ref. [299] hints that the yrast states up to spin $4\hbar$ in ^{32}Mg are deformed and some of the excited 0^+ and 2^+ states are spherical, thus pointing at the possibility of shape coexistence in this nuclide. These results demonstrated that most likely ^{32}Mg is not an isolated case, proving the conclusions of [312, 299]. Spectroscopic measurements have been extended to other magnesium isotopes. The collectivity of ^{34}Mg was investigated via in-beam γ-ray spectroscopy [293], which led to the observation of the transitions $2_1^+ \rightarrow 0_{g.s.}^+$, and $4_1^+ \rightarrow 2_1^+$. These measurements gave $E(4_1^+)/E(2_1^+) \simeq 3.2$, very close to the rotational limit, thus suggesting a very large prolate deformation.

It is still unclear how far the "island of inversion" extends in the direction of neutron excess. The proximity of these nuclei to the limits of stability make the experimental measurements very difficult at the present time, but there are many speculations based on theoretical models and trends in neutron separation energies. Early systematics [313] suggested the presence of the two-neutron drip line at N=28, which was supported by RMF calculations [314]. However, a recent experimental mass measurement [315] suggests that the Mg isotopes may become unbound earlier.

4.2.1 Theoretical Interpretations

Many mean field approaches have predicted and studied deformed ground states in the ^{32}Mg region. As early as 1975, the HF study by Campi *et al.* [316], based on early Skyrme forces SIII and SIV, suggested the possibility of prolate configurations in ^{31,32}Na, associated with excitations of the *s*-*d* neutrons to the $f_{7/2}$ shell. This conclusion was later confirmed by other approaches [317]. The effect of weakening of the shell effects in the Ne-Mg drip line nuclei was first introduced by Tondeur in 1978 [230] and studied extensively later [318, 319, 231, 320, 321, 322]. One of the first calculations of excited states in ^{32}Mg, using the energy density formalism in the framework of the interacting quasiparticle model [323], predicted the low-lying 2_1^+ states for N=20 isotones, while failing to reproduce correctly their excitation energies. By the beginning of the 1980's, the sudden onset of deformation in this region was explained [324, 325].

The breaking of the N=20 closed shell means that one has to include both the *s*-*d* and *p*-*f* orbitals in calculations. Since the earliest experimental studies of ^{32}Mg [306], the collective properties of this nuclide have been attributed to the appearance of the ν $f_{7/2}$ [330]1/2 intruder state (Figs. 2.1,4.2), and in 1980 Wildenthal and Chung [326] demonstrated the "collapse" of the conventional (spherical) shell model for very neutron-rich Na and Mg nuclei. During the 1980's, through the work of Poves and Retamosa [327] and others [311], it became a paradigm that the neutron $f_{7/2}$ orbitals need to be included in the structure analysis in this region. The shell-model interpretation of this mechanism ascribes the deformation-driving effect to particle-hole excitations across the magic gap, which is sufficient to produce the stable deformation, even in configurations containing as few as two $f_{7/2}$ neutrons.

[1] Values of this ratio approaching 3.3 are indicative of deformed rotors, while those closer to 2 indicate vibrational structures [309]

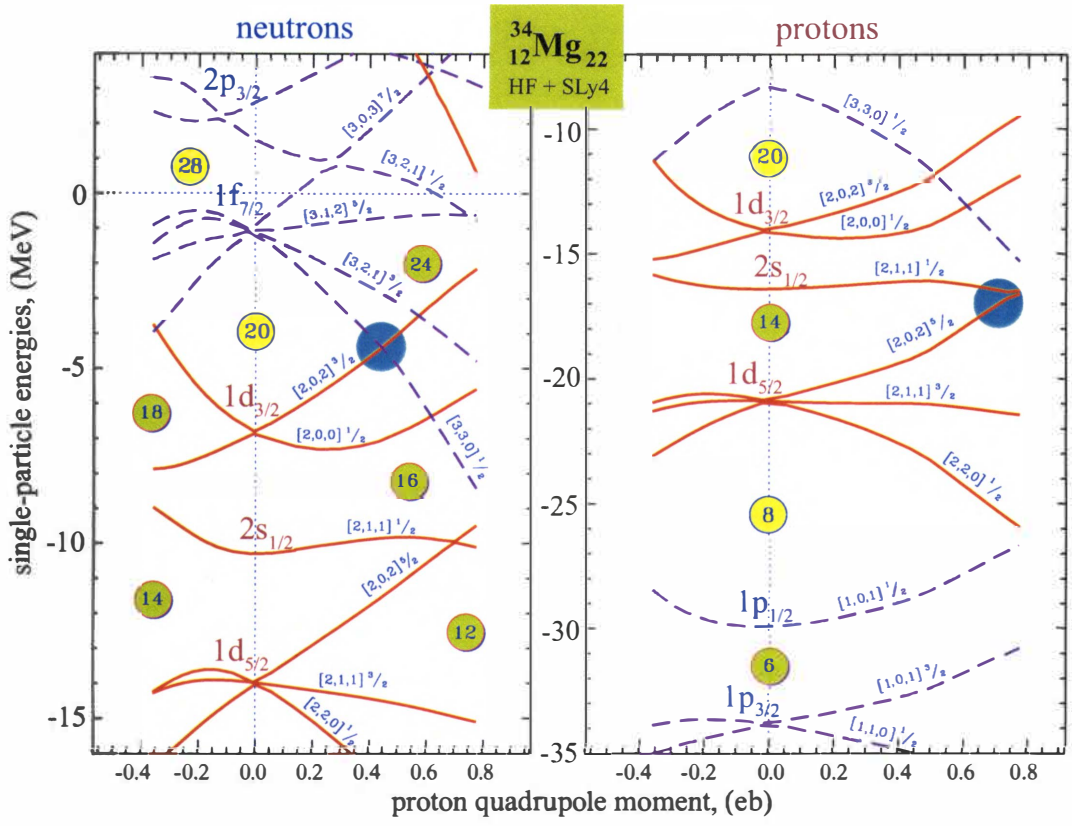

Figure 4.2: Neutron (left) and proton (right) Nilsson diagrams in the vicinity of ^{34}Mg Fermi level as a function of Q^{π}_{20}, calculated in CHF (*cf.* Fig. 2.1). Solid/dashed lines represent positive/negative parity states. The shaded area in the neutron diagram indicates the crossing between the extruder $d_{3/2}$ and the intruder $f_{7/2}$ orbitals.

A series of theoretical calculations in the framework of the RMF theory [314, 328, 329] predicted a spherical ground-state shape for ^{32}Mg. Sphericity was also found in several Skyrme HF calculations [330, 331, 332], although it was indicated that dynamic correlations could cause deformation [330]. However, the recent survey of Ref. [312] demonstrates that the shape transition around ^{32}Mg strongly depends on the nucleon–nucleon interaction; same Skyrme forces do in fact yield deformation at N=20.

In this work, we would like to address the likelihood of stabilization of deformed shapes in this region as a result of rotation.

4.3 Rotational Properties of Neutron–Rich Na and Mg Nuclei : Skyrme HF Results

Our calculations were carried out using the cranked Hartree–Fock method with the Skyrme interaction parametrization SLy4, and involved the quantitative study of characteristics of rotational bands for the deformed configurations in ^{30,32,34,36,38}Ne and ^{32,34,36,38,40}Mg (Fig. 4.1). The success of similar studies in SD nuclei [77, 333, 334, 2] has indicated that pairing effects may be considered unessential for the description of highly–deformed and superdeformed configurations at high rotational frequencies. Although it is clear *a priori* that a proper inclusion of pairing correlations, clustering, and so forth, in the theoretical picture of the neutron drip–line systems is significant at low spins, our ambition here is to explore the effect of fast nuclear rotation — in this context we consider pairing correlations of lesser importance.

4.3.1 The N=20 and N=22 Isotones

Deformation and rotational properties of neutron–rich Ne and Mg nuclei are determined by the underlying shell structure. This is clearly visible in the isotones close to N=20, for which the magic spherical gap of nearly 5 MeV all but disappears as a function of deformation (see Fig. 4.2, left). The lightest of the systems in our study, ^{30}Ne, has in its ground state configuration $[2,2,3,3]_p$ two protons in the $1d_{5/2}$ orbital and the neutron *s-d* shell is filled completely. As quadrupole deformation increases above β_2=0.2, the lowest intruder from the negative–parity $\mathcal{N}$=3 shell (3_1 and 3_2) becomes energetically favored ($Q_0^\pi \simeq 0.55$ eb in Fig. 4.2). In the lowest configuration of the N=20 isotones we thus have a 2p–2h excitation to the $f_{7/2}$ level.

The addition of pairs of neutrons gradually fills the negative–parity $f_{7/2}$ states from the bottom up. Since, in the frequency range considered in this work, no crossings between positive– and negative–parity Routhians occur, we can easily determine proton configurations ($[2,2,3,3]_p$ for Ne and $[3,3,3,3]_p$ for Mg nuclei) and fill the neutron $f_{7/2}$ orbital through the sequence of deformed bands lowest in energy : $[6,6,5,5]_n/[7,7,4,4]_n$ (N=22), $[7,7,5,5]_n$ (N=24), $[7,7,6,6]_n$ (N=26), and $[7,7,7,7]_n$ (N=28).

Figure 4.3 presents a side–by–side comparison between the CHF results for the N=20 isotones of Ne and Mg. Although there are many similarities in the location and spacings of the neutron levels, the presence of two extra protons in the ^{32}Mg gives rise to a large–interaction crossing in protons at $\hbar\omega \simeq 1.5$ MeV (see below). The adiabatic crossing in ^{30}Ne between the $\pi 1d_{5/2}$ [220]1/2 (r =+i) Routhian and the [211]3/2 level causes the gradual slope change from a prolate shape to a weakly–deformed oblate shape at high rotational frequencies. In the magnesium isotopes, the interaction between the second and third $\mathcal{N}$ =2 Routhians gives rise to an abrupt shape change. At very large deformations, this proton interaction is with the $2s_{1/2}$ [211]1/2 state, which appears in the vicinity of the Fermi level (marked by shaded circle in Fig. 4.2). In the ^{30}Ne case, the 3^2 band is lowest in energy. The signature splitting of the lowest $1f_{7/2}$ Routhians reaches nearly 2 MeV at the termination point. The magnesium isotone shows the same features; however, the interaction of three $1d_{5/2}$ (+,+i) proton Routhians causes a more abrupt shape change towards termination around $\hbar\omega$=1.3 MeV. This analysis provides more insight when related to the diagrams of the total aligned angular momentum (top of Fig. 4.3), combined with the behavior of the moments of inertia. For frequencies below the termination point ($\hbar\omega \approx$1.35 MeV) we see the gradual alignment of the spins of the nucleons building up the total angular momentum, and reaching a plateau at the termination point. The transition occurs very close to the crossing of the last occupied proton orbital with r =i. In ^{30}Ne it leads to a gradual transition to oblate shape at the high end of the cranking–frequency interval. In

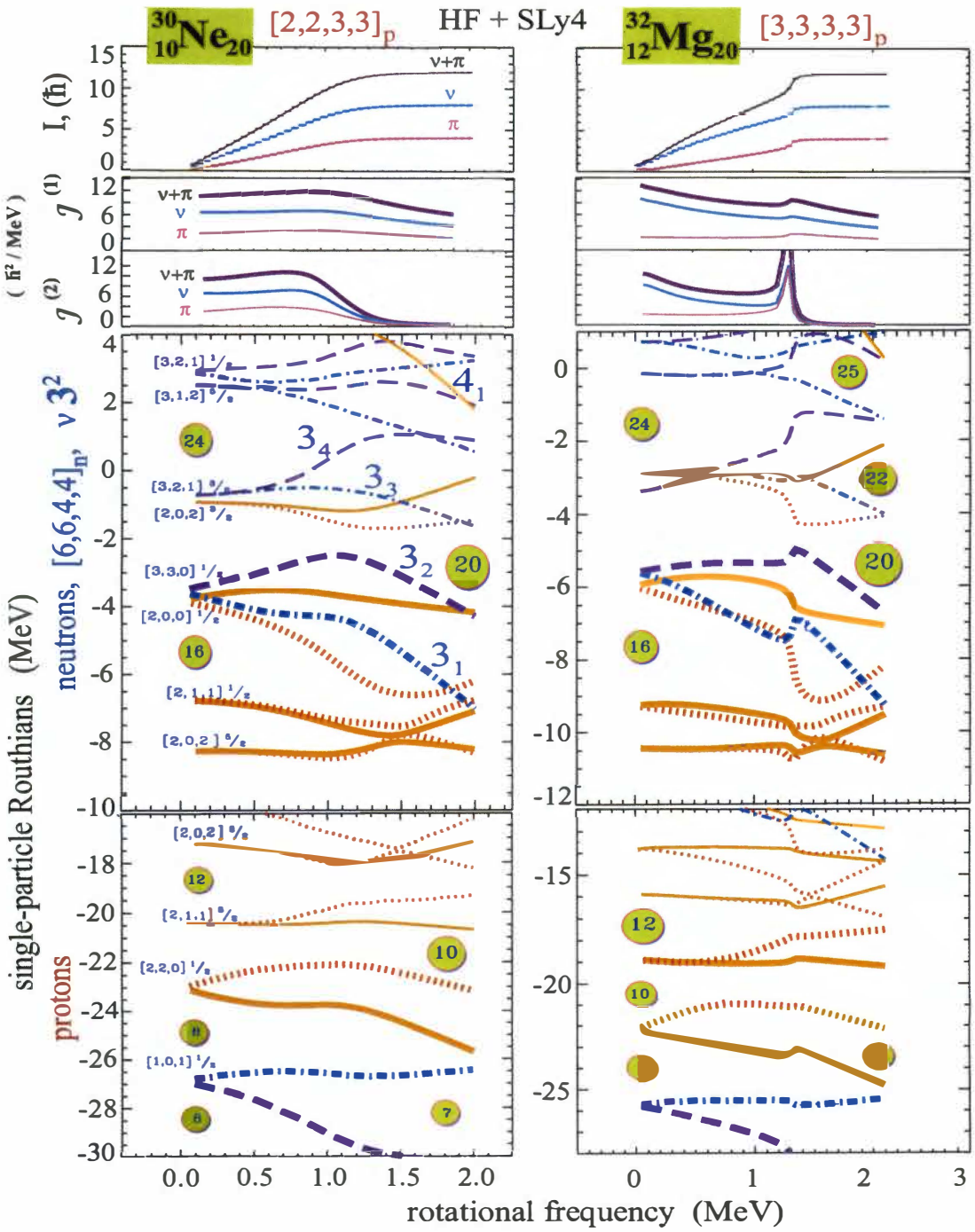

Figure 4.3: Single–particle Routhians, moments of inertia, and total angular momenta for the N=20 isotones of Ne and Mg as a function of ω. The line convention follows previous Chapters. The top panels show the neutron and proton contributions.

^{32}Mg the total spin at termination is also 12 $\hbar$, the only difference being that the 4$\hbar$ comes from the aligned proton levels, (3/2 + 5/2)$\hbar$. The transition towards termination shape is more abrupt, showing a kink in the vicinity of $\hbar\omega$=1.3 MeV.

As it was illustrated in Chapter 2, the transition from prolate to oblate shape at high frequencies causes a decrease in the moment of inertia. The abrupt shape change in ^{32}Mg is associated with well pronounced kink in $\mathcal{J}^{(2)}$ at the termination frequency (*cf.* Fig. 2.7). The proton crossing in the lightest Mg isotopes prompts the transition to oblate shape associated with band termination; this behavior will be illustrated better for the lowest bands in ^{34}Mg.

A further analysis can be carried out by looking into the N=22 isotones, where more combinations of neutron occupation numbers are possible, and several rotational bands can compete. In order to look into the structural effects, stemming from the consecutive occupation of the $f_{7/2}$ orbitals, we explore configurations $[7,7,4,4]_n$, $[7,6,5,4]_n$ and $[6,6,5,5]_n$, containing two, three, and four $\mathcal{N}$=3 states, respectively. In all these cases the aligned protons contribute with the maximum alignment of 4$\hbar$ to the total spin. In configuration $[7,7,4,4]_n$ (Fig. 4.4, left), the two lowest $\mathcal{N}$ =3 states neutrons smoothly align with 5/2 + 7/2 = 6 $\hbar$ at termination ($\hbar\omega \simeq$1.0 MeV). The addition of the third $\mathcal{N}$=3 neutron (middle panel), and the emptying of the highest up-sloping $1d_{3/2}$ state adds 3/2 + 3/2 = 3 units to the aligned neutron angular momentum, and delays the termination point to higher frequency, $\hbar\omega \simeq$1.3 MeV. The interaction between 3_2 and 3_3 Routhians (marked in Fig. 4.4 with a shaded area) causes a rapid increase in $\mathcal{J}^{(2)}$ right before termination. In the third case (Fig. 4.4, right) the fourth $\mathcal{N}$=3 neutron Routhian becomes occupied at the expense of the next up-sloping $1d_{3/2}$ state, with the net result of an even further delay of termination. At the highest frequencies, the neutrons in $[6,6,5,5]_n$ carry approximately 11 $\hbar$. Part of this alignment is due to the interaction with the higher–lying neutron states with $\mathcal{N}$=3.

It is noteworthy to observe the appearance of the lowest highly deformed $\mathcal{N}$=4 neutron (+,–i) intruder $1g_{9/2}$ (denoted $\nu\ 4_1$) at the highest frequencies. For the $[7,7,4,4]_n$ band (extended in frequency for illustration purposes) the intruder is not expected to cause any effects, because it experiences a crossing well beyond the termination point, and its influence would not manifest itself in a rotational spectrum. However, in other configurations, such as the 3^4, it descends to the Fermi surface. It is certainly of interest to study the crossing(s) of this intruder in detail, although the frequencies at which it is expected to play a role are far above the experimental possibilities at the moment. For N$\geq$26, the lowest $\nu\ 1g_{9/2}$ orbital is expected to be occupied, at frequencies around and above 2.0 MeV.

The structures in ^{32}Ne can be seen also in the corresponding neutron configurations in ^{34}Mg. Figure 4.5 shows the single–particle Routhians corresponding to two rotating configurations $[7,7,4,4]_n$, which have different occupation numbers of the lowest (+,+i) protons. The band that is lower in energy at low frequencies, "$[7,7,4,4]_n$ A", is approached by "$[7,7,4,4]_n$ B" at about 0.8 MeV. The gaps in the single–particle Routhians mark the positions of the corresponding proton–level crossing, where the Hartree–Fock procedure does not converge. The bands terminate at frequencies comparable to those for ^{32}Ne.

Figure 4.6 shows the neutrons in the configuration $[6,6,5,5]_n$ which extends to a frequency as high as 3.4 MeV, at which the $\nu\ 4_1$ orbital interacts with the second neutron $1d_{3/2}$ state. In the entire frequency interval above 2.2 MeV there appears to occur a significant mixing of (–,–i) neutrons and (+,i) protons. As we shall see below, the $[6,6,5,5]_n$ bands in the N=22 isotones have bigger prolate deformations than the $[7,7,4,4]_n$ bands.

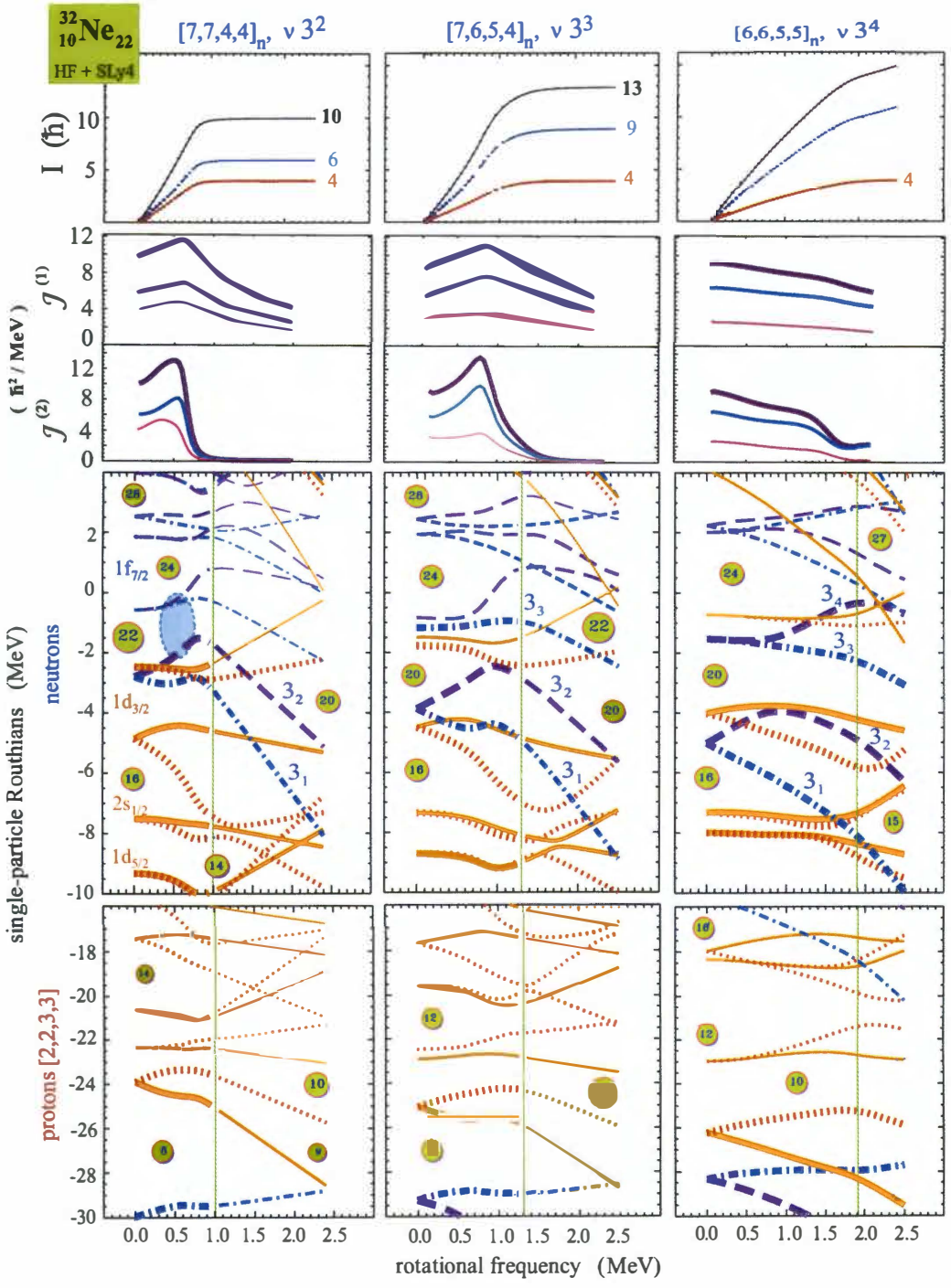

Figure 4.4: Similar to Fig. 4.3 but for the lowest configurations in ^{32}Ne.

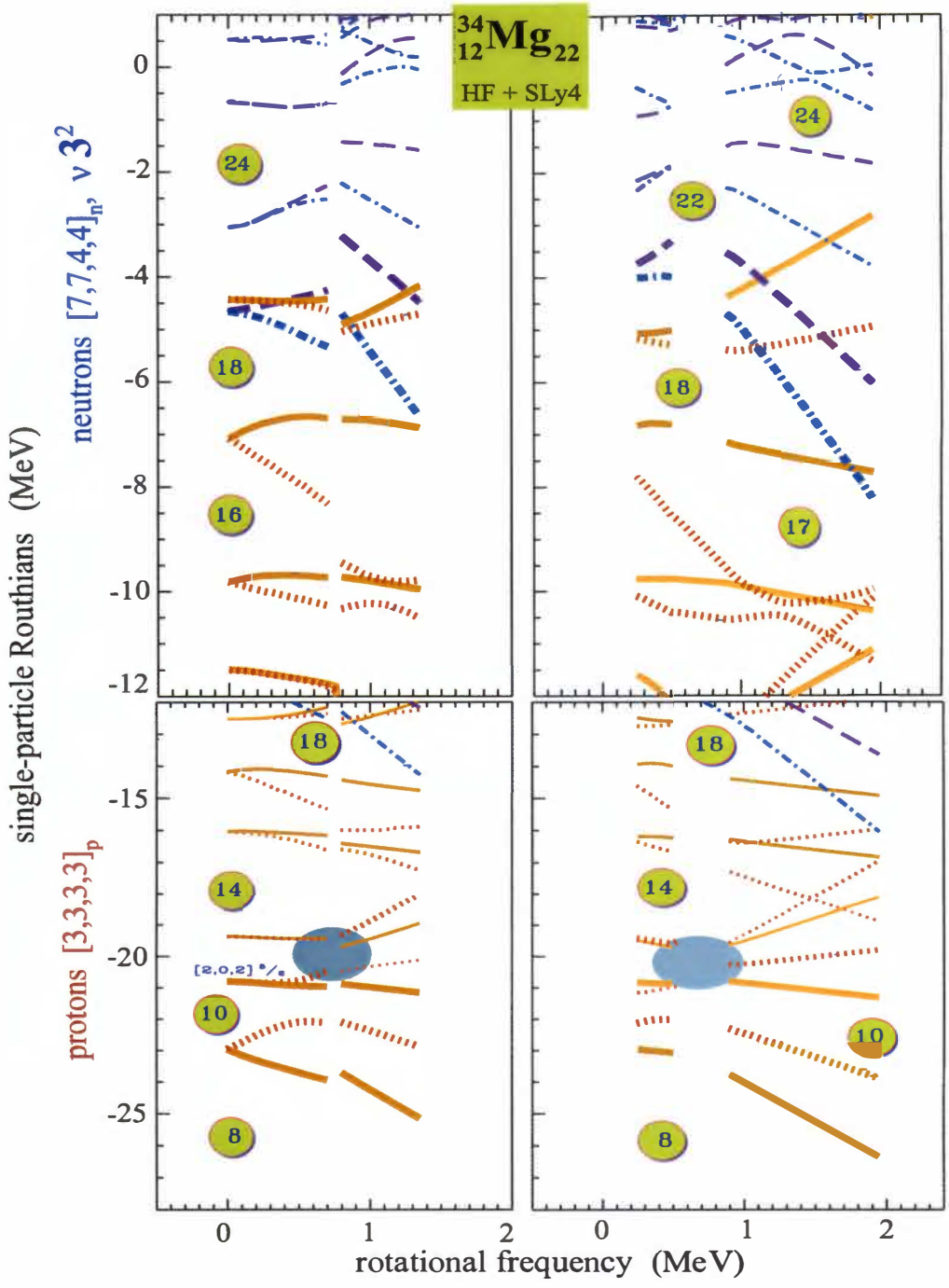

Figure 4.5: Single-particle Routhian diagram for the $[7,7,4,4]_n$ configuration in ^{34}Mg

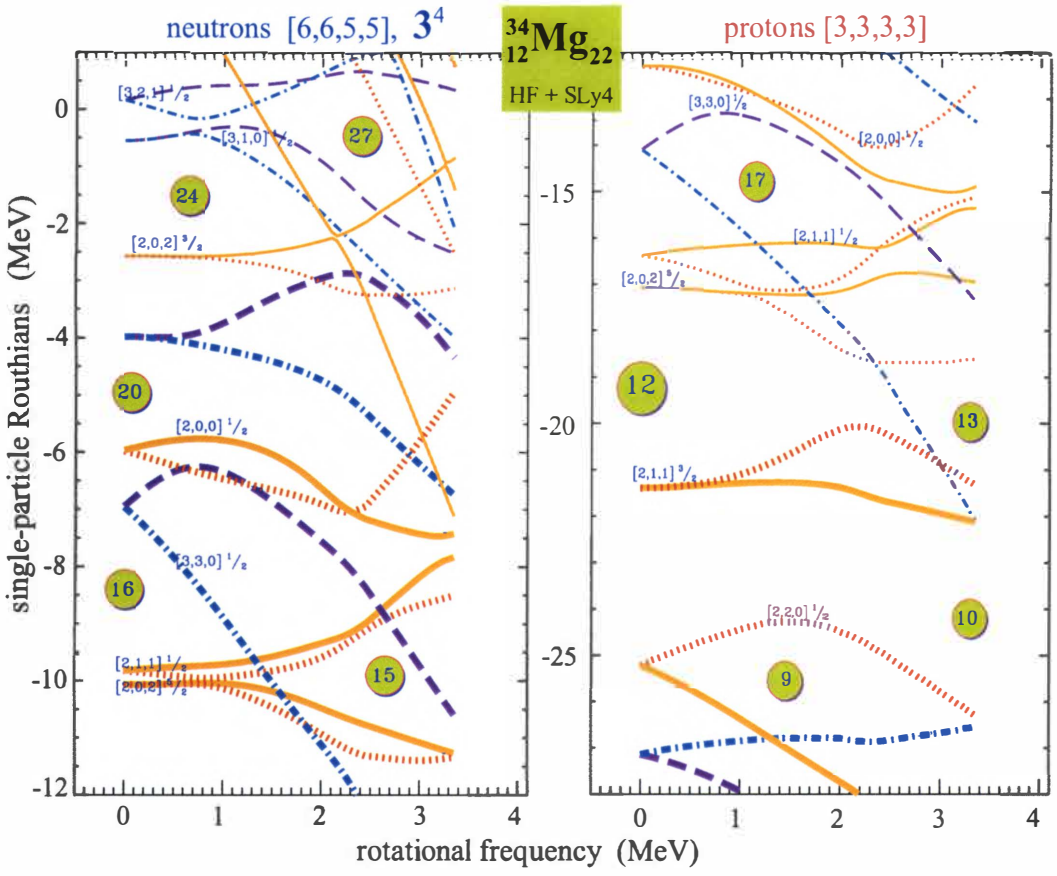

Figure 4.6: Single-particle Routhian diagram for the $\nu 3^4$ band in ^{34}Mg

4.3.2 N=24 Isotones

With the addition of two more neutrons (Fig. 4.7, bottom), the interaction between the proton $1d_{5/2}$ (+,+i) Routhians becomes much weaker, which allows the lowest bands in both isotones to extend to $\hbar\omega \geq 1.5$ MeV before terminating. The neutron Fermi level for ^{34}Ne is very close to zero, suggesting that the excited bands are likely to become unbound. The total angular momentum smoothly approaches 12 $\hbar$; however, the main reason for the band's ending abruptly at $\hbar\omega$=2.0 MeV is the crossing of the highest $d_{3/2}$ neutron (+,–i) state with the $\mathcal{N}$=4 intruder.

In ^{36}Mg (Fig. 4.7, right), the proton interaction in the (+,i) parity–signature block causes considerable disturbance in the nuclear shape because of the presence of a third state, the $2s_{1/2}$, appearing in the proximity of the top two $1d_{5/2}$ orbitals, the lower of which is occupied. This causes a band crossing at $\hbar\omega$=1.5 MeV, with the rapid deformation change clearly visible in the plots of the moments of inertia.

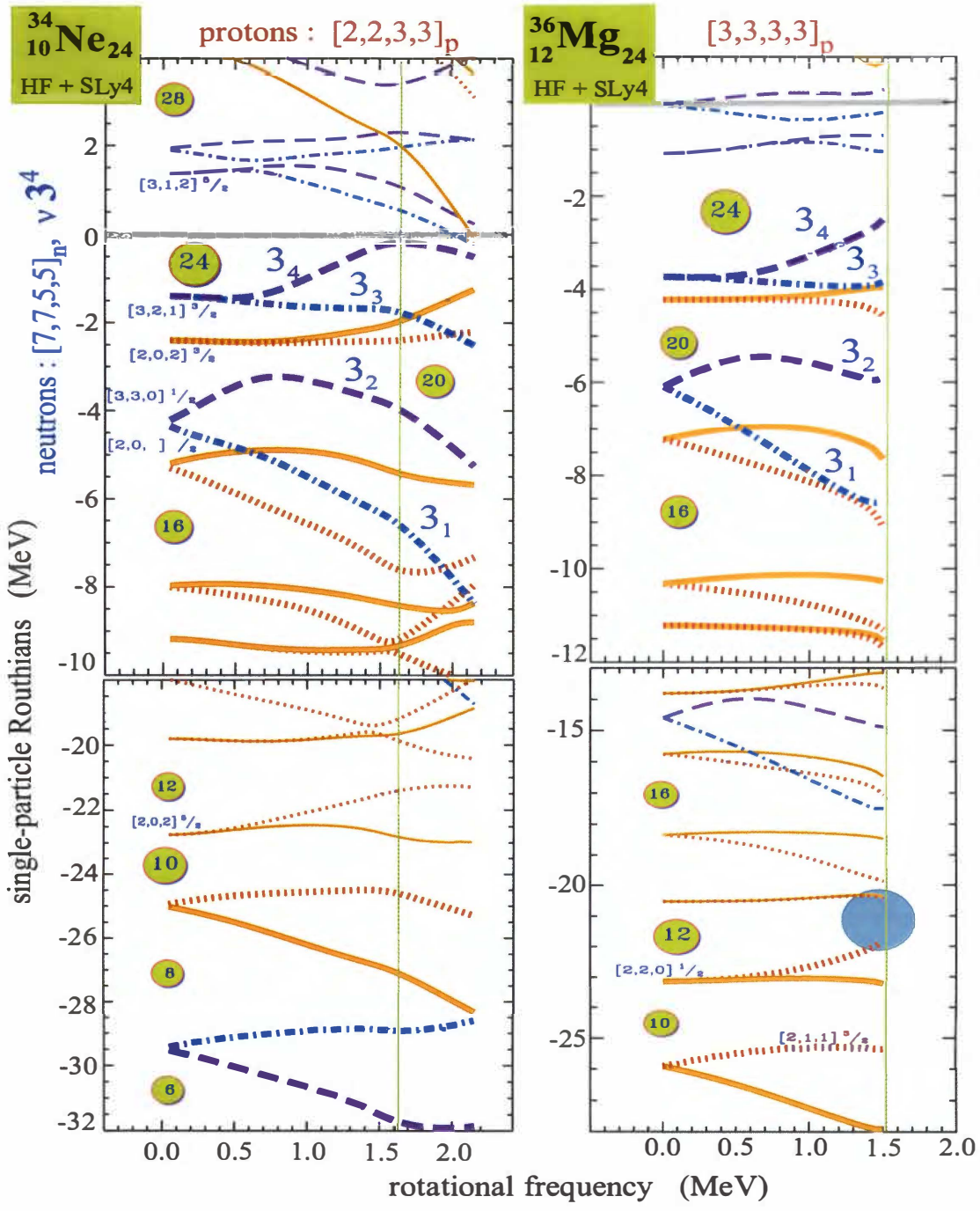

Figure 4.7: Single–particle Routhian diagram for the lowest bands in the N=24 isotones of Ne and Mg.

4.3.3 Drip–Line Ne and Mg Isotopes with N=26 and 28

The addition of two more neutrons to form the configuration $[7,7,6,6]_n$ in ^{36}Ne (Fig. 4.8) makes them occupy two negative-parity states with *positive* Routhians around 0.5 MeV. They become bound only for $\hbar\omega$ >2.0 MeV. The mixings of negative–parity states, clearly seen in the behavior of $\mathcal{J}^{(1)}$ and $\mathcal{J}^{(2)}$, are associated with the crossing of the extruder $1f_{7/2}$ [303]7/2 with the intruder $2p_{3/2}$ [321]1/2 at around Q^{π}=0.25 eb (Fig. 4.2).

The $\mathcal{N}$=4 intruder with r =–i would form a hole state in the corresponding configuration in the same high–frequency interval. Its presence, together with its expected prolate deformation-driving effect, may become essential for the stabilization of well–deformed bands at very high frequencies.

In the nuclide ^{38}Mg (Fig. 4.8, right) the added $1f_{7/2}$ neutron pair to $[7,7,5,5]_n$, forming the lowest configuration, reduces the influence of the mixing in the proton (+,i) states even further, so that it remains significant only beyond $\hbar\omega$=1.6 MeV. The proximity of the $\mathcal{N}$=4 intruder to the Fermi-level for $\hbar\omega$ above 1.8 MeV implies that the neutron configurations $[7,8,6,5]_n$ and $[7,8,5,6]_n$ would likely become yrast in this frequency region.

For ^{38}Ne (Fig. 4.9) the valence neutrons are likely to become unbound. As one can see, at least three out of the four negative-parity states stay around or above 0.0 MeV in the entire frequency interval — a fact normally associated with an instability towards neutron emission.

Filling completely the $f_{7/2}$ shell yields the $[7,7,7,7]_n$ band in ^{40}Mg. The N=28 gap at frequencies below 1.2 MeV is widely open. However, at higher frequencies the unoccupied $\mathcal{N}$=4 neutron intruder with (π,r)=(+,–i) drops rapidly below the Fermi–level, making the bands $[7,8,7,6]_n$ and $[7,8,6,7]_n$ energetically favorable.

4.3.4 Shapes and Angular Momentum Alignments

For the $[6,6,5,5]_n$ configuration in ^{32}Ne, the neutron spin comes from the aligned particles in $\nu(1f_{7/2})^4$ (7/2 + 5/2 + 3/2 + 1/2)$\hbar$, and $\nu(1d_{3/2})^{-2}$ (1/2 + 3/2)$\hbar$; however, because of the mixing of the highest (–,–i) $f_{7/2}$ orbital with higher–lying Routhian, this value is higher by about 1$\hbar$. As a result, the total angular momentum at termination reaches 15 $\hbar$. The corresponding configuration in ^{34}Mg carries more than 16 $\hbar$. In the two $[7,7,4,4]_n$ configurations the proton angular momentum contributions have two different values at termination. For configuration "A" it is 2 = 3/2 + 1/2 from the two $d_{5/2}$ holes in the $1d_{5/2}$ states, while in configuration "B" it is 4 = 5/2 + 3/2. Both bands terminate early — right after the crossing at $\hbar\omega$=0.8 MeV. For the heavier Ne and Mg isotopes, the total angular momentum at termination reaches 15–17 $\hbar$.

It is interesting to look at the ratios of the neutron and proton angular momenta (I_ν and I_π respectively) to the total angular momentum I (Fig. 4.10). These quantities can provide plenty of structural information : in the macroscopic picture of a rigidly–rotating nucleus the ratios I_ν/I and I_π/I are simply equal to N/A and Z/A, respectively. The deviations of these quantities from the rigid–rotor limit are, therefore, indications for changes of gyromagnetic factors in the rotating system. For example, the diagram for ^{32}Ne shows the sizeable proton contribution, which we discussed in the context of the three–level proton crossing. The heaviest Mg nuclei, with N=24,26,28, show that the angular momentum is built proportionally from neutrons and protons, and there is no indication for the decoupling of the neutron skin. This is a surprising and very interesting result. Although the heaviest of the nuclei in our study have the highest N/Z ratios, the rotational behavior of the neutrons does not deviate significantly from that of the protons. The values of the ratios for these nuclei stay within a narrow range around the corresponding ones for a "rigid" rotor, and even get closer to them with the increase of rotational frequency.

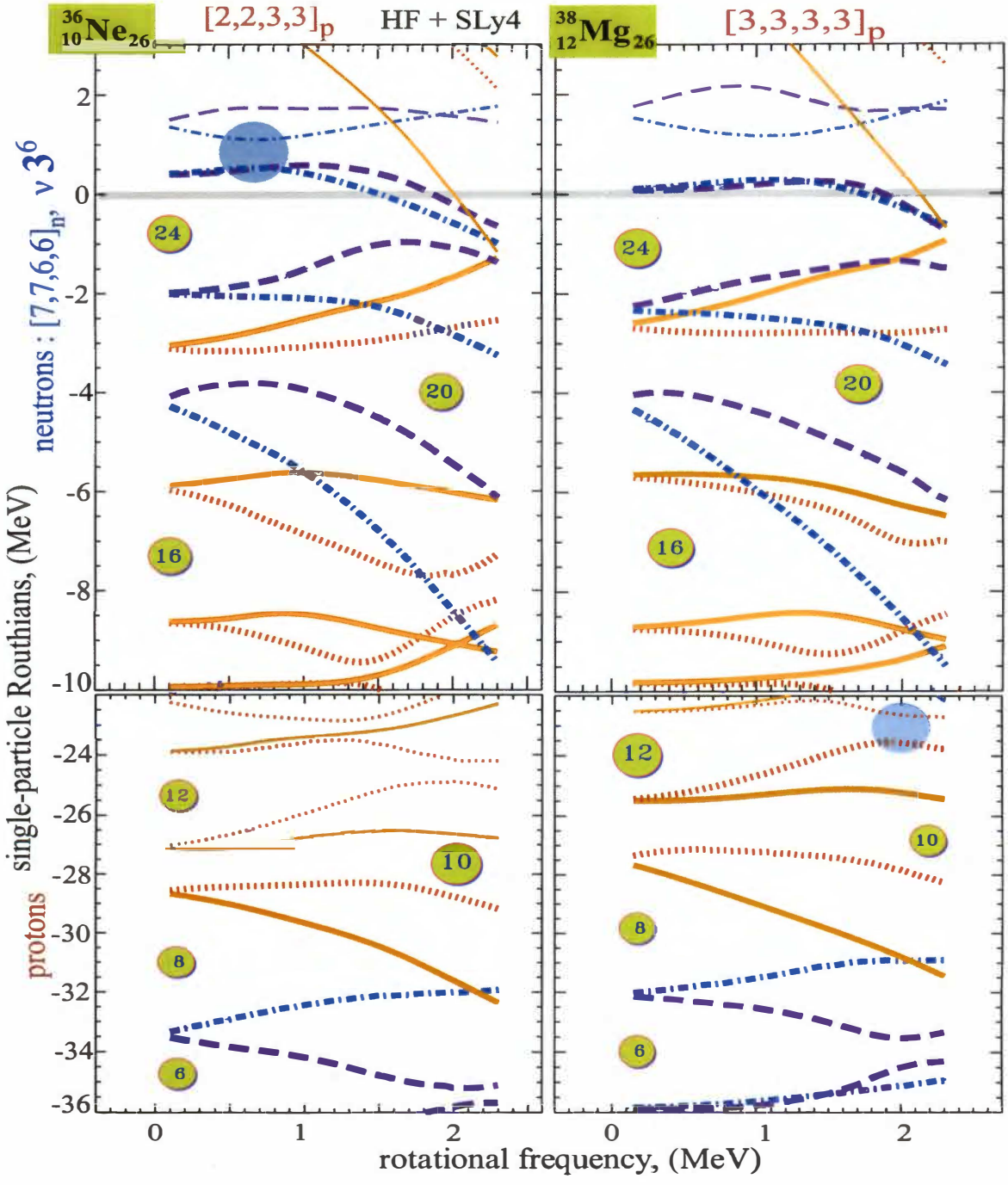

Figure 4.8: Single-particle Routhian diagrams for the lowest bands in the N=26 isotones of Ne and Mg.

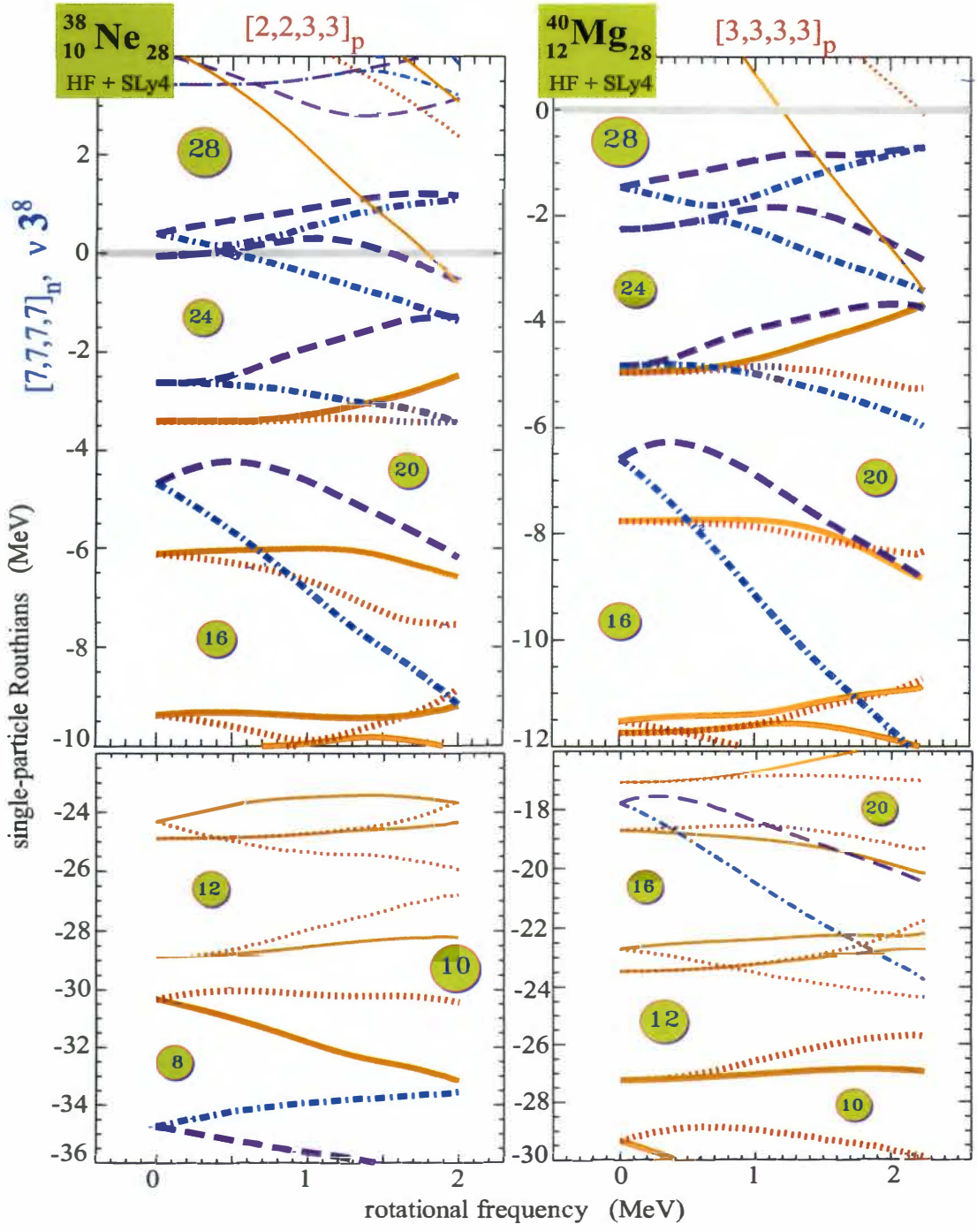

Figure 4.9: Single–particle Routhian diagrams for the N=28 isotones. Note the positive energy of the highest negative–parity neutron states and the occurrence of the $\mathcal{N}$ =4 intruder at high frequencies.

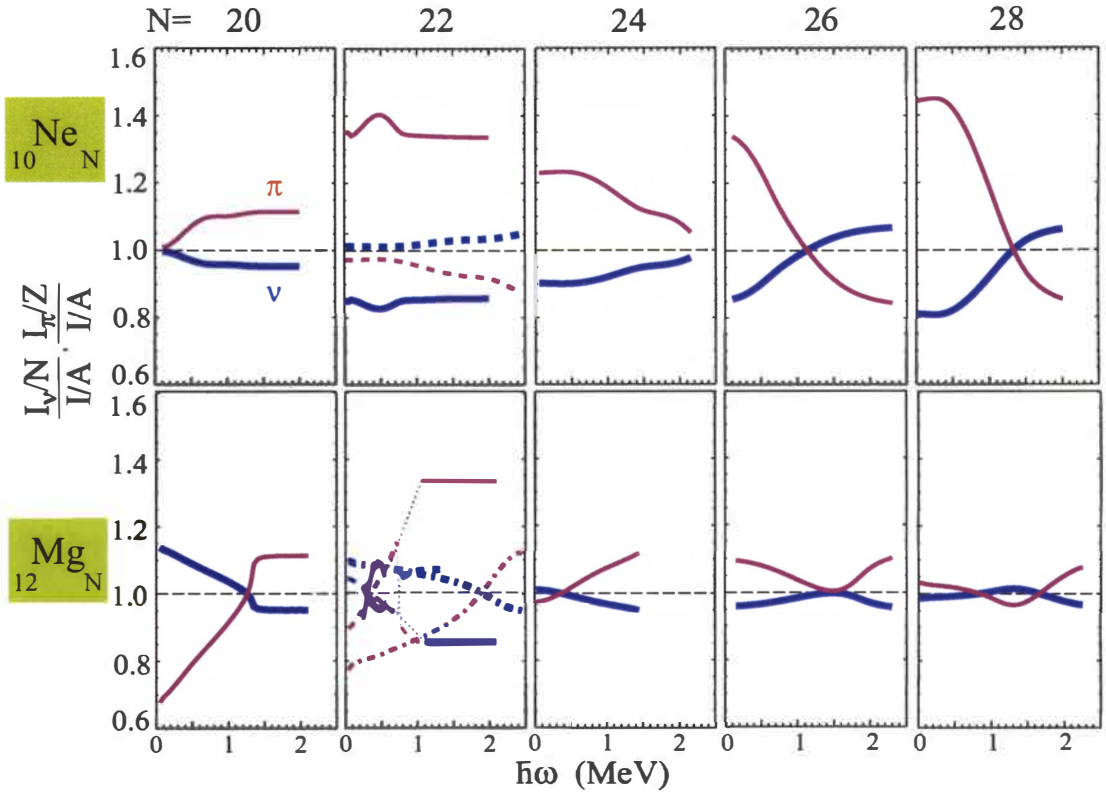

Figure 4.10: The ratio $\frac{I_\nu A}{IN}$ and $\frac{I_\pi A}{IZ}$ versus rotational frequency for the calculated bands in Ne and Mg. The $\frac{I_\nu A}{IN}$ values are shown by /thicker lines.

For further interpretation of the changes of collectivity we can analyze the total energy of the bands, (Fig. 4.11). The solid circles mark the terminated configurations, while the dashed circles indicate bands, for which only the protons have terminated. An interesting feature in the magnesia in Fig. 4.11 is that the energy decreases uniformly and almost additively with the gradual filling of the $f_{7/2}$ shell. The sequences 3^2, 3^3, 3^4 in the N=22 isotones show a lot of similarities. Here, the bands with fewer $\mathcal{N}$=3 occupied states are favored in energy. The occupation of the [321]3/2 neutron state instead of the [202]3/2 state shifts the band up by about 1.2 MeV, while delaying the termination until higher spins are reached.

Figure 4.12 shows the behavior of the static and dynamic moments of inertia. This plot should be analyzed together with the deformation trends given in Fig. 4.13. For all bands reaching or approaching termination at high frequencies, the dynamic moment of inertia drops to very small values because the total angular momentum stops increasing.

The trends observed in Fig. 4.12 can be better understood when we look at the changes of nuclear shape with angular momentum. Figure 4.13 shows the (β_2,γ) deformation trajectories, evaluated using equations (2.130–2.131) for all nuclei considered. One can see that, for both protons and neutrons, they start at $\beta_2 \approx$0.25–0.40 at the $\hbar\omega$=0 MeV and then smoothly proceed towards smaller β_2–values while increasing γ–deformation until they reach termination. Note that neutron deformations follow the proton ones very closely, their deviations being most visible

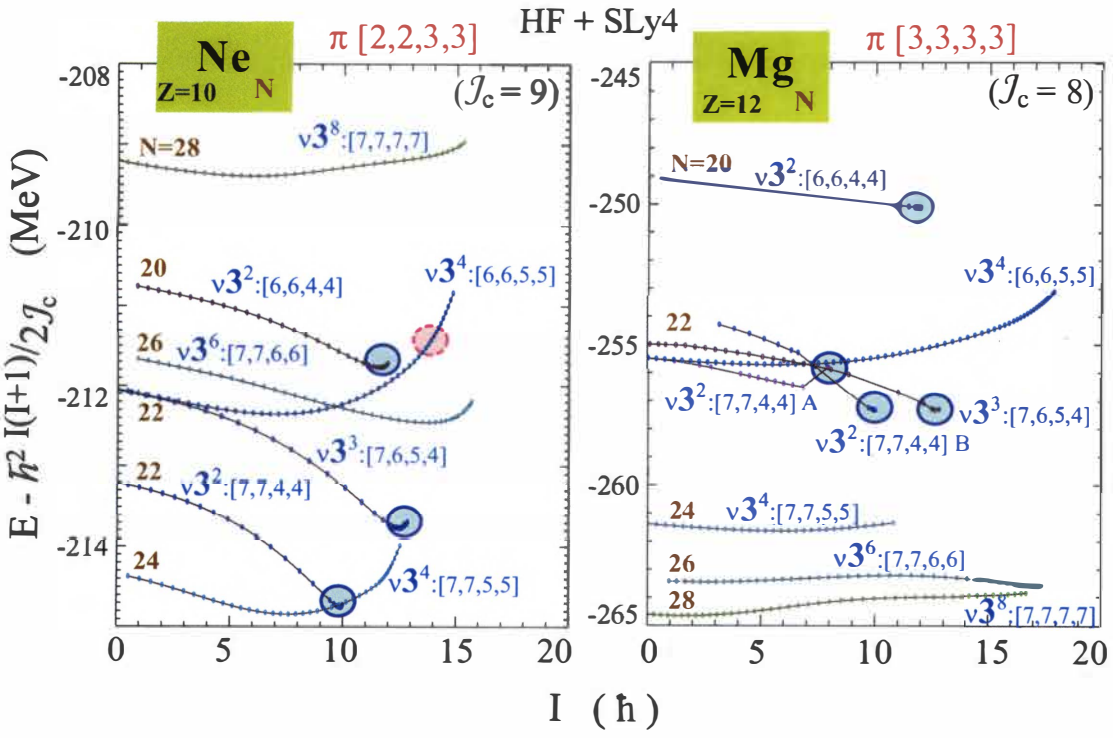

Figure 4.11: Total energy, plotted with respect to a smooth reference, as a function of angular momentum in Ne bands (left), and Mg (right) isotopes. The labels "A" and "B" refer to the two crossing configurations in ^{34}Mg.

at low spins. The isovector effect (deviation between neutron and proton deformations) appears to be the strongest in the N=26 isotones, where $\Delta\beta_2 \equiv \beta_2^p - \beta_2^n$ is nearly 0.05 at the lowest-frequency end of the trajectory. It is interesting to note for these isotones that the differences between β_2^p and β_2^n change signs as the angular momentum increases, causing the protons to be visibly less deformed at the top of the band. The behavior shown in Fig. 4.13 is characteristic of rotational structures built upon relatively few valence nucleons. The loss of collectivity with cranking frequency is rather fast due to the alignment of $\mathcal{N}$ =3 neutrons, which causes the termination at relatively low spins. Returning to Fig. 4.12, we see how the deformation changes are reflected in the moments of inertia.

In view of the small binding energy of the outermost ("skin") neutrons in these rapidly rotating nuclei, it would be interesting to look into the question of how likely they are to be ejected by the large centrifugal forces at high angular momenta. Although in our study there is little basis for speculation on this subject, the study of proton and neutron radii with cranking frequency could give some qualitative indications to guide us in such a study. Figure 4.14 shows the root–mean–square radii calculated in CHF. The immediate conclusion one can make from it is that there are insignificant changes in their values of less than 3% — indicating that, even at the

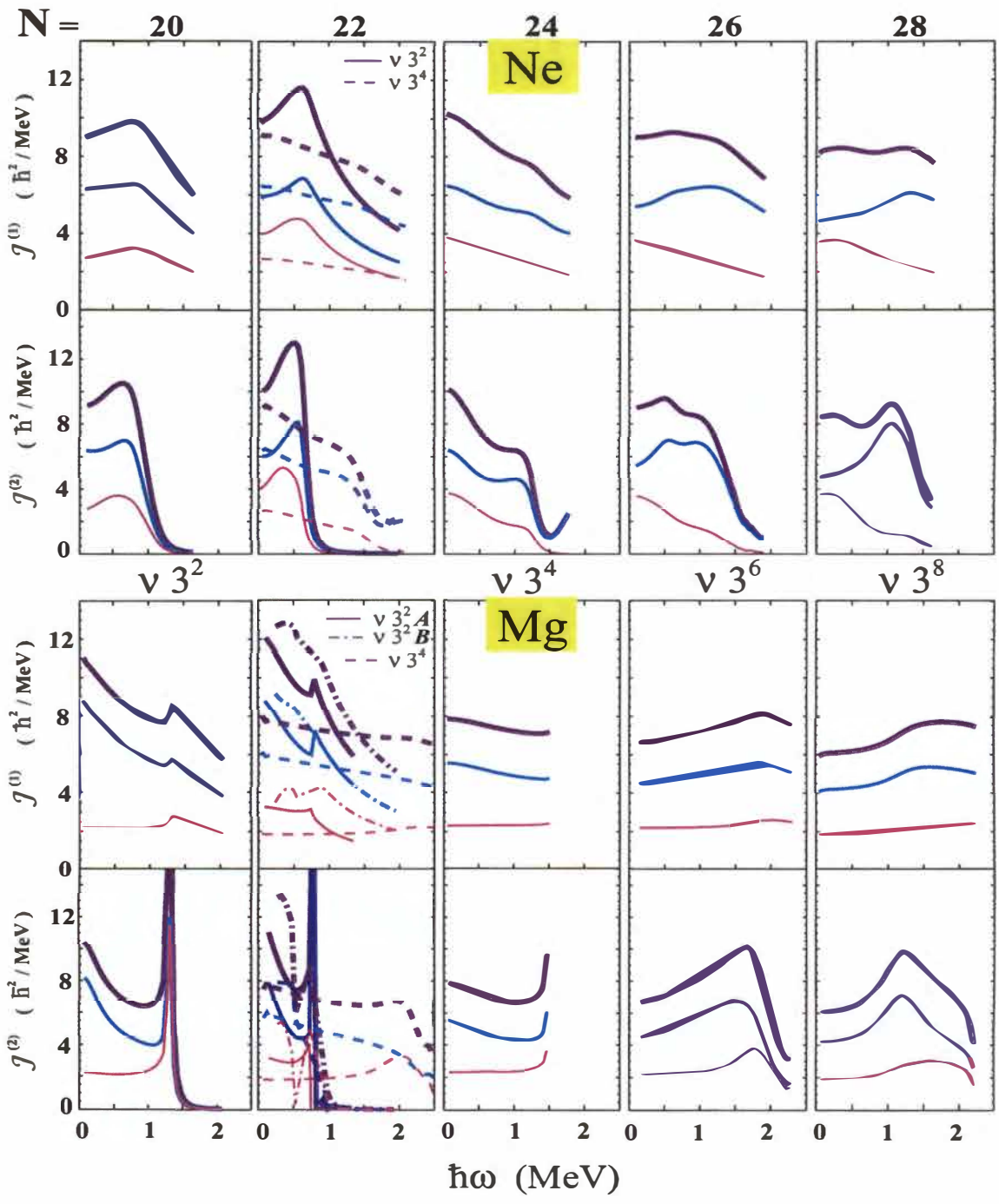

Figure 4.12: Neutron and proton static ($\mathcal{J}^{(1)}$) and dynamic ($\mathcal{J}^{(2)}$) moments of inertia in Ne and Mg isotopes. The total value is indicated by a thick line; proton and neutron contributions are also shown.

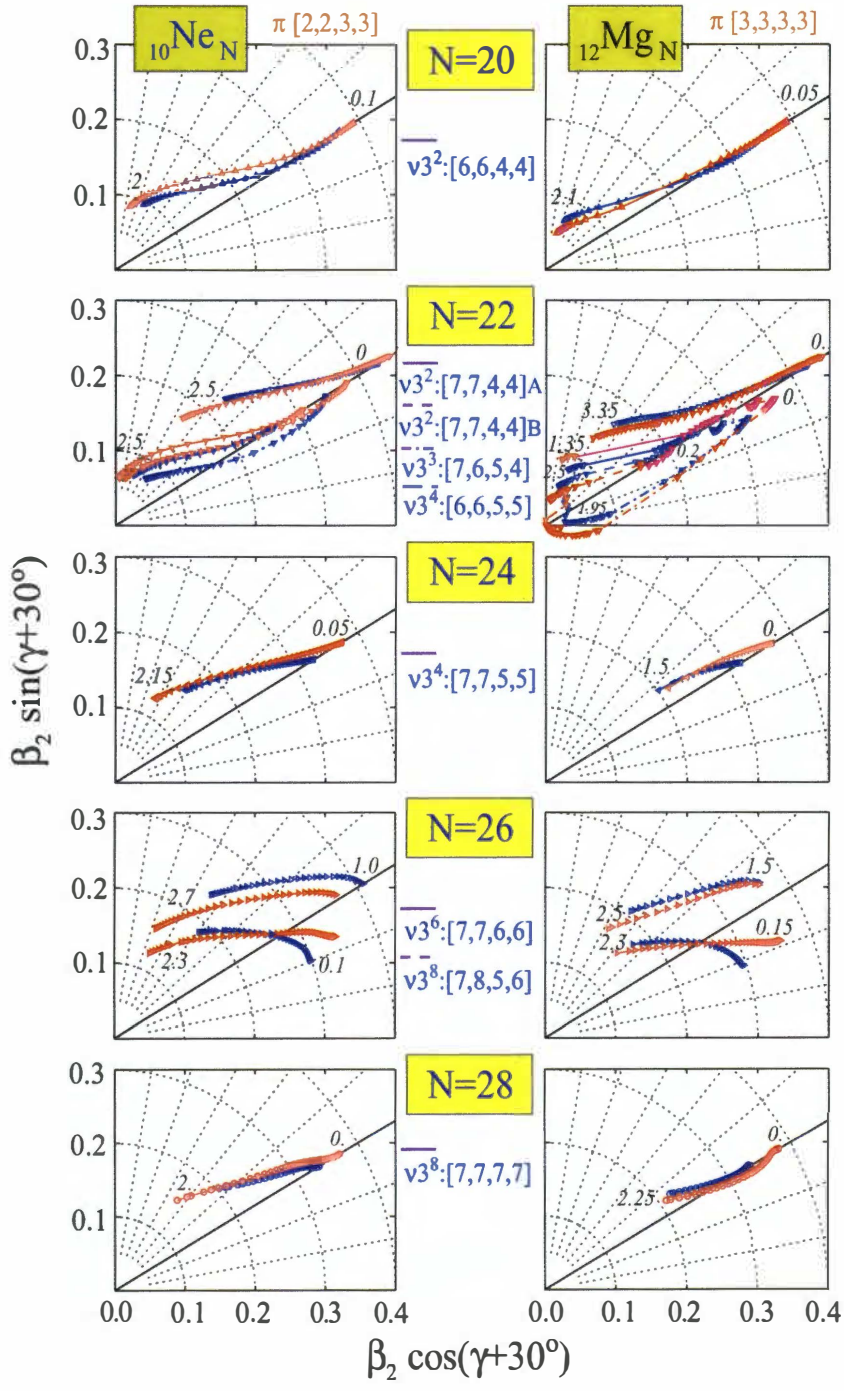

Figure 4.13: Neutron and proton (β_2,γ) deformation trajectories of the lowest band(s) in neutron–rich Ne and Mg isotopes starting with zero frequency (right ends). Protons are shown in lighter color. Values of $\hbar\omega$ in MeV are indicated by numbers next to the data points.

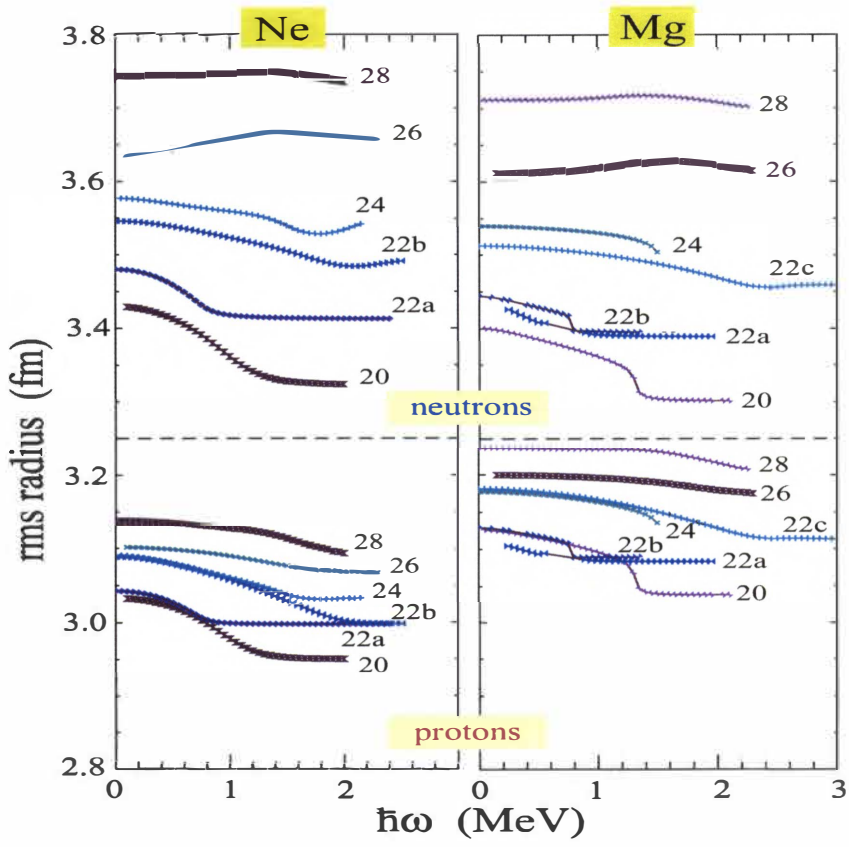

Figure 4.14: Root–mean–square radii as functions of rotational frequency for several rotational bands in Ne (left) and Mg (right) isotopes.

highest frequencies, the weakly–bound neutrons do not depart considerably from the remaining nucleons. The slight overall reduction is attributed predominantly to the decrease in β_2 as the band approaches termination. The neutron radii in the equivalent neutron configurations of different isotopes remain very similar, while the presence of the two extra protons in the Mg isotopes increase the proton radii by 0.1 fm on the average. Their numerical values seem to be entirely determined by their dependence on proton and neutron number.

Considering the results presented above, one can conclude that the expected isovector effects are not well pronounced at high angular momenta in the neutron-rich Ne and Mg isotopes. The valence neutrons in their configurations occupy $\mathcal{N}$=3 intruder states which, due to their large orbital angular momenta (causing them to face high centrifugal barriers), are fairly well localized within the nuclear volume, in spite of their weak binding.

We can summarize that in most cases, as a result of the Coriolis forces, the low–ℓ states (which are the most likely candidates for halo effects) will be crossed at high rotational frequencies by the high–ℓ intruder orbitals. Consequently, one shall not expect halo nuclei at high spins. In particular, our results show no indications in favor of a possible separation of the valence (skin) neutrons at high spins.

Chapter 5

Conclusion

"I would rather understand one cause than be King of Persia."
— Democritus of Abdera, 460–370 B.C.

This dissertation presents a systematic study of rotational configurations in nuclei away from the line of β–stability. The nuclear systems in the A$\sim$130 mass region, explored in Chapter 3 have moderate proton excess, with the lightest systems closely approaching the proton drip line. In the neutron–rich Ne–Mg region of Chapter 4 the isotopes were the farthest away from the stability valley, with more than twice as many neutrons as protons. Our work demonstrates that such exotic nuclei can have quasistable deformed states even at very high spins. The success of the mean–field approach for describing deformed nuclear states at high spins makes it possible to prove the central point in our analysis — that the self–consistent mean–field theories are well justified to be applied to a variety of different rotating nuclear systems with the benefit of conceptual clarity and significant predictive power across wide regions of nuclei.

The main results and conclusions of the dissertation can be summarized as follows :

- We carried out the first global self–consistent high–spin calculations in the A$\sim$130 superdeformed region, employing two different mean field theories in a comparative study. The extracted set of effective single–particle quadrupole moments and angular momentum alignments can be directly used in experimental analyses.

- The success of the comparative study, being based on the additivity approach demonstrated its validity and applicability in the A$\sim$130 region, implying that the extreme shell model concept is well justified at high angular momenta.

- The results of this study provide important information for experimentalists, allowing them to easily calculate the expected deformations and alignments in superdeformed bands. The predictive power of such calculations is a result of the systematized statistics and the impressive precision of the additivity analysis. In addition to the above, the information about the relative total Routhians for the bands in the same nucleus can serve as a guideline for in experimental ordering.

- In the theoretical results we included for the first time the quantitative impact of the effective values of q_{22} as corrections to the main effective quadrupole components q_{20} for the evaluation of the transition quadrupole moments q_t. This allows us to separate out the deformation components of a nuclear shape in the region in a systematic way, providing a basis for quantitative analysis of the role of single–particle contributions to the γ–softness.

- We made predictions for a large number of highly–deformed bands in the A$\sim$130 mass region, which includes structures yet unobserved experimentally. We also propose candidate configurations sorted by Routhian energy and parity–signature quantum numbers.

- The presented results indicate that the single–particle alignments are remarkably robust quantities, which in some cases do not vary significantly between self–consistent models, including the non–relativistic density–dependent Skyrme model and the relativistic mean field model.

- The remarkable precision of the additivity results for the quadrupole moments, on par with the results for the A$\sim$150 region [77], offers evidence that there is a conceptual universality of the theoretical models for both regions, thus establishing an intellectual bridge for the physical interpretation of superdeformation in the proton–rich nuclei in the wider mass range A=128–160. The two highly deformed regions might be treated comfortably on the same basis, within the framework of additivity using Skyrme Hartree–Fock methods, as the example of ^{142}Sm implies.

- The results of the additivity analysis for the values of q_{22} show the effects of γ–softness of the collective nuclear potential, The broadness of the Q_{22} distributions (Fig. 3.4) confirm the γ–softness in this region.

- In our Skyrme HF calculations, the effective alignments are overall different from the corresponding values of single–particle alignments. This indicates the importance of the shape polarization effects in the self–consistent mean field studies. In a number of cases, these effects alter drastically the single–particle alignments. Similarly, the effective quadrupole moments are also different from the single–particle quadrupole moments, suggesting a sizeable modification to their deformation–driving effects due to shape polarization.

  These deviations teach important lessons on the impact of self–consistency on single–particle quantities. Even more exciting is the fact that in some cases the "bare" and effective values are rather close — a puzzling observation, for which we do not have satisfactory explanation at the moment. Based on these comparisons, we are led to conclude that the use of bare single–particle values, as one is doing in, *e.g.*, the cranked shell model, can be quite misleading. In particular, angular momentum alignments extracted from the slopes of single–particle Routhians can not be trusted because they do not include the shape polarization effects.

- There are sound physical reasons preventing the weakly bound intruder neutrons from "breaking away" under the influence of Coriolis and centrifugal forces at high cranking frequencies, thus offering a possibility for observation of associated rotational bands. On the one hand, the variation of the neutron shell structure with neutron number, mainly influencing the position of the high-j unique–parity shell, is expected to modify the pattern of non–collective excitations in the rotating nucleus. On the other hand, since the Coriolis force mainly acts on the high-j orbitals, which are strongly localized within the nuclear

volume, no strong isovector effects (due to neutron halo or skin) are expected at high spins.

- Our calculations indicate that proton and neutron deformations are very similar even at extremely high rotational frequencies.
- The results show that the root–mean–square radii for protons and neutrons remain constant within a narrow interval throughout the cranking frequency range considered.
- We make predictions for the extent of the neutron drip line in the even–even Ne–Mg region and carry out the very first cranking calculations for rotational bands in halo/skin nuclei, and discuss the structure of their yrast bands.

Bibliography

Bibliography

[1] R. Bradbury, *Long After Midnight* (Alfred A. Knopf, New York, 1976).

[2] R. W. Laird *et al.*, Phys. Rev. Lett. **88**, 152501 (2002).

[3] E. Rutherford, Phil. Mag. **21**, 669 (1911).

[4] E. Rutherford, Phil. Mag. **37**, 537 (1919).

[5] W. Pauli, Naturwissenschaften **12**, 741 (1924).

[6] H. Schüler and T. Schmidt, Z. Physik **94**, 35 (1935).

[7] J. Chadwick, Nature **129**, 312 (1932).

[8] J. Chadwick, Proc. R. Soc. London, Ser. A **136**, 692 (1932).

[9] I. Curie and F. Joliot, C.R. Acad. Sci. **194**, 273,708,876,2208 (1932).

[10] C. F. von Weizsäcker, Z. Physik **96**, 431,461 (1935).

[11] N. Bohr, Nature **137**, 344 (1936).

[12] N. Bohr and F. Kalckar, Kgl. Dan. Vid. Selsk. **14**, (1937).

[13] N. Bohr and F. Kalckar, *Niels Bohr's Collected Work* (North–Holland Publ. Co., Amsterdam, 1985), Vol. 9.

[14] E. Teller and J. A. Wheeler, Phys. Rev. **53**, 778 (1938).

[15] E. Feenberg, Phys. Rev. **55**, 504 (1939).

[16] L. Meitner and O. Frisch, Nature **143**, 239 (1939).

[17] N. Bohr and J. A. Wheeler, Phys. Rev. **56**, 426 (1939).

[18] O. Haxel, T. H. D. Jensen, and H. E. Suess, Phys. Rev. **75**, 1766 (1949).

[19] M. Göppert-Mayer, Phys. Rev. **76**, 185 (1949).

[20] L. J. Rainwater, Phys. Rev. **79**, 432 (1950).

[21] A. Bohr and B. R. Mottelson, Phys. Rev. **90**, 717 (1953).

[22] A. Bohr, B. Mottelson, and J. Rainwater, Rev. Mod. Phys. **48**, 365,375,385 (1976).

[23] S. G. Nilsson, Dan. Mat.-Fys. Medd. **29**, (1955).

[24] S. Flügge, Ann. Physik **39**, 373 (1941).

[25] S. Polikanov *et al.*, Zh. Eksp. Teor. Fiz. **15**, 1016 (1962), Zh. Eksp. Teor. Fiz. **42**, 1464 (1962).

[26] C. Gustafsson, I. L. Lamm, B. Nilsson, and S. G. Nilsson, Ark. Fys. **36**, 613 (1966).

[27] V. M. Strutinsky, Nucl. Phys. A **95**, 420 (1967).

[28] H. J. Specht, J. Weber, E. Konecny, and D. Heunemann, Phys. Lett. B **41**, 43 (1972).

[29] Z. Szymański, *Fast Nuclear Rotation* (Clarendon Press, Oxford, 1983).

[30] S. G. Nilsson and I. Ragnarsson, *Shapes and Shells in Nuclear Structure* (Cambridge Univ. Press, Cambridge, 1995).

[31] S. Cohen, F. Plasil, and W. J. Swiatecki, Ann. Phys. (N.Y.) **82**, 557 (1974).

[32] A. Bohr and B. R. Mottelson, Physica Scr. A **10**, 13 (1974).

[33] A. Johnson, H. Ryde, and J. Sztarkier, Phys. Lett. B **34**, 7 (1971).

[34] A. Johnson, H. Ryde, and J. Sztarkier, Nucl. Phys. A **179**, 753 (1972).

[35] F. S. Stephens *et al.*, Phys. Rev. Lett. **29**, 438 (1972).

[36] F. S. Stephens and R. S. Simon, Nucl. Phys. A **183**, 257 (1972).

[37] C. Baktash *et al.*, Phys. Rev. Lett. **54**, 978 (1985).

[38] T. Bengtsson *et al.*, Physica Scr. **24**, 200 (1981).

[39] J. L. Wood *et al.*, Phys. Rep. **215**, 101 (1992).

[40] V. P. Perelygin *et al.*, Zh. Eksp. Teor. Fiz. **15**, 1022 (1962), Zh. Eksp. Teor. Fiz. **42**, 1470 (1962).

[41] S. Åberg, Physica Scr. **25**, 23 (1982).

[42] V. M. Strutinsky, Nucl. Phys. A **122**, 1 (1968).

[43] R. Bengtsson *et al.*, Phys. Lett. B **57**, 301 (1975).

[44] P. J. Nolan and P. J. Twin, Annu. Rev. Nucl. Part. Sci. **38**, 533 (1988).

[45] I. Ragnarsson, T. Bengtsson, G. Leander, and S. Åberg, Nucl. Phys. A **347**, 287 (1980).

[46] J. Dudek and W. Nazarewicz, Phys. Rev. C **31**, 298 (1985).

[47] B. M. Nyakó *et al.*, Phys. Rev. Lett. **52**, 507 (1984).

[48] Y. Schutz *et al.*, Phys. Rev. Lett. **48**, 1535 (1982).

[49] P. J. Twin *et al.*, Phys. Rev. Lett. **57**, 811 (1986).

[50] A. J. Kirwan *et al.*, Phys. Rev. Lett. **58**, 467 (1987).

[51] R. B. Firestone, B. Singh, and S. Y. F. Chu, At. Data Nucl. Data Tables (1997).

[52] X.-L. Han and C.-L. Wu, At. Data Nucl. Data Tables **73**, 43 (1999).

[53] B. Singh, R. Zywina, and R. B. Firestone, Nucl.Data Sheets **97**, 241 (2002).

[54] A. Akmal, V. R. Pandharipande, and D. G. Ravenhall, Phys. Rev. C **58**, 1804 (1998).

[55] W. Kohn and L. J. Sham, Phys. Rev. A **140**, 1133 (1965).

[56] R. M. Dreizler and E. K. U. Gross, *Density Functional Theory* (Springer Verlag, Berlin, 1990).

[57] N. Argaman and G. Makow, Am. J. Phys. **68**, 69 (2000).

[58] B. A. Brown, Phys. Rev. C **58**, 220 (1998).

[59] J. P. Perdew, K. Burke, and M. Ernzerhof, Phys. Rev. Lett. **77**, 3865 (1996).

[60] J. P. Perdew, K. Burke, and M. Ernzerhof, Phys. Rev. Lett. **78**, 1396 (1997).

[61] J. P. Perdew, S. Kurth, A. Zupan, and P. Blaha, Phys. Rev. Lett. **82**, 2544 (1999).

[62] P. Ring, Prog. Part. Nucl. Phys. **37**, 193 (1996).

[63] B. D. Serot and J. D. Walecka, Adv. Nucl. Phys. **16**, 1 (1986).

[64] B. D. Serot, Rep. Prog. Phys. **55**, 1855 (1992).

[65] B. D. Serot and J. D. Walecka, Int. J. Mod. Phys. E **6**, 515 (1997).

[66] F. S. Stephens, Rev. Mod. Phys. **47**, 43 (1975).

[67] S. Frauendorf and F. R. May, Phys. Lett. B **125**, 245 (1983).

[68] A. Faessler, M. Ploszajczak, and K. R. Sandya Devi, Phys. Rev. **36**, 1028 (1976).

[69] H. A. Jahn and E. Teller, Proc. R. Soc. London, Ser. A **161**, 220 (1937).

[70] B. R. Mottelson and J. G. Valatin, Phys. Rev. Lett. **5**, 511 (1969).

[71] B. Banerjee, H. J. Mang, and P. Ring, Nucl. Phys. A **215**, 564 (1973).

[72] Y. R. Shimizu *et al.*, Rev. Mod. Phys. **61**, 131 (1989).

[73] A. Bohr, Mat. Fys. Medd. Dan. Vid. Selsk. **26**, (1952).

[74] W. Satuła, J. Dobaczewski, and W. Nazarewicz, Phys. Rev. Lett. **81**, 3599 (1998).

[75] P.-G. Reinhard and E. W. Otten, Nucl. Phys. A **420**, 173 (1984).

[76] W. Nazarewicz, Nucl. Phys. A **574**, 27c (1994).

[77] W. Satuła, J. Dobaczewski, J. Dudek, and W. Nazarewicz, Phys. Rev. Lett. **77**, 5182 (1996).

[78] P. Ring and P. Schuck, *The Nuclear Many-Body Problem* (Springer Verlag, Berlin, 1980).

[79] B. R. Mottelson and S. G. Nilsson, Phys. Rev. **99**, 1615 (1955).

[80] J. Dudek *et al.*, J. Phys. G **5**, 1359 (1987).

[81] S. Cwiok *et al.*, Comput. Phys. Commun. **46**, 379 (1987).

[82] R. Bengtsson, J. Dudek, W. Nazarewicz, and P. Olanders, Physica Scr. **39**, 196 (1989).

[83] G. Andersson *et al.*, Nucl. Phys. A **268**, 205 (1976).

[84] W. Nazarewicz and I. Ragnarsson, *Handbook of Nuclear Properties, Eds. D.N. Poenaru and W. Greiner* (Clarendon Press, Oxford, 1996), p. 80.

[85] B. H. Smith, Ph.D. thesis, University of Tennessee, 1998.

[86] E. A. Rosenkilde, J. Math. Phys. **8**, 84,88,98 (1967).

[87] R. A. Lyttleton, *The Stability of Rotating Liquid Masses* (Cambridge Univ. Press, Cambridge, 1958).

[88] M. J. A. de Voigt, J. Dudek, and Z. Szymanski, Rev. Mod. Phys. **55**, 949 (1983).

[89] H. Hubel *et al.*, Nucl. Phys. A **453**, 316 (1986).

[90] D. Ye *et al.*, Nucl. Phys. A **537**, 207 (1992).

[91] I. G. Bearden *et al.*, Nucl. Phys. A **574**, 27c (1994).

[92] D. R. Inglis, Phys. Rev. **97**, 71 (1955).

[93] D. R. Inglis, Phys. Rev. **103**, 1786 (1956).

[94] R. Bengtsson and S. Frauendorf, Nucl. Phys. A **314**, 27 (1979).

[95] A. Bohr and B. R. Mottelson, *Nuclear Structure, vol. 2* (W. A. Benjamin, New York, 1975).

[96] D. Gogny, in *Nuclear Self-Consistent Fields*, edited by G. Ripka and M. Porneuf (North–Holland Publ. Co., Amsterdam, 1975), p. 333.

[97] T. H. R. Skyrme, Phil. Mag. **1**, 1043 (1956).

[98] D. Vautherin and D. M. Brink, Phys. Rev. C **5**, 626 (1972).

[99] J. W. Negele and D. Vautherin, Phys. Rev. C **5**, 1472 (1972).

[100] J. W. Negele and D. Vautherin, Phys. Rev. C **11**, 1031 (1975).

[101] D. W. L. Sprung *et al.*, Nucl. Phys. A **253**, 1 (1975).

[102] P. Quentin and H. Flocard, Annu. Rev. Nucl. Part. Sci. **28**, 523 (1978).

[103] S. Åberg, H. Flocard, and W. Nazarewicz, Annu. Rev. Nucl. Part. Sci. **40**, 439 (1990).

[104] C. Baktash, B. Haas, and W. Nazarewicz, Annu. Rev. Nucl. Part. Sci. **45**, 485 (1995).

[105] P. Butler and W. Nazarewicz, Rev. Mod. Phys. **68**, 349 (1996).

[106] T. H. R. Skyrme, Nucl. Phys. **9**, 615 (1959).

[107] S. A. Moszkowski, Phys. Rev. C **2**, 402 (1970).

[108] K. L. G. Heyde, *The Nuclear Shell Model* (Springer Verlag, New York, 1994), second Edition.

[109] E. Chabanat *et al.*, Nucl. Phys. A **635**, 231 (1998).

[110] J. Dobaczewski and J. Dudek, Comput. Phys. Commun. **102**, 166 (1997).

[111] P. Bonche *et al.*, Nucl. Phys. A **443**, 39 (1985).

[112] D. Baye and P.-H. Heenen, J. Phys. A **19**, 2041 (1986).

[113] A. S. Umar, M. R. Strayer, J. S. Wu, and M. C. Güçlü", Phys. Rev. C **44**, 2512 (1991).

[114] C. Chinn, A. Umar, M. Valliéres, and M. R. Strayer, Phys. Rev. E **50**, 5096 (1994).

[115] C. Chinn, A. Umar, M. Valliéres, and M. R. Strayer, Comput. Phys. Commun. **86**, 40 (1995).

[116] K. T. R. Davies, H. Flocard, S. Krieger, and M. S. Weiss, Nucl. Phys. A **342**, 111 (1980).

[117] J. Dobaczewski, H. Flocard, and J. Treiner, Nucl. Phys. A **422**, 103 (1984).

[118] J. L. Egido, H.-J. Mang, and P. Ring, Nucl. Phys. A **334**, 1 (1980).

[119] J. L. Egido, J. Lessing, V. Martin, and L. M. Robledo, Nucl. Phys. A **594**, 70 (1995).

[120] D. Gogny, Nucl. Phys. A **237**, 399 (1975).

[121] M. Girod and B. Grammaticos, Phys. Rev. C **27**, 2317 (1983).

[122] Y. M. Engel *et al.*, Nucl. Phys. A **249**, 215 (1975).

[123] M. Waroquier, K. Heyde, and G. Wenes, Nucl. Phys. A **404**, 269; 298 (1983).

[124] D. Vautherin and D. M. Brink, Phys. Rev. C **5**, 626 (1972).

[125] X. Campi, D. W. Sprung, and J. Martorell, Nucl. Phys. A **223**, 541 (1974).

[126] W. Bertozzi, J. Friar, J. Heisenberg, and J. W. Negele, Phys. Lett. B **41**, 408 (1972).

[127] J. C. Slater, Phys. Rev. **81**, 385 (1951).

[128] C. Titin-Schnaider and P. Quentin, Phys. Lett. B **49**, 397 (1974).

[129] R. B. Wiringa, V. Fiks, and A. Fabrocini, Phys. Rev. C **38**, 1010 (1988).

[130] J. Dobaczewski and J. Dudek, Comput. Phys. Commun. **102**, 183 (1997).

[131] T. Werner *et al.*, Phys. Lett. B **333**, 303 (1994).

[132] T. Werner *et al.*, Nucl. Phys. A **597**, 327 (1996).

[133] J. Dobaczewski and J. Dudek, Phys. Rev. C **52**, 1827 (1995).

[134] J. Dobaczewski and J. Dudek, Phys. Rev. C **55**, 3177 (1997).

[135] J. D. Walecka, Ann. Phys. (N.Y.) **83**, 491 (1974).

[136] J. Boguta and A. R. Bodmer, Nucl. Phys. A **292**, 413 (1977).

[137] Y. K. Gambhir, P. Ring, and A. Thimet, Ann. Phys. (N.Y.) **198**, 132 (1990).

[138] C. J. Horowitz and B. D. Serot, Nucl. Phys. A **399**, 529 (1983).

[139] A. Bouyssy, J. F. Mathiot, N. Van Giai, and S. Marcos, Phys. Rev. C **36**, 380 (1987).

[140] P.-G. Reinhard, Rep. Prog. Phys. **52**, 439 (1989).

[141] M. M. Sharma, G. A. Lalazissis, J. König, and P. Ring, Phys. Rev. Lett. **74**, 3744 (1995).

[142] P.-G. Reinhard and H. Flocard, Nucl. Phys. A **584**, 467 (1995).

[143] Z. Ren *et al.*, Z. Phys. A **353**, 363 (1996).

[144] J. P. Maharana, L. S. Warrier, and Y. K. Gambhir, Ann. Phys. (N.Y.) **250**, 237 (1996).

[145] R. J. Furnstahl, B. D. Serot, and H. B. Tang, Nucl. Phys. A **598**, 539 (1996).

[146] P.-G. Reinhard *et al.*, Z. Phys. A **323**, 13 (1986).

[147] Y.-X. Luo *et al.*, Z. Phys. A **329**, 125 (1988).

[148] R. M. Clark *et al.*, Phys. Rev. Lett. **76**, 3510 (1996).

[149] R. A. Sorensen, Rev. Mod. Phys. **45**, 353 (1973).

[150] I. Hamamoto, Phys. Lett. B **61**, 343 (1976).

[151] E. Marshalek and A. Goodman, Nucl. Phys. A **294**, 92 (1978).

[152] T. Bengtsson and I. Ragnarsson, Nucl. Phys. A **436**, 14 (1985).

[153] W. Nazarewicz *et al.*, Nucl. Phys. A **435**, 397 (1985).

[154] K. Rutz *et al.*, Nucl. Phys. A **634**, 67 (1998).

[155] K. Rutz, M. Bender, P.-G. Reinhard, and J. Maruhn, Phys. Lett. B **468**, 1 (1999).

[156] J. Engel *et al.*, Phys. Rev. C **60**, 014302 (1999).

[157] M. Bender, J. Dobaczewski, J. Engel, and W. Nazarewicz, Phys. Rev. C **65**, 054322 (2002).

[158] F. R. Xu, R. Wyss, and P. M. Walker, Phys. Rev. C **60**, 051301 (1999).

[159] R. Wyss *et al.*, Phys. Lett. B **215**, 211 (1988).

[160] I. Hamamoto and B. Mottelson, Phys. Lett. B **127**, 281 (1983).

[161] A. T. Semple *et al.*, Phys. Rev. Lett. **76**, 3671 (1996).

[162] D. Santos *et al.*, Phys. Rev. Lett. **74**, 1708 (1995).

[163] K. Hauschild *et al.*, Phys. Rev. C **52**, R2283 (1995).

[164] R. Bengtsson, S. Frauendorf, and F. R. May, At. Data Nucl. Data Tables **35**, 15 (1986).

[165] O. Hausser *et al.*, Nucl. Phys. A **179**, 465 (1972).

[166] A. Afanasjev *et al.*, Phys. Rep. **??**, ?? (2000).

[167] I. Hamamoto and Z. Xing, Physica Scr. **33**, 210 (1986).

[168] G. de France, C. Baktash, B. Haas, and W. Nazarewicz, Phys. Rev. C **53**, R1070 (1996).

[169] S. Åberg, L.-O. Jönsson, L. B. Karlsson, and I. Ragnarsson, Z. Phys. A **358**, 269 (1997).

[170] L. B. Karlsson, I. Ragnarsson, and S. Åberg, Phys. Lett. B **416**, 16 (1998).

[171] L. B. Karlsson, I. Ragnarsson, and S. Åberg, Nucl. Phys. A **639**, 654 (1997).

[172] P. R. Bevington, *Data Reduction and Error Analysis for the Physical Sciences* (McGraw–Hill Publ. Co., New York, 1969).

[173] C. H. Lawson and R. J. Hanson, *Solving Least Squares Problems* (Prentice–Hall, New York, 1974).

[174] M. T. Matev *et al.*, to be published (unpublished).

[175] D. Laertius, *Lives of the Philosophers : Life of Heraclitus* **VI**, *transl. C. D. Yonge* (Henry G. Bohn, London, 1853).

[176] K. Löbner, M. Vetter, and V. Höning, Nucl. Data, Sect. A **7**, 495 (1970).

[177] J. Dudek, Prog. Part. Nucl. Phys. **28**, 131 (1992).

[178] H. El-Samman *et al.*, Nucl. Phys. A **427**, 397 (1984).

[179] E. M. Beck *et al.*, Phys. Rev. Lett. **58**, 2182 (1987).

[180] E. M. Beck *et al.*, Phys. Lett. B **195**, 531 (1987).

[181] R. Wadsworth *et al.*, J. Phys. G **13**, L207 (1987).

[182] E. S. Paul *et al.*, Phys. Rev. Lett. **61**, 42 (1988).

[183] Y.-X. Luo *et al.*, Z. Phys. A **329**, 125 (1987).

[184] A. Galindo-Uribarri *et al.*, Phys. Rev. C **50**, R2655 (1994).

[185] F. G. Kondev *et al.*, Eur. Phys. J. A **2**, 249 (1998).

[186] F. G. Kondev *et al.*, J. Phys. G **25**, 893 (1999).

[187] A. Galindo-Uribarri *et al.*, Phys. Rev. C **54**, 1057 (1996).

[188] A. V. Afanasjev and I. Ragnarsson, Nucl. Phys. A **608**, 176 (1996).

[189] A. Galindo-Uribarri *et al.*, Phys. Rev. C **54**, R454 (1996).

[190] F. G. Kondev *et al.*, Phys. Rev. C **59**, 3076 (1999).

[191] R. Wadsworth *et al.*, Nucl. Phys. A **526**, 188 (1991).

[192] F. Lerma *et al.*, Phys. Rev. Lett. **83**, 5447 (1999).

[193] P. H. Regan *et al.*, J. Phys. G **18**, 847 (1992).

[194] D. Nisius *et al.*, Phys. Lett. B **392**, 18 (1997).

[195] B. C. Busse *et al.*, Phys. Rev. C **57**, R1017 (1998).

[196] F. G. Kondev *et al.*, Phys. Rev. C **60**, 011303 (1999).

[197] S. M. Mullins *et al.*, Phys. Rev. C **45**, 2683 (1992).

[198] M. A. Deleplanque *et al.*, Phys. Rev. C **52**, R2302 (1995).

[199] T. B. Brown *et al.*, Phys. Rev. C **56**, R1210 (1997).

[200] B. H. Smith *et al.*, Phys. Lett. B **443**, 89 (1998).

[201] K. Hauschild *et al.*, Phys. Rev. C **50**, 707 (1994).

[202] S. Shi *et al.*, Phys. Rev. C **37**, 1478 (1988).

[203] D. Bazzacco *et al.*, Phys. Rev. C **49**, R2281 (1994).

[204] D. Bazzacco *et al.*, Phys. Rev. C **58**, 2002 (1998).

[205] R. Wadsworth *et al.*, Nucl. Phys. A **526**, 188 (1991).

[206] D. Bazzacco *et al.*, Phys. Lett. B **309**, 235 (1993).

[207] H. Flocard, P. Quentin, A. K. Kerman, and D. Vautherin, Nucl. Phys. A **203**, 433 (1973).

[208] W. Koepf and P. Ring, Nucl. Phys. A **493**, 61 (1989).

[209] A. V. Afanasjev, J. König, and P. Ring, Nucl. Phys. A **608**, 107 (1996).

[210] A. V. Afanasjev, G. A. Lalazissis, and P. Ring, Nucl. Phys. A **634**, 395 (1998).

[211] A. V. Afanasjev, I. Ragnarsson, and P. Ring, Phys. Rev. C **59**, 3166 (1999).

[212] G. Hackman *et al.*, Phys. Rev. C **47**, R433 (1993).

[213] G. Hackman *et al.*, Phys. Rev. C **52**, R2293 (1995).

[214] G. Hackman *et al.*, Phys. Lett. B **416**, 268 (1998).

[215] S. M. Mullins *et al.*, Phys. Rev. Lett. **66**, 1677 (1991).

[216] J. N. Wilson *et al.*, Phys. Rev. C **55**, 519 (1997).

[217] A. T. Semple *et al.*, J. Phys. G **24**, 1125 (1998).

[218] W. Nazarewicz, G. A. Leander, and J. Dudek, Nucl. Phys. A **467**, 437 (1987).

[219] W. Nazarewicz, R. Wyss, and A. Johnson, Nucl. Phys. A **503**, 285 (1989).

[220] W. Nazarewicz, B. Sherril, I. Tanihata, and P. van Duppen, Nucl. Phys. News **6**, 17 (1996).

[221] Technical report, D.O.E., (unpublished), report 1997, `http://www.er.doe.gov/-production/henp/isolpaper.pdf`.

[222] E. P. Wigner, Phys. Rev. **73**, 1002 (1948).

[223] U. Fano, Phys. Rev. **124**, 1866 (1961).

[224] T. Uchiyama and H. Morinaga, Z. Phys. A **320**, 273 (1985).

[225] S. A. Fayans, Phys. Lett. B **267**, 443 (1991).

[226] M. Yokoyama, T. Otsuka, and N. Fukunishi, Phys. Rev. C **52**, 1122 (1995).

[227] H. Sagawa *et al.*, Z. Phys. A **351**, 385 (1995).

[228] I. Hamamoto, H. Sagawa, and X. Zhang, Phys. Rev. C **53**, 765 (1996).

[229] E. G. Lanza, Nucl. Phys. A **649**, 344 (1999).

[230] F. Tondeur, Z. Phys. A **288**, 97 (1978).

[231] J. Dobaczewski, I. Hamamoto, W. Nazarewicz, and J. A. Sheikh, Phys. Rev. Lett. **72**, 981 (1994).

[232] J. Dobaczewski *et al.*, Phys. Rev. C **53**, 2809 (1996).

[233] *Physics and Techniques of Secondary Nuclear Beams*, edited by J. F. Brouandet, B. Fernandez, and M. Bex (Editions Frontières, Gif-sur-Yvette, 1992).

[234] E. Roeckl, Rep. Prog. Phys. **55**, 1661 (1992).

[235] J. Dobaczewski and W. Nazarewicz, Phil. Trans. R. Soc. Lond. A **356**, 2007 (1998).

[236] The RIA White Paper, 2002, `http://www.orau.org/ria/`.

[237] K. L. G. Heyde, *Basic Ideas and Concepts in Nuclear Physics : An Introductory Approach, 2nd Ed.* (Institute of Physics, Bristol and Philadelphia, 1999).

[238] Workshop on the Physics of Halo Nuclei, 2001, `http://www.ph.surrey.ac.uk/npg/-confs/ecthalo.html`.

[239] W. Benenson, in *Proc. Int. Workshop XXIV, Extremes of Nuclear Structure* (GSI, Hirschegg, Austria, 1996), p. 252.

[240] M. V. Zhukov *et al.*, Phys. Rep. **231**, 151 (1993).

[241] K. Riisager, A. S. Jensen, and P. Møller, Nucl. Phys. A **548**, 393 (1992).

[242] A. Mueller and B. Sherril, Annu. Rev. Nucl. Part. Sci. **43**, 529 (1993).

[243] K. Riisager, Rev. Mod. Phys. **66**, 1105 (1994).

[244] P. G. Hansen, A. S. Jensen, and B. Jonson, Annu. Rev. Nucl. Part. Sci. **45**, 591 (1995).

[245] T. Misu, Ph.D. thesis, University of Tennessee, Knoxville, 1997.

[246] S. Mizutori *et al.*, Phys. Rev. C **61**, 044326 (2000).

[247] I. Tanihata *et al.*, Phys. Lett. B **160**, 380 (1985).

[248] I. Tanihata *et al.*, Phys. Lett. B **206**, 592 (1988).

[249] R. J. Glauber, *Lectures in Nuclear Physics* (Interscience Publ. Co., New York, 1959), p. 315.

[250] I. Tanihata *et al.*, Phys. Rev. Lett. **55**, 2676 (1985).

[251] Halo Physics, 2001, `http://fy.chalmers.se/subatom/halo/halo.html`.

[252] N. Fukunishi, T. Otsuka, and I. Tanihata, Phys. Rev. C **48**, 1648 (1993).

[253] P. E. Hodgson, *Nuclear Reactions and Nuclear Structure* (Clarendon Press, Oxford, 1971).

[254] C. J. Batty, E. Friedman, H. J. Gills, and H. Rebel, Adv. Nucl. Phys. **19**, 1 (1989).

[255] A. Krasznahorkay *et al.*, Phys. Rev. Lett. **66**, 1287 (1991).

[256] T. Suzuki *et al.*, Phys. Rev. Lett. **75**, 3241 (1995).

[257] L. Chulkov *et al.*, Nucl. Phys. A **603**, 219 (1996).

[258] T. Suzuki *et al.*, Nucl. Phys. A **616**, 286 (1997).

[259] T. Suzuki *et al.*, Nucl. Phys. A **630**, 661 (1998).

[260] O. Bochkarev *et al.*, Eur. Phys. J. A **1**, 15 (1998).

[261] F. Maréchal *et al.*, Phys. Rev. C **60**, 034615 (1999).

[262] R. H. Helm, Phys. Rev. **104**, 1466 (1956).

[263] M. Rosen, R. Raphael, and H. Überall, Phys. Rev. **163**, 927 (1967).

[264] M. Rosen and R. Raphael, Phys. Rev. C **1**, 547 (1970).

[265] P. Durgapal and D. S. Onley, Nucl. Phys. A **368**, 429 (1981).

[266] J. Friedrich and N. Vögler, Nucl. Phys. A **373**, 192 (1982).

[267] J. Friedrich and P.-G. Reinhard, Phys. Rev. C **33**, 335 (1986).

[268] J. Friedrich, N. Vögler, and P.-G. Reinhard, Nucl. Phys. A **459**, 10 (1986).

[269] D. W. L. Sprung, N. Yamanishi, and D. C. Zheng, Nucl. Phys. A **550**, 89 (1992).

[270] V. E. Starodubsky and M. M. Hintz, Phys. Rev. C **49**, 2118 (1994).

[271] T. W. Donnely, J. Dubach, and I. Sick, Nucl. Phys. A **503**, 589 (1989).

[272] S. J. Pollock, E. N. Fortson, and L. Wilets, Phys. Rev. C **46**, 2587 (1992).

[273] C. J. Horowitz, Phys. Rev. C **47**, 826 (1993).

[274] C. J. Horowitz, S. J. Pollock, P. A. Souder, and R. Michaels, Technical report, Los Alamos, (unpublished), archive `nucl-th/9912038`.

[275] W. M. Alberico and A. Molinari, Technical report, Los Alamos, (unpublished), nucl-th/9904026.

[276] D. Vretenar *et al.*, Phys. Rev. C **61**, 064307 (2000).

[277] K. Heyde *et al.*, Phys. Rep. **102**, 291 (1983).

[278] I. Tanihata, Prog. Part. Nucl. Phys. **35**, 505 (1995).

[279] R. Estep *et al.*, Phys. Rev. C **39**, 76 (1989).

[280] C. Y. Wu *et al.*, Phys. Rev. C **57**, 3466 (1998).

[281] H. Dejbakhsh and S. Bouttchenko, Phys. Rev. C **52**, 1810 (1995).

[282] J. A. Shannon *et al.*, Phys. Lett. B **336**, 136 (1994).

[283] S. Schoedder *et al.*, Z. Phys. A **352**, 237 (1995).

[284] H. Iwasaki *et al.*, Phys. Lett. B **481**, 7 (2000).

[285] H. Iwasaki *et al.*, Phys. Lett. B **491**, 8 (2000).

[286] S. J. Asztalos *et al.*, Phys. Rev. C **60**, 044307 (1999).

[287] G. J. Lane *et al.*, Nucl. Phys. A **682**, 71c (2001).

[288] A. Navin *et al.*, Phys. Rev. Lett. **81**, 5089 (1998).

[289] T. Aumann *et al.*, Phys. Rev. Lett. **84**, 35 (2000).

[290] F. Azaiez *et al.*, in *AIP Conference Proceedings 481*, edited by C. Baktash (Amer. Inst. Phys., Gatlinburg, Tennessee, 1998), p. 243.

[291] S. Wan *et al.*, Eur. Phys. J. A **6**, 167 (1999).

[292] M. Belleguic *et al.*, Phys. Scripta Topical Issues **T88**, 122 (2000).

[293] K. Yoneda *et al.*, Phys. Lett. B **499**, 233 (2001).

[294] T. Motobayashi *et al.*, Phys. Lett. B **346**, 9 (1995).

[295] H. Scheit *et al.*, Phys. Rev. Lett. **77**, 3967 (1996).

[296] T. Glasmacher *et al.*, Phys. Lett. B **395**, 163 (1997).

[297] T. Glasmacher, Annu. Rev. Nucl. Part. Sci. **48**, 1 (1998).

[298] R. W. Ibbotson *et al.*, Phys. Rev. Lett. **80**, 2081 (1998).

[299] M. Belleguic *et al.*, Nucl. Phys. A **682**, 136c (2001).

[300] C. Thibault *et al.*, Phys. Rev. C **12**, 644 (1975).

[301] F. Touchard *et al.*, Phys. Rev. C **25**, 2756 (1982).

[302] E. K. Warburton, J. A. Becker, and B. A. Brown, Phys. Rev. C **41**, 1147 (1990).

[303] N. A. Orr *et al.*, Phys. Lett. B **258**, 29 (1991).

[304] D. J. Vieira *et al.*, Phys. Rev. Lett. **57**, 3253 (1986).

[305] X. G. Zhou *et al.*, Phys. Lett. B **260**, 285 (1991).

[306] C. Détraz *et al.*, Phys. Rev. C **19**, 164 (1979).

[307] C. Détraz *et al.*, Nucl. Phys. A **394**, 378 (1983).

[308] D. Guillemaud-Müller *et al.*, Nucl. Phys. A **426**, 37 (1984).

[309] R. F. Casten, *Nuclear Structure from a Simple Perspective* (Oxford University Press, New York, 2000).

[310] T. Otsuka, Y. Utsuno, T. Mizusaki, and M. Honma, Nucl. Phys. A **685**, 100c (2001).

[311] T. Otsuka, Y. Utsuno, T. Mizusaki, and M. Honma, Nucl. Phys. A **682**, 155c (2001).

[312] P.-G. Reinhard *et al.*, Phys. Rev. C **60**, 014316 (1999).

[313] P. E. Haustein Editor, At. Data Nucl. Data Tables **39**, 185 (1988).

[314] Z. Ren, Z.Y. Zhu, Y.H. Cai, and G. Xu, Phys. Lett. B **380**, 241 (1996).

[315] F. Sarazin *et al.*, Phys. Rev. Lett. **84**, 5062 (2000).

[316] X. Campi, H. Flocard, A. K. Kerman, and S. Koonin, Nucl. Phys. A **251**, 193 (1975).

[317] T. Otsuka *et al.*, Nucl. Phys. A **588**, 113c (1995).

[318] P. Haensel, J. Zdunik, and J. Dobaczewski, Asron. Astrophys. **222**, 353 (1989).

[319] R. Smolańczuk and J. Dobaczewski, Phys. Rev. C **48**, R2166 (1993).

[320] J. Dobaczewski, W. Nazarewicz, and T. Werner, Phys. Scripta Topical Issues **56**, 15 (1995).

[321] B. Chen *et al.*, Phys. Lett. B **355**, 37 (1995).

[322] J. M. Pearson, R. C. Nayak, and S. Goriely, Phys. Lett. B **387**, 455 (1996).

[323] M. Barranco and R. J. Lombard, Phys. Lett. B **78**, 542 (1978).

[324] P. Moller and J. R. Nix, At. Data Nucl. Data Tables **26**, 165 (1981).

[325] R. Bengtsson, P. Møller, J. R. Nix, and J.-y. Zhang, Physica Scr. **29**, 402 (1984).

[326] B. H. Wildenthal and W. Chung, Phys. Rev. C **22**, 2260 (1980).

[327] A. Poves and J. Retamosa, Phys. Lett. B **184**, 311 (1987).

[328] G. Lalazissis, A. R. Farhan, and M. M. Sharma, Nucl. Phys. A **628**, 221 (1998).

[329] S. K. Patra and C. R. Praharaj, Phys. Lett. B **273**, 13 (1991).

[330] J.-F. Berger*et al.*, Inst. Phys. Conf. Ser. **132**, 487 (1992).

[331] F. Grümmer, B. Q. Chen, Z. Y. Ma, and S. Krewald, Phys. Lett. B **387**, 673 (1996).

[332] J. Terasaki, H. Flocard, P.-H. Heenen, and P. Bonche, Nucl. Phys. A **621**, 706 (1997).

[333] N. El Aouad *et al.*, Nucl. Phys. A **676**, 155 (2000).

[334] M. A. Riley *et al.*, Acta Phys. Polonica B **32**, 2683 (2001).

[335] T. K. Alexander and J. S. Forster, Adv. Nucl. Phys. **10**, 197 (1978).

[336] R. W. Laird, Ph.D. thesis, Florida State University, 2000.

[337] E. F. Moore *et al.*, in *Proc. Conf. Nuclear Structure at the Limits* (ANL/PHY-97/1, Argonne, IL, 1996), p. 72.

[338] J. F. Ziegler, J. P. Biersack, and U. Littmark, *The Stopping and Range of Ions in Solids* (Pergamon Press, New York, 1985).

Appendix

Appendix A

Doppler–Shift Attenuation Measurement of Q_O^π

The *centroid-shift* technique [335] can be used with the DSAM in many different ways [336]. The Doppler–shifted energy (defined as the centroid of the energy distribution) of a γ–ray E_0 emitted by a compound nucleus recoiled in the target with a velocity $v(t)$ at angle θ with respect to the recoil direction is

$$E_\gamma(\theta, t) = E_0 \frac{\sqrt{1-\beta(t)^2}}{1-\beta(t)\cos\theta}, \tag{A.1}$$

where $\beta(t) = v(t)/c$ is the relativistic velocity factor. The velocity is typically less than $0.1c$ for the commonly–used heavy–ion reactions, which allows for the approximation $(1-\beta(t)\cos\theta)^{-1} \approx 1+\beta(t)\cos\theta$. The fact that the nucleus is slowed down in the backing material of the target leads to a smearing–out of the function $\beta(t)$ as a distribution of velocity factors $F(\tau)\beta'$ around the mid–target recoil velocity β', which defines the so–called *fractional Doppler shift* $F(\tau)$, a function of the transition's lifetime τ, Fig. A (hence the name of the technique).

This allows the expression for the Doppler–shifted centroid transition energy to be rewritten as

$$E_\gamma(\theta) = E_0(1 + F(\tau)\beta'\cos\theta), \tag{A.2}$$

which gives the following explicit form for the fractional Doppler shift

$$F(\tau) = \frac{E_\gamma(\theta) - E_0}{E_0\beta'\cos\theta}, \tag{A.3}$$

and can be extracted from the "forward" and "backward" angle spectra. This simple equation is valid for bands without feeding from higher levels (its inclusion requires some modification of the above formula). The relation of the function $F(\tau)$ to the mean lifetime τ is

$$F(\tau) = \frac{1}{\tau\beta(t=0)} \int_0^\infty \beta(t) e^{-\frac{t}{\tau}} dt. \tag{A.4}$$

The integrated kernel $\beta(t)$ in this case needs to be evaluated using the stopping powers of the target and its backing material leaving τ as the only unknown parameter. The lifetime determined this way can be associated with the reduced $E2$ transition probability

$$B(E2, I_i \to I_f) = \frac{5}{16\pi} Q_0^2 \langle I_i K, 20 | I_f K \rangle^2 \tag{A.5}$$

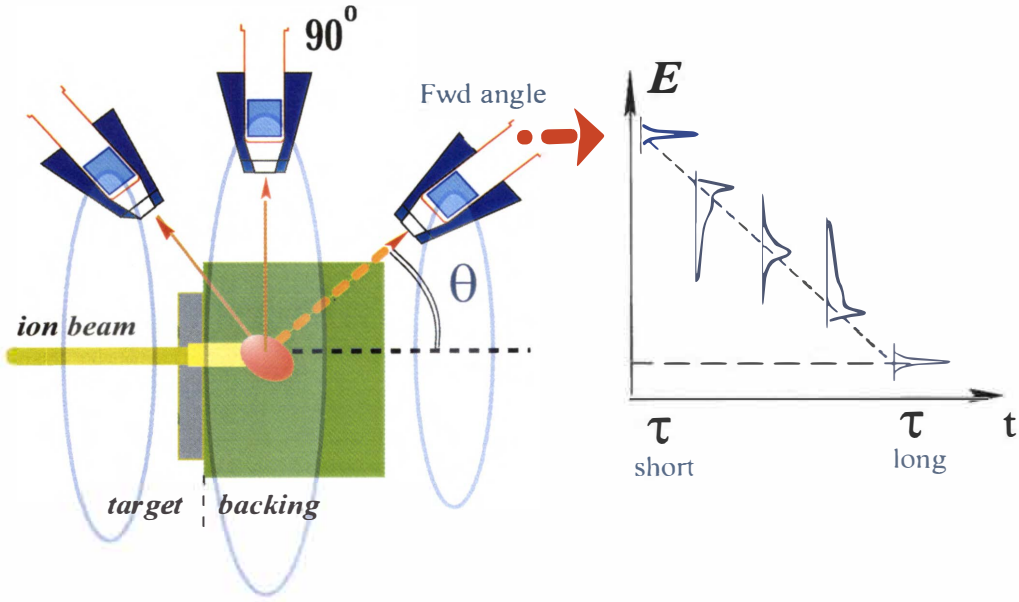

Figure A.1: Schematic diagram of the Doppler Shift Attenuation (DSAM), illustrating the relation between lifetime and the range between unshifted and fully shifted centroids of the transitions. Refer to the text for details and definitions. Adapted from [336].

for $I_i = I$ and $I_f = I - 2$, expressed in units of $(e\ \mathrm{fm}^2)^2$

$$\tau = \frac{817.66\lambda}{E_0^5 B(E2)}\,[ps]\,, \tag{A.6}$$

and E_0 is given in MeV. The branching ratio λ in this formula is defined as the ratio between the intensity of the $E2$ transition depopulating the level, $I(E2)$, and the total intensity of all depopulating levels, $\sum_i I_i(1+\alpha_{\mathrm{tot}})$, in which α_{tot} is the total. The intrinsic quadrupole moment, in units of eb, is then obtained as

$$Q_0 = \frac{0.907}{\langle IK20\,|(I-2)K\rangle}\sqrt{\frac{\lambda}{\tau E_0^5}} \tag{A.7}$$

In the example of experimental study quoted above there are two major methods for applying the centroid–shift method :

- For the most intense bands, the data are sorted into two-dimensional matrices for two sets of axes for the following groups of detectors : i) the "forward" angle (θ=31.7°, 37.4° rings on GAMMASPHERE), and the "backward" angle group (θ=142.6°, 148.3° rings) detectors; ii) the axis consisted of any coincident detector in the setup. The spectra are used to extract the fractional Doppler shift, F(τ), (*i.e.*, the fraction of the full shift), as

a function of the lifetime τ for transitions within the band using the expression

$$F(\tau) = \frac{E_\gamma(\theta) - E_0}{E_0 \beta' \cos(\theta)}. \tag{A.8}$$

The spectra are generated by summing up the gates at the bottom of the selected band (which are the cleanest, corresponding to fully–stopped transitions), and then the collected events are projected onto the "forward" and "backward" axes. The measured value of $F(\tau)$ depends not only on the lifetime of particular states, but also on the entire cascade of transitions preceding it,

- The data are sorted into double–gated spectra from chosen groups of detectors, for example, when the bands are strongly populated, the gates can be set on in–band Doppler–shifted, *i.e.* moving transitions in any of the rings of detectors, and then sorted out into separate spectra for *forward*, *90°*, and *backward* angles (*Doppler–shifted*, or *moving* gates). The gated transitions are Doppler–shifted and the Doppler corrections applied in the sorting of the gates are estimated from the uncorrected channel numbers C_0 using the formula

$$C = C_0(1 + F(\tau)\beta' \cos\theta), \tag{A.9}$$

in which $E_\gamma(\theta)$ is the centroid of the γ–ray energy distribution as measured in a detector at some angle θ with respect to the beam direction, and E_0 is the unshifted γ-ray energy. The values of $F(\tau)$ are calculated by iteratively varying the in–band value of Q_0 until the Doppler–corrected peaks in the spectra match in the detector rings at all angles. When the Doppler-shifted gates are set on the highest spin transitions of the chosen band, it becomes easy to eliminate the sidefeeding effect for the band states appearing lower in the cascade, which makes transitions with very low intensity distinguishable from the rest, when other approaches to detect them would fail.

It was observed, for example [148], that for the highly–deformed bands built on the ν $i_{13/2}$ intruder states of interest in the A$\simeq$130 region, the quadrupole moment obtained using method A is increased by about 10%, as compared with the value extracted using method A by gating on the transitions at the bottom of the same band. The fitting procedure [337] assumes a constant value of Q_0. In the modeling of the slowing processes of the recoiling nuclei, the stopping powers can be calculated using the code TRIM [338].

Although the uncertainties in the stopping powers and the modeling of the side–feeding may contribute an additional systematic error of 15−20% in the absolute Q_0 values, the relative values are considered to be accurate to about 5−10%. Such precision allows for a clear differentiation between the polarizability of different orbital configurations for a variety of N and Z values.

Vita

Mladen T. Matev was born on April 19, 1962 in Sofia, Bulgaria. He graduated from the Sofia Mathematical High School "Paisij Hilendarsky" in Sofia in the Spring of 1980. While in high school, he participated in science olympic competitions at city and national level, achieving 2nd prize in mathematics in 1979 (a research paper on the properties of regular polyhedra). Having passed the highly competitive entrance exams the same year, he was admitted for study at Sofia University "St. Clement Okhridsky", and enrolled as a student at the Physics Department. In 1982–83 he started working in the field of nuclear physics, as a Research Assistant to Prof. Borislav D. Slavov at the Department of Physics. He graduated *cum laude* with a *Master of Science* degree in Nuclear and Elementary Particle Physics from Sofia University in November of 1985, after defending a *Thesis* entitled "Multipole Moments as Deformation Parameters for the Description of Fission Fragment Mass Asymmetry", and receiving an Award for Best Graduate Student Research presentation (Sofia University, 1984). The next year he was employed as a *Physicist* at the Division of Nuclear Technology and Nuclear Energy of the Department of Physics, Sofia University. In June 1986 Mr. Matev won the competition for admission to *Ph.D.* studies at Sofia University involving research in the field of computational methods for the study of diabaticity in large amplitude collective nuclear motion, and their applications to the nuclear fission process at low energies. He completed all requirements for the Ph.D. degree, passed comprehensive examinations in Nuclear Physics, Philosophy, and Foreign Languages. During the period of 1986–1992 he specialized in the field of Physics of the Atomic Nucleus and Computational Physics, and in 1990 he was employed as a *System Manager* of the Laboratory for Computational Methods in Physics, Center for Space Research and Technologies, and *Physicist* at the Division of Theoretical Physics, Sofia University. In addition to his studies in nuclear collective motion, he participated in the numeric design of an experimental Mössbauer spectrometer at the Division of Atomic Physics of the Physics Department, maintained the Department's computational and network facilities, assisted the faculty with their numerically intensive work, and taught undergraduate classes in physics, mathematics, and numerical methods.

In the Summer of 1992 Mr. Matev was admitted to the Ph.D. program of the University of Tennessee, Knoxville, accepting a Teaching Assistantship, and later — a Research Assistantship in Nuclear and Computational Physics under the leadership of Prof. Michael W. Guidry. He was involved in computational reseach using the Fermion Dynamical Symmetry Model, the Projected Shell Model, and numerical methods for angular momentum projection at high spins. Pursuing further his interest in Nuclear Physics and Structure studies, he was admitted to candidacy, and continued his research with Prof. W. Nazarewicz at UT/ORNL in 1997. This dissertation is the culmination of his research over a period of the last 5 years at the UT Department of Physics and ORNL.

Mr. Matev became a member of the Bulgarian Physical Society (1984), *Sigma Pi Sigma*, the Physics Honor Society (1994), and the American Physical Society (1998). In 1993–94 he won the Hilton A. Smith Graduate Fellowship from the UT Graduate School. He participated in the *Sigma Xi* Graduate Student Research Competitions (2001–2002), winning a Second Prize in 2002, and was involved in the U.S. D.O.E. Computational Science Educational Project as a student participant. His other interests include optics, software design, computer imaging and visualization, electronics, and photography, as well as history and human civilization, geography, travel, marine culture and archaeology, music, and a variety of hobbies and sports.

7797 0196 34
11/05/03 MAB